

**SISSA**

Scuola  
Internazionale  
Superiore di  
Studi Avanzati

Physics Area - PhD course in  
Theory and Numerical Simulation  
of Condensed Matter Physics

Lattice gauge theories and constrained  
systems: from quantum simulation to  
non-equilibrium dynamics

Candidate:  
Federica Maria SURACE

Advisors:  
Dr. Marcello DALMONTE  
Prof. Alessandro SILVA

Academic Year 2020-21





## Preface

In the last decade the non-equilibrium dynamics of isolated quantum systems has raised a huge interest for both its conceptual and practical implications. Simulation of quantum dynamics represents by now a very active research effort, with highly controllable quantum devices composed of hundreds of qubits already being realized in numerous setups. These offer the unprecedented possibility to access real-time quantum dynamics and strongly correlated quantum many-body states, opening numerous avenues not only for future quantum technologies, but also for long-standing theoretical problems.

One of the most sought-after applications is the computation of real-time evolution in theories of fundamental interactions. Since Wilson's proposal in 1974, the equilibrium phase diagrams of lattice gauge theories have been successfully investigated with Monte Carlo simulations in a wide range of parameters. Nonequilibrium properties, on the other hand, cannot be accessed with conventional techniques. Thanks to the recent advances in numerics (e.g. tensor networks) and experiments (quantum simulation), new promising tools are now available for tackling these questions. Remarkable works have already demonstrated that applying these techniques to simple theories, such as one-dimensional quantum electrodynamics, can help to detect the signatures of confinement and pair creation. Despite these impressive achievements, investigating the non-equilibrium dynamics of gauge theories with quantum simulators turned out to be extremely challenging. This is mostly due to the complex constrained dynamics of these theories, which make their simulation with realistic atomic platforms particularly difficult.

At the same time, the dynamical constraints can play a key role in determining novel interesting phenomena and peculiar non-equilibrium properties. These phenomena – which include, for example, quantum scars, fractons, Hilbert space fragmentation – can lead to anomalous dynamics, eventually evading the paradigm of thermalization, which predicts the relaxation of physical observable to their thermodynamic values.

The aim of this thesis is twofold: first, we want to address through a combination of numerical and analytical tools some of the open questions regarding the non-equilibrium dynamics of quantum many-body systems with constrained Hilbert spaces, including lattice gauge theories. In addition, the work reported here is part of a large effort of the community towards the quantum simulation of complex phenomena of condensed matter and high-energy physics.

The thesis is structured as follows. Part [I](#) focuses on the emergence of non-thermal states (quantum scars) in the non-equilibrium dynamics of constrained quantum many-body systems. In [Chapter 1](#) we introduce the general phenomenology of quantum thermalization and some exceptions to it (many-body localization and quantum many-body scars). Quantum many-body scars and their stability are studied more in detail in the rest of

Part I: in Chapter 2 we investigate if quantum scars are stable with respect to perturbations in the Hamiltonian and if they persist when the dynamical constraints are enlarged; a different perspective on the stability of quantum scars is presented in Chapter 3, where we focus on the network structure of constrained models; finally, in Chapter 4 we study the emergence of scars in supersymmetric lattice models. In Part II the quantum simulation of lattice gauge theories is discussed: after introducing the main challenges of the field in Chapter 5, we show that a  $U(1)$  lattice gauge theory can be simulated with Rydberg atoms arrays and we characterize the dynamics of the model (Chapter 6); finally, in Chapter 7 we propose a protocol for the scalable quantum simulation of  $SU(N)\times U(1)$  lattice gauge theories with alkaline-earth like atoms in optical lattices. In Part III we give a unifying perspective on the previous Parts: we focus on the non-equilibrium dynamics of lattice gauge theories (a topic partially addressed in Chapter 6) and, more specifically, on the dynamics induced by the confinement of excitations. In Chapter 8 we explain what confinement is and why it affects the real-time evolution; in Chapter 9 we analyse more in detail the mechanisms that lead to quasilocalized dynamics in models with confinement and the associated time scales; in Chapter 10 we use the tools developed in the previous Chapter to study the interaction between the excitations of a confined model and to characterize their scattering properties; a related question is addressed in Chapter 11, where we focus on the decay of a metastable (false vacuum) state; in Chapter 12 we show how the previous results about the confined nature of excitations in an Ising spin chain generalize to a more complicated model, namely a Heisenberg-Ising spin ladder; finally, in Chapter 13 we discuss how another mechanism can induce localization in lattice gauge theories, even in a deconfined regime. Part IV contains additional information about the results presented in the previous Parts.

## List of publications

The thesis is based on the following publications:

- Chapter 2** – [1] F.M. Surace, M. Votto, E.G. Lazo, A. Silva, M. Dalmonte and G. Giudici, *Exact many-body scars and their stability in constrained quantum chains*, *Phys. Rev. B* **103** (2021) 104302.
- Chapter 3** – [2] F.M. Surace, M. Dalmonte and A. Silva, *Quantum local random networks and the statistical robustness of quantum scars*, [2107.00884](#).
- Chapter 4** – [3] F.M. Surace, G. Giudici and M. Dalmonte, *Weak-ergodicity-breaking via lattice supersymmetry*, *Quantum* **4** (2020) 339.
- Chapter 6** – [4] F.M. Surace, P.P. Mazza, G. Giudici, A. Lerose, A. Gambassi and M. Dalmonte, *Lattice Gauge Theories and String Dynamics in Rydberg Atom Quantum Simulators*, *Phys. Rev. X* **10** (2020) 021041.
- Chapter 7** – [5] F.M. Surace, P. Fromholz, F. Scazza and M. Dalmonte, *A scalable, ab initio protocol for quantum simulating  $SU(N)\times U(1)$  Lattice Gauge Theories with alkaline-earth like atoms*, to appear
- Chapter 9** – [6] A. Lerose, F.M. Surace, P.P. Mazza, G. Perfetto, M. Coltura and A. Gambassi, *Quasilocalized dynamics from confinement of quantum excitations*, *Phys. Rev. B* **102** (2020) 041118.
- Chapter 10** – [7] F. Surace and A. Lerose, *Scattering of mesons in quantum simulators*, *New Journal of Physics* **23** (2021) 062001.
- Chapter 11** – [8] G. Lagnese, F.M. Surace, M. Kormos and P. Calabrese, *False vacuum decay in quantum spin chains*, [2107.10176](#).
- Chapter 12** – [9] G. Lagnese, F.M. Surace, M. Kormos and P. Calabrese, *Confinement in the spectrum of a Heisenberg–Ising spin ladder*, *J. Stat. Mech.* **2009** (2020) 093106.
- Chapter 13** – [10] G. Giudici, F.M. Surace, J.E. Ebot, A. Scardicchio and M. Dalmonte, *Breakdown of ergodicity in disordered  $U(1)$  lattice gauge theories*, *Phys. Rev. Research* **2** (2020) 032034.

Other articles published during the Ph.D. course:

- [11] A. Russomanno, S. Notarnicola, F.M. Surace, R. Fazio, M. Dalmonte and M. Heyl, *Homogeneous Floquet time crystal protected by gauge invariance*, *Phys. Rev. Research* **2** (2020) 012003

- [12] A. Offei-Danso, F.M. Surace, F. Iemini, A. Russomanno and R. Fazio, *Quantum clock models with infinite-range interactions*, *Journal of Statistical Mechanics: Theory and Experiment* **2020** (2020) 073107
- [13] P. Sierant, G. Chiriacò, F.M. Surace, S. Sharma, X. Turkeshi, M. Dalmonte et al., *Dissipative Floquet Dynamics: from Steady State to Measurement Induced Criticality in Trapped-ion Chains*, [2107.05669](#)

# Contents

<b>I</b>	<b>Non-equilibrium dynamics in constrained quantum systems</b>	<b>1</b>
<b>1</b>	<b>Non-equilibrium dynamics of quantum many-body systems</b>	<b>3</b>
1.1	Thermalization in quantum systems . . . . .	4
1.1.1	The eigenstate thermalization hypothesis . . . . .	5
1.2	Many body localization . . . . .	6
1.3	Weak ergodicity breaking: quantum many-body scars . . . . .	8
1.3.1	Rydberg atom experiment . . . . .	9
1.3.2	PXP model . . . . .	10
1.3.3	Open questions . . . . .	12
<b>2</b>	<b>Exact many-body scars and their stability in constrained quantum chains</b>	<b>15</b>
2.1	PXP model . . . . .	16
2.2	Perturbation theory and Eigenstate Thermalization Hypothesis	18
2.3	Models with radius of constraint $\alpha > 1$ . . . . .	22
2.3.1	Spectral statistics . . . . .	23
2.3.2	Exact scars with $E = 0$ . . . . .	23
2.3.3	Exact scars with $E \neq 0$ . . . . .	25
2.3.4	Relation with exact scars for $\alpha = 1$ . . . . .	27
2.3.5	Stability . . . . .	27
2.4	Conclusions . . . . .	28
<b>3</b>	<b>Quantum local random networks and the statistical robustness of quantum scars</b>	<b>31</b>
3.1	Quantum local random networks . . . . .	32
3.2	Localized eigenstates . . . . .	34
3.3	Statistical scars . . . . .	36
3.4	Conclusions and outlook . . . . .	37
<b>4</b>	<b>Weak-ergodicity-breaking via lattice supersymmetry</b>	<b>39</b>
4.1	Supersymmetric lattice models . . . . .	40
4.2	Exact eigenstates at finite energy density: two-leg ladders . . . . .	41
4.3	Exact scars in $d$ -dimensional hypercubic lattices . . . . .	43
4.4	Spectral statistics in two-leg ladders . . . . .	43

4.5	Robustness to perturbations . . . . .	45
4.6	Connection to the Shiraishi-Mori construction . . . . .	47
4.7	Conclusions and outlook . . . . .	47
<b>II</b>	<b>Quantum simulation of lattice gauge theories</b>	<b>49</b>
<b>5</b>	<b>Quantum simulation of high-energy physics</b>	<b>51</b>
5.1	Hamiltonian formulation of lattice gauge theories . . . . .	52
5.1.1	Example: the lattice Schwinger model . . . . .	53
5.2	Quantum Link Models . . . . .	55
5.3	Strategies for quantum simulation of lattice gauge theories . . . . .	55
5.4	Quantum simulation platforms . . . . .	59
5.5	Conclusions . . . . .	62
<b>6</b>	<b>Lattice gauge theories and string dynamics in Rydberg atom quantum simulators</b>	<b>65</b>
6.1	Rydberg atom arrays . . . . .	66
6.2	Rydberg blockade as a gauge symmetry constraint . . . . .	67
6.3	Real-time dynamics of lattice gauge theories in Rydberg atom experiments . . . . .	70
6.3.1	Gauge-theory interpretation of slow dynamics . . . . .	70
6.3.2	Slow dynamics in the Schwinger model . . . . .	73
6.3.3	Propagation of particle-antiparticle pairs . . . . .	75
6.3.4	Spectral properties and bands of non-thermal states . . . . .	77
6.3.5	Tuning the topological $\theta$ -angle in Rydberg experiments . . . . .	80
6.4	Conclusions . . . . .	82
<b>7</b>	<b>Non-Abelian lattice gauge theories with alkaline-earth-like atoms</b>	<b>85</b>
7.1	<i>Ab initio</i> derivation of the lattice model . . . . .	88
7.2	Resonance conditions . . . . .	89
7.3	Off-resonance conditions . . . . .	89
7.4	1D lattice setup and parameters . . . . .	90
7.5	Generalization to $N > 2$ and 2D lattice setup . . . . .	91
7.6	Preparation of the initial state . . . . .	92
7.7	Discussion and conclusion . . . . .	93
<b>III</b>	<b>Non-equilibrium dynamics of lattice gauge theories</b>	<b>95</b>
<b>8</b>	<b>Confinement: physical mechanism and consequences on non-equilibrium</b>	<b>97</b>
8.1	What is confinement? . . . . .	98
8.1.1	Confinement and gauge flux lines . . . . .	99

8.1.2	String breaking . . . . .	100
8.2	Confinement in one-dimensional ferromagnets and antiferromagnets . . . . .	101
8.2.1	The quantum Ising chain in transverse and longitudinal field . . . . .	102
8.2.2	The quantum Ising chain as a lattice gauge theory . . . . .	102
8.3	Non-equilibrium dynamics . . . . .	103
8.4	Outlook . . . . .	104
<b>9</b>	<b>Quasilocalized dynamics from confinement of quantum excitations</b> . . . . .	<b>107</b>
9.1	Exponential suppression of string breaking . . . . .	109
9.1.1	Perturbative construction . . . . .	110
9.1.2	Time scale . . . . .	111
9.2	Prethermalization and Stark localization . . . . .	112
9.2.1	Two-body effective model and delocalization time . . . . .	112
9.3	Slow entanglement growth . . . . .	114
9.4	Outlook . . . . .	115
<b>10</b>	<b>Scattering of mesons</b> . . . . .	<b>117</b>
10.1	Confinement and mesons . . . . .	118
10.2	Scattering amplitudes . . . . .	119
10.3	Quantum simulation . . . . .	123
10.4	Outlook . . . . .	125
<b>11</b>	<b>False vacuum decay in quantum spin chains</b> . . . . .	<b>127</b>
11.1	False vacuum decay . . . . .	128
11.2	Quench protocol and methods . . . . .	129
11.3	Time scales . . . . .	130
11.4	Results . . . . .	131
11.5	XXZ ladder . . . . .	132
11.6	Conclusions and outlook . . . . .	134
<b>12</b>	<b>Confinement in the spectrum of a Heisenberg-Ising spin ladder</b> . . . . .	<b>137</b>
12.1	Elementary excitations in the strong anisotropy regime . . . . .	140
12.1.1	‘Type 1’ intrachain mesons . . . . .	142
12.1.2	‘Type 2’ interchain mesons . . . . .	146
12.2	A semiclassical approach for finite $\Delta_{  }$ . . . . .	149
12.3	Composite excitations . . . . .	153
12.4	A transition for the first excited states . . . . .	156
12.5	Conclusions . . . . .	157

<b>13 Breakdown of ergodicity in disordered U(1) lattice gauge theories</b>	<b>161</b>
13.1 Model Hamiltonian . . . . .	163
13.2 Spectral diagnostics: average level spacing ratio . . . . .	164
13.3 Spectral diagnostics: form factor . . . . .	166
13.4 Origin of ergodicity breaking . . . . .	168
13.5 Conclusions and outlook . . . . .	170
<b>IV Appendix</b>	<b>171</b>
<b>A Non-equilibrium dynamics in constrained quantum systems</b>	<b>173</b>
A.1 Properties of the PXP and the other constrained models . . . . .	173
A.1.1 Scars . . . . .	173
A.2 Stability to other perturbations . . . . .	174
A.3 Exact scars in the PXP model – properties of the edges . . . . .	174
A.4 Exact scars with $E = \sqrt{3}$ – Proof . . . . .	176
A.5 Exact scars with $E = \sqrt{2}$ , $\alpha = 3$ . . . . .	178
A.5.1 Proof . . . . .	179
A.6 Spectra of QLRN . . . . .	182
A.7 Generalized QLRN . . . . .	183
A.8 Participation ratio and system size . . . . .	184
A.9 Centrality and degree of statistical scars . . . . .	184
A.10 Eigenstate phase transition at different $\epsilon^*$ . . . . .	185
<b>B Quantum simulation of lattice gauge theories</b>	<b>187</b>
B.1 Entanglement evolution in the FSS model . . . . .	187
B.2 Spectral properties of the FSS model . . . . .	188
B.3 Continuum limit of the massive Schwinger model . . . . .	189
B.4 Non-Abelian lattice gauge theories with alkaline-earth-like atoms: derivation of the lattice Hamiltonian . . . . .	191
B.4.1 Localized Wannier functions . . . . .	191
B.4.2 Amplitude formulae . . . . .	194
B.5 Resonance condition and derivation of QLM Hamiltonian . . . . .	194
B.5.1 Resonance condition . . . . .	195
B.5.2 Off-resonance condition . . . . .	195
B.5.3 Projected Hamiltonian in 1D . . . . .	196
B.5.4 Correction to the resonance condition . . . . .	198
B.6 <i>Ab initio</i> values: additional data . . . . .	199
<b>C Non-equilibrium dynamics of lattice gauge theories</b>	<b>201</b>
C.1 Exact mapping between quantum spin chains and lattice gauge theories in one spatial dimension . . . . .	201
C.1.1 The quantum Ising chain as a $\mathbb{Z}_2$ LGT . . . . .	202
C.1.2 The quantum Ising chain as a U(1) LGT . . . . .	204

C.2	Construction of the effective Hamiltonian . . . . .	206
C.2.1	Effective Hamiltonian of the quantum Ising chain . . .	207
C.3	Solution of the two-body problem . . . . .	209
C.4	Solution of the four-body problem . . . . .	213
C.5	Mesonic current . . . . .	214
C.5.1	Proof of the continuity equation . . . . .	217
C.6	Finite fermion mass . . . . .	217
C.7	Kink scattering phases . . . . .	219
C.8	Spectral statistics for non-zero topological angle . . . . .	220
<b>Bibliography</b>		<b>223</b>



# Part I

## Non-equilibrium dynamics in constrained quantum systems



# Chapter 1

## Non-equilibrium dynamics of quantum many-body systems

Statistical mechanics is based on the concept of thermal equilibrium. In virtue of this fundamental assumption, we can use few relevant quantities to describe our system of interest and discard the majority of the information about the enormous number of degrees of freedom that it contains. Understanding the origin of this assumption from microscopic dynamics is in general very difficult. In classical mechanics, the problem has long been studied and some rigorous foundations have been established based on the concept of ergodicity. In quantum physics, on the other hand, the field is relatively young and the major breakthroughs have been achieved only in the last 30 years. The problem of *quantum thermalization* has become of prominent interest thanks to recent experimental progress: it is now possible to control quantum systems that are – to very good approximation – isolated from any environment. It is then natural to ask whether, in the absence of a thermal bath, a quantum system can act as its own reservoir.

In these experiments, the simplest and most popular protocol for studying non-equilibrium properties is the *quantum quench*: a parameter of the Hamiltonian is changed abruptly at a time  $t_0$  and the time evolution of the system after this sudden change is monitored. In a typical case, expectation values of observables after a quench tend to relax to stationary values. For a thermalizing system, these values coincide with the ones prescribed by equilibrium statistical mechanics, and only depend on the energy density (and on the other conserved quantities, if present) of the initial state. However, this is not the only possibility: in *many-body localized* systems, the stationary values are non-thermal, meaning that they depend non-trivially on the initial state; in systems with *quantum scars*, for some initial states one can find that observables do not reach a stationary value, but they have persistent oscillations in time.

In this chapter we discuss all these scenarios<sup>1</sup>: in Section 1.1 we introduce

---

<sup>1</sup>Another scenario is represented by integrable systems, whose equilibrium properties

the concept of thermalization for closed quantum many-body systems and we show how it emerges from the *eigenstate thermalization hypothesis*; in Section 1.2 we examine the non-equilibrium phases of matter that can exist in virtue of *many-body localization*; in Section 1.3 we consider the case of *quantum many-body scars*, discussing both the experimental findings and the constrained lattice model that can explain their phenomenology.

For a comprehensive discussion of quantum thermalization we refer the reader to [14], for many-body localization to [15–17] for quantum scars to [18].

## 1.1 Thermalization in quantum systems

A closed quantum system undergoes a unitary evolution, that is apparently at odds with the concept of thermal equilibrium. To solve this paradox and understand how the information about the initial state  $|\psi_{\text{in}}\rangle$  can be lost in the time evolution, we should focus on a finite region  $A$  of our system. We are interested in the expectation value of a generic operator  $O_A$  with support on  $A$  in the thermodynamic limit (i.e., when the number  $N$  of degrees of freedom of the full system goes to infinity). We say that the system thermalizes if the long time limit of observables is given by the statistical ensemble average

$$\lim_{t \rightarrow \infty} \lim_{N \rightarrow \infty} \langle O_A \rangle (t) = \text{Tr}[O_A \rho_A^{\text{eq}}], \quad (1.1)$$

where  $\rho_A^{\text{eq}} = \text{Tr}_{\bar{A}}[Z^{-1} e^{-\beta H}]$  is the density matrix of the region  $A$  in the canonical ensemble at a temperature  $T = \beta^{-1}$  ( $H$  is the Hamiltonian of the full system,  $Z = \text{Tr}[e^{-\beta H}]$  is the partition function, and  $\bar{A}$  is the complement of  $A$ ). The inverse temperature  $\beta$  is such that the equilibrium energy density  $E^{\text{eq}}/N = \text{Tr}[Z^{-1} e^{-\beta H} H/N]$  is equal to the energy density of the initial state. If Eq. (1.1) holds for any observable on the region  $A$ , we have that the state  $\rho_A(t) = \text{Tr}_{\bar{A}}[e^{iHt} |\psi_{\text{in}}\rangle \langle \psi_{\text{in}}| e^{-iHt}]$  converges in the long-time limit to

$$\lim_{t \rightarrow \infty} \lim_{N \rightarrow \infty} \rho_A(t) = \rho_A^{\text{eq}}. \quad (1.2)$$

Crucially, the equilibrium state  $\rho_A^{\text{eq}}$  depends on the initial state  $|\psi_{\text{in}}\rangle$  only through the energy density: all the other information is effectively lost, as it is encoded in highly non-local degrees of freedom and cannot be accessed with local measurements on a finite portion of the system.

We also note that one of the consequences of Eq. (1.2) is that the (bipartite) von Neumann entanglement entropy, defined as  $S_A = -\text{Tr} \rho_A \ln \rho_A$ , corresponds – at long times – to the thermodynamic entropy of the subsystem  $A$  and is hence proportional to its volume  $N_A$  (up to subleading corrections).

---

are described by the generalized Gibbs ensemble. These systems, which represent an extremely vast subject on their own, will not be discussed in this thesis.

### 1.1.1 The eigenstate thermalization hypothesis

In the previous section, we have defined thermalization in a quantum system as the condition in Eq. (1.1). However, to this end it is not clear under which assumptions this property will hold. To answer this question, Deutsch and Srednicki proposed a conjecture that goes under the name of *eigenstate thermalization hypothesis* (ETH) [19, 20] and represents one of the pillars of the theory of quantum thermalization. The fundamental assumption behind ETH is that the matrix elements of observables in the basis of energy eigenstates  $\{|E_n\rangle\}$  in each symmetry sector of the Hamiltonian  $H$  have the form

$$O_{mn} \equiv \langle E_m | O | E_n \rangle = O(\bar{E})\delta_{mn} + e^{-S(\bar{E})/2} f_O(\bar{E}, \omega) R_{mn} \quad (1.3)$$

where  $\bar{E} \equiv (E_m + E_n)/2$ ,  $\omega \equiv E_n - E_m$ , and  $S(E)$  is the thermodynamic entropy at energy  $E$ . Both  $O(\bar{E})$  and  $f_O(\bar{E}, \omega)$  are smooth functions of their arguments, while  $R_{mn}$  is a random variable with zero mean and unit variance. The value  $O(\bar{E})$  represents the expectation value of the microcanonical ensemble at energy  $\bar{E}$ .

We now analyze what are the consequences of ETH on the properties of a quantum system. We consider the time evolution of a quantum system from an initial state  $|\psi_{\text{in}}\rangle$  and we are interested in the long-time average of an observable  $O$ . Under the assumption that there are no degeneracies in the spectrum, the long-time average of this quantity is given by the diagonal ensemble

$$\overline{\langle O \rangle} = \lim_{T \rightarrow \infty} \frac{1}{T} \int_0^T \langle O(t) \rangle \quad (1.4)$$

$$= \lim_{T \rightarrow \infty} \frac{1}{T} \int_0^T \sum_{n,m} O_{nm} e^{-i(E_m - E_n)t} \langle \psi_{\text{in}} | E_n \rangle \langle E_m | \psi_{\text{in}} \rangle \quad (1.5)$$

$$= \sum_n |\langle E_n | \psi_{\text{in}} \rangle|^2 O_{nn}. \quad (1.6)$$

If the energy fluctuations of  $|\psi_{\text{in}}\rangle$  are small in the thermodynamic limit (which is the case, for example, in a quantum quench), the assumption in Eq. (1.3) implies that  $\overline{\langle O \rangle}$  coincides with the microcanonical expectation value  $O(E)$  with  $E = \langle \psi_{\text{in}} | H | \psi_{\text{in}} \rangle$ . Moreover, ETH implies that the time fluctuations of  $\langle O \rangle$  are exponentially small in the system size (for a proof see for instance Ref. [14]). The convergence of the expectation values to the ones prescribed by equilibrium statistical mechanics is the very essence of quantum thermalization, and, as we showed, is a direct consequence of ETH.

The ETH has been tested numerically in a number of lattice models, both for diagonal and off-diagonal matrix elements [21–26]. As an example, in Fig. 1.1 we report the data for a lattice model of hard-core bosons. For  $J' = V' = 0$  the model is integrable and expectation values are non-thermal;

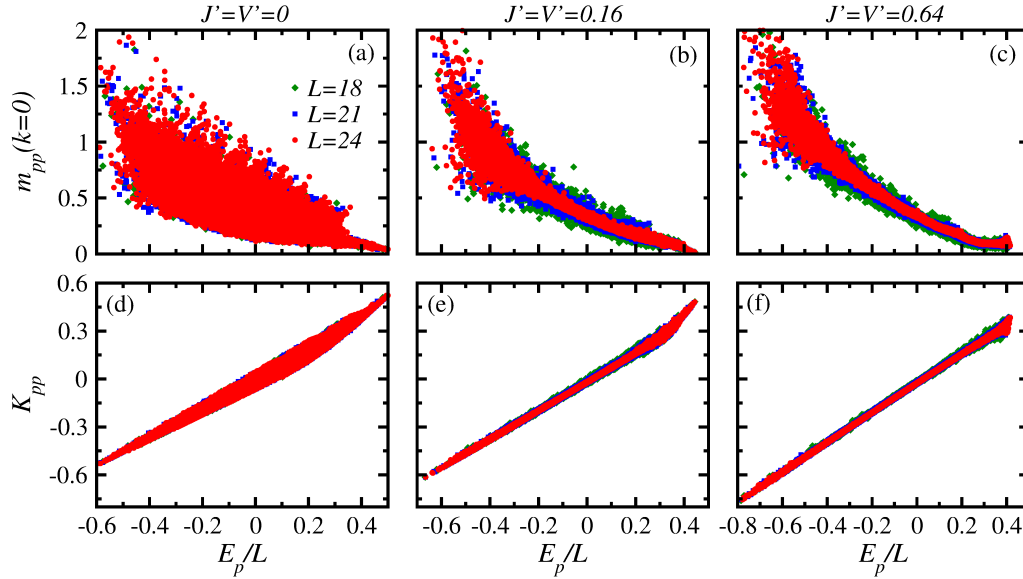


Figure 1.1: Eigenstate expectation values of the occupation of the zero momentum mode [(a)–(c)] and the kinetic energy per site [(d)–(f)] of hard-core bosons as a function of the energy per site. Figures taken from Ref. [14].

when the integrability breaking term is turned on, they show a trend towards the thermal expectation value for increasing system size.

## 1.2 Many body localization

Transport is a fundamental ingredient in the process of thermalization: excitations need to move across the system in order to allow for exchanges of energy between different regions. In the presence of quenched disorder, however, there might exist some excitations that are localized in space and do not decay. This phenomenon was first studied by Anderson in [27] for non-interacting fermions and goes under the name of Anderson localization. For a model of fermions hopping on a lattice with random on-site potential in one or two dimensions, the energy eigenstates are exponentially localized in space: a particle occupying one such state is a local excitation that does not relax. It was later found [28–31] that a similar mechanism – dubbed many-body localization (MBL) – occurs for interacting systems: in the presence of sufficiently strong disorder, local integrals of motion called  $l$ -bits emerge [16]; these  $l$ -bits locally retain the information about the initial state, hindering thermalization. As a consequence of the emergence of  $l$ -bits, many of the properties of thermalizing systems are not satisfied. For example, the bipartite entanglement entropy of energy eigenstates is proportional to the area of the cut, because only the  $l$ -bits that are located close to the cut (within a distance of the order of the localization length) contribute to the entanglement. This area law scaling of entanglement is satisfied also

by high-energy eigenstates, and is in sharp contrast with the volume law generically expected in virtue of equilibrium statistical mechanics. Many-body localized systems do not thermalize and the ETH is violated in the full spectrum: matrix elements of local observables in the energy eigenbasis are not smooth functions of the energy (the local spectrum is discrete). All these properties have been extensively studied with numerical methods in quantum spin chains [29,31–34]. As an example, we report here some of the results obtained for the XXZ chain in random longitudinal field

$$H_{XXZ} = \sum_i [J(S_i^x S_{i+1}^x + S_i^y S_{i+1}^y) + J_z S_i^z S_{i+1}^z + h_i S_i^z], \quad (1.7)$$

where  $S_i^\alpha$  are spin 1/2 operators and the static-random fields  $h_i$  are independent random variables at each site  $i$ , each with a probability distribution uniform in  $[-h, h]$ .

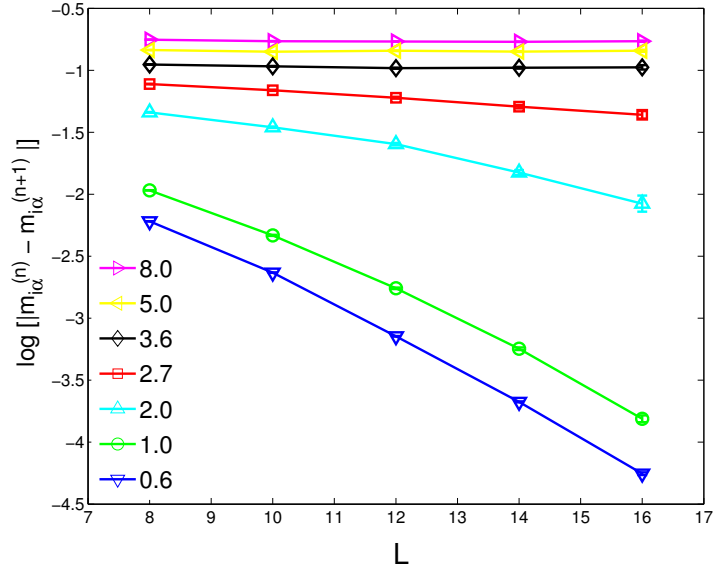


Figure 1.2: Logarithm of the averaged difference between the local magnetizations in adjacent eigenstates, with  $J = J_z = 1$ , and  $h$  as indicated in the legend. The average is over disorder realizations, states and sites. Figure taken from Ref. [31].

Fig. 1.2 shows that for weak disorder strength (small  $h$ ) the difference of the expectation values of local magnetization between adjacent eigenstates decays exponentially in  $L$ , as predicted by the ETH. On the other hand, for large disorder strength the difference is non-vanishing for large system sizes, suggesting that ETH is violated.

In Fig. 1.3 the scaling with system size  $L$  of the bipartite entanglement entropy  $S^E$  of the eigenstates is reported. As the disorder strength  $h$  is increased there is a transition from a volume law ( $S^E/L$  goes to a constant) to an area law ( $S^E/L$  decays to 0).

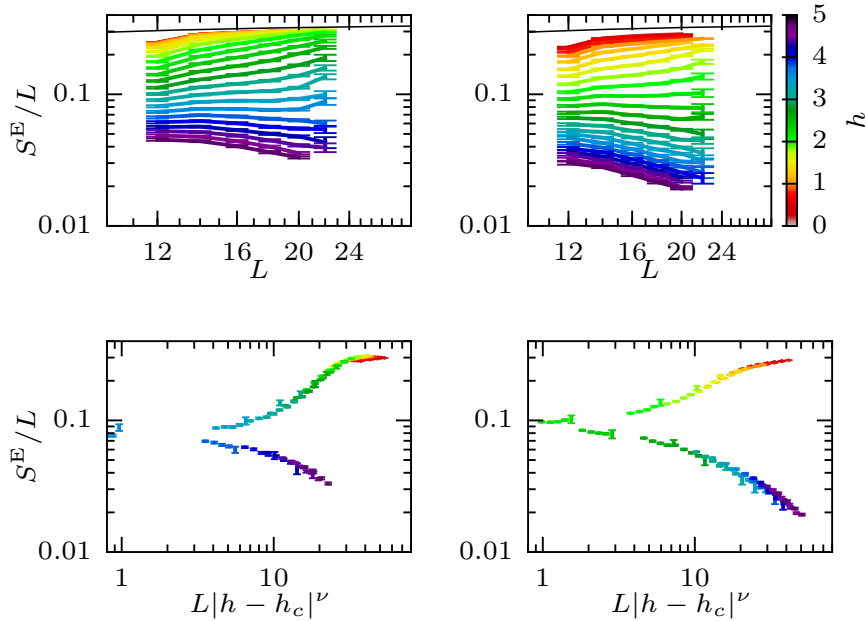


Figure 1.3: Finite size scaling of bipartite entanglement entropy of  $S^E$  in the middle of the spectrum (left) and in the upper part (right). Figure taken from Ref. [34].

Because it evades thermalization, MBL cannot be framed under the concepts of conventional equilibrium statistical mechanics. In particular, it has been shown that MBL can protect phases of matter that are not possible at equilibrium [15]. For example, high-energy eigenstates of one-dimensional MBL systems can spontaneously break discrete symmetries. This is not possible, instead, for thermalizing systems, whose high-energy eigenstates have the same properties of equilibrium states at finite temperature: spontaneous symmetry breaking in those eigenstates would imply a violation of Mermin-Wagner theorem [35], which prohibits symmetry-breaking at finite temperature for short-range interacting systems in one dimension. Other remarkable examples of MBL-protected quantum order were found for symmetry protected topological phases [15,32,36,37] and for periodically-driven systems [38–42]. In the latter case, in particular, it has been shown that MBL allows for the existence of the so-called "Floquet time crystals" [43,44]. A time crystal is a system with spontaneous breaking of time-translation symmetry, a feature that is not possible at equilibrium [45].

### 1.3 Weak ergodicity breaking: quantum many-body scars

Many-body localized and integrable systems are the most studied exceptions to the ETH. However, the emergence of local integrals of motion is

not the only mechanism that allows to avoid thermalization. A new phenomenon – *quantum many-body scars* – has recently been observed in a Rydberg atom experiment and has later been numerically identified in numerous spin chains. We now illustrate the concept of quantum many-body scars starting from the experimental observation and then introducing the theoretical results and the main open questions on the topic.

### 1.3.1 Rydberg atom experiment

The setting of the experiment performed by Bernien et al. [46] consists of a one-dimensional array of Rydberg atoms trapped in optical tweezers. Each atom of the chain is modelled by a spin 1/2: the state  $|0\rangle$  corresponds to the ground state and the state  $|1\rangle$  is an excited Rydberg state with high principal quantum number. A laser can couple the two states, inducing single-atom Rabi oscillations (in some experimental scenarios, such transition is actually driven by a pair of laser fields, via an intermediate, low-lying excited state). The Hamiltonian of the system is

$$H_{Rydberg} = \frac{\Omega}{2} \sum_i \sigma_i^x - \Delta \sum_i n_i + \sum_{i<j} V_{ij} n_i n_j, \quad (1.8)$$

where  $\Omega$  is the Rabi frequency inducing the transition ( $\sigma_i^x = |1\rangle_i \langle 0|_i + \text{h.c.}$ ) between the ground state and the Rydberg state,  $\Delta$  is the detuning of the lasers from the Rydberg state,  $n_i = |1\rangle_i \langle 1|_i$  is the occupation of the Rydberg state on site  $i$ , and  $V_{ij}$  is the interaction energy between Rydberg excitations.

The system is prepared in a charge density wave (CDW) state, with a Rydberg excitation at every odd trap, and the detuning  $\Delta$  is quenched from a large value to  $\Delta = 0$  (Fig. 1.4). The subsequent dynamics is rather unexpected: measurements of the Rydberg occupation  $n_i$  show that the many-body state oscillates between the initial state and the inverted state with a Rydberg excitation at every even trap. The oscillations persist on the full time range accessible in the experiment, longer than the timescales  $\Omega^{-1}$  and  $V_{i,i+1}^{-1}$ .

The persistent oscillations observed in this experiment represent a conundrum in the context of non-equilibrium dynamics. Although the energy density of the CDW state corresponds to the one of an infinite temperature state with respect to the quenched Hamiltonian, it seems that this state does not relax to thermal equilibrium, or it does well beyond observable timescales. However, for different initial states (e.g., for an initial state with no Rydberg excitations) the decay to thermal expectation values is rather fast, and no anomalous oscillations are observed. This phenomenon has been attributed to the so-called "quantum many-body scars" [47, 48], in analogy with a similar phenomenon in single-particle quantum chaos [49].

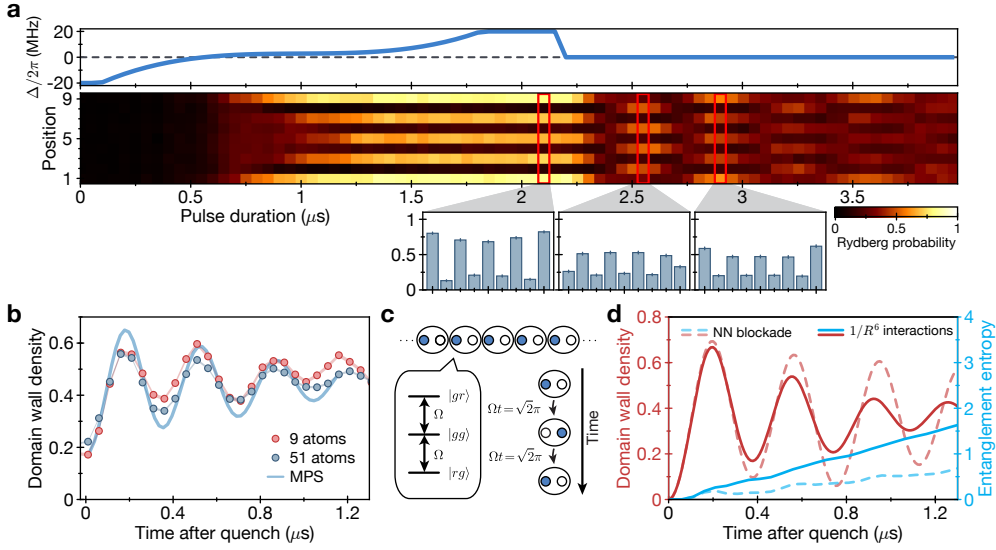


Figure 1.4: (a) The parameter  $\Delta$  is controlled in time in such a way to adiabatically prepare the CDW state, then quenched to  $\Delta = 0$ . The spatially resolved Rydberg probability is shown for an array of 9 atoms. (b) Domain-wall density after the quench. (c) Illustration of a toy model for the oscillations. (d) Numerical simulation of domain-wall density and entanglement entropy after the quench. Figure taken from Ref. [46].

### 1.3.2 PXP model

To understand the oscillations described above, it is convenient to consider the so-called PXP model. This model was first introduced in the context of constrained quantum models that can be directly related, in some parameter regimes, to exactly soluble classical statistical mechanics systems [50]. In Ref. [51], it was shown how the same type of dynamics describes Rydberg excitations in an atomic chain in the regime of nearest-neighbour blockade. In this regime, the interaction between Rydberg states on neighbouring sites is so large that the dynamics is effectively constrained to the subspace generated by the states with no consecutive "1"s.

Defining  $X_i, Y_i, Z_i$  as the Pauli matrices at site  $i$  and  $P_i = (1 - Z_i)/2$ ,  $n_i = (1 + Z_i)/2$ , the dynamics in the constrained space is described by

$$H_{PXP} = \sum_j P_{j-1} X_j P_{j+1}. \quad (1.9)$$

Because of Rydberg blockade, the Hamiltonian acts on the space constrained by the conditions  $n_i n_{i+1} = 0$  for every  $i$ .

The spectrum of the model was studied by Turner et al. [48] using exact diagonalization and shift-invert algorithm. As shown in the top panel of Fig. 1.5, for the majority of the eigenstates the expectation value of local

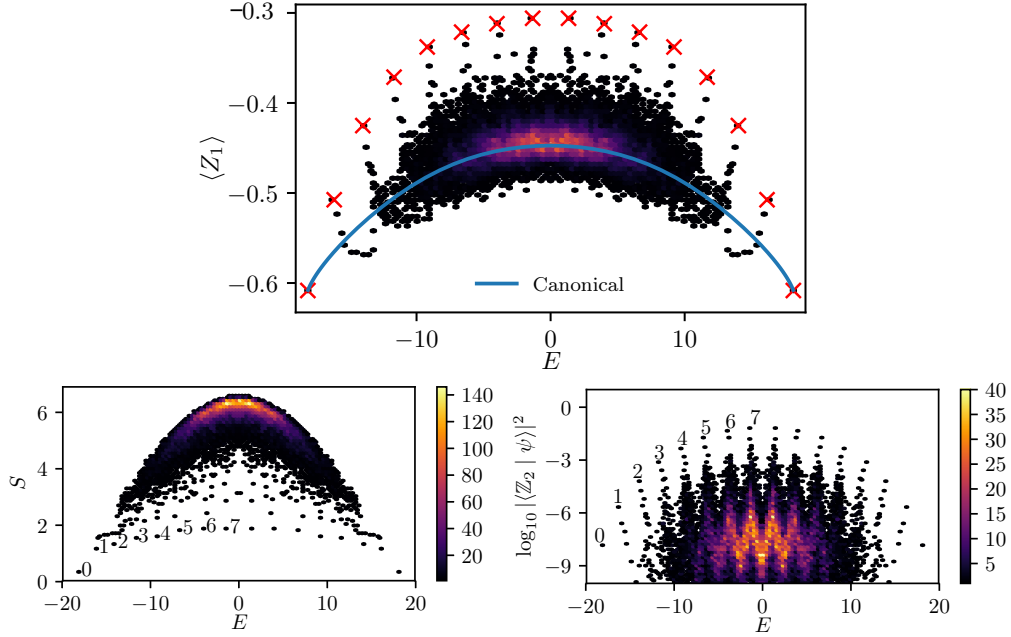


Figure 1.5: Expectation value of the local observable  $Z_1$  (top), bipartite entanglement entropy (bottom left) and logarithm of the overlap with the CDW state (bottom right) of the eigenstates as a function of their energy. Figures taken from Ref. [48].

observables lies close to the prediction of the canonical ensemble. However, there are some states (the "scars", indicated by a red cross) with highly non-thermal expectation values, and other states that look like towers departing from them, with weakly non-thermal values. The first states are almost equally spaced in energy, their number grows linearly with system size, and they form a band which extends across the whole spectrum, from the ground state to the highest energy state. Also the entanglement entropy  $S$  of these eigenstates shows non-thermal scaling (Fig. 1.5, lower left panel): compared to the cloud of thermal states with volume law entanglement entropy, the scarred eigenstates have anomalously small values, that scale with  $\log L$ . All these observations suggest that this model "weakly" breaks ergodicity, in the sense that few states [ $O(L)$  out of  $O(e^{cL})$  eigenstates] do not satisfy the ETH. One may expect that such a small number of states does not alter significantly the non-equilibrium dynamics after a quantum quench. While this is true for the majority of states that can be prepared in an experiment, the CDW state is a remarkable exception. The reason for this is illustrated in the lower right panel of Fig. 1.5: the CDW state ( $|\mathbb{Z}_2\rangle$ ) has substantially larger overlap with the band of scarred states than with the other eigenstates; therefore its dynamics is predominantly affected by them and exhibits persistent oscillations at a frequency given by the energy gap between the scars.

### 1.3.3 Open questions

Quantum scars are the origin of the anomalous dynamics observed in the Rydberg atom array, but this explanation is far from being conclusive, because the existence of scars poses a number of questions for future research. First of all, whether these states continue to exist in the thermodynamic limit still stands as an open problem: numerical studies reveal that for  $L \geq 34$  some signals of a possible hybridization between scars and thermal states start to appear. In this context, understanding the stability of scars under perturbations and the mechanism underlying their hybridization is an important direction, that we investigate in Chapter 2.

Together with the fate of scars in the thermodynamic limit, another – perhaps even more fundamental – question is what their origin is, and in what kind of systems we can expect to find them. Different general mechanisms have been studied and a number of models with various types of quantum scars have already been identified. Lin and Motrunich [52] found that the PXP model supports other scars, that do not belong to the band previously studied: these new scars can be written as exact MPS states with finite bond dimension, they have area law entanglement, non-thermal expectation values of local observables, and they survive in the thermodynamic limit. More on these states and their stability is discussed in Chapter 2, where we also introduce novel MPS states for generalized PXP models.

Some of the known mechanisms for quantum scars rely on the presence of a spectrum-generating algebra: in these models a tower of scarred eigenstates is obtained by repeated application of an operator, which can be interpreted as a creation operator of a quasi-particle. Examples of these kinds of scars include  $\eta$ -pairing states of the Hubbard model, the scars of the AKLT model and of spin-1 XY magnets [53–63]. Some examples of scars that do not fall in this category are illustrated in Chapter 3, where we show that scars emerge "statistically" in a class of quantum random networks, and in Chapter 4, where we show that quantum scars can appear in models with lattice supersymmetry.

Another mechanism for embedding ETH-violating eigenstates in a thermal spectrum was already known before the scars of the PXP model were discovered. This construction, proposed by Shiraishi and Mori [64], is based on local projectors  $P_j$  and a subspace  $\mathcal{T}$  of the Hilbert space for which  $P_j\mathcal{T} = 0$ . Given a Hamiltonian  $H'$  that satisfies  $[H', P_j] = 0$ , the (generically non-integrable) Hamiltonian

$$H = \sum_j P_j h_j P_j + H' \quad (1.10)$$

has  $\dim \mathcal{T}$  candidate scarred eigenstates (the eigenstates of  $H$  restricted to  $\mathcal{T}$ ).

Despite various mechanisms and many examples that have been discovered, the origin of quantum scars still requires vast investigation. In particular, the possible connections of quantum scars with lattice gauge theories, with confinement and with kinetic constraints – which have been partially explored in the works reported in this thesis – are intriguing directions for future research.



## Chapter 2

# Exact many-body scars and their stability in constrained quantum chains

Quantum scars in the PXP model were originally used to explain the slow dynamics observed by evolving a charge-density wave (CDW) initial state in the above-mentioned experiment with Rydberg atoms: for a chain of length  $L$ , there are  $L + 1$  scar eigenstates, with a large overlap with the CDW, spread throughout the spectrum and (approximately) equally spaced in energy. Crucially, numerical results reveal hybridization of these scars with thermal eigenstates, implying that they are not stable in the thermodynamic limit [48]. Therefore the resulting dynamics from this initial state is expected to eventually thermalize. However, two exact uniform matrix product eigenstates have been found for all (even) system sizes [52]. This fact demonstrated the existence of ETH violating eigenstates that survive in the infinite size limit, and motivated the study of their stability against perturbation. In Ref. [65] the authors address this problem by using perturbation theory: from the scaling of the averaged matrix elements, they find no qualitative difference between the scars and thermal eigenstates, and thus deduce that the scars are not stable against perturbations. Nonetheless, they claim that thermalization is slow, because of parametrically small matrix elements and prove the rigorous lower bound for the thermalization time  $t^* \sim O(\lambda^{-1/(1+d)})$ , where  $d$  is the spatial dimension and  $\lambda$  is the perturbation strength.

Here, we analyse a different quantity (the fidelity susceptibility), which is a renowned probe of quantum chaos [66–68], and is not subject to the arbitrariness of the averaging procedure. Part of our results contrast with Ref. [65], showing that the scars with zero energy have a completely different behavior from thermal eigenstates and are anomalously stable to first order in perturbation theory. These findings suggest that thermalization of quantum scars is even slower than previously expected, being originated from effects beyond the first perturbative order.

We remark that this anomalous stability is observed only for scars with zero energy, so we cannot conjecture a similar mechanism for explaining the persistence of non-exact scars at finite energy in the PXP model. In fact, although a construction based on a "single mode approximation" suggests a possible connection between the band of  $L + 1$  quantum scars at all energies to the MPS quantum scars at zero energy [52], these two sets of low-entropy eigenstates appear to have different origin. For example, while the former are stabilized by a specific fine-tuned perturbation [69] and have logarithmic scaling of entanglement entropy with system size, the latter are destroyed by the same perturbation and have finite entanglement entropy in the thermodynamic limit.

In order to frame our finding about scar stability in the broader picture of ETH violations in constrained quantum systems, we prove that a novel set of exact eigenstates arising at zero energy (and at non-zero energy, when open boundary conditions are imposed) exist in generalized PXP models with radius of constraint  $\alpha > 1$ . We do not find a band of eigenstates equally spaced in energy like the one observed in the PXP model. These results suggest that exact scars are a generic property of one-dimensional models constrained by Rydberg blockade. We then extend our stability analysis to this second set of scars, and show how, in analogy with the  $\alpha = 1$  case, they display anomalous stability.

The chapter is structured as follows. In Sec. 2.1, we introduce the PXP model and the scar eigenstates, and we set the notation for the following sections. In Sec. 2.2 we introduce the fidelity susceptibility and the eigenstate thermalization hypothesis, and put forward a link between such observable and a recently proposed spectral version of the adiabatic gauge potential [68, 70]. In Sec. 2.3 we focus on the models with radius of constraints  $\alpha > 1$ : we discuss their properties in light of the ETH, we show that they obey Wigner-Dyson spectral statistics (Sec. 2.3.1); we describe the exact scars with  $E = 0$  as product states of "dimers" (Sec. 2.3.2), and the exact scars with  $E \neq 0$  as matrix product states (Sec. 2.3.3); finally, we show that the exact scars with  $E = 0$  are anomalously stable against perturbations (Sec. 2.3.5).

## 2.1 PXP model

The model we consider is the PXP model, introduced in Section 1.3. We report here, for convenience, the Hamiltonian in terms of the Pauli matrices  $X_i, Y_i, Z_i$  at site  $i$  and the operators  $P_i = (1 - Z_i)/2$ ,  $n_i = (1 + Z_i)/2$ . In the constrained space we define

$$H_0 = X_1 P_2 + \sum_{j=2}^{L-1} P_{j-1} X_j P_{j+1} + P_{L-1} X_L \quad (2.1)$$

for open boundary conditions and

$$H_0 = \sum_{j=1}^L P_{j-1} X_j P_{j+1} \quad (2.2)$$

with the identification of the sites  $j \equiv j+L$  for periodic boundary conditions. We are interested in the effects induced by a perturbation  $V$  that has the same symmetries of  $H_0$ . More concretely, the Hamiltonian is  $H = H_0 + \lambda V$ , where

$$V = X_1 P_2 Z_3 + \sum_{j=2}^{L-2} P_{j-1} X_j P_{j+1} Z_{j+2} + \sum_{j=3}^{L-1} Z_{j-2} P_{j-1} X_j P_{j+1} + Z_{L-2} P_{L-1} X_L \quad (2.3)$$

for the case of open boundary conditions and

$$V = \sum_{j=1}^L (P_{j-1} X_j P_{j+1} Z_{j+2} + Z_{j-2} P_{j-1} X_j P_{j+1}) \quad (2.4)$$

for periodic boundary conditions.

Both  $H_0$  and  $V$  commute with the space reflection symmetry  $I$  and anti-commute with the particle-hole symmetry  $C_{ph} = \prod_i \sigma_i^z$ . As a consequence, the spectrum is symmetric with respect to the eigenvalue  $E = 0$  and the energy zero eigenspace has a dimension growing exponentially with system size [71]. For more details about the peculiar properties of the spectrum we refer to Appendix A.1.

### Many-body scars

As stated above, many-body scars are states that do not satisfy ETH. It was shown in Ref. [47] that the spectrum of the PXP model exhibits a band of equally-spaced many-body scars. These scars were responsible for the observation of long-lived oscillation in the Rydberg atom experiment [46]. Their exact form is not known analytically, and their persistence in the thermodynamic limit is still an open question. However, as was shown in Ref. [52],  $H_0$  has also some exact scars in the form of MPS eigenstates at finite energy density. For open boundary conditions they are defined as

$$|\Gamma_{i,j}\rangle = \frac{1}{\sqrt{\mathcal{N}_{i,j}}} \sum_{\{\sigma\}} v_i^T A_{\sigma_1 \sigma_2} \dots A_{\sigma_{L-1} \sigma_L} v_j |\sigma_1 \sigma_2 \dots \sigma_{L-1} \sigma_L\rangle \quad (2.5)$$

with

$$A_{00} = \begin{pmatrix} 0 & -1 \\ 1 & 0 \end{pmatrix}, \quad A_{01} = \begin{pmatrix} \sqrt{2} & 0 \\ 0 & 0 \end{pmatrix}, \quad A_{10} = \begin{pmatrix} 0 & 0 \\ 0 & -\sqrt{2} \end{pmatrix}, \quad (2.6)$$

$i, j = 1, 2$ ,  $\mathcal{N}_{i,j} = 2[3^{L/2} + (-1)^{L/2+i+j}]$  and  $v_1 = (1, 1)^T$ ,  $v_2 = (1, -1)^T$ .  $\Gamma_{12}$  has energy  $\sqrt{2}$ ,  $\Gamma_{21}$  has energy  $-\sqrt{2}$ , whereas  $\Gamma_{11}$  and  $\Gamma_{22}$  have energy 0. In the next sections, we will focus on scars with well-defined inversion quantum number, so we define  $|\Gamma_I\rangle = (|\Gamma_{11}\rangle - |\Gamma_{22}\rangle)/\sqrt{2 - 2\langle\Gamma_{11}|\Gamma_{22}\rangle}$ .

For periodic boundary conditions, the two scarred eigenstates  $|\Phi_1\rangle$  and  $|\Phi_2\rangle$  are defined as

$$|\Phi_1\rangle = \frac{1}{\sqrt{\mathcal{N}_\Phi}} \sum_{\{\sigma\}} \text{Tr}[A_{\sigma_1\sigma_2} \dots A_{\sigma_{L-1}\sigma_L}] |\sigma_1\sigma_2 \dots \sigma_{L-1}\sigma_L\rangle \quad (2.7)$$

and  $|\Phi_2\rangle = T_x |\Phi_1\rangle$ , where  $T_x$  is the translation operator and  $\mathcal{N}_\Phi = 3^{L/2} + 2 + (-1)^{L/2}$ . Both have energy 0. Their properties under the symmetries are the following:  $I|\Phi_i\rangle = (-1)^{L/2}|\Phi_i\rangle$  and  $C_{ph}|\Phi_i\rangle = (-1)^{L/2}|\Phi_i\rangle$  for  $i = 1, 2$ . We will work with the linear combinations  $|\Phi_{K=0,\pi}\rangle = (|\Phi_1\rangle \pm |\Phi_2\rangle)/\sqrt{2 \pm 2\langle\Phi_1|\Phi_2\rangle}$ . Even though these are not responsible for the persistent oscillations observed in experiments, their putative stability in the thermodynamic limit outlines their importance.

## 2.2 Perturbation theory and Eigenstate Thermalization Hypothesis

It is crucial to understand how to define *stability* for these kind of eigenstates. In general, we will say that an eigenstate of  $H_0$  is stable if it can be deformed to an eigenstate of  $H_0 + \lambda V$  with a local unitary transformation in the thermodynamic limit. Usually this criterion is satisfied by ground states in gapped systems. Here we are interested in the scars  $|\Gamma_{\alpha\beta}\rangle$  and  $|\Phi_i\rangle$  which are in the middle of a dense spectrum, in the absence of a gap to protect them. The local character of the transformation, if it exists, should guarantee that a stable scar retains its character (no ETH and area law entanglement) in the thermodynamic limit. For generic eigenstates, no stability is expected. This can be understood as a consequence of the Eigenstate Thermalization Hypothesis (ETH): to first order in the perturbation strength  $\lambda$ , the perturbed eigenstate can be written as

$$|n^0\rangle + \lambda |n^1\rangle = |n^0\rangle + \lambda \sum_{m \neq n} \frac{\langle m^0 | V | n^0 \rangle}{E_n^0 - E_m^0} |m^0\rangle. \quad (2.8)$$

According to ETH, the off-diagonal matrix element  $\langle m^0 | V | n^0 \rangle$  scales as  $\exp(-S/2)$ , where  $S$  is the extensive thermodynamic entropy of the system. The energy denominator, on the other hand, scales as  $\exp(-S)$  for nearby eigenstates. This simple argument implies that the first order correction diverges exponentially in the system size  $L$ .

Hence, a natural question to answer is whether the first order correction to the scars behaves according to the scaling predicted by ETH or not. In

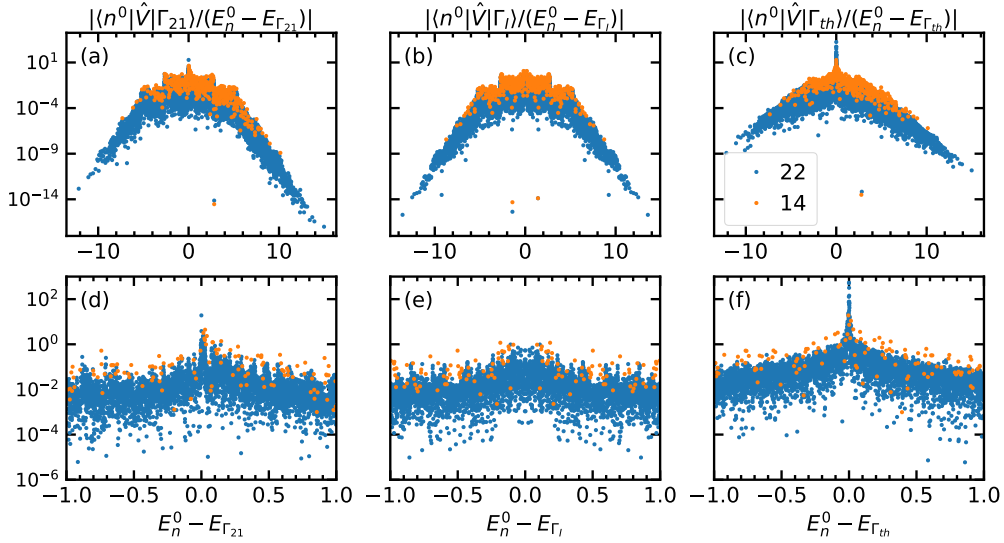


Figure 2.1: Absolute value of the ratio between the matrix element and the energy difference between a target state and a state of the spectrum. The same data are represented in a larger (first row) and in a smaller (second row) range of energy difference. The target states are the scars eigenstates  $|\Gamma_{21}\rangle$  (a,d),  $|\Gamma_I\rangle$  (b,e) defined in Sec. 2.1 and a thermal eigenstate  $|\Gamma_{th}\rangle$  (c,f) taken as the third eigenstate after  $|\Gamma_{21}\rangle$  in order of increasing energy. The clear peak observed when a thermal eigenstate  $|\Gamma_{th}\rangle$  is considered is not present for the scars eigenstates, pointing at a suppression of the matrix elements of the perturbation for the latter states.

Ref. [65], it was found that the matrix elements  $\langle m^0|V|\Gamma\rangle$  averaged over a certain set of eigenstates  $\{|m^0\rangle\}$  close in energy to  $|\Gamma\rangle$  do indeed scale as  $\exp(-S/2)$ , where  $|\Gamma\rangle$  is one of the scars for the case of open boundary conditions. This is however not sufficient to claim instability: the matrix elements which are responsible for the divergence are the ones involving states that are very close in energy. As can be seen in Fig. 2.1, the matrix elements weighted with the inverse energy gaps behave very differently for the scars and for generic thermal states: the vanishing denominator produces a peak in the case of a thermal state; the scars, despite the vanishing energy gaps, do not exhibit this peak, signalling a suppression of matrix elements for small gaps. Moreover, the averaging procedure of matrix elements introduces some arbitrariness in this respect: the result depends on the choice of the set of eigenstates that are included in the average.

In this work, we propose to diagnose the stability of scar eigenstates by studying the fidelity susceptibility, defined as [72]

$$\chi_F[|n^0\rangle] = \lim_{\lambda \rightarrow 0} \frac{-2 \ln |\langle n^0|n^\lambda\rangle|}{\lambda^2} \quad (2.9)$$

where  $|n^0\rangle$  is an eigenstate of  $H_0$  and  $|n^\lambda\rangle$  is the eigenstate of  $H_0 + \lambda V$

obtained from  $|n^0\rangle$  with a perturbative construction in  $\lambda$ . From the explicit construction of the state, one finds<sup>1</sup>

$$\chi_F [|n^0\rangle] = \sum_{m \neq n} \left| \frac{\langle m^0 | V | n^0 \rangle}{E_n^0 - E_m^0} \right|^2. \quad (2.10)$$

The fidelity susceptibility is a measure of the response of an eigenstate to perturbations: when averaged over different eigenstates, for example, it has been very recently used as a measure of quantum chaos [68, 70]. For gapped ground states of local Hamiltonians, it is expected to scale as  $\chi_F \sim L$  with the system size  $L$ . On the other hand, as argued above, ETH implies a scaling  $\chi_F \sim \exp(L)$  for eigenstates at finite energy density.

Note that, due to the special properties of this perturbation, all the matrix elements of  $V$  between zero energy states vanish (see Appendix A.1): as a consequence, the fidelity susceptibility is well-defined even for states in the exponentially degenerate zero-energy manifold and can be computed for all the scarred eigenstates.

We obtain that only a subset of the exact scars appear to be stable. Indeed the scaling of the fidelity susceptibility for the scars  $|\Phi_{K=0}\rangle$  (for the case of periodic boundary conditions) and  $|\Gamma_I\rangle$  (for the case of open boundary conditions) shown in Fig. 2.2 suggests a linear dependence<sup>2</sup>  $\chi_F \sim L$ , as evidenced by the solid lines. On the contrary, the scaling for  $|\Gamma_{21}\rangle$  and for the generic thermal eigenstates  $|\Gamma_{th}\rangle$  and  $|\Phi_{th}\rangle$ <sup>3</sup> are compatible with an exponential growth (dashed lines), as predicted by ETH. These results show that  $|\Phi_{K=0}\rangle$  and  $|\Gamma_I\rangle$  are perturbatively stable to an infinitesimal perturbation. We note that these differences are not only qualitatively manifest (power versus exponential scaling), but also quantitatively striking, so that the different scaling regimes can be diagnosed despite the fact that our analysis is limited to modest system sizes up to  $L = 32$  spins.

We now want to understand if they are also stable to a finite strength  $\lambda$  of the perturbation. If these states were akin to gapped ground states, we would have expected stability to hold in the thermodynamic limit for a finite  $\lambda$  as long as it is much smaller than the gap. The absence of a gap makes the quest for an energy scale associated with scars much less obvious.

To address this problem, we compute the states  $|\Phi_{K=0}^\lambda\rangle$  and  $|\Gamma_i^\lambda\rangle$  obtained by perturbing the scars  $|\Phi_{K=0}\rangle$  and  $|\Gamma_I\rangle$  in the following way

$$|\Phi_{K=0}^\lambda\rangle = \frac{1}{\mathcal{N}_\Phi^\lambda} \frac{1}{1 + \lambda Q H_0^{-1} Q V} |\Phi_{K=0}\rangle \quad (2.11)$$

<sup>1</sup>We use that  $|n^\lambda\rangle = (|n^0\rangle + |n_\perp\rangle) / \sqrt{\langle n^0 | n^0 \rangle + \langle n_\perp | n_\perp \rangle}$ , with  $\langle n_\perp | n^0 \rangle = 0$  to obtain  $\langle n^0 | n^\lambda \rangle = \frac{1}{\sqrt{\langle n^0 | n^0 \rangle + \langle n_\perp | n_\perp \rangle}} = (1 + \langle n_\perp | n_\perp \rangle)^{-1/2} = 1 - \frac{1}{2} \lambda^2 \langle n^1 | n^1 \rangle + O(\lambda^3)$ .

<sup>2</sup>On top of the linear growth, the scaling for the scar  $|\Phi_{K=0}\rangle$  is subject to an even-odd effect related to the different parity under inversion symmetry of the state ( $I = (-1)^{L/2}$ ).

<sup>3</sup>The state  $|\Gamma_{th}\rangle$  is chosen as the third eigenstate after  $|\Gamma_{21}\rangle$  in increasing order of energy. The state  $|\Phi_{th}\rangle$  is the state with energy closest to  $-0.3$ .

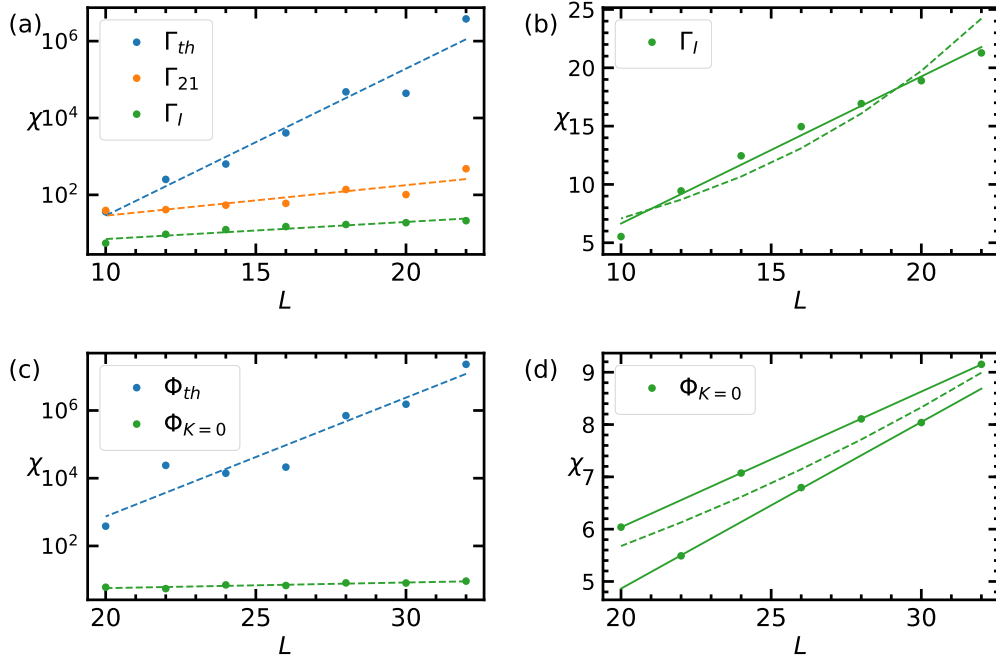


Figure 2.2: Scaling of the fidelity susceptibility with system size. The results shown refer to the states (a)  $|\Gamma_{th}\rangle$ ,  $|\Gamma_{21}\rangle$  and  $|\Gamma_I\rangle$  with open boundary conditions and to the states (c)  $|\Phi_{th}\rangle$  and  $|\Phi_{K=0}\rangle$  with periodic boundary conditions. As can be seen in the panels with linear  $y$ -scale (b), (d), the scaling of the fidelity susceptibility of a zero energy scar eigenstate is polynomial with the system size, in sharp contrast to what happens for thermal eigenstates or scars at non-zero energy (a),(c). Solid lines are fits for the linear scalings (the two different lines for  $\Phi_{K=0}$  capture the even-odd effect), dashed lines are fits for exponential scalings.

$$|\Gamma_I^\lambda\rangle = \frac{1}{\mathcal{N}_\Gamma^\lambda} \frac{1}{1 + \lambda Q H_0^{-1} Q V} |\Gamma_I\rangle \quad (2.12)$$

where  $Q$  projects on the subspace with  $E_0 \neq 0$ , and  $\mathcal{N}_\Phi^\lambda, \mathcal{N}_\Gamma^\lambda$  are normalizing factors. The states  $|\Phi_{K=0}^\lambda\rangle$  and  $|\Gamma_I^\lambda\rangle$  are the perturbed eigenstates to infinite order in perturbation theory<sup>4</sup>. We numerically compute the von Neumann bipartite entanglement entropy  $S(\lambda)$  of these states for different system sizes (Fig. 2.3). This quantity exhibits peaks that get closer to  $\lambda = 0$  as  $L$  increases, indicating a stronger and stronger hybridization with other eigenstates in the spectrum. This fact strongly suggests that, despite the stability observed to first order in perturbation theory, the scars are ultimately not stable for finite  $\lambda \neq 0$ <sup>5</sup>.

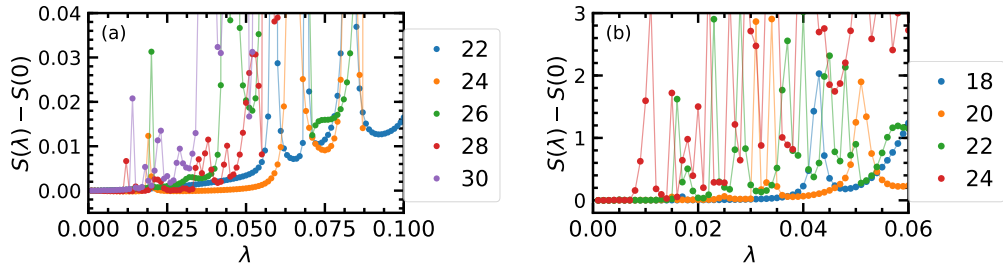


Figure 2.3: Bipartite entanglement entropy of the states (a)  $|\Phi_{K=0}^\lambda\rangle$  and (b)  $|\Gamma_I^\lambda\rangle$  as a function of  $\lambda$ . Peaks in this quantity signal hybridization of the perturbed state with thermal eigenstates. By increasing the system size, we find peaks closer and closer to  $\lambda = 0$ , suggesting that the scar eigenstates are not stable in the thermodynamic limit.

## 2.3 Models with radius of constraint $\alpha > 1$

Since the first studies on the PXP model, several other instances of quantum many-body scars have been put forward [3, 4, 55, 56, 58–62, 73–80]. While it is tempting to extend some of the findings above to a general setting, we refrain from this for the very simple reason that PXP models have a

<sup>4</sup>The expressions are obtained using the fact that the perturbative corrections to the energy of the scars  $|\Gamma_I\rangle$  and  $|\Phi_{K=0}\rangle$  are zero for all orders in perturbation theory. For a state with this property one has that  $H_0 |n^{j+1}\rangle = V |n^j\rangle$ , where  $\sum_{j=0}^{\infty} \lambda^j |n^j\rangle$  is the formal expression of the perturbative series of the eigenstate. A resummation of the geometric series yields the expressions in Eqs. (2.11) and (2.12).

<sup>5</sup>We note that performing a rigorous finite-size scaling analysis for the position of the first peak versus system size is tricky for two reasons: (i) we can only consider a coarse grained set of values of  $\lambda$ , so that we can only put an upper bound on the position of the peak, and (ii) the peaks may be due in principle to different level crossing, making a finite-size extrapolation not fully reliable. Our conclusion is based on the fact that we systematically observe the peak moving towards vanishing perturbations, with no exception, very rapidly with system size.

characteristic feature - a constrained Hilbert space that cannot be reduced in tensor product form - that is not present in other instances of quantum scars. We pursue instead an alternative route, based on investigating the stability of quantum scars in an enlarged class of constrained models.

Specifically, we consider a generalization of the PXP model, where we extend the constraint to the sites within an integer radius  $\alpha$ , i.e.  $n_i n_j = 0$  whenever  $|i - j| \leq \alpha$ , with  $n_j = \frac{Z_j + 1}{2}$ . The Hamiltonian has the form:

$$H_0^\alpha = \sum_i P_{i-\alpha} \dots P_{i-1} X_i P_{i+1} \dots P_{i+\alpha}, \quad (2.13)$$

where  $P_j$  is the projector on the state  $|0\rangle$ . The Hamiltonian (2.13) coincides with the PXP model for  $\alpha = 1$  and arises as an effective approximation of the long-range Hamiltonian describing Rydberg atom arrays when the (continuous) blockade radius is increased (by, e.g., tuning the distance between the atoms). Similarly to the PXP model, this Hamiltonian commutes with the reflection symmetry  $I$  and anticommutes with the particle-hole symmetry  $C_{ph}$ , and the spectrum has the same properties (see Appendix A.1).

### 2.3.1 Spectral statistics

In this section we analyze the spectral statistics of the Hamiltonian in Eq. (2.13) for different values of  $\alpha$ . We use as a measure the ratio between nearby gaps:

$$r = \left\langle \frac{\text{Min}\{\Delta E_n, \Delta E_{n+1}\}}{\text{Max}\{\Delta E_n, \Delta E_{n+1}\}} \right\rangle, \quad (2.14)$$

where the average is taken over the full spectrum. For an ergodic system, this quantity is expected to flow to the value  $r_{WD} \simeq 0.53$  associated with a Wigner-Dyson statistics. While for  $\alpha = 1$  ergodicity has been already verified in various works [48, 81], we check this assumption when  $\alpha > 1$  in Figs. 2.4, where we show the values of  $r$  for different  $\alpha$  and system sizes. In all the cases considered (reflection sector  $I = +1$  with open boundary condition, reflection sectors  $I = +1$  and  $I = -1$  with momentum  $K = 0$  and periodic boundary conditions) we find a clear flow to  $r_{WD}$  for increasing system sizes. We can therefore argue that the system has a spectral statistics that is compatible with ergodicity.

### 2.3.2 Exact scars with $E = 0$

We now show that, although the models considered here satisfy the Wigner-Dyson spectral statistics, some states in the spectrum have finite entanglement entropy in the thermodynamic limit and hence violate the eigenstate thermalization hypothesis.

For a system with  $L = (\alpha + 2)n$  (with  $n$  integer), consider the following state

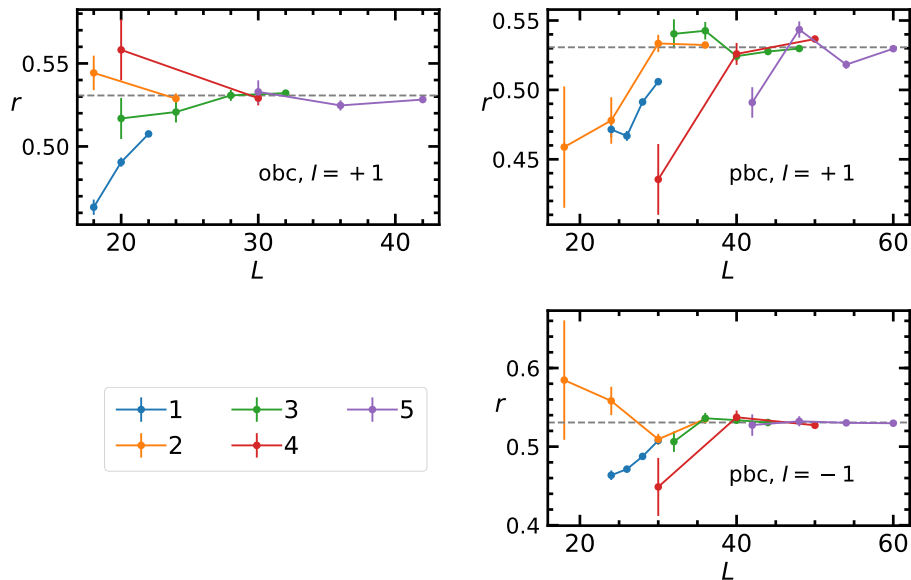


Figure 2.4: Ratio  $r$  defined in Eq. (2.14) averaged over the full spectrum. The colors label different values of  $\alpha$ . The dashed horizontal line is the value  $r_{WD}$  associated with Wigner-Dyson statistics, that appears to be satisfied for all the values of  $\alpha$  considered.

$$|\phi_\alpha\rangle = \bigotimes_{i=0}^{n-1} [ (|01\rangle - |10\rangle) \underbrace{|0 \dots 0\rangle}_\alpha ]_{b_i} \quad (2.15)$$

where the index  $b_i$  labels blocks of  $\alpha + 2$  sites. The state of the first two sites of a block is an antisymmetric superposition (that we call a *dimer*) and hence is annihilated by the summed spin flip. All the other sites of a block cannot be flipped: they are "frozen" by the previous or the next dimer. Therefore, the state  $|\phi_\alpha\rangle$  (and all the states obtained from it by translations) is a scar with energy  $E = 0$  for generic  $\alpha > 1$ .

We can construct many exact scars with  $E = 0$  by placing dimers (depicted in red in Fig. 2.5) on the chain. Two dimers must be separated by a number  $\ell$  of zeros in the range  $\alpha \leq \ell \leq 2\alpha - 2$ . We can also have longer-range dimers involving sites that are not nearest neighbours. In this case, the number  $\ell$  of zeros between two dimers of range  $r_1$  and  $r_2$  must be in the interval  $\alpha \leq \ell \leq 2\alpha - r_1 - r_2$ . This last condition implies that the ranges of two consecutive dimers are bounded by  $r_1 + r_2 \leq \alpha$ .

This construction works also in the case of open boundary conditions, with the following rules for the boundaries: if the first (last) dimer of the chain has range  $r$ , then the number of zeros preceding (following) it must be  $\ell \leq \alpha - r$ .

We note that the structure of these states, that we write as product states of dimers, is reminiscent of the construction of scar eigenstates found

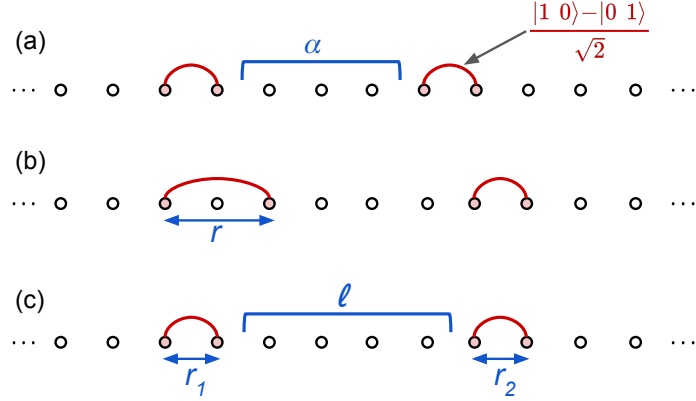


Figure 2.5: Some eigenstates with  $E = 0$ . (a) The state  $|\phi_\alpha\rangle$  is made of dimers (in red) separated by sequences of 0s of length  $\alpha$ . (b) Dimers can have range  $r > 1$ . (c) Dimers can be separated by any distance  $\ell$ , such that  $\alpha \leq \ell \leq 2\alpha - r_1 - r_2$ .

in other constrained models [3, 82].

### 2.3.3 Exact scars with $E \neq 0$

In the following, we will show that the models of Eq. (2.13) have scars also at  $E \neq 0$  when open boundary conditions are imposed. While, as we have shown in Sec. 2.3.2, it is possible to write many exact  $E = 0$  eigenstates as product states of dimers, for these scars we need to resort to a more involved construction: we write them as matrix product states with finite bond dimension, independent of the system size.

#### Exact scars with $E = \pm\sqrt{3}$

For system sizes  $L = (\alpha + 2)n + 3$ , with  $n$  integer, we are able to write two exact scars with energy  $E = \pm\sqrt{3}$  as matrix product states. To define these states, we divide the chain in blocks labelled from 1 to  $2n + 1$ : the blocks labelled by odd numbers contain 3 sites, while the blocks labelled by even numbers contain  $\alpha - 1$  sites. As we prove in Appendix A.4, the following state is an exact eigenstate with energy  $E = \sqrt{3}$ :

$$|\psi_\alpha^{(3)}\rangle = \sum_{\vec{s}} \left[ (1, 0)^T \cdot N^{s_1} M^{s_2} \dots M^{s_{2n}} N^{s_{2n+1}} \cdot (0, 1) \right] |\vec{s}\rangle \quad (2.16)$$

where  $s_1, s_2, \dots, s_{2n+1}$  label the states of the blocks and

$$M^s = \begin{cases} 1 & \text{if } s = 00 \dots 00 \\ 0 & \text{otherwise,} \end{cases} \quad (2.17)$$

$$N^{000} = \begin{pmatrix} 0 & \sqrt{3} \\ 0 & 0 \end{pmatrix}, \quad N^{100} = \begin{pmatrix} 0 & 1 \\ 0 & 1 \end{pmatrix}, \quad (2.18)$$

$$N^{010} = \begin{pmatrix} 1 & 1 \\ 0 & -1 \end{pmatrix}, \quad N^{001} = \begin{pmatrix} -1 & 1 \\ 0 & 0 \end{pmatrix}. \quad (2.19)$$

From the relation  $C_{ph}H_0^\alpha = -H_0^\alpha C_{ph}$  we immediately find that the state  $|\psi_\alpha^{(-3)}\rangle = C_{ph}|\psi_\alpha^{(3)}\rangle$  is another eigenstate of  $H_0^\alpha$  with eigenvalue  $E = -\sqrt{3}$ . We also note that the state obtained by taking the trace in Eq. (2.16) is a zero energy eigenstate for  $L = (\alpha + 2)n + 3$  when open boundary conditions are imposed. Moreover, removing the matrix  $N$  at one of the two boundaries we can construct an MPS that is invariant under translations of  $\alpha + 2$  sites

$$|\varphi_\alpha\rangle = \sum_{\vec{s}} \text{Tr}(B^{s_1} B^{s_2} \dots B^{s_n}) |\vec{s}\rangle, \quad (2.20)$$

where  $B = MN$  and  $s_i$  runs through the 3 allowed states of the  $i$ -th block, made of  $\alpha + 2$  sites. This state is a zero energy eigenstate for periodic boundary conditions and system sizes  $L = (\alpha + 2)n$ , and it has non-vanishing overlap with the dimer eigenstates of Sec. 2.3.2; however, for generic  $\alpha$  it has a component that is independent of those states. The matrix  $B$  yields a non-injective MPS, whose parent Hamiltonian has a degenerate groundspace [83]. In fact, the state in Eq. (2.20) can be written as a cat state

$$\begin{aligned} |\varphi_\alpha\rangle &= \left[ \left( |L\rangle + \frac{1}{2} |R\rangle - \frac{3}{2} |C\rangle \right) \underbrace{|0 \dots 0\rangle}_{\alpha-1} \right]^{\otimes n} \\ &+ \left[ \left( \frac{1}{2} |L\rangle + |R\rangle - \frac{3}{2} |C\rangle \right) \underbrace{|0 \dots 0\rangle}_{\alpha-1} \right]^{\otimes n} \\ &= |\varphi_\alpha^1\rangle + |\varphi_\alpha^2\rangle, \end{aligned} \quad (2.21)$$

where  $|L\rangle = |100\rangle$ ,  $|C\rangle = |010\rangle$  and  $|R\rangle = |001\rangle$ . The parent Hamiltonian of this state has  $|\varphi_\alpha^1\rangle \pm |\varphi_\alpha^2\rangle$  as the two degenerate ground states. This is in contrast with the eigenstates of Ref. [52] ( $|\Phi_1\rangle$  and  $|\Phi_2\rangle$  in Sec. 2.1) which are injective MPSs, and thus unique ground states of their parent Hamiltonian.

### Exact scars with $E = \pm\sqrt{q}$

We find that other (possibly degenerate) MPS scars appear at energies  $E = \pm\sqrt{q}$  with  $q$  integer. This property is a consequence of the structure of these matrix product states. Similarly to the case of periodic boundary conditions, the action of the Hamiltonian on these states is such that the complicated interaction is decoupled into smaller non-interacting blocks.

Their energies are therefore determined by the energy of a single block: in the cases we consider, the energy of a block can be 0 or  $\pm\sqrt{q}$  where  $q \leq \alpha + 1$  is the size of the block. In Appendix A.5 we write down explicitly some exact eigenstates of  $H_0^\alpha$  with energy  $E = \pm\sqrt{2}$  for  $\alpha = 3$ .

### 2.3.4 Relation with exact scars for $\alpha = 1$

The exact scars described here are reminiscent of the ones found in Ref. [52]: there, it was shown that the PXP model ( $\alpha = 1$ ) has exact MPS scars at  $E = 0$  for periodic boundary conditions, and both at  $E = 0$  and  $E = \pm\sqrt{2}$  when open boundary conditions are imposed. The states we study for  $\alpha \geq 2$ , however, show a qualitative difference with respect to them: in the case of open boundary conditions, the energy density profile does not have peaks at the edges, but has a pattern that is uniformly repeated in the full system. As we will explain in this Section, this difference can be understood from the MPS structure of these states.

The scars in Eq. (2.5) have the form of AKLT states in which two-site blocks play the role of  $S = 1$  spin variables. As we show in Appendix A.3, the energy density of the PXP model corresponds to the local magnetization of the AKLT state in the  $z$  direction. The boundary properties of the scars can be interpreted using the "dilute antiferromagnet" representation of the AKLT state: in the  $S_z$  basis, the state is a superposition of configurations with alternating  $+$  and  $-$ , and with an arbitrary number of 0 placed in between. The different boundary vectors  $\alpha, \beta$  of  $|\Gamma_{\alpha\beta}\rangle$  fix the sign of the first and last non-zero spins of the configurations. Therefore, the local magnetization is non-zero close to the boundaries but goes to 0 far from them.

The state in Eq. (2.16), on the other hand, has a very different structure: if we use, once again, a basis in which the local energy corresponds to a local magnetization, we can write  $|\psi_\alpha^{(3)}\rangle$  as a superposition of configurations with a single  $+$  (on one of the 3-site blocks), and 0 magnetization everywhere else. Therefore, in contrast with the dilute antiferromagnet of the scars  $|\Gamma_{\alpha\beta}\rangle$ , this state is reminiscent of a spin wave, with a single magnetic excitation uniformly spread over the chain.

### 2.3.5 Stability

We now analyse the response of the exact scars described above to a perturbation. The perturbation we apply is

$$V^\alpha = \sum_i Z_{i-\alpha-1} P_{i-\alpha} \dots P_{i-1} X_i P_{i+1} \dots P_{i+\alpha} + P_{i-\alpha} \dots P_{i-1} X_i P_{i+1} \dots P_{i+\alpha} Z_{i+\alpha+1}. \quad (2.22)$$

This term has the same symmetries of  $H_0^\alpha$ , namely it commutes with  $I$  and anticommutes with  $C_{ph}$ . Similarly to the PXP case, we use the fi-

delity susceptibility to check whether these states are stable to first order in perturbation theory.

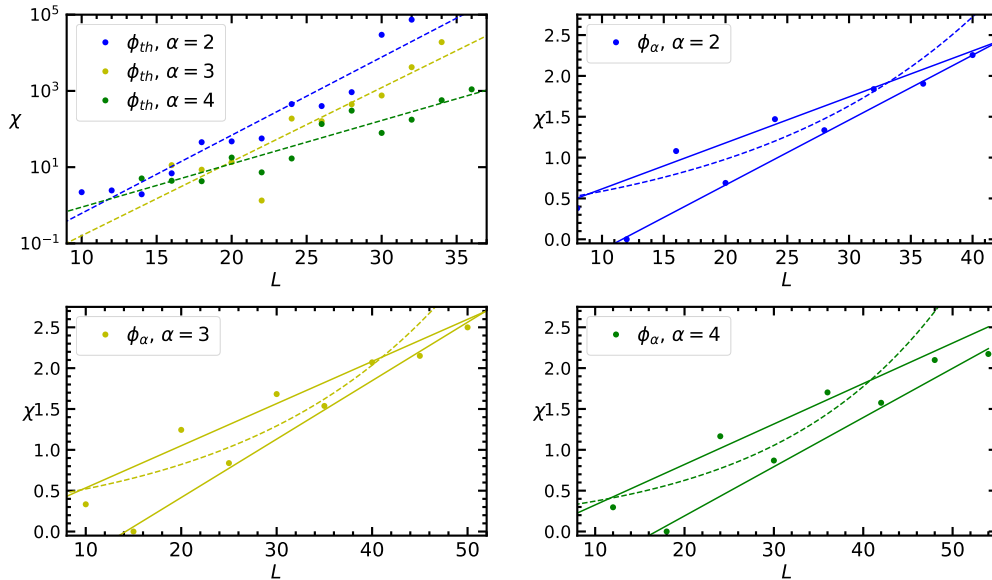


Figure 2.6: Scaling of the fidelity susceptibility with system size. The results shown refer to the generic states  $|\phi_{th}\rangle$  (upper left panel) and the scarred eigenstates  $|\phi_\alpha\rangle$  (upper right panel and lower panels). Dashed lines are obtained from fits with an exponential scaling, solid lines with linear scaling. The result points at the same behavior occurring in the PXP model.

In Fig. 2.6, we present the results of the stability analysis. In the upper left panel, we plot the fidelity susceptibility of a generic (thermal) eigenstate of the spectrum  $|\phi_{th}\rangle$  (chosen as the eigenstate with energy closest to 1.9, 1.7, 1.35 for  $\alpha = 2, 3, 4$  respectively): for every  $\alpha$ , the scaling with system size is exponential, as expected from ETH (dashed lines). In the other panels, we plot instead the fidelity susceptibility of the scars  $|\phi_\alpha\rangle$  defined in Eq. (2.15): the scaling here is linear<sup>6</sup> (solid lines) for every  $\alpha$ , signalling a clear violation of ETH. These results suggest that the anomalous stability of the scars with  $E = 0$  is a generic feature of this class of one-dimensional models constrained by Rydberg blockade.

## 2.4 Conclusions

In this work, we investigated the stability against perturbations of exact quantum scars arising in spin chains constrained by Rydberg blockade. We first analysed the PXP model and found that some of the MPS scars found in Ref. [52] exhibit a power law scaling of the fidelity susceptibility with

<sup>6</sup>Similarly to the state  $|\Phi_{K=0}\rangle$  in Fig.2.2-(d), the scaling for  $|\phi_\alpha\rangle$  is subject to an even-odd effect related to the different parity under inversion symmetry ( $I = (-1)^{L/(\alpha+2)}$ ).

system size. This result is a signature of their stability, a remarkable feature for eigenstates in the middle of a dense many-body spectrum. This fact is however limited to first order in perturbation theory, as a numerical analysis of the higher-order perturbative corrections reveals hybridization of exact scars eigenstates with thermal eigenstates. This behavior is reminiscent of the many-body "dark states" observed in Refs. [84, 85]. We find the anomalous scaling of the fidelity susceptibility only for scars with zero energy, suggesting that the properties of the  $E = 0$  subspace, such as the exponential degeneracy enforced by the invariance of this subspace under particle-hole and inversion symmetries, may be a key factor in stabilizing these states. Although not shown here, if we perturb with a term that breaks these properties, we find no signatures of stability for any of these low-entropy eigenstates.

To validate these conclusions, we extended our discussion to models with larger blockade radius  $\alpha$ . First, we constructed novel classes of states that are exact scars eigenstates for any  $\alpha$  and have energy eigenvalues  $E = 0$  and  $E = \pm\sqrt{q}$  (with  $q$  integer). The construction is based on an effective decoupling of the sites of the chain into "non-interacting blocks", and allows us to write these states into simple matrix product form. We then studied their fidelity susceptibility under perturbations that do not spoil the exponential degeneracy of the zero-energy eigenspace, a common property of the family of constrained models we analysed. Also in this case, we found these eigenstates to be stable at first perturbative order when they belong to the  $E = 0$  subspace.

Our results suggest that an increasing number of exact MPS scars appear in the spectrum for larger values of  $\alpha$ , and their complete classification is beyond the scope of this work. It is also worth noticing that, contrarily to the  $\alpha = 1$  case (PXP model), no "approximate scars" eigenstates – akin to the ones found in Ref. [47] – appear for  $\alpha > 1$ , as can be seen from an inspection of the bipartite entanglement entropy of each eigenstate as a function of the energy. This fact provides strong indications that there is, in general, no relationship between the appearance of eigenstates with low entanglement entropy, equally spread uniformly in the energy spectrum, and the existence of exact MPS eigenstates in spin models constrained by Rydberg blockade. It stands as an open question whether these new exact MPS states can lead to clear experimental signatures, since, having no recurrent spectral structure, they are not expected to play any role in anomalous oscillations observed in experiments (that, indeed, were not reported for larger constraint radii).

From a methodological standpoint, our results suggest that generalizations of the fidelity susceptibility to spectral properties can provide useful quantitative insights on the stability of ETH, in agreement with recent applications to quantum chaos diagnostics proposed in Ref. [68, 70].



## Chapter 3

# Quantum local random networks and the statistical robustness of quantum scars

As discussed in Section 1.3, the field of quantum scars has by now rapidly grown, both theoretically and experimentally. However, a crucial question has remained largely unanswered: are those states genuine many-body effects, that persist in the thermodynamic limit, or are they ultimately going to disappear due to the inevitable mixing to 'thermal' states? As speculated in [65], the bands of (approximate) scars of the PXP model may arise from the similarity with another model possessing exact scars. To understand if the approximate scars survive in the thermodynamic limit, it would then be crucial to understand whether exact scars are robust to perturbation or they disappear due to the hybridization with thermal states.

In Chapter 2, we investigated the stability of exact scars, showing that these states are sensitive to arbitrarily small perturbations (though extremely weakly), which cause them to ultimately disappear in the thermodynamic limit. We now want to investigate a different type of "stability": while the approach to quantum scarring typically pivots around the analysis of spectral properties of "deterministic" models, here, we pursue a different approach, and analyze the stability of scar manifolds statistically. It was already noticed that the network representation of the Hamiltonian is particularly convenient to understand many properties of constrained models displaying scars [51] (or even shattering of the Hilbert space [86, 87]): these models are geometrically equivalent to unweighted simple<sup>1</sup> networks, with a number of nodes exponentially large in system size  $N$ , but an average degree per node only linear in  $N$  as a result of the locality of the Hamiltonian [47]. We build upon this analogy to define a general ensemble of Hamiltonians, called *quantum local random network models*, which includes

---

<sup>1</sup>A simple graph is a graph that does not have more than one edge between any two vertices and no edge starts and ends at the same vertex.

the PXP model as a particular realization. Hamiltonians belonging to this ensemble are the adjacency matrices of networks whose nodes are indexed by a string of quantum numbers (e.g.,  $\{01001\dots\}$ ) while edges are drawn randomly with probability  $p$  only among vertices differing by local moves (spin flips): in this way, the constraints are statistically encoded in the dynamics.

We study in detail the spectra and the corresponding eigenfunctions and prove that generic Hamiltonians in this class can display two types of scars, *stochastic* and *statistical* which are both localized on the network. Their difference is reminiscent of the difference between size dependent [47] and exact scars [52] in the PXP model: *stochastic* scars occur at parameter-dependent energies which, for our models below, fluctuate wildly among different realizations, while *statistical* scars occur always at specific energies  $\epsilon = 0, \pm 1, \pm\sqrt{2}, \pm\sqrt{3}, \pm(\sqrt{5} \pm 1)/2, \dots$ , whose values are governed by spectral graph theory [88, 89]. A study of the scaling of the average degeneracy of statistical scars as a function of system size suggests the possible occurrence of (a series of) an eigenstate phase transition around  $p_c \simeq 0.2$  between a phase in which scars proliferate and one in which their number decreases.

### 3.1 Quantum local random networks

The first model in which quantum scars were discovered is the PXP model [51] which, on a chain of  $N$  sites with open boundary conditions, is defined by

$$H_{PXP} = \sum_{i=1}^{N-2} P_i X_{i+1} P_{i+2} + X_1 P_2 + P_{N-1} X_N, \quad (3.1)$$

where  $P_i = (1 - Z_i)/2$  and  $X_i, Z_i$  are local Pauli matrices. The dynamics of the PXP model is highly constrained (reflecting the microscopic mechanism of Rydberg blockade [46, 90]): it is impossible to flip a spin from down to up, if one of its nearest neighbours is up. Interestingly, the model in the subspace containing the spin-down state  $|\circ\circ\circ\dots\rangle$  can be represented as a tight-binding Hamiltonian on a specific network (Fibonacci or Lucas cube) [47].

While the majority of scars, identified through their overlap with the  $\mathbb{Z}_2$  state  $|\circ\bullet\circ\bullet\dots\rangle$  and their low entanglement entropy, feature size-dependent effects, it was recently shown [52] that this model possesses also a few exact scar states (of the form of exact matrix product states) in the thermodynamic limit at the special energies  $\epsilon = 0, \pm\sqrt{2}$ . Individual scars are unstable with respect to perturbations: perturbations respecting the symmetries of the PXP model make them evaporate in the continuum of ergodic states. The instability of individual scars does not imply however that deformations of the PXP model cannot possess a *scar manifold*, i.e., a set of non-ergodic, low-entangled states immersed in the ergodic continuum,

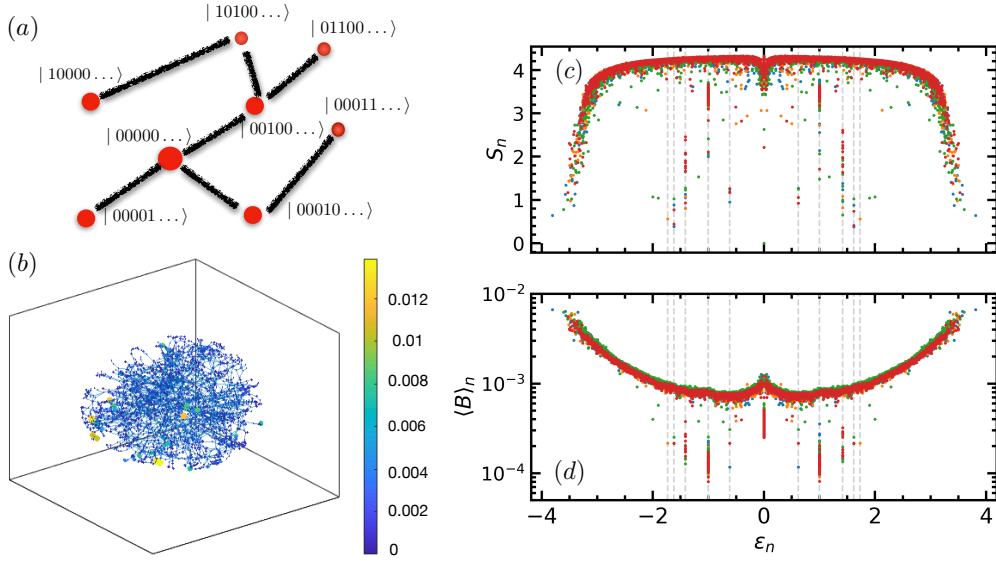


Figure 3.1: (a) Illustrative example of a QLRN: states differing by a single spin flip have probability  $p$  of being connected by an edge. (b) Graphical representation of an eigenstate with  $\epsilon = 0$  localized in the periphery of the network for  $N = 13$ ,  $p = 0.15$ . The color indicates the weight of the eigenstate on each node. The weight is concentrated on few nodes that are loosely connected with the rest of the network. (c) Bipartite entanglement entropy and (d) betweenness centrality of the eigenstates vs their energy for  $p = 0.15$ ,  $N = 14$ . The different colors refer to different realizations. Dashed grey lines indicate the special energies ( $\epsilon^* = \pm 1, \pm\sqrt{2}, \pm(\sqrt{5} \pm 1)/2, \pm\sqrt{3}$ ) associated with stochastic scars. At these energies, degenerate eigenstates are found, whose entanglement entropy and betweenness centrality are anomalously small with respect to the other eigenstates belonging to the thermal cloud.

which are *not* continuous deformations of PXP scars. In this case, the existence of a scar manifold as a whole could be described as *statistically stable*.

In order to address such statistical stability we notice that a common tract of constrained models is their representability as hopping Hamiltonians on networks whose nodes are indexed in the computational basis ( $|\{\sigma\}\rangle$  with  $\sigma = \circ, \bullet$  for the PXP model). It is therefore appealing to embed the PXP in a much broader ensemble of Hamiltonians, which we call *Quantum Local Random Networks* (QLRN) sharing the common ingredients of *locality* (in a way we specify below) and *constrained dynamics*.

Let us illustrate the construction of a QLRN in the simplest case (see Fig. 3.1-(a)): consider the network whose vertices are the sequences of  $N$  elements  $\{\sigma_i\}$ , where  $\sigma_i = 0, 1$  and  $i = 1, \dots, N$ , representing the computational basis of the Hilbert space of a spin system. Each pair of vertices is connected by an edge with probability  $0 \leq p \leq 1$  provided they differ by

a single flip of a boolean variable. The adjacency matrix of the resulting network is then the Hamiltonian whose spectrum and eigenfunctions will be the subject of our study. We note that, in this context, locality is intended in the sense that states connected by the Hamiltonian only differ by the properties of a single site. Evidently, while the PXP model is just a particular realization of a QLRN, we expect the latter to be mimicking the physics of the PXP model for  $p = 0.25$  since in this model only one in four configurations of the nearest neighbours of a spin allows it to be flipped.

Note that, similarly to the PXP model, each Hamiltonian of the QLRN ensemble has matrix elements only between states with opposite  $Z$  parity (is a bipartite graph), and hence anticommutes with the operator  $\mathcal{C} = \prod_i Z_i$ . As a consequence, the spectrum is symmetric around  $\epsilon = 0$  and has a degeneracy in  $\epsilon = 0$  that scales exponentially with  $N$  [71]. Another consequence is that, from the point of view of network theory, in a QLRN the clustering coefficient of each node (which is proportional to the number of triangles through that node [91]) is always zero, because the nearest neighbours of a vertex have the same parity, so they cannot be joined by an edge.

## 3.2 Localized eigenstates

The use of the language of network theory in condensed matter physics has a long history, starting from studies of Anderson-type localization in generic networks [92], disorder-free localization on random trees [88] or as a function of clustering coefficient [93, 94]. The possibility to generate localized states without disorder by taking advantage of geometrical constraints suggests that models of this type could be of interest for numerous problems, as was recently recognized in the context of the physics of many-body localization [95] and thermalization [96, 97].

For QLRN, the physics of localization emerges immediately when one considers the density of states vs.  $\epsilon$  for fixed system size  $N$  at different  $p$  (see Section A.6 in the Appendix): while for  $p = 1$  the spectrum is obviously the sequence of peaks associated to a spin of size  $N$  in unit magnetic field, as  $p$  diminishes the peaks first broaden, merging in a bell shaped DOS with a clear delta-function peak at  $\epsilon = 0$ . This peak, also observed in the DOS of tight-binding models defined on random Erdős-Rényi networks [93], is typically associated with localized states.

In our case, the peak is a consequence of the properties of the Hamiltonian under parity symmetry, as commented above. In the case of QLRN one has to pay attention to a trivial type of localization associated to disconnected vertices which get isolated as  $p$  diminishes (a phenomenon similar to the fragmentation of Hilbert spaces observed in Ref. [86, 98]). Since in this work we will be interested in non-trivial localized states on QLRN and their connection to the physics of scars, in the following we will always identify the giant connected component of a QLRN and study localized states in this

subspace. As expected a peak at  $\epsilon = 0$  in its spectrum is present also under this restriction. We find that within this degenerate subspace it is possible to find non-trivial eigenstates localized on the *periphery* of the network as depicted in Fig. 3.1-(b).

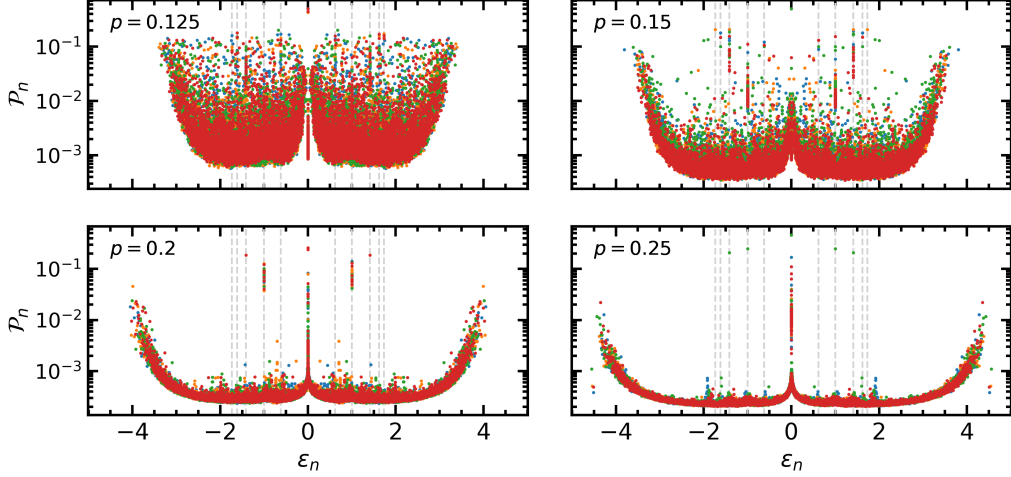


Figure 3.2: Participation ratio  $\mathcal{P}_n$  of the eigenstates for different values of  $p$  for system size  $N = 14$ . The colors indicate different realizations of the network. Statistical scars have large value of  $\mathcal{P}_n$ : they are localized in the computational basis. For large  $p$  their number goes to zero.

The localized states at  $\epsilon = 0$  are just the simplest of a class of nontrivial localized states on the QLRN emerging at sufficiently small  $p$ . In order to characterize the localization properties of these and other eigenstates one may write them in the computational basis  $|\Psi_n\rangle = \sum_i c_n(\{\sigma\})|\{\sigma\}\rangle$  and study the participation ratio  $\mathcal{P}_n = \sum_{\{\sigma\}} |c_n(\{\sigma\})|^4$ . In addition, the structure of wave functions on the QLRN can be studied using standard measures of the character of nodes: *i*) the degree  $k(\{\sigma\})$ ; *ii*) the centrality  $C(\{\sigma\}) = 1/\sum_{\sigma' \neq \sigma} l_{\sigma'\sigma}$ , where  $l_{\sigma'\sigma}$  is the distance between two sites on the lattice; and *iii*) the betweenness centrality  $B(\{\sigma\})$  defined as the number of shortest paths among different vertices passing through  $\{\sigma\}$ . One can easily use these quantities to study eigenstates by defining their averages over a generic eigenstate  $|\Psi_n\rangle$ , e.g., for the betweenness

$$\langle B \rangle_n = \sum_{\{\sigma\}} |c_n(\{\sigma\})|^2 B(\{\sigma\}). \quad (3.2)$$

Finally, since these eigenstates can be interpreted as many-body states of a spin chain of size  $N$  one may compute the half-chain entanglement entropy  $\mathcal{S}_n$  to connect localization on QLRN to the physics of scars.

As seen in Fig. 3.1-(c) by plotting the half-chain entanglement entropy  $\mathcal{S}_n$  for a QLRN at  $p = 0.15$  as a function of eigenstate energy  $\epsilon$  one can easily identify a number of eigenstates whose  $\mathcal{S}_n$  is significantly lower than the

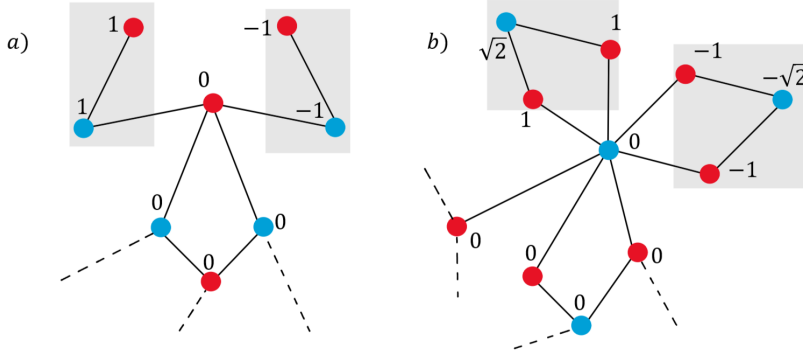


Figure 3.3: Graphical representation of examples of localized eigenstates with energy (a)  $\epsilon^* = 1$  and (b)  $\epsilon^* = \sqrt{2}$ . The color of each node indicates the parity of the corresponding state in the computational basis. Edges connect states with opposite parity. The number written on each node is the coefficient  $c_n(\{\sigma\})$  of the eigenstate  $|\Psi_n\rangle$  in the computational basis. Each state is localized in the grey rectangles: all other nodes have  $c_n(\{\sigma\}) = 0$ . In both examples, the eigenstate of the full graph is constructed using as building block an eigenstate of a small motif (of two sites in (a) and three sites in (b)): the graph contains two copies of the motif; the coefficient of the motif eigenstate are assigned with opposite signs on the two copies. The construction can be generalized to all the energies  $\epsilon^*$  that are eigenvalues of small motifs.

typical value at that energy, therefore behaving as quantum scars. Most of these eigenstates share the feature of having significant (and untypical) participation ratio (see Fig. 3.2), and are therefore localized on the network. However, the way they are localized is not always the same, as shown by plotting the eigenstate average betweenness  $\langle B \rangle_n$  vs.  $\epsilon$  (Fig. 3.1-(c), lower panel): localized scars at specific energies (vertical lines at  $\epsilon^* = 0, \pm 1, \pm\sqrt{2}, \pm(\sqrt{5} \pm 1)/2, \pm\sqrt{3}, \dots$ ) tend to have a lower betweenness than the rest, indicating that they are not just localized, but localized on the periphery of the network. Those are the key features that define statistical scars: oppositely, stochastic scars occur at system size and realization dependent energies, and are not necessarily localized at the edges of the network or have low betweenness. As shown in Fig. 3.2, both types of scars proliferate as  $p$  is lowered below a certain threshold  $p \simeq 0.2$ .

### 3.3 Statistical scars

We now further investigate the presence of statistical scars at specific energies. The special energies  $\epsilon^*$  are well known to be the eigenvalues of the adjacency matrices of small trees [88, 89]. The fact that various figures of merit, including the centrality and degree (see Section A.9 in the Appendix), suggest that statistical scars are localized on the periphery of the network,

indicates that small elementary subgraphs (motifs) might be the basic elements associated to statistical scars. This is indeed the case as shown in Fig. 3.3: the eigenfunction of subgraphs of two vertices (eigenvalues  $\pm 1$ ) or three vertices (eigenvalues  $\pm\sqrt{2}, 0$ ) can be easily incorporated into eigenfunctions of the whole QLRN whenever geometrical structures of the type of Fig. 3.3-a or Fig. 3.3-b occur on its periphery.

The occurrence of network motifs associated to statistical scars depends both on the overall system size  $N$  and, most crucially, on  $p$ . In order to investigate how many scars are to be expected as a function of system size, we studied how the degeneracy of statistical scars with a given value of  $\epsilon^*$ , averaged over realizations of the QLRN, scales with  $N$  for a fixed  $p$ . This is shown in Fig. 3.4 for  $\epsilon^* = 1$ : while for  $p = 0.25$  the degeneracy of these scars does not increase with  $N$ , a completely different behavior, characterized by a continuous growth, is seen for smaller  $p$ . This fact seems to suggest the presence of an eigenstate transition as a function of  $p$ , with a critical  $p_c(\epsilon = 1) \simeq 0.2$ . A similar behaviour is observed for other values of  $\epsilon^*$  (see Section A.10 in the Appendix). We note that, differently from eigenstate phase transitions in the context of many-body localization, in the present case, the transition occurs at exactly known values of the energy only, and not in a continuous part of the spectrum. This may facilitate future studies, targeting, e.g., exact energy manifolds.

As a last comment, we note that some of the characteristic energies of statistical scars correspond to the energies of the exact scars found in the PXP [52] and in the generalized PXP models in Section 2.3. This is not a coincidence: those scars, of the form of matrix product states (MPS), realize an effective “decoupling” of the system in small blocks; the eigenenergies are then originated from the diagonalization of the small blocks, akin to the motifs of statistical scars. Despite this similarity, we do not find a direct connection between the two types of scars. In contrast with statistical scars, the number of MPS scars does not grow with the size of the system; moreover, the structure of MPS scars is specific of the low dimensionality of the model. We leave the question of a deeper connection between the two types of scars to future works.

### 3.4 Conclusions and outlook

We studied the statistical stability of a scar manifold by introducing a class of Hamiltonians, Quantum Local Random Networks, that combine locality and constrained dynamics, and that include PXP as a particular instance. Focusing on the giant connected component of a QLRN we have shown that it is expected to display two types of scars for sufficiently small  $p$ : *stochastic scars*, which occur at realization and system size dependent energies, and *statistical scars* which occur at special energies,  $\epsilon^* = 0, \pm 1, \pm\sqrt{2}, \pm(\sqrt{5} \pm 1)/2, \pm\sqrt{3}, \dots$ . The latter are solely dictated by

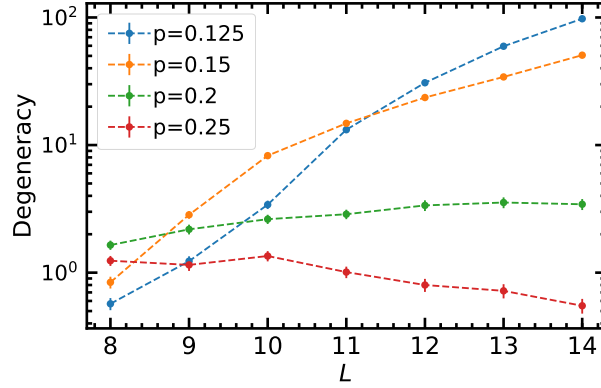


Figure 3.4: Average degeneracy of the eigenspace with  $\epsilon^* = 1$  as a function of system size  $N$ . For  $p < p_c$  ( $p_c \simeq 0.2$ ) the degeneracy increases with  $N$ , while it decays for  $p > p_c$ .

random graph theory, and are associated to localized states on certain geometrical motifs on the periphery of the QLRN. A study of the degeneracy of statistical scars for various  $p$  as a function of systems size indicates the possibility of a quantum phase transition occurring at a critical value  $p_c \simeq 0.2$  between a phase in which scars proliferate and one in which their number saturates for increasing  $N$ . These states appear in a variety of specific realizations, from (generalized) PXP [1, 52] to Hubbard models [99]. Studying in detail this phenomenon, together with potential generalizations to other QLRN, is an intriguing perspective, that we leave to future investigations.

# Chapter 4

## Weak-ergodicity-breaking via lattice supersymmetry

In many-body theories, generic phenomena are often associated to and characterized by the presence of symmetries [100]. Examples include quantum critical points and topological insulators [101], whose universal properties are dictated by the presence of microscopic global symmetries, and the confining properties of gauge theories, which are often related to the structure of local conservation laws [102]. While these examples concern the equilibrium properties of matter, the role of symmetries has also been widely investigated in systems out-of-equilibrium, for instance, in connection to universal behavior [103, 104].

A paradigmatic phenomenon that lies 'in-between' equilibrium and out-of-equilibrium is represented by quantum many-body scars. While a number of models supporting scars have recently been found [55, 56, 58–62, 73–80], the general conditions (if any) for stabilizing ETH-violating states are still unknown, and the role of symmetries in this context stands as an open question. Some of the recent works in this direction link the presence of quantum scars to signatures of integrability [81], to semiclassical trajectories [105, 106], to quasiparticle excitations [52, 57] and to the emergence of an algebraic structure [69]. Another candidate mechanism was put forward in Ref. [4], in which scarred bands of Rydberg atom chains are interpreted as special eigenstates that survive the lattice regularization of an integrable field theory. While integrability does not have an immediate counterpart in more than one dimension, the Coleman-Mandula theorem shows how supersymmetry provides a feasible way of extending the set of conservation laws without resulting in a trivial (in the sense of S-matrix being the identity) theory [107].

Here, we show how supersymmetry (SUSY) provides a route to formulate lattice models with 'scarred' states in the middle of the spectrum, whose stability is guaranteed as long as supersymmetry itself is not violated. Specifically, we consider  $D$ -dimensional lattice models of constrained spin-less fermions, that realize an exact  $N = 2$  supersymmetry at the lattice

level [108–116], and show how these models support scarred eigenstates (as SUSY doublets) in any  $D$ . After the general proof, we discuss in detail the ladder case, and address the resilience of scarred eigenstates in the presence of supersymmetry-breaking terms.

## 4.1 Supersymmetric lattice models

The model we study was introduced in Ref. [108]. The degrees of freedom are spinless fermions  $c_{\mathbf{r}}$ , with  $\mathbf{r}$  being a site on a generic lattice, and the operators satisfy the canonical anticommutation relations  $\{c_{\mathbf{r}}^\dagger, c_{\mathbf{s}}\} = \delta_{\mathbf{r},\mathbf{s}}$ . The Hamiltonian can be written in terms of the supercharge operators  $Q$  and  $Q^\dagger$  defined as

$$Q^\dagger = \sum_{\mathbf{r}} \alpha_{\mathbf{r}} P_{\mathbf{r}} c_{\mathbf{r}}^\dagger, \quad Q = \sum_{\mathbf{r}} \alpha_{\mathbf{r}}^* P_{\mathbf{r}} c_{\mathbf{r}}, \quad (4.1)$$

where  $\alpha_{\mathbf{r}}$  is a complex coefficient, and  $P_{\mathbf{r}}$  is a projector which constrains all the neighbours of site  $i$  to be unoccupied. The Hamiltonian has the form

$$H = \{Q^\dagger, Q\}. \quad (4.2)$$

The supercharge operators satisfy

$$Q^2 = (Q^\dagger)^2 = 0, \quad [H, Q] = [H, Q^\dagger] = 0. \quad (4.3)$$

In addition to these, the model has a symmetry associated to the fermion number  $F = \sum_{\mathbf{r}} P_{\mathbf{r}} c_{\mathbf{r}}^\dagger c_{\mathbf{r}}$ , with  $[F, Q^\dagger] = Q^\dagger$ ,  $[F, Q] = -Q$ . The Hamiltonian can be explicitly rewritten as  $H = H_0 + V$  with

$$H_0 = \sum_{\langle \mathbf{r}, \mathbf{s} \rangle} (\alpha_{\mathbf{r}} \alpha_{\mathbf{s}}^* P_{\mathbf{r}} c_{\mathbf{r}}^\dagger c_{\mathbf{s}} P_{\mathbf{s}} + \text{H.c.}), \quad (4.4)$$

$$V = \sum_{\mathbf{r}} |\alpha_{\mathbf{r}}|^2 P_{\mathbf{r}} \quad (4.5)$$

where  $\langle \mathbf{r}, \mathbf{s} \rangle$  indicates pairs of neighbouring sites. Below, we will focus on  $D$ -dimensional hypercubic lattices of linear dimension  $L$ : some of the results are extendable to other bipartite lattices. The supersymmetric algebra imposes a specific structure of the spectrum. Eigenstates can be classified in singlets and doublets: all the singlets satisfy  $Q|\psi\rangle = Q^\dagger|\psi\rangle = H|\psi\rangle = 0$ ; doublets are pairs of states of the form  $|\psi\rangle, Q^\dagger|\psi\rangle$  (with the condition  $Q|\psi\rangle = 0$ ) and have strictly positive energy. As discussed in detail in Ref. [108], this set of constraints realizes a  $N = 2$  SUSY which is exact at the lattice level.

Before moving to the core of our work, we note that, in 2D and 3D, the models presented above draw strong similarities to the dynamics of fermionic isotopes confined in optical lattices, and laser-dressed with Rydberg  $s$ - or  $p$ -states [117–122]. In particular, the tunneling dynamics subjected to the constraints discussed above has been pointed out in Ref. [123, 124], and experimentally demonstrated in Ref. [125].

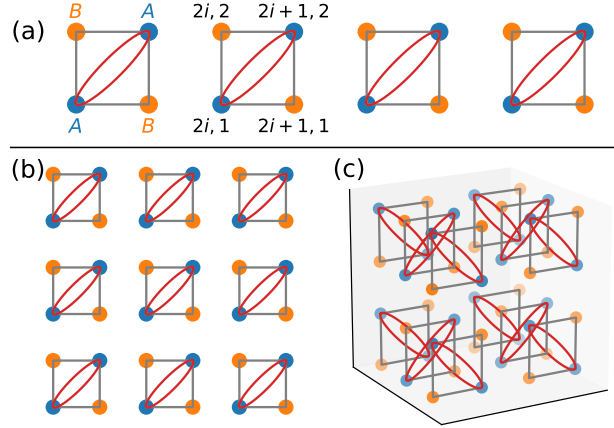


Figure 4.1: (a) Exact eigenstate  $|\psi_{A,e}\rangle$  in two-leg ladders. Sites belonging to sublattices  $A$  and  $B$  are colored in blue and orange respectively. Grey rectangles indicate the plaquettes, and for each plaquette there is a fermion in a superposition of the sites on the diagonal as in Eq. 4.6. The square (b) and cubic (c) lattices are split into plaquettes. On each plaquette we put a fermion in a superposition between the  $A$  sites, in such a way that hopping terms annihilate the state. States with larger fermionic numbers can be constructed by placing two fermions, one on each  $A$  site.

## 4.2 Exact eigenstates at finite energy density: two-leg ladders

We now construct exact eigenstates in the middle of the spectrum. These states can be written as product states of square plaquettes, and can be found for any filling  $F \geq L/2$ , as we will detail in the following subsections. For the sake of readability, we first discuss the conceptually simpler 2-leg ladder case, and then move forward to the generic bipartite lattice in  $D$  spatial dimensions.

To set the notation, we define the two sublattices  $A$  and  $B$  as in Fig. 4.1-a, such that each  $A$  site has only neighbours of type  $B$  and vice versa. We split the ladder in plaquettes (the grey squares in Fig. 4.1-a): we can choose to put the plaquettes either between neighbouring even/odd or odd/even rungs. From now on, we choose to place them between even and odd rungs as in Fig. 4.1-a. From the set of states that we will construct following this choice, we can then obtain a new set of states by applying a translation of one site along the ladder (the new states will be product states of odd/even plaquettes).

*Half-filling.* Since the total number of fermions  $F$  is conserved, we can construct eigenstates with a fixed filling. We first consider the sector  $F = L/2$ . We define the states  $|\psi_{A,e}\rangle$  as follows:

$$|\psi_{A,e}\rangle = \prod_{i=0}^{L/2-1} \frac{1}{\mathcal{N}_{i,A}} \left( d_{2i,1}^\dagger - d_{2i+1,2}^\dagger \right) |0\rangle, \quad (4.6)$$

where  $d_{i,j}^\dagger = \alpha_{i,j}^{-1} P_{i,j} c_{i,j}^\dagger$  and  $\mathcal{N}_{i,A}$  is a normalization constant. We choose the convention that the product is ordered from left to right. The state is constructed as a product state of plaquettes, with a fermion in each plaquette: each fermion sits in a superposition between the two sites of a diagonal (of type  $A$ ).

In order to prove that  $|\psi_{A,e}\rangle$  is an eigenstate, it is convenient to treat separately the hopping terms within a plaquette and those between different plaquettes. Within the plaquette, the fermions can hop from sites of the sublattice  $A$  to the sublattice  $B$ : however, the coefficients in the superposition are such that the two contributions from the  $A$  sites cancel due to destructive interference for each of the  $B$  sites. On the other hand, the terms between different plaquettes would bring a fermion in a site  $B$  which cannot be occupied due to the hard-core constraint, and hence annihilate the state. These two arguments prove that  $H_0 |\psi_{A,e}\rangle = 0$ . The interaction term can also be easily computed by noting that  $P_{i,j} = 0$  for sites of lattice  $B$  and  $P_{i,j} = 1$  for those of lattice  $A$ . Therefore we have

$$H |\psi_{A,e}\rangle = V |\psi_{A,e}\rangle = \sum_{(i,j) \in A} |\alpha_{i,j}|^2 |\psi_{A,e}\rangle. \quad (4.7)$$

We can similarly construct the state  $|\psi_{B,e}\rangle$ , having fermions on sublattice  $B$ ,

$$|\psi_{B,e}\rangle = \prod_{i=0}^{L/2-1} \frac{1}{\mathcal{N}_{i,B}} \left( d_{2i,2}^\dagger - d_{2i+1,1}^\dagger \right) |0\rangle. \quad (4.8)$$

As anticipated, other two states can be obtained by applying the translation operator, namely  $|\psi_{A/B,o}\rangle = T |\psi_{B/A,e}\rangle$ . We note that, while eigenstates that occupy different sublattices are orthogonal ( $\langle \psi_A, \cdot | \psi_B, \cdot \rangle = 0$ ), the eigenstates defined on the same sublattice have the same energy and are not orthogonal ( $\langle \psi_{A,e} | \psi_{A,o} \rangle \neq 0$  and  $\langle \psi_{B,e} | \psi_{B,o} \rangle \neq 0$ ), but they are linearly independent. These states have energy  $E_{A/B} = \sum_{(i,j) \in A/B} |\alpha_{i,j}|^2$ : being eigenstates at a finite energy density above the zero-energy ground state, their entanglement entropy is expected to be proportional to the volume  $L$ . This is not the case: when the ladder is cut in two, the entanglement entropy is either 0 (if the cut is between two plaquettes) or a finite quantity (if the cut is within a plaquette). These eigenstates satisfy an area law entanglement at a finite energy density and hence they qualify as many-body quantum scars.

*Above half-filling.* For number of fermions  $F > L/2$ , a number of exact eigenstates can be similarly constructed as a product state of plaquettes. We start from one of the four states  $|\psi_{A/B,e/o}\rangle$ , and we choose  $F - L/2$  plaquettes where to increase the fermion occupancy from 1 to 2 fermions:

on the selected plaquettes we place fermions on both sites of the diagonal. For example, we can add a fermion to the  $j$ -th plaquette on top of the state  $|\psi_{A,e}\rangle$  by substituting  $(d_{2j,1}^\dagger - d_{2j+1,2}^\dagger)/\mathcal{N}_{j,A}$  with  $P_{2j,1}c_{2j,1}^\dagger P_{2j+1,2}c_{2j+1,2}^\dagger$  in the product in Eq. 4.6. In this way, we obtain  $\binom{F-L/2}{L/2}$  states, one for each choice of the positions of the doubly occupied plaquettes.

With the same argument used for the states at filling  $F = L/2$ , it is possible to prove that these states are annihilated by  $H_0$  and are eigenstates of  $V$  with eigenvalue  $\sum_{(i,j)\in A/B} |\alpha_{i,j}|^2$ .

### 4.3 Exact scars in $d$ -dimensional hypercubic lattices

We now generalize the construction of exact eigenstates for the square ladder presented above to hypercubic lattices in dimension  $D$ . To do so, we group all the sites of the lattice into square plaquettes, and we construct the eigenstates as product states of plaquettes. We define the two sublattices  $A$  and  $B$ , such that neighbouring sites belong to different sublattices. We find two classes of eigenstates: in  $A$ -states ( $B$ -states) fermions occupy the sites on sublattice  $A$  ( $B$ ) only. To construct the states, on each plaquette we create either one or two fermions on the ( $A/B$ ) diagonal, with the same operators as in the ladder. A pictorial representation of one of these states is shown in Fig. 4.1 for  $d = 2$  and  $d = 3$ .

The number of exact eigenstates depends on the number of ways in which the lattice sites can be grouped in square plaquettes and it grows with the system size. For example, in the specific case  $d = 2$  and  $F = L_x L_y / 4$  (where  $L_x$  and  $L_y$  are even and are the number of sites in the  $x$  and  $y$  directions), we can construct  $2^{L_x/2} + 2^{L_y/2} - 2$  different states for each sublattice ( $A$  or  $B$ ).

### 4.4 Spectral statistics in two-leg ladders

In the previous section we found an extensive number of states with finite energy density and an entanglement entropy which does not depend on  $L$ . We now show that the rest of the spectrum for a two-leg ladder with periodic boundary conditions is compatible with ETH.

We study the model in Eq. 4.4 using exact diagonalization. Since the construction above works for arbitrary, site-dependent coefficients  $\alpha_{i,j}$ , we choose random real coefficients  $\alpha_{i,j}$  from a uniform distribution in the interval  $[1, 2)$ , and average over a certain number of disorder realizations. We compute the spectrum in the sector with fermionic number  $F = L/2$ . Thanks to the supersymmetric algebra, the Hilbert space can be split in three sectors: (i)  $\mathcal{H}_{Q^\dagger} = \{|\psi\rangle : Q|\psi\rangle = 0, Q^\dagger|\psi\rangle \neq 0\}$ , (ii)  $\mathcal{H}_Q = \{|\psi\rangle : Q|\psi\rangle \neq 0, Q^\dagger|\psi\rangle = 0\}$ , (iii)  $\mathcal{H}_0 = \{|\psi\rangle : Q|\psi\rangle = 0, Q^\dagger|\psi\rangle = 0\}$ . The

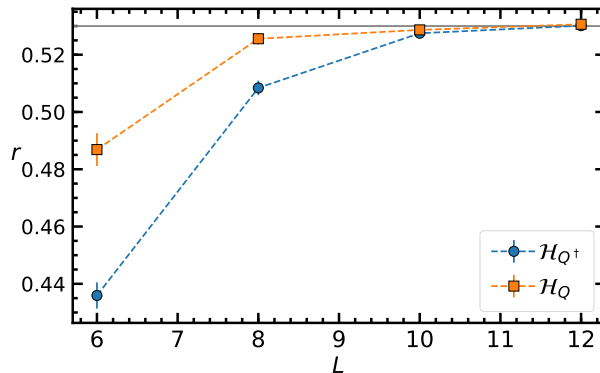


Figure 4.2: Average level spacing ratio as a function of the number of rungs  $L$  in the two sectors of non-zero energy states. The grey line indicates the value predicted for Wigner-Dyson spectral statistics. For increasing  $L$ , in both sectors  $r$  flows towards  $r_{WD}$ , signalling compatibility with the ETH.

Hamiltonian is block-diagonal in these sectors: the states of the last sectors are singlets with energy  $E = 0$ ; we focus on the other two sectors, where the structure of the spectrum is non-trivial. We remark that each state of these sector belongs to a SUSY doublet and hence has a SUSY partner with the same energy, but different fermionic number ( $F = L/2 + 1$  for the first sector and  $F = L/2 - 1$  for the second sector). Therefore, no degeneracies and no other conservation laws are expected in the spectrum we analyze. To test the validity of the ETH for the majority of the eigenstates, we study the ratio between nearby gaps

$$r_n = \frac{\text{Min}\{\Delta E_n, \Delta E_{n+1}\}}{\text{Max}\{\Delta E_n, \Delta E_{n+1}\}}. \quad (4.9)$$

Here  $\Delta E_n = E_n - E_{n-1}$ , with  $n$  labelling the eigenvalues  $E_n$  of  $H$  in increasing order, for a given disorder realization. We then average  $r_n$  over  $n$  and over 100 disorder realizations; we consider the full energy spectrum. The results, plotted in Fig. 4.2 clearly show that in both sectors  $r$  converges to the value expected for a Wigner-Dyson distribution  $r_{WD} = 0.536$  for increasing  $L$ , and thus validate the assumption that the majority of the eigenstates satisfy the ETH.

We then check that the eigenstates we found are the only anomalous states in the spectrum. We choose coefficients  $\alpha_{i,j} = 1$  for all sites. In Fig. 4.3-a, we show the half-chain entanglement entropy for ladders of  $L = 12, 14$  rungs with  $L/2$  fermions in the translation- and reflection-invariant sector. In both sectors  $\mathcal{H}_{Q^\dagger}$  and  $\mathcal{H}_Q$ , the majority of the eigenstates approximate a smooth profile with large entanglement in the middle of the spectrum, as expected in an ergodic system. A single outlier (circled in red) with anomalously small entanglement entropy is present in a region

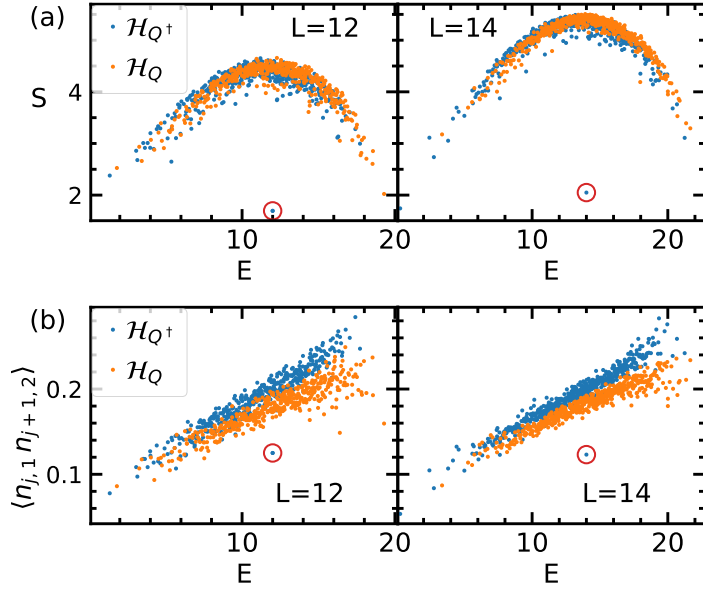


Figure 4.3: (a) Bipartite entanglement entropy as a function of the energy of the eigenstates in the translation- and reflection-invariant sector. (b) Expectation value of the local observable  $n_{j,1}n_{j+1,2}$  a function of the energy of the eigenstates in the translation- and reflection-invariant sector. Blue (orange) dots correspond to states in the sector  $\mathcal{H}_{Q^\dagger}$  ( $\mathcal{H}_Q$ ).

of high energy density and corresponds to the translation- and reflection-invariant superposition of the eigenstates defined above. Similar conclusions are corroborated by the analysis of diagonal correlations, depicted in Fig. 4.3-b.

## 4.5 Robustness to perturbations

We now discuss the stability of SUSY scarred eigenstates with respect to external perturbations. As discussed above, the states are stable under arbitrary supersymmetric perturbations. In particular, the construction above does not rely on any specific structure of the coefficients  $\alpha_i$ . In this section, we will investigate the robustness of these scarred eigenstates to other perturbations, which break the supersymmetry of the model.

As a first case, we consider the Hamiltonian  $H_\eta = H_0 + \eta V$  in any  $D$ . If we move away from the supersymmetric point  $\eta = 1$ , the Hamiltonian does not commute with the supercharges and the spectrum cannot be split in sectors. However, since the scars we construct (both for half and higher filling) are simultaneous eigenstates of  $H_0$  and  $V$ , they are exact eigenstates of  $H_\eta$  for arbitrary  $\eta$ .

Next, we consider the ladder case, and a perturbation of the type  $H_\lambda =$

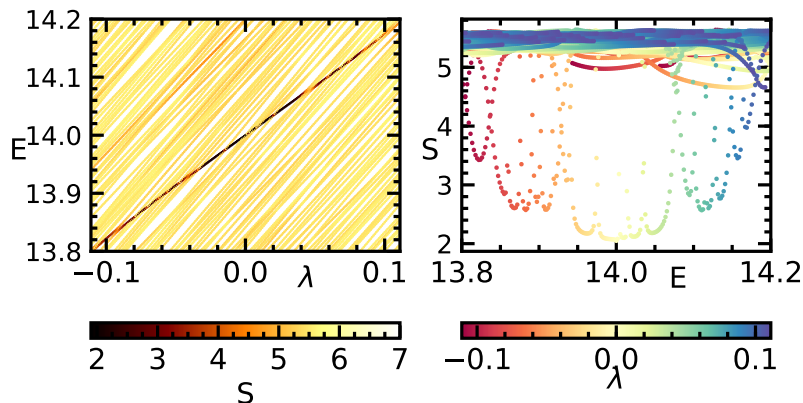


Figure 4.4: Bipartite entanglement entropy as a function of the energy of the eigenstates for different values of  $\lambda$  ( $L = 14$ ). The eigenstates are in the translation- and reflection-invariant sector.

$\lambda \sum_{i=0}^{L-1} (n_{i,1}n_{i+1,2} + n_{i,2}n_{i+1,1})$ , with  $n_{i,j} = c_{i,j}^\dagger c_{i,j}$ . The scars we construct for  $\lambda = 0$  are not exact eigenstates for  $\lambda \neq 0$ . We perform a numerical analysis following a previous study of perturbations in constrained spin chains [65].

In Fig. 4.4 we plot the bipartite entanglement entropy as a function of the energy for different values of  $\lambda$ . For  $\lambda = 0$  there is a single scar in the half-filling case in the translation- and reflection-invariant sector. For some values of  $\lambda$ , this scar hybridizes strongly with the continuum of states belonging to the thermal cloud, but small values of the entropy persist in a large region of  $\lambda$  (large with respect to average gap at this energy density), excluding the aforementioned points. As is clear from Fig. 4.4, the scarred state undergoes a large number of level crossing as  $\lambda$  is varied but its entanglement entropy remains anomalously small. The phenomenology is extremely similar to the case of constrained spin-models, and, while system sizes here are insufficient to draw conclusions that hold in the thermodynamic limit, we can still observe the same type of resilience of scarred features at finite size.

In terms of physical implementations, the models we discussed have been partly addressed in works related to fermionic Rydberg-dressed atoms (at least, for the case of ladders). We note, however, that in terms of experimental signatures the connection to experiments requires some extra care with respect to other spin models. In order to have long-time coherent oscillations, like the ones observed in [46], a set of equally-spaced energy eigenstates is needed. In our case, this could be achieved by adding a chemical potential, which shifts the scars according to the number of particles. However, to detect the oscillations, one should be able to prepare an initial state in a superposition with different numbers of particles. While this might be possible for spin systems (a similar mechanism is used, for example, in [56]), it is not feasible for number-conserving fermionic particles. A

more direct experimental proof of the existence of scars would be obtained using the scar itself as initial state of the dynamics: every observable should remain approximately constant in time.

## 4.6 Connection to the Shiraishi-Mori construction

We now comment on the connection of the eigenstates discussed above with the Shiraishi-Mori construction for embedding ETH-violating states in an otherwise ergodic spectrum [64]. The construction consists of local projectors  $P_j$  and a subspace  $\mathcal{T}$  of the Hilbert space satisfying  $P_j\mathcal{T} = 0$ . Then the Hamiltonian

$$H = \sum_j P_j h_j P_j + H' \quad [H', P_j] = 0 \quad (4.10)$$

has candidate scarred eigenstates in the subspace  $\mathcal{T}$ . It can be shown that the Hamiltonian (4.4) can be recast in the form of Eq. (4.10) with  $\mathcal{T}$  being the subspace with a single scar state. We examine, for instance, the scar  $|\psi_{A,e}\rangle$  in Eq. (4.6). To prove the construction, we define  $P_j$  as a local projector acting on the  $j$ -th plaquette and on its neighbours,

$$P_j = 1 - |j_{A,e}\rangle \langle j_{A,e}|, \quad (4.11)$$

$$|j_{A,e}\rangle = \prod_{i=j-1}^{j+1} \frac{1}{\mathcal{N}_{i,A}} \left( d_{2i,1}^\dagger - d_{2i+1,2}^\dagger \right) |0\rangle_i. \quad (4.12)$$

This projector annihilates the state that has a single fermion in a superposition on the  $A$  diagonal in each of the plaquettes considered (as in the state  $|\psi_{A,e}\rangle$ ) and acts trivially on the other states. We find that the term  $V$  commutes with the projectors  $P_j$  and corresponds to  $H'$  in the Shiraishi-Mori construction. The hopping terms, on the other hand, need some further manipulation. We define  $h_j$  as made of two parts: (i) the sum of the hopping terms in the  $j$ -th plaquette, (ii) the sum of the hopping terms between the  $j$ -th plaquette and its neighbors (with a factor  $1/2$ ). With this definition, we see that  $h_j = P_j h_j P_j$  and  $H_0 = \sum_j h_j$ , resulting in the desired form of Eq. (4.10). This construction can be applied to the other scars, and to the case of higher dimensionality. Each scar represents an isolated embedded subspace, and hence its entanglement entropy does not scale with  $L$ .

## 4.7 Conclusions and outlook

We have shown that  $N = 2$  supersymmetric lattice models display weak-ergodicity breaking in the form of scarred eigenstates in any  $D$ -dimensional

hypercubic lattice. SUSY is not a sufficient ingredient for quantum scars in  $D > 1$ : for instance, even within the model we consider, the spectrum at low-filling does not feature ergodicity breaking. Instead, we find important to emphasize that the results reported here underline that insights from quantum field theory - in our case, provided by the Coleman-Mandula theorem - can provide a very simple tool to easily diagnose conditions that favor quantum scarring, that is complementary to other approaches based on exact lattice solutions, that are typically applicable to single models [52, 55, 62, 73]. It is important to stress that it would not be sufficient for a lattice model to recover SUSY as a low-energy symmetry, since the phenomena we are concerned with require finite-energy-density above the ground state. Due to the fact that formulating explicit supersymmetric theories on the lattice is challenging, it stands as an open quest to determine if there exist additional features that, in combination with SUSY, can guarantee the appearance of quantum scars in given lattice models. To resolve such questions, it would thus be important to formulate lattice models with richer supersymmetric structures, and investigate their SUSY-specific dynamical effects [126].

## Part II

# Quantum simulation of lattice gauge theories



## Chapter 5

# Quantum simulation of high-energy physics

The Standard Model describes all known elementary particles and the fundamental forces (with the exception of gravity) in our universe. Thanks to a collective effort of many research groups around the world, it is now possible to test its predictions against experiments with unprecedented precision. One of the outstanding challenges that the community has to face is the difficulty of deriving information of physical phenomena from the Standard Model: in particular, solving the fundamental equations of the quantum chromodynamics (QCD) theory of quarks and gluons is a complicated problem that requires non-perturbative approaches based on computationally-expensive Monte Carlo simulations. These methods allow for very precise calculations of the masses of hadrons and of many other quantities. There are, however, some properties that are intrinsically prohibitive for this type of classical computation. Calculations at finite baryon density, for example, which are relevant for studying the early universe and neutron stars, are affected by the sign problem, meaning that numerical evaluations of the integrals become unfeasible because of the near-cancellation of terms with opposite signs. The sign problem also arises in calculations of real-time evolution and was proven to be NP hard [127]. This limits our predictive power on many important non-equilibrium phenomena: for example, the products of the high-energy collisions of hadrons cannot be computed from first principle. This knowledge would be very useful in the research for physics beyond the Standard Model.

The need for alternative solutions that do not rely on Monte Carlo methods has recently motivated an increasing interest in the possible applications of quantum simulation and computation [128–130]. The idea of using quantum systems to simulate the (quantum-mechanical) laws of nature traces back to the early 1980s, with the foreseeing work of Richard Feynman [131]. However, it has only been in the last two decades that quantum simulation has become a realistic goal. At present, quantum systems of up to hundreds of qubits can already be controlled with a good degree of flexibility,

and both the achievable coherence time and size of the systems are rapidly increasing [132–138]. In these experiments, highly entangled states of matter can be realized: these states are very difficult to deal with in classical simulation, but are efficiently encoded in quantum systems. Moreover, the real-time dynamics that is out of reach of Monte Carlo simulations is instead the most natural application of quantum simulators.

While technical advances are improving the capabilities of quantum simulators, a complementary effort is required on the theoretical side: the encoding of the theory of interest into the physical degrees of freedom needs to be tailored to the quantum hardware at disposal. This represents an outstanding challenge, because the dynamics of a gauge theory does not have any direct counterpart in quantum simulators: so far, there exists no physical systems that is easy to manipulate in experiments and possesses an intrinsic gauge symmetry. Therefore, it is necessary to explore the possible formulations of lattice gauge theories and conceive the most suitable strategies for implementing them with available quantum simulators. In the following, we will introduce some of the basic ideas in this direction: in Section 5.1 we define the fundamental ingredients of a lattice gauge theory in the Hamiltonian formulation; in Section 5.2 we introduce the quantum link formulation of lattice gauge theories; in Section 5.3 we review some of the main strategies that have been proposed for simulating lattice gauge theories; in Section 5.4 we describe some of the most important experimental platforms; finally, in Section 5.5 we comment on the current status of the field and on the future opportunities.

## 5.1 Hamiltonian formulation of lattice gauge theories

Classical lattice simulations for quantum field theory are typically performed in Euclidean space, by exploiting a Wick rotation of the Lagrangian from real to imaginary time [139]. A quantum simulation, instead, naturally reproduces a real time evolution: therefore, it is best to use a Hamiltonian formulation [140].

We consider a lattice in  $d$  spatial dimensions: the discretized matter field  $\psi_{\mathbf{r}}$  is defined on the sites of the lattice (see Fig. 5.1). Gauge fields are instead defined on the links of the lattice. On each link  $\mathbf{r}, \mathbf{r}'$ , we define the *parallel transporter*  $U_{\mathbf{r}, \mathbf{r}'}$ . The gauge symmetry is, by definition, the invariance of the model under a certain group of local transformations: on each site a generic gauge transformation  $\Omega_{\mathbf{r}}$  acts as

$$\psi_{\mathbf{r}} \rightarrow \Omega_{\mathbf{r}} \psi_{\mathbf{r}}, \quad U_{\mathbf{r}, \mathbf{r}'} \rightarrow \Omega_{\mathbf{r}} U_{\mathbf{r}, \mathbf{r}'} \Omega_{\mathbf{r}'}^{\dagger}. \quad (5.1)$$

It is useful to define the infinitesimal generators  $G_{\mathbf{r}}^a$  of the local transformations. The requirement of gauge invariance corresponds to property that

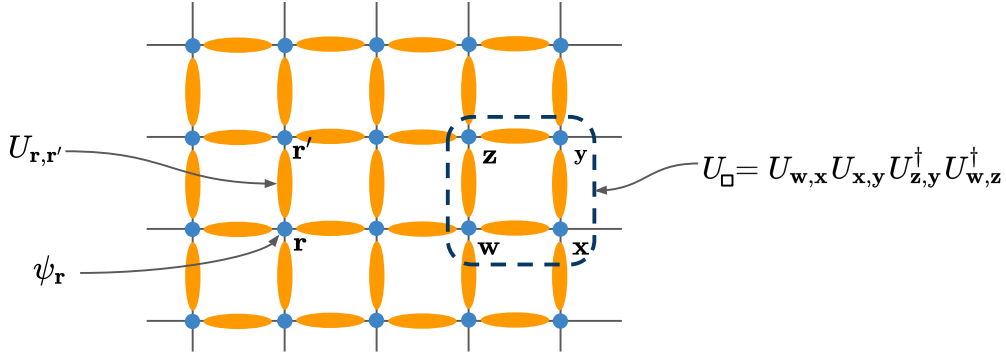


Figure 5.1: Matter resides on the sites of the lattice (in blue), gauge fields are on the link (in orange). The dashed rectangle indicates a plaquette term.

$[H, G_{\mathbf{r}}^a] = 0 \forall \mathbf{r}$ , where  $H$  is the Hamiltonian of the system<sup>1</sup>. Moreover, every *physical* state  $|\Psi\rangle$  also needs to be gauge-invariant, meaning that  $\Omega_{\mathbf{r}} |\Psi\rangle = |\Psi\rangle$  for any local transformation  $\Omega_{\mathbf{r}}$ : therefore, we define the physical states as those that satisfy  $G_{\mathbf{r}}^a |\Psi\rangle = 0 \forall \mathbf{r}$  (*Gauss' law*).

We note that the requirement of a local symmetry puts many constraints on the possible terms in the Hamiltonian: for example, hopping terms of the type  $\psi_{\mathbf{r}}^{\dagger} \psi_{\mathbf{r}'}$  between two neighbouring sites  $r, r'$  are not gauge-invariant; from Eq. (5.1) we see that, to make them gauge-invariant, we need to include the parallel transporter, obtaining  $\psi_{\mathbf{r}}^{\dagger} U_{\mathbf{r},\mathbf{r}'} \psi_{\mathbf{r}'}$ . With the same reasoning, one can see that the simplest gauge-invariant terms made only of  $U_{\mathbf{r},\mathbf{r}'}$  consist of plaquette terms of the type  $U_{\square} = U_{\mathbf{w},\mathbf{x}} U_{\mathbf{x},\mathbf{y}} U_{\mathbf{z},\mathbf{y}}^{\dagger} U_{\mathbf{w},\mathbf{z}}^{\dagger}$  (see Fig. 5.1).

The challenges for quantum simulating a gauge symmetry consist in i) implementing a model which possesses the local symmetry of interest, ii) restricting the dynamics to gauge-invariant states only, iii) realizing the multi-body terms (e.g., plaquette terms) that drive the dynamics of gauge theories. As we will see in the following, meeting all these conditions requires specific strategies, that have to be designed depending on the gauge theory of interest and of the available experimental platform.

### 5.1.1 Example: the lattice Schwinger model

To make the discussion above more concrete, we will consider the example of the *lattice Schwinger model* [141, 142], consisting of fermions coupled to a  $U(1)$  gauge field in one spatial dimension. The Hamiltonian of the model is

<sup>1</sup>In this Chapter we are considering only the case of continuous groups (e.g.,  $U(1)$  or  $SU(N)$ ), for which infinitesimal generators can be defined. For the case of discrete groups, the requirement is that  $[H, \Omega_{\mathbf{r}}] = 0$  for every local transformation in the group.

$$H = -w \sum_{j=1}^{L-1} (\psi_j^\dagger U_{j,j+1} \psi_{j+1} + \text{h.c.}) + m \sum_{j=1}^L (-1)^j \psi_j^\dagger \psi_j + J \sum_{j=1}^{L-1} E_{j,j+1}^2, \quad (5.2)$$

where  $\psi_j, \psi_j^\dagger$  are annihilation/creation operators of spinless fermions<sup>2</sup> of mass  $m$ ,  $U_{j,j+1}$  is the parallel transporter and  $E_{j,j+1}$  is the electric field, which satisfies the commutation relation  $[E_{j,j+1}, U_{k,k+1}] = \delta_{j,k} U_{j,j+1}$ . Note that in one spatial dimension the pure gauge term, of amplitude  $J$ , contains the energy of the electric field, but no magnetic term is present. The matter-field coupling, of strength  $w$ , is of the form introduced above. The Hamiltonian has a  $U(1)$  gauge symmetry, whose generators have the form

$$G_j = E_{j,j+1} - E_{j-1,j} - Q_j, \quad (5.3)$$

where  $Q_j = \psi_j^\dagger \psi_j + [1 - (-1)^j]/2$  is the *charge* on site  $j$ <sup>3</sup>. Thus, the gauge-invariant subspace  $\mathcal{H}_{\text{gauge-inv}} = \{|\Psi\rangle : G_j |\Psi\rangle = 0 \forall j\}$  corresponds to the subspace of states that satisfy Gauss' law, i.e., the states for which at every site the charge is equal to the net electric flux.

### The $\theta$ -angle

Because of the commutation relation  $[E_{j,j+1}, U_{j,j+1}] = U_{j,j+1}$ , the electric field will have the form  $E_{j,j+1} = L_{j,j+1} - \theta/(2\pi)$ , where  $L_{j,j+1}$  has integer spectrum. The fractional part  $0 \leq \theta/(2\pi) < 1$  represents a uniform classical background field. But why is this background electric field represented by an angle? The meaning of the  $\theta$ -angle in the Schwinger model was explained by Coleman [144]: because of Gauss law, the creation of a pair can change the value of electric field between the particles by  $\pm 1$ , so particles can screen the integer part of the background field (see Fig. 5.2-a). The angle  $\theta \in [0, 2\pi)$  accounts for the remaining non-integer part, which cannot be screened.

For  $\theta \neq \pi$  the particles are known to be confined: a particle and an antiparticle placed at distance  $\ell$  on top of the bare vacuum are separated by a string of electric flux which has an energy  $V(\ell) \propto \ell$  (see Chapter 8). The case  $\theta = \pi$  is special: in this case it is possible to create a pair of a particle and an antiparticle with distance  $\ell$  without changing the electrostatic energy of the system (see Fig. 5.2-b).

<sup>2</sup>In the continuum, the fermions of the Schwinger model form a spin doublet. On the lattice, instead, the fermions are spinless because the doublet is split between even and odd sites (*staggered* fermions). Because of this choice, the Hamiltonian is only invariant under translations of even sites; translations of odd sites, instead, corresponds to the chiral symmetry that is explicitly broken by the mass. Staggered fermions are one of the possible formulation of lattice fermions that allows to retrieve the correct continuum limit, avoiding the problem of *fermion doubling* [143].

<sup>3</sup>The choice of the constant in  $Q_j$  is such that the non-interacting vacuum belongs to the gauge-invariant subspace.

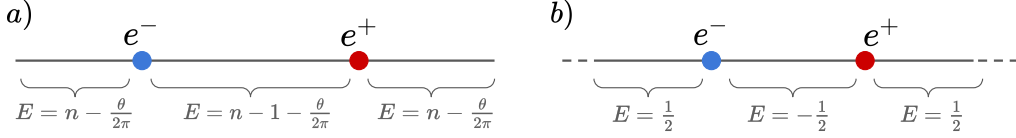


Figure 5.2: a) Pairs of particles (electron and positron) can change only the integer part of the electric field. b) for  $\theta = \pi$  the electric field has half-integer spectrum. In the case depicted here, the change in electrostatic energy (proportional to  $E^2$ ) induced by the creation of a pair is zero: the particles are deconfined.

## 5.2 Quantum Link Models

Implementing the Hilbert space of dynamical gauge fields in a quantum computer or a quantum simulator is, in principle, a complicated task. For example, in Wilson's formulation the local Hilbert space on each link can be seen as the one of a quantum "particle" moving on the group manifold (a circle in the  $U(1)$  case, with the identification  $U_{\mathbf{r},\mathbf{r}'} = e^{i\varphi_{\mathbf{r},\mathbf{r}'}}$  and the angle  $\varphi_{\mathbf{r},\mathbf{r}'}$  is the position on the circle). This means that the local dimension is infinite. In most cases, however, the degrees of freedom at disposal are represented by qubits (or qudits) and have finite-dimensional Hilbert space.

To solve this problem, it is useful to consider an alternative formulation, known as *quantum link* formulation [145–148], where the gauge fields are represented by spin-like variables or fermions<sup>4</sup>. For example, for the case of a  $U(1)$  gauge symmetry, the parallel transporter and the electric field on a link  $\mathbf{r}, \mathbf{r}'$  are represented by the spin- $S$  operators  $S_{\mathbf{r},\mathbf{r}'}^\alpha$ :

$$U_{\mathbf{r},\mathbf{r}'} = S_{\mathbf{r},\mathbf{r}'}^x + iS_{\mathbf{r},\mathbf{r}'}^y, \quad U_{\mathbf{r},\mathbf{r}'}^\dagger = S_{\mathbf{r},\mathbf{r}'}^x - iS_{\mathbf{r},\mathbf{r}'}^y, \quad E_{\mathbf{r},\mathbf{r}'} = S_{\mathbf{r},\mathbf{r}'}^z. \quad (5.4)$$

This choice satisfies the commutation relation  $[E_{\mathbf{r},\mathbf{r}'}, U_{\mathbf{s},\mathbf{s}'}] = \delta_{\mathbf{r},\mathbf{s}}\delta_{\mathbf{r}',\mathbf{s}'}U_{\mathbf{r},\mathbf{r}'}$ . For the case of a  $SU(N)$  non-Abelian gauge symmetry, in the quantum link formulation the gauge fields are represented by bilinear fermionic operators (Schwinger representation). In both cases, the local Hilbert space dimension is finite, allowing for simpler implementations in quantum simulators.

## 5.3 Strategies for quantum simulation of lattice gauge theories

The typical experimental platforms used for quantum simulation do not naturally possess any local symmetry. Therefore, quantum-simulating a lattice gauge theory requires some ad hoc strategies to mimick the desired gauge symmetry. Here we summarize some of the most used ones.

<sup>4</sup>Note that many different models, including quantum dimer and quantum loop models, can be constructed as specific instances of quantum links.

**"Brute force" Hamiltonian engineering** — The most immediate approach is to engineer all the Hamiltonian terms of the model of interest, which are gauge-invariant by construction. This method is often used in digital proposals: the Hamiltonian evolution is trotterized and the single terms are implemented as single gates of a quantum circuit. Some proposals of this type are in Refs. [149–152]. This approach, however, is not always possible due to the presence of spurious terms that spoil the gauge symmetry. Moreover, it typically requires more resources than the ones actually needed, because the full Hilbert space of the theory is encoded, and not only the gauge-invariant subspace.

**Intrinsic symmetry** — A slightly more robust method relies on the presence of intrinsic (global) symmetries in the system. The global symmetry does not protect from local violations of Gauss' law, so an accurate engineering of the Hamiltonian terms is still required. This approach has been used, for example, in Refs. [153–157]: these works show that the  $SU(N)$  symmetry associated with the hyperfine structure of alkaline-earth-like atoms can be exploited to simulate various gauge symmetries (including cQED,  $\mathbb{Z}_n$ ,  $SU(N)$ ,  $U(N)$ ). In Chapter 7 we will discuss an implementation of a  $U(N)$  gauge symmetry based on a combination of intrinsic symmetry and energy penalty.

**Energy penalty** — This method allows to simulate a gauge theory by implementing Gauss' law as a local constraint at low energies, in analogy with the emergence of gauge symmetry in frustrated quantum magnets, and is often used in condensed matter to engineer quantum dimer models. The basic idea is the following: the Hamiltonian of the system will contain both the desired gauge-invariant terms ( $H_0$ ) and gauge-breaking terms ( $H_1$ ); to suppress the effect of the gauge-breaking part, an additional Hamiltonian term is engineered:

$$H_{\text{EP}} = H_0 + H_1 + \Lambda \sum_{\mathbf{r}, a} (G_{\mathbf{r}}^a)^2, \quad (5.5)$$

where  $\Lambda$  is much larger than the energy scales in  $H_1$ . This large term effectively constrains the dynamics to the gauge-invariant subspace defined by  $G_{\mathbf{r}}^a |\Psi\rangle = 0 \forall \mathbf{r}$  (if the energy is not too large). The effective Hamiltonian in this subspace is then obtained using perturbation theory. For some examples of applications of this approach see Refs. [158–163].

**Zeno dynamics** — Another method, similar to energy penalty, exploits the dissipative dynamics induced by the so-called quantum Zeno effect [164]. The Hamiltonian of the system contains a classical noise term linear in the

local generators  $G_{\mathbf{r}}^a$ :

$$H_{\text{ZD}}(t) = H_0 + H_1 + \sqrt{2\kappa} \sum_{\mathbf{r},a} \xi_{\mathbf{r}}^a(t) G_{\mathbf{r}}^a \quad (5.6)$$

where  $\xi_{\mathbf{r}}^a(t)$  are white-noise processes with  $\overline{\xi_{\mathbf{r}}^a(t)\xi_{\mathbf{r}'}^b(t')} = \delta_{\mathbf{r},\mathbf{r}'}\delta_{a,b}\delta(t-t')$ . The density matrix  $\rho = |\psi(t)\rangle\langle\psi(t)|$  of the state averaged over noise fluctuations evolves according to the following master equation

$$\dot{\rho} = -iH_{\text{eff}}\rho + i\rho H_{\text{eff}}^\dagger + 2\kappa \sum_{\mathbf{r},a} G_{\mathbf{r}}^a \rho G_{\mathbf{r}}^a, \quad H_{\text{eff}} = H_0 + H_1 - i\kappa \sum_{\mathbf{r},a} (G_{\mathbf{r}}^a)^2. \quad (5.7)$$

The Hamiltonian  $H_{\text{eff}}$  contains a damping term that suppresses any violation of Gauss' law. Similarly to the case of energy penalty, the effective Hamiltonian in the gauge-invariant subspace can be computed using perturbation theory.

**Gauge integration** — This approach consists of explicitly solving the local constraint of Gauss' law to eliminate the gauge field and thus remove redundancy in the physical Hilbert space. This allows, on the one hand, to have a quantum simulator that, by construction, fully preserves gauge-invariance. On the other hand, the number of qubits needed is significantly reduced, so larger system sizes can be reached with the same amount of resources.

To explain how this method works, we consider the case of the lattice Schwinger model in Eq. (5.2). We are now going to show how this model, restricted to the gauge-invariant subspace spanned by wavefunctions  $|\Psi\rangle$  which satisfy the Gauss laws  $G_j|\Psi\rangle = 0$ , can be conveniently simulated by exactly mapping it to an unconstrained chain of spin-1/2 degrees of freedom in the case of open boundary conditions [165].

The spins  $\sigma_j^\alpha$  are obtained from the fermionic operators via a combination of a Jordan-Wigner transformation and a gauge transformation, expressed as

$$\psi_j = \prod_{l=1}^{j-1} \left( \sigma_l^z U_{l,l+1}^\dagger \right) \sigma_j^-. \quad (5.8)$$

This transformation decouples spins and gauge degrees of freedom, and thus the Hamiltonian in Eq. (5.2) takes the form

$$H = -w \sum_{j=1}^{L-1} (\sigma_j^+ \sigma_{j+1}^- + \text{h.c.}) + \frac{m}{2} \sum_{j=1}^L (-1)^j \sigma_j^z + J \sum_{j=1}^{L-1} E_{j,j+1}^2. \quad (5.9)$$

The electric field can be rewritten in terms of the spin operators by means of the Gauss law,

$$E_{j,j+1} = \frac{1}{2} \sum_{l=1}^j [\sigma_l^z + (-1)^l] - \alpha, \quad (5.10)$$

where  $\alpha$  is the electric field at the boundary<sup>5</sup>. Inserting Eq. (5.10) into Eq. (5.9) we obtain three additional terms: a long-range spin-spin interaction corresponding to a Coulomb interaction, a local energy offset that modifies the effective mass of the fermions and a linear potential given by the constant background field. The electric field part of the Hamiltonian can be cast in the form:

$$H_{\text{lat}}^E = \frac{J}{2} \sum_{n=1}^{L-2} \sum_{l=n+1}^{L-1} (L-l) \sigma_n^z \sigma_l^z - \frac{J}{4} \sum_{n=1}^{L-1} [1 - (-1)^n] \sum_{l=1}^n \sigma_l^z - J\alpha \sum_{j=1}^{L-1} (L-j) \sigma_j^z. \quad (5.11)$$

In this form, the non-equilibrium dynamics of the lattice Schwinger model can be efficiently simulated. This method was employed in the experiment with trapped ions reported in Ref. [166]: thanks to the possibility of implementing long-range interactions, trapped ions are particularly suited for this type of Hamiltonians.

The origin of long-range spin-spin interactions as a consequence of the linear confining Coulomb potential in one spatial dimension is made more evident when Eq. (5.11) is formulated in terms of the charges  $Q_j = [\sigma_j^z + (-1)^j] / 2$  [167]. In the neutral charge sector where  $\sum_{j=1}^L Q_j = 0$  we have

$$H_{\text{lat}}^E = -J \sum_{j=1}^{L-1} \sum_{k=j+1}^L (k-j) Q_j Q_k - J \sum_{j=1}^L (L+1-j) \alpha Q_j + J \sum_{j=1}^L j \alpha Q_j. \quad (5.12)$$

The first term describes the Coulomb interaction between charges, while the remaining two terms can be interpreted as interactions with two static charges  $-\alpha$  and  $\alpha$ , placed at the boundaries of the chain (sites 0 and  $L+1$  respectively) and effectively producing the constant background field.

A similar method can be used to eliminate the gauge field in the case of a non-Abelian lattice gauge theory in one spatial dimension [167], obtaining an effective linear interaction between  $SU(N)$  charges. This method was exploited to simulate a  $SU(2)$  LGT on an IBM superconducting platform [168].

Despite the success of this method on the first (small) quantum simulators for LGTs, this approach is difficult to scale to larger system sizes. One of the problems is that linearly raising potentials are not natural in typical experimental platforms, and lead to energy scales of the order of the system size. Since the overall timescale of most experiments is limited by noise, having couplings with relative ratios of order  $L$  is a severe limitation for analogue experiments, and partially affects also digital efforts.

Even more dramatically, the elimination of gauge fields is not possible for spatial dimension  $d > 1$ . To understand why, consider Gauss' law in

---

<sup>5</sup>To make connection with the  $\theta$  angle introduced above, we can write  $\alpha = k + (\theta/2\pi)$ , with  $k \in \mathbb{Z}$ .

classical electrodynamics:  $\nabla \cdot \mathbf{E}(\mathbf{r}) = \rho(\mathbf{r})$ . In  $d > 1$ , solving this equation for the electric field is generally complicated. The case  $d = 1$  is special, because the equation  $\partial_x E = \rho(x)$  can be solved in general with a simple integration

$$E(x) = E(x_0) + \int_{x_0}^x dx' \rho(x'). \quad (5.13)$$

This argument shows why this method can be easily applied in  $d = 1$ , while generalizing this approach to higher dimensions is intrinsically difficult.

**Matter integration** — A method that has the same advantage of the gauge integration (i.e., built-in gauge invariance and efficient usage of resources) but does not suffer from the same limitations is the elimination of matter degrees of freedom by explicitly solving Gauss' law. This method can be applied to any spatial dimension  $d$ : compared to the integration of gauge fields in the classical argument above, the integration of matter fields does not require the solution of a differential equation, because the charge is already explicitly expressed as a function of the gauge fields. To illustrate how this method work, we refer to Chapter 6, where matter integration is used to map a U(1) QLM to a model of Rydberg atoms in optical traps. We note that, in general, this method may lead to systems with local constraints [169]. These constraints are generally much simpler to implement than the original ones: Rydberg atoms, in particular, naturally exhibit emergent constraints (the so-called *Rydberg blockade*) so they are best-suited for this type of quantum simulation.

One of the theoretical limitations of this approach is that it only works for a single matter field: in case of multi-flavour matter fields the charge obtained from Gauss' law does not unambiguously determine the matter content of the theory, so additional degrees of freedom have to be included.

On a more practical level, one of the main challenges of this approach is that the implementation of the local constraint has to be designed case by case, depending on the LGT and on the experimental platform. Complex LGTs often imply complicated local constraints and complicated Hamiltonian terms in the effective model after the matter integration.

Another approach for SU( $N$ ) gauge symmetry (similar in spirit to gauge and matter integration) is the so-called *loop-string-hadron* formulation [170], in which the redundancy in the gauge-invariant subspace is partially removed and the non-Abelian constraints are transformed into Abelian ones. The disadvantage is that the number of Hamiltonian terms is very large, making this formulation impractical for present quantum simulators.

## 5.4 Quantum simulation platforms

After illustrating some of the general strategies, we now review some of the most common experimental platforms for the quantum simulation of LGTs

(see Fig. 5.3).

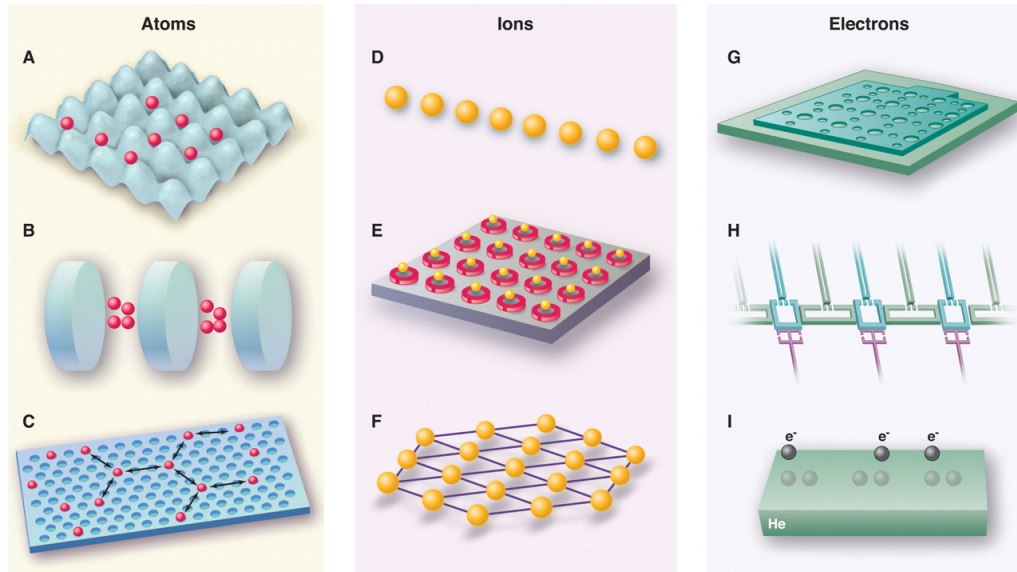


Figure 5.3: Examples of physical systems that could implement analog quantum simulators: atoms in optical lattices (A) or in 1D (B) or 2D (C) arrays of cavities; ions in linear ion chains (D), 2D arrays of planar traps (E), or 2D Coulomb crystals (F); electrons in quantum dot arrays created by a 2D mesh (G), or arrays of superconducting circuits (H), or trapped on the surface of liquid helium (I). Figure from [171].

**Ultracold atoms in optical lattices** — In the presence of counter-propagating laser beams, ultra-cold neutral atoms experience a potential that is periodic in space (an *optical lattice*): in a tight-binding approximation, the system can be described with a lattice Hamiltonian containing chemical potentials, hopping terms and interactions. By tuning the intensity, the angle, and the frequency of the lasers, it is possible to change the lattice geometry and the parameters of the effective lattice Hamiltonian.

One of the main advantages of this platform in the quantum simulation of LGTs is that it encompasses the manipulation of both fermions and bosons, allowing for a direct identification with the fermionic and bosonic degrees of freedom of the desired theory. For examples of proposals based on ultra-cold atoms see Refs. [150, 153–155, 158, 160, 172, 173] and the reviews [174, 175]. A protocol for simulating a non-Abelian gauge theory using alkaline-earth-like atoms is discussed in detail in Chapter 7.

**Rydberg atoms** — A specific type of cold-atom-based quantum simulators is represented by Rydberg-atom platforms. In these experiments, internal states of the atoms with large principal quantum number (*Rydberg*

states) are employed. Due to the large polarizability, two atoms in Rydberg states interact strongly via interactions of van der Waals type. These interactions can be used for different purposes: for example, they can be employed to engineer two-body gates in digital implementations. Another very convenient application is the realization of local Abelian constraints (that emerge, for example, from matter integration): the strong interaction of nearby atoms induces an effective constraint at low energies, known as *Rydberg blockade*; if two atoms are separated by a distance smaller than a certain *blockade radius* they cannot be simultaneously excited to a Rydberg state. In Chapter 6 we will employ Rydberg blockade to simulate a  $U(1)$  lattice gauge theory; other proposals based on Rydberg atoms are in Refs. [121, 149–151].

**Trapped ions** — Trapped ions represent another very flexible platform for quantum simulation [134]. For each ion, some chosen internal energy levels can be used to represent an effective spin. The interactions between the ions are modulated by applying optical fields, leading to tunable long-range spin-spin interactions. The ions are then measured using state-dependent fluorescence techniques.

The long-range nature of the interactions makes this platform particularly suitable for simulating the effective Coulomb interactions between the charges in one-dimensional lattice gauge theories. This property has been exploited to simulate the real-time dynamics of the lattice Schwinger model [166]. Upon integration of the gauge field, the lattice Schwinger model is reformulated as a spin model with long-range interactions (see Section 5.3), that was simulated using a digital quantum simulation scheme.

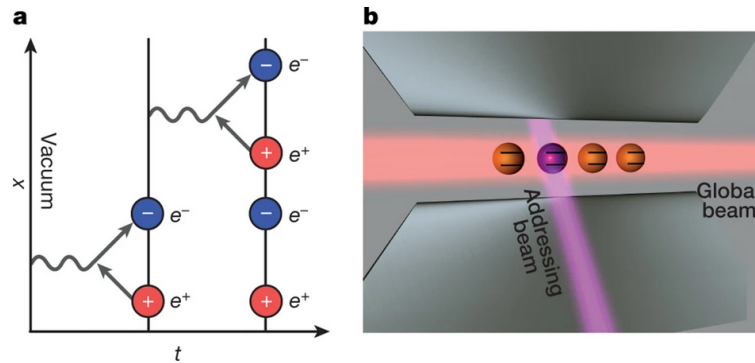


Figure 5.4: a) The non-equilibrium dynamic simulated in the experiment. The instability of the vacuum due to quantum fluctuations leads to particle anti-particle creation (Schwinger mechanism). b) Experimental setup. A string of four ions is confined in a linear Pauli trap and manipulated using laser beams. Figure from [166].

**Superconducting qubits** — Superconducting circuits can be used to engineer "artificial atoms" that are controlled via currents, voltages and microwave photons. The qubits are represented by two energy levels of a certain building block of the system: for example they can correspond to two different values of the charge in a superconducting island (*charge qubits*), to two eigenstates of magnetic flux (*flux qubits*), or two states with different phase of a Josephson junction (*phase qubits*). Differently from neutral atoms and ions, superconducting qubits are not intrinsically identical objects, but they are microfabricated solid state devices. This implies, on the one hand, that their characteristic properties can be tailored depending on the desired application, and, on the other hand, that a certain amount of inhomogeneity is unavoidable in any sample of qubits. Some proposals for quantum simulation of lattice gauge theories using this platform are reported in Refs. [152, 176, 177].

## 5.5 Conclusions

It is expected that quantum computers will one day be capable of efficiently performing some tasks that are difficult or even impossible for classical computers. Quantum error correction is crucial for achieving practical advantages over classical algorithms, but requires large-scale devices with huge controllability and long coherence time and is currently a far-fetched goal. A more realistic goal is to use the already available Noisy Intermediate-Scale Quantum (NISQ) technology [178] to have some novel insights on some specific problems, in areas that include, for example, quantum chemistry, condensed matter physics, high-energy and nuclear physics. At this stage, analog quantum simulation probably represents the most powerful tool, as it allows to manipulate larger number of qubits. Digital (universal) quantum computation based on quantum gates, on the other hand, has clear advantages in terms of flexibility, but is currently limited in the number of qubits that can be controlled with good fidelity.

To date, some important steps in the quantum simulation of lattice gauge theories have already been achieved. The first experiment, performed with an array of trapped ions, reported the digital simulation of the real-time dynamics of the Schwinger mechanism [166]; some years later, it was shown that a Rydberg atom experiment realized the quantum simulation of a similar  $U(1)$  lattice gauge theory (see Chapter 6) on much large system sizes (up to 51 qubits); another simulation of the same model was realized with ultracold bosons in an optical lattice with 71 sites [179]; recently, the first proof-of-principle digital simulations of non-Abelian lattice gauge theories were performed on an IBM quantum computer [168, 180].

The next steps will require significant improvements both on the theoretical side and on the technical one. Firstly, a large scale simulation of a non-Abelian lattice gauge theory has not yet been demonstrated: to simu-

late non-Abelian theories a larger number of resources are needed to encode all the degrees of freedom of the theory (that include, for example, the color indices); moreover, the complicated non-commuting constraints can be implemented only with more ingenious schemes. An example of how this could be achieved with alkaline-earth-like atoms in optical lattices is discussed in detail in Chapter 7, where we perform an ab-initio calculation to specify in a quantitative way the energy scales involved in the quantum simulation.

Another fundamental advancement is related with the dimensionality of the simulated theory. So far, only one-dimensional gauge theories have been experimentally realized. The recent progress in the quantum simulation of two-dimensional systems [135, 181–183] bodes well for future realizations of simple  $(2 + 1)$ -d lattice gauge theories. These theories also have a fundamental importance in the context of quantum spin liquids and topology.

Finally, for translating the results of a lattice quantum simulation to a quantum field theory, it is necessary to achieve a regime close to the continuum limit, where the resource requirements are typically very demanding. Better lattice regularization techniques, specifically designed for the purpose, may help to reduce the number of qubits needed and to predict with higher precision the properties of the continuum theory.

These are all necessary steps in the route towards a full-fledged quantum simulation of quantum chromodynamics. This goal will remain a formidable challenge for the years to come, but the progress in this direction is rapidly advancing. At this moment, it is important to identify simpler theories and interesting physical phenomena that can be studied with quantum simulators on shorter terms: some of them are for example discussed in Part III of this thesis, where we focus on the non-equilibrium dynamics of lattice gauge theories.



## Chapter 6

# Lattice gauge theories and string dynamics in Rydberg atom quantum simulators

Here, we show that (1+1)-dimensional LGTs akin to quantum electrodynamics are naturally realized in state-of-the-art experiments with Rydberg atom arrays [46, 184]. In particular, we show how the dynamics of Rydberg excitations in these chains is exactly mapped onto a spin-1/2 quantum link model (QLM), a  $U(1)$  LGT where the gauge fields span a finite-dimensional Hilbert space, equivalent to a lattice Schwinger model in the presence of a topological term [144]. The key element of our mapping, which is schematically illustrated in Fig. 6.2, is that gauge invariance has a natural counterpart in the Rydberg blockade mechanism, which constrains the Hilbert space in the same way as Gauss law does in gauge theories. This provides an immediate interpretation of the recent experiment with Rydberg-blockaded atom arrays in Ref. [46] as the first large-scale quantum simulation of a LGT at the edge of classical computational methods [174].

From a theoretical viewpoint, the mapping offers a hitherto unexplored perspective on the anomalously slow relaxation recently observed in experiments: the long-lived oscillations in the population of excited Rydberg atoms correspond to a string inversion, a phenomenon which is directly tied to string breaking [185–187] prototypical of gauge theories including dynamical matter. The mapping indicates that this phenomenon has a natural interpretation in the LGT framework, and suggests the occurrence of slow dynamics in other  $U(1)$  gauge theories, such as higher-spin QLMs [147], Higgs theories [163, 188], and the Schwinger model [141, 189]. These theories have been widely discussed in the context of Schwinger pair production (taking place, for example, at high-intensity laser facilities), thus providing a highly unexpected, direct link between apparently unrelated experimental platforms [187, 190–193].

We discuss the generality of this type of quantum evolution by extending our analysis to other relevant instances of "slow dynamics", characterized by

the absence of relaxation on all time scales corresponding to any microscopic coupling present in the system. As initial states, we focus on those consisting of particle-antiparticle pairs, corresponding to regular configurations of the Rydberg-atom arrays with localized defects, which are accessible within the setup of Ref. [46]. We show that these defects propagate ballistically with long-lived coherent interference patterns. This behavior is found to be governed by special bands of highly excited eigenstates characterized by a regularity in the energy-momentum dispersion relation. These findings open up a novel perspective which complements and extends towards gauge theories recent approaches to slow relaxation in Rydberg-blockaded atomic chains [47, 48, 52, 69, 81, 105].

## 6.1 Rydberg atom arrays

We are interested here in the dynamics of a one-dimensional array of  $L$  optical traps, each of them hosting a single atom, as schematically illustrated in Fig. 6.1a. The atoms are trapped in their electronic ground state (black circle), denoted by  $|\downarrow\rangle_j$ , where  $j$  numbers the trap. These ground states are quasi-resonantly coupled to a single Rydberg state, i.e., a highly excited electronic level, denoted by  $|\uparrow\rangle_j$ . The dynamics of this chain of qubits  $\{|\uparrow, \downarrow\rangle_j\}_{j=1, \dots, L}$  is governed by the following Ising-type Hamiltonian [51, 194]:

$$\hat{H}_{\text{Ryd}} = \sum_{j=1}^L (\Omega \hat{\sigma}_j^x + \delta \hat{\sigma}_j^z) + \sum_{j < \ell=1}^L V_{j,\ell} \hat{n}_j \hat{n}_\ell, \quad (6.1)$$

where  $\hat{\sigma}_j^\alpha$  are Pauli matrices at site  $j$ , the operator  $\hat{n}_j = (\hat{\sigma}_j^z + 1)/2$  signals the presence of a Rydberg excitation at site  $j$ ,  $2\Omega$  and  $2\delta$  are the Rabi frequency and the detuning of the laser excitation scheme, respectively, and  $V_{j,\ell}$  describes the interactions between atoms in their Rydberg states at sites  $(j, \ell)$ . For the cases of interest here, this interaction is strong at short distances and decays as  $1/|j - \ell|^6$  at large distances. The dynamics described by  $\hat{H}_{\text{Ryd}}$  has already been realized in several experiments utilizing either optical lattices or optical tweezers [46, 184, 195]. In particular, Ref. [46] investigated the case in which  $V_{j,j+1}$  is much larger than all other energy scales of the system, resulting in the so-called Rydberg *blockade effect*: atoms on neighboring sites cannot be simultaneously excited to the Rydberg state, hence the constraint  $\hat{n}_j \hat{n}_{j+1} = 0$ .

In this regime, the resulting Hamiltonian — introduced by Fendley, Sen Gupta and Sachdev (FSS) in Ref. [50] — is

$$\hat{H}_{\text{FSS}} = \sum_{j=1}^L (\Omega \hat{\sigma}_j^x + 2\delta \hat{n}_j), \quad (6.2)$$

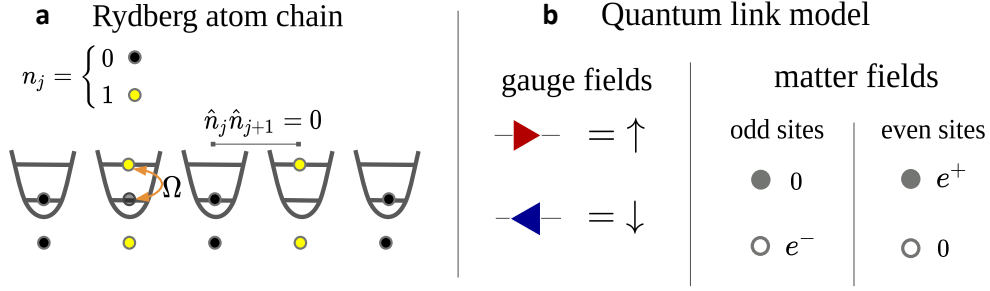


Figure 6.1: **a**: Schematics of a Rydberg atom chain. Each potential well of the optical lattice hosts a single atom, which can be either in the ground (black) or excited Rydberg (yellow) state. The two levels are coupled by a coherent laser field. The Rydberg blockade prevents the simultaneous excitations of neighboring atoms. **b**: Degrees of freedom of a  $U(1)$  LGT in the spin-1/2 quantum link model (QLM) formulation. Gauge fields are represented by spin variables residing on links. Matter fields are represented by Kogut-Susskind fermions: an occupied site corresponds to the vacuum on odd sites, and to a positron  $e^+$  on even sites. An empty site, instead, to the vacuum on even sites and to an electron  $e^-$  on odd sites.

where we neglect longer-range terms which do not affect qualitatively the dynamics.  $\hat{H}_{\text{FSS}}$  acts on the constrained Hilbert space without double occupancies on nearest-neighbor sites, as illustrated in Fig. 6.1a. As we show below, the direct connection between Rydberg atomic systems and gauge theories is indeed provided by this constraint at the level of the Hilbert space.

## 6.2 Rydberg blockade as a gauge symmetry constraint

We establish here the exact mapping between the FSS Hamiltonian in Eq. (6.2) governing the dynamics of the Rydberg atom quantum simulator in Ref. [46] and a  $U(1)$  LGT. The latter describes the interaction between fermionic particles, denoted by  $\hat{\psi}_j$  and residing on the lattice site  $j$ , mediated by a  $U(1)$  gauge field, i.e., the electric field  $\hat{E}_{j,j+1}$ , defined on lattice bonds, as depicted in Fig. 6.1b. We use here Kogut-Susskind (staggered) fermions [141], with the conventions that holes on odd sites represent electrons  $e^-$ , while particles on even sites represent positrons  $e^+$ . Their dynamics is described by:

$$\hat{H} = -w \sum_{j=1}^{L-1} (\hat{\psi}_j^\dagger \hat{U}_{j,j+1} \hat{\psi}_{j+1} + \text{h.c.}) + m \sum_{j=1}^L (-1)^j \hat{\psi}_j^\dagger \hat{\psi}_j + J \sum_{j=1}^{L-1} \hat{E}_{j,j+1}^2, \quad (6.3)$$

where the first term provides the minimal coupling between gauge and matter fields through the parallel transporter  $\hat{U}_{j,j+1}$  with  $[\hat{E}_{j,j+1}, \hat{U}_{j,j+1}] = \hat{U}_{j,j+1}$ , the second term is the fermion mass, and the last one is the electric field energy. The generators of the  $U(1)$  gauge symmetry are defined as

$$\hat{G}_j = \hat{E}_{j,j+1} - \hat{E}_{j-1,j} - \hat{\psi}_j^\dagger \hat{\psi}_j + \frac{1 - (-1)^j}{2}, \quad (6.4)$$

and satisfy  $[\hat{H}, \hat{G}_j] = 0$ , so that gauge invariant states  $|\Psi\rangle$  satisfy Gauss law  $\hat{G}_j |\Psi\rangle = 0$  for all values of  $j$ . Restricting the dynamics to their subspace is by far the most challenging task for quantum simulators.

Different formulations of  $U(1)$  LGTs are obtained for different representations of gauge degrees of freedom  $\hat{E}_{j,j+1}$ . While in the standard Wilsonian formulation — i.e., the lattice Schwinger model — they span infinite-dimensional Hilbert spaces, here we first focus on the  $U(1)$  QLM formulation [145, 147], where they are represented by spin variables, i.e.,  $\hat{E}_{j,j+1} = \hat{S}_{j,j+1}^z$  and  $\hat{U}_{j,j+1} = \hat{S}_{j,j+1}^+$ , so that  $[\hat{S}_{j,j+1}^z, \hat{S}_{j,j+1}^+] = \hat{S}_{j,j+1}^+$ . As noted in Ref. [160], this formulation is particularly suited for quantum simulation purposes.

In the following, we consider the QLM with spin  $S = 1/2$ , in which all the possible configurations of the electric field have the same electrostatic energy, rendering the value of  $J$  inconsequential; in Section 6.3.2 we show that this model is equivalent to the lattice Schwinger model in the presence of a  $\theta$ -angle with  $\theta = \pi$ <sup>1</sup>. The Hilbert space structure following Gauss law is particularly simple in this case [160]: as depicted in Fig. 6.2, for each block along the chain consisting of two electric fields neighbouring a matter field at site  $j$ , there are only three possible states, depending on the parity of  $j$ . In fact, in a general (1+1)-dimensional  $U(1)$  LGT, the configuration of the electric field along the chain determines the configuration of the charges via the Gauss law. Accordingly,  $\hat{H}$  in Eq. (6.3) can be recast into a form in which the matter fields  $\hat{\psi}_j$  are integrated out.

We now provide a transformation which maps exactly the latter form into the FSS Hamiltonian (6.2). The correspondence between the two Hilbert spaces is realized by identifying, alternately on odd and even lattice sites, the computational basis configurations of the atomic qubits allowed by the Rydberg blockade with the classical configurations of the electric field allowed by the Gauss law (see Fig. 6.2). In terms of the two Hamiltonians (6.2) and (6.3), this unitary transformation consists in identifying the operators  $\hat{\sigma}_j^z \leftrightarrow (-1)^j 2\hat{S}_{j-1,j}^z$ ,  $\hat{\sigma}_j^x \leftrightarrow (\hat{\psi}_{j-1}^\dagger \hat{S}_{j-1,j}^+ \hat{\psi}_j + \text{h.c.})$ ,  $\hat{\sigma}_j^y \leftrightarrow -i(-1)^j (\hat{\psi}_{j-1}^\dagger \hat{S}_{j-1,j}^+ \hat{\psi}_j - \text{h.c.})$  and the parameters  $\Omega = -w$ ,  $\delta = -m$ . This mapping can be applied both for open and periodic boundary conditions and it overcomes the most challenging task in quantum simulat-

<sup>1</sup>The similarity between the phenomenology of the two models was pointed out in Ref. [160]. Here, we are instead interested in establishing an exact relation.

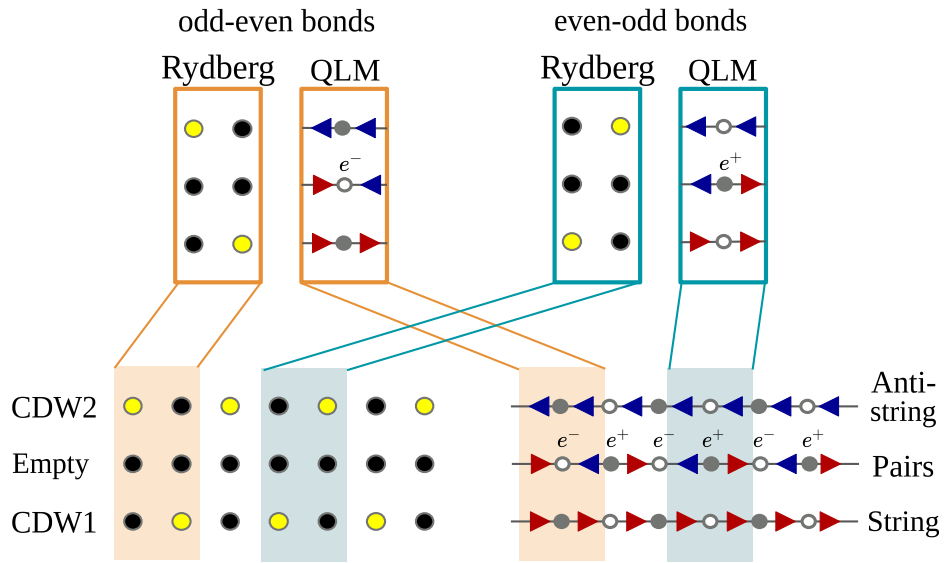


Figure 6.2: Mapping between Rydberg-blockaded states and configurations of the electric field constrained by the Gauss law in the QLM. Due to the staggered electric charge, the allowed configurations of the electric field depend on the link, as illustrated. The two so-called charge-density wave configurations “CDW1” and “CDW2” of the Rydberg-atom arrays are mapped onto the “string” and “anti-string” states, respectively, characterized by uniform rightward or leftward electric fluxes. The empty configuration with all Rydberg atoms in their ground state is mapped to a state filled by adjacent particle-antiparticle pairs.

ing gauge theories, by restricting the dynamics directly within the gauge-invariant Hilbert space.

Compared to the opposite strategy of integrating out the gauge fields, our procedure based on integrating out matter degrees of freedom has major experimental implications. With the first approach one would obtain linearly raising potentials which do not appear easily in the synthetic quantum systems, and lead to very large energy scales (of the order of the system size, see Section 5.3).

With our mapping, the only states that would violate Gauss law are nearest-neighbor occupied sites which are strongly suppressed by the Rydberg blockade. Additional terms in the Hamiltonian, such as next-nearest neighbour interactions of Rydberg excitations, are mapped to gauge invariant terms (e.g., next-nearest neighbour interactions between electric fields). From a theoretical viewpoint, the line of thought of our scheme is similar to the one used in hybrid Monte Carlo schemes, where one first integrates out the matter fields, and then deals with a purely bosonic action.

Beyond providing a direct link between Gauss law and the Rydberg blockade mechanism, the most important feature of the mapping is that, differently from other remarkable relations between  $\hat{H}_{\text{FSS}}$  and lattice models with gauge symmetries [196, 197], it provides an immediate connections between Rydberg experiments and particle physics phenomena, as we describe below.

## 6.3 Real-time dynamics of lattice gauge theories in Rydberg atom experiments

### 6.3.1 Gauge-theory interpretation of slow dynamics

The exact description of Rydberg-blockaded chains in terms of a  $U(1)$  LGT allows us to shed a new light on the slow dynamics reported in Ref. [46], by interpreting them in terms of well-studied phenomena in high-energy physics, related to the plasma oscillations of the electric field and to the production of particle-antiparticle pairs after a quench.

In the experiment, the system was initialized in a charge density wave state (CDW1 in Fig. 6.2), and subsequently, the Hamiltonian was quenched, inducing slowly-decaying oscillations between CDW1 and CDW2. As shown in Fig. 6.2, CDW1 and CDW2 are mapped onto the two states of the  $S = 1/2$ -QLM with uniform electric field  $\hat{S}_{j,j+1}^z = \pm 1/2$ . The experimental results in Ref. [46] may thus be interpreted as the evolution starting from one of the two degenerate bare particle vacua  $|0_{\pm}\rangle$  (i.e, the vacua in the absence of quantum fluctuations,  $w = 0$ ) of the gauge theory. In Fig. 6.3a and in the first column of Fig. 6.4, we illustrate these dynamics as it would be observed in the excitation density  $\langle n_j \rangle$  along the Rydberg-atom quantum simulators ("Rydberg") and compare it with that of the electric field  $\langle E_{j,j+1} \rangle$  within

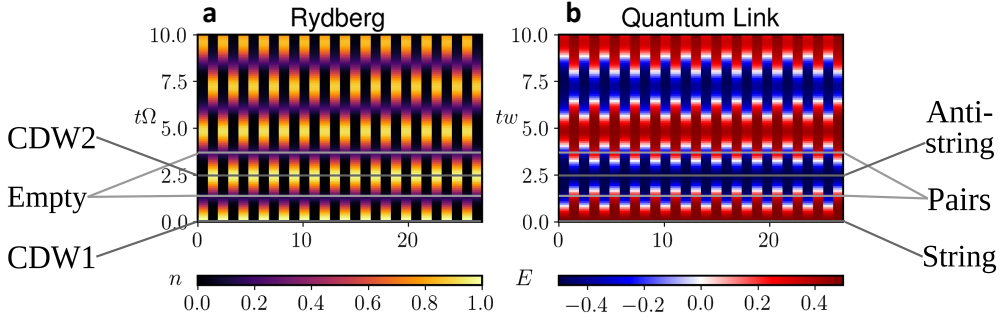


Figure 6.3: **a**: Time evolution of the Rydberg array governed by the effective Hamiltonian  $H_{\text{FSS}}$  in Eq. (6.2), starting from the CDW1 state. The plot shows the space and time resolved population  $\langle n_j \rangle$  of the excited Rydberg atoms. **b**: Evolution of the expectation value of the electric field operator  $\hat{E}_{j,j+1}$  in the QLM. These dynamics map exactly onto the ones shown in panel **a** via the mapping illustrated in Fig. 6.2. The thin lines highlight the oscillation between CDW1, CDW2 (left, bottom of Fig. 6.2) or string and anti-string (right) states. In these simulations,  $L = 24$  and  $\delta = m = 0$ .

its gauge-theory description ("Quantum link model") in Fig. 6.3b and in the second column of Fig. 6.4, respectively, utilizing exact diagonalization<sup>2</sup>.

The qualitative features of this evolution are strongly affected by quantum fluctuations, whose impact is quantified by the ratio between the coupling constant  $w$  and the particle mass  $m$ . For small values of  $m/w$  (first two lines in Fig. 6.4), production of particle-antiparticle pairs occurs at a finite rate. These particles get accelerated by the electric field and progressively screen it, until coherent pair annihilation takes place and eventually brings the system to a state with opposite electric flux. This process, referred to as *string inversion*, occurs several times in a coherent fashion; similarly to what is observed in string breaking scenarios (e.g., in other LGTs [192, 198]), this causes a dramatic slowdown of thermalization and of quantum information propagation. As a further evidence, we compute both the total electric flux and the vacuum persistence amplitude (or Loschmidt echo), defined as  $G_+(t) = |\langle 0_+ | e^{-i\hat{H}t} | 0_+ \rangle|^2$ , whose large value  $\simeq 1$  was already noted in Ref. [199]. The anomalous long-lived oscillations of these quantities experimentally detected with Rydberg atom arrays in Ref. [46] show a clear analogy with several previous numerical studies of the real-time dynamics of higher-spin QLMs [192] as well as of the Schwinger model [190, 191, 200] and Higgs theories [188]. In addition, as noted in Ref. [160], the dynamics discussed here describes the coherent oscillations of the parity-symmetric order parameter (in our case,  $\langle \hat{E}_{j,j+1} \rangle$ ) as a function of time, reminiscent

<sup>2</sup>Exact diagonalization is performed on the gauge invariant subspace: for large  $L$ , its dimension grows as  $\phi^L$ , where  $\phi$  is the golden ratio, thus allowing for large system sizes.

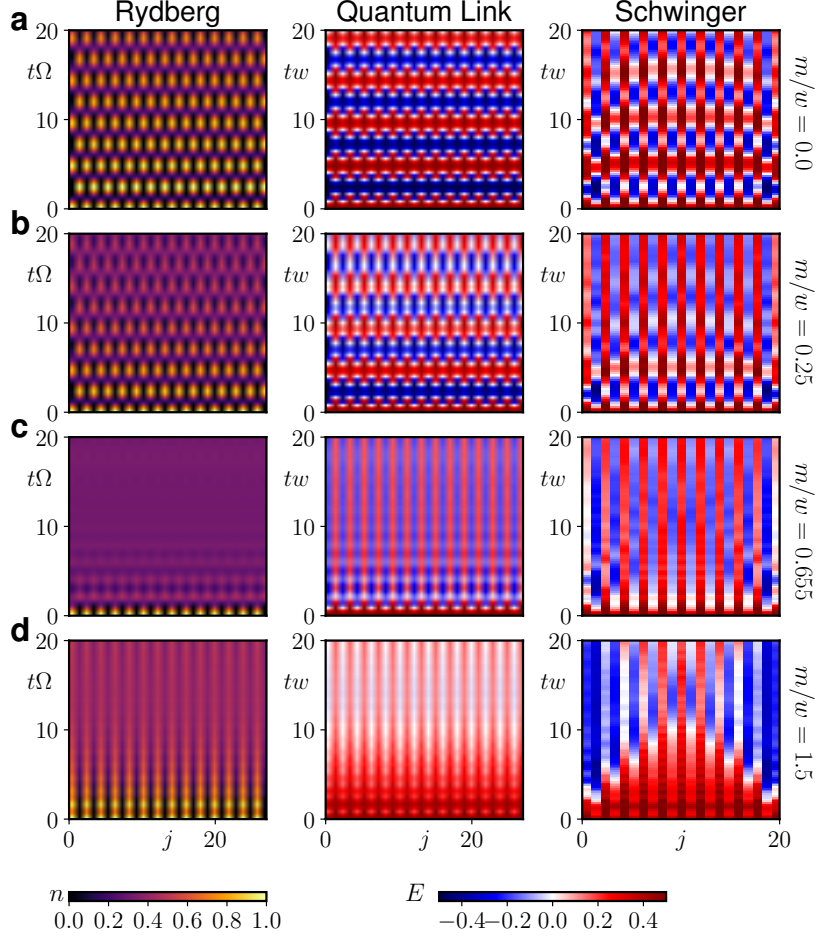


Figure 6.4: Slow dynamics in Rydberg atoms,  $U(1)$  quantum link model (QLM), and the lattice Schwinger model. Coherent quantum evolution of (first column) the local Rydberg excitation density profile  $n_j(t) = \langle \hat{n}_j(t) \rangle$  in the FSS model [see Eq. (6.2)], of the local electric field profile (second column)  $E_{j,j+1}(t) = \langle \hat{S}_{j,j+1}^z(t) \rangle$  in the QLM, and (third column)  $\langle \hat{L}_{j,j+1}(t) - \theta/(2\pi) \rangle$  (see further below in the main text) in the lattice Schwinger model [see Eq. (6.3)] with  $J/w = 1.5$  and  $\theta = \pi$ . Data in the first and second columns are connected by a unitary transformation, while a remarkable similarity is manifest between the second and third column despite the larger Hilbert space of the gauge degrees of freedom in the Schwinger model.

of the decay of a chiral condensate in QCD [193]. We thus provide here a bridge among all these observations.

However, if fermionic particles are sufficiently heavy, with  $m/w$  exceeding a critical threshold, pair production is a virtual process and string inversion cannot be triggered, as shown in the third and fourth line of Fig. 6.4. We find that this behavior is related to the quantum phase transition occurring in the FSS model at  $\delta_c = -0.655|\Omega|$  [50]. This transition corresponds

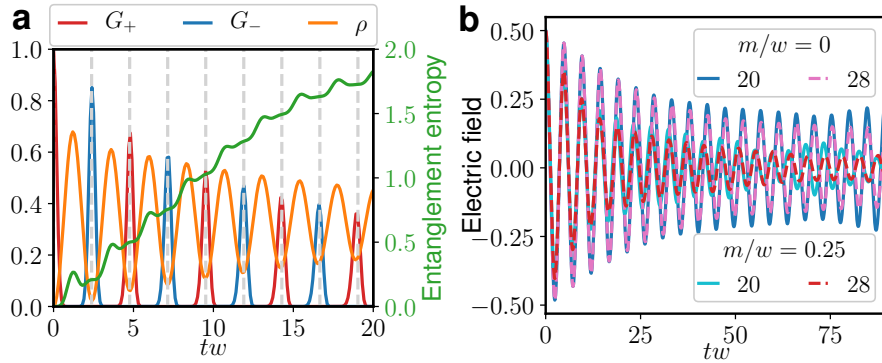


Figure 6.5: Characterization of slow dynamics in the FSS model. **a**: Hilbert space characterization of the persistent string inversions ( $m = 0$ ,  $L = 28$ ): alternating strong revivals of the overlaps  $G_{\pm}(t) = |\langle 0_{\pm} | e^{-i\hat{H}t} | 0_{+} \rangle|^2$  with the two bare vacuum states  $|0_{\pm}\rangle$ , corresponding to the two charge-density wave configurations of Rydberg-atom arrays. Both the total density  $\rho = \langle \hat{\rho}_j \rangle$  of particle-antiparticle pairs, with  $\hat{\rho}_j = (-1)^j \hat{\psi}_j^{\dagger} \hat{\psi}_j + [1 - (-1)^j]/2$  and the half-chain entanglement entropy (see the Appendix B.1) have regularly-spaced maxima between the peaks. **b**: Persistent oscillations of electric field for two values of the mass and of the system size.

to the spontaneous breaking of the chiral symmetry in the LGT (6.4) at  $m_c = 0.655|w|$  [201]. The four rows in Fig. 6.4 show the temporal evolution of the same initial uniform flux configuration (CDW or “string” in Fig. 6.2) upon increasing values of the mass  $m/w = 0, 0.25, 0.655, 1.5$  corresponding to the dynamics (a, b) at  $m < m_c$ , (c) at the quantum critical point  $m = m_c$ , and (d) at  $m > m_c$ .

Figure 6.5 further illustrates the appearance of string inversions for  $m < m_c$  and the corresponding slow dynamics. Panel a shows the long-lived revivals of the many-body wavefunction in terms of the evolution of the probability  $G_{\pm}(t)$  of finding the system at time  $t$  in the initial bare vacuum state  $|0_{+}\rangle$  or in the opposite one  $|0_{-}\rangle$ , corresponding to  $G_{+}$  or  $G_{-}$ , respectively, as well as in terms of the time-dependent density  $\rho$  of particle-antiparticle pairs. The entanglement entropy of half system also displays an oscillatory behavior (see Appendix B.1). Panel b shows the scaling of the collective oscillations of the electric field with respect to the system size  $L$ , as well as their persistence with a small but non-vanishing fermion mass  $m < m_c$ .

### 6.3.2 Slow dynamics in the Schwinger model

The above phenomenology is not restricted to QLMs, but is expected to be a generic feature of LGTs including dynamical matter. We show this in the context of a Wilsonian LGT, i.e., the lattice version of the Schwinger model in Eq. (6.3). As discussed below, the model dynamics is, at the lattice level,

remarkably different from the PXP model (no constraints when written in spin language, different Hilbert space scaling, different interactions, etc.). The key aspect is, instead, the common field-theoretical framework.

In this case,  $\hat{U}_{j,j+1} = e^{i\hat{\vartheta}_{j,j+1}}$  are  $U(1)$  parallel transporters with vector potential  $\hat{\vartheta}_{j,j+1}$ , the corresponding electric field operator is  $\hat{E}_{j,j+1} = \hat{L}_{j,j+1} - \theta/(2\pi)$ , where  $\hat{L}_{j,j+1}$  have integer spectrum and  $\theta/(2\pi)$  represents a uniform classical background field parameterized by the  $\theta$ -angle. Canonical commutation relations for the gauge degrees of freedom read  $[\hat{\vartheta}_{j,j+1}, \hat{L}_{p,p+1}] = i\delta_{jp}$ . In our numerical simulations, we utilize the spin formulation of the model obtained upon integration of the gauge fields under open boundary conditions (see Section 5.3 and Refs. [202, 203]).

We consider the case of a  $\theta$ -angle with  $\theta = \pi$ , such that the electric field  $\hat{E}_{j,j+1}$  has half-integer spectrum. Then, in the limit  $J/w \rightarrow \infty$  the term  $J\hat{E}_{j,j+1}^2$  in the Hamiltonian suppresses all the values of the electric field that are different from  $\pm 1/2$ . This implies that the electric field can be represented by a spin-1/2  $\hat{S}^z$  operator and that the lattice Schwinger model is equivalent to the spin-1/2 QLM discussed above. We find evidence that the corresponding behaviour persists qualitatively down to  $J \simeq w$ , when the electrostatic energy competes with the matter-field interaction, as shown in the third column of Fig. 6.4. Despite the strong quantum fluctuations allowed in principle by the exploration of a locally infinite-dimensional Hilbert space, a qualitative similarity with the case of the locally finite-dimensional Hilbert space of the QLM is manifest in the second column of Fig. 6.4, related to the observed dynamics in Ref. [46]. At a more quantitative level, we see that the periods of the oscillations in the lattice Schwinger model and in the QLM (for the same couplings) are in good agreement. The oscillations persist also down to  $J \ll w$  (see Fig. 6.6), a regime in which the period becomes larger when decreasing  $J$ .

We remark that the lattice Schwinger model with unbounded levels of the gauge fields is substantially different from the QLM: not only the Hilbert space is much larger, but also the effective spin-1/2 model describing it (see Section 5.3) features long-range Coulomb interactions. Therefore, the generality of the occurrence of oscillations which do not decay on time scales immediately related to the microscopic couplings points to a rather robust underlying mechanism. In fact, we suggest here that this behavior may arise from a universal field-theoretical description of the nonequilibrium dynamics of states possessing a well-defined continuum limit. Concerning the  $U(1)$  LGTs discussed in this work, the reference continuum field-theory description is provided by the Schwinger model, representing quantum electrodynamics in one spatial dimension [202]. In the massless limit  $m = 0$ , this model can be exactly mapped by bosonization to a free scalar bosonic field theory [185]. For a non-zero mass, the model is described in terms of

the canonically conjugate fields  $\hat{\Pi}$  and  $\hat{\phi}$  by the Hamiltonian

$$\hat{H}_B = \int dx \left[ \frac{1}{2} \hat{\Pi}^2 + \frac{1}{2} (\partial_x \hat{\phi})^2 + \frac{1}{2} \frac{e^2}{\pi} \hat{\phi}^2 - cm\omega_0 \cos(2\sqrt{\pi} \hat{\phi} - \theta) \right]. \quad (6.5)$$

Within this bosonized description, the field  $\hat{\phi}(x, t)$  represents the electric field, and for  $m = 0$  all its Fourier modes  $\tilde{\phi}(k)$  are decoupled. In this case, the single uniform mode with  $k = 0$ , oscillates with a frequency  $\omega_0 = e/\sqrt{\pi}$ , where  $e$  is the charge of the fermion. For an initial state with a uniform string of non-vanishing electric field  $\langle \hat{\phi}(x, t = 0) \rangle = \text{const} \neq 0$ , the uniform mode with  $k = 0$  is excited, and hence the electric field will show uniform periodic string inversions around zero, with frequency  $\omega_0$ . A non-vanishing value of  $m$  leads to the additional anharmonic term in Eq. (6.5). The resulting total potential shows a transition from a shape with a single minimum for  $m < m_c$  to two symmetric minima for  $m > m_c$ , analogous to the spontaneous breaking of chiral symmetry on the lattice (see Appendix B.3 for details). This weak local non-linearity introduced by a small  $m$  couples the various Fourier modes and hence induces a weak integrability breaking. In this case, the uniform string inversions of the electric field evolving from a false vacuum configuration with  $\langle \tilde{\phi}(k = 0) \rangle \neq 0$  are expected to be superseded by slow thermalization processes at long times (see, e.g., Ref. [204]). In the context of cold gases, a reminiscent slow relaxation has been observed in interfering bosonic Luttinger liquids, whose Hamiltonian dynamics has some similarities to the one discussed here [205].

We suggest that a remnant of this slow dynamics induced by the underlying integrable field theory may persist in lattice versions of this gauge theory for some initial states. At a quantitative level, we test our prediction on the lattice Schwinger model with  $\theta = \pi$ , whose continuum limit is obtained by scaling the parameters with the lattice spacing  $a$  in such a way that  $J = e^2 a/2$ ,  $w = 1/(2a)$ , and  $a \rightarrow 0$  [165]. According to the field theory (Eq. 6.5), in this limit the period of the oscillations scales as  $T \propto 1/\sqrt{Jw}$ : as shown in Fig. 6.6, this scaling is indeed satisfied, within a good approximation, in the region  $J \ll w$ .

### 6.3.3 Propagation of particle-antiparticle pairs

States of the QLM corresponding to particle-antiparticle pairs in the bare vacuum can be constructed in Rydberg-atom quantum simulators by preparing two or more defects in a charge-density wave configuration, each corresponding to pairs of adjacent non-excited Rydberg atoms.

As an illustration, we discuss how the time-evolution of one or two particle-antiparticle pairs for  $m < m_c$  features the emergence of slow dynamics. In Fig. 6.7, we show the time evolution of both the particle density

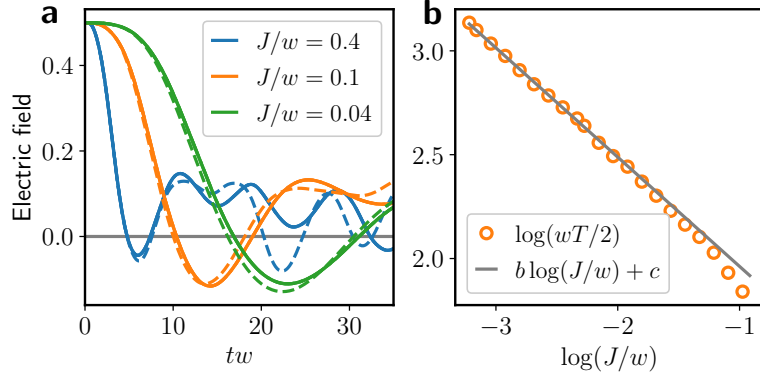


Figure 6.6: Oscillation of the electric field in the Schwinger model with  $\theta = \pi$ . **a**: Time evolution of the average electric field. The initial state is the bare vacuum with  $E_{j,j+1} = 1/2$  and the chain has periodic boundary conditions. The solid and dashed lines correspond to  $L = 14$  and  $L = 12$  respectively. Exact simulations are performed via truncation of the local Hilbert space to dimension 16, i.e.  $|E_{j,j+1}| < 15/2$ , and the constrained Hamiltonian for the electric field is obtained by exactly eliminating matter degrees of freedom. **b**: Period of the oscillations as a function of  $J$  and  $w$ . The dots are the values of the half-period obtained for  $L = 14$ . The solid line is the function  $b \log(J/w) + c$ , where  $b = -0.526$  and  $c = 4.2$  are obtained through a fit in the region  $J/w < 0.1$ .

in the QLM and the corresponding density of excitations in the Rydberg chain, fixing for simplicity  $m = 0$ . The pairs in the initial state break and ballistic spreading of electron and positron takes place. The string inversion dynamics induced by this propagation shows coherent interference patterns with long-lived oscillations. Due to retardation effects induced by the constrained dynamics, these oscillations are shifted by half a period with respect to the vacuum oscillation.

These unusual dynamics turn out to be robust under experimentally realistic conditions: In Fig. 6.8 we consider the evolution of a particle-antiparticle pair, the simulated dynamics of which is not constrained to the subspace satisfying  $\hat{n}_j \hat{n}_{j+1} = 0$  and includes the effect of the long-range Rydberg interactions between atoms. The evolution is performed via Krylov subspace techniques in the unconstrained Hilbert space with the Hamiltonian in Eq. (6.1), with  $\delta = 0$  and  $V_{j,k} = V_1 |j - k|^{-6}$ . The value of  $V_1/\Omega = 25.6$  is the same as considered in Ref. [46]. The dynamics displayed Fig. 6.8 is similar to the constrained one in Fig. 6.7b,c at short times, after which the effects of having realistic interactions gradually kick in.

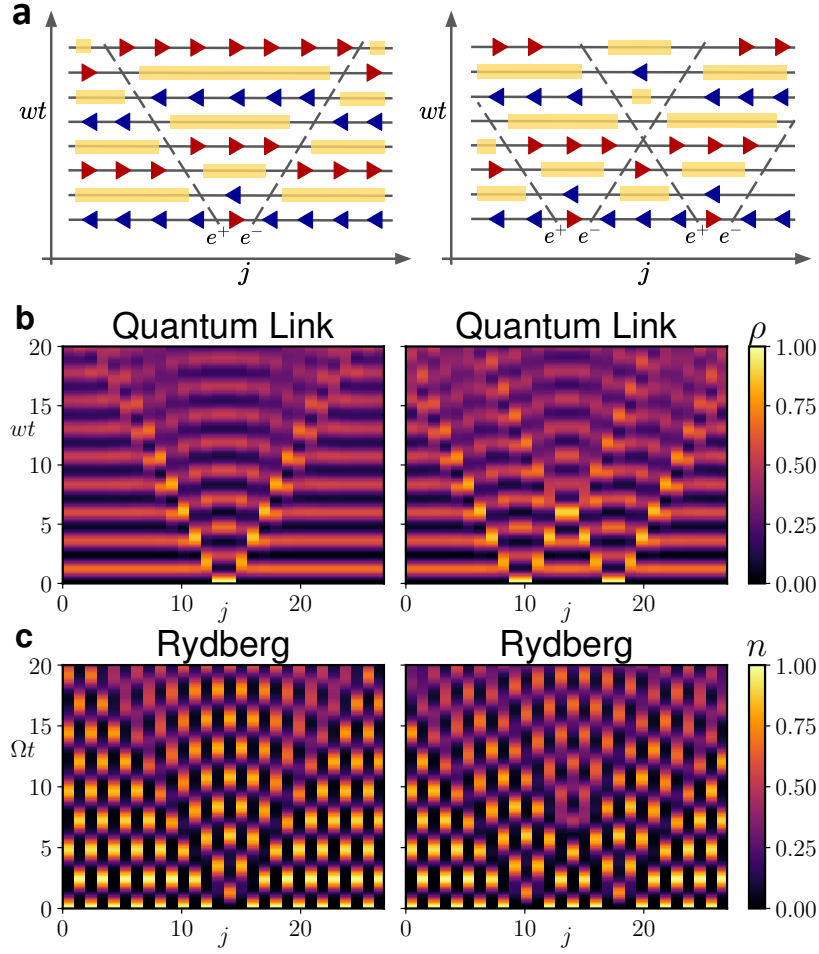


Figure 6.7: Slow dynamics of particle-antiparticle pairs. **a**: Cartoon states representing the propagation of particle-antiparticle pairs  $e^+e^-$ . The notation is the same as in Fig. 6.2, while the yellow stripes denote regions of space with largest particle density and therefore  $\langle \hat{E}_{j,j+1} \rangle \simeq 0$ . **b**: Evolution of the particle density in the QLM starting from a bare vacuum or "string" state, see Fig. 6.2, with initial particle-antiparticle pairs. **c**: Same as in panel **b**, but in the Rydberg excitation density representation. Left column: the oscillations observed in the light-cone shaped region originating from the particles is expected to be out of phase with respect to those of the bare vacuum. Right column: In the presence of two  $e^+e^-$  pairs, an additional change of periodicity is expected in correspondence of elastic scattering. In these simulations,  $m = \delta = 0$ .

### 6.3.4 Spectral properties and bands of non-thermal states

We characterize the anomalous ballistic spreading of particle-antiparticle pairs discussed in the previous Section in terms of the emergence of corresponding anomalous spectral properties of the FSS model. These properties generalize those recently observed [47] in some families of special energy

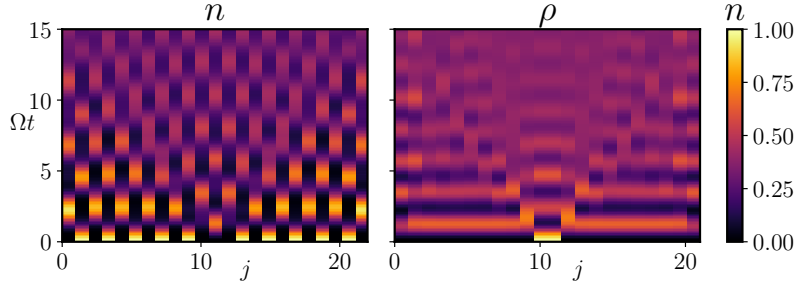


Figure 6.8: Propagation of a particle-antiparticle pair  $e^+e^-$  with realistic Rydberg interactions. Left panel: density of Rydberg excitations. Right panel: density of particles/antiparticles ( $\rho$  in the QLM language). Results are obtained for a chain of  $L = 23$  sites governed by the realistic Hamiltonian (6.1) with  $V_{ij} = V_1 r_{ij}^{-6}$  and no constraints in the Hilbert space. Parameters:  $\delta = 0$ ,  $V_1/\Omega = 25.6$ . We checked explicitly that the violation of Rydberg blockade is always small,  $\langle n_j n_{j+1} \rangle < 10^{-2}$ .

eigenstates referred to as “many-body quantum scars”. The latter are constituted by towers of regularly-spaced states in the many-body spectrum with alternating pseudo-momentum  $k = 0$  and  $k = \pi$ , characterized by non-thermal expectation values of local observables as well as by anomalously large overlaps with the charge-density wave initial states. The long-lived coherent oscillating behavior has been attributed in Ref. [47] to the existence of these “scarred” eigenstates.

Fig. 6.9a shows that the modulus of the overlap between the energy eigenstate  $|\psi\rangle$  with energy  $E$  and the above described inhomogeneous states  $|\phi_{e^+e^-}\rangle$  with momentum  $k$  clearly identifies a number of special bands of highly-excited energy eigenstates characterized each by an emerging functional relationship  $E(k)$ . As shown in Fig. 6.9d some of the states in these bands strongly deviate from the thermal value  $\langle n_j \rangle_{th} \simeq 0.276$ . This fact has already been observed in the previously studied quantum-scarred eigenstates, which coincide with the extremal points of these bands at momenta  $k = 0$  and  $k = \pi$ . A closer inspection of these energy-momentum relations, presented in Fig. 6.9b, shows that they are close to cosine-shaped bands, suggesting the emergence of single-particle excitations in the middle of the many-body energy spectrum.

We further characterize this spectral structure by constructing a quasi-particle variational ansatz  $|\chi_k\rangle$  on top of the exact matrix-product-state zero-energy eigenstate of the Hamiltonian (6.2) with  $\delta = 0$ , recently put forward in Ref. [52] (see Appendix B.2). As shown in Fig. 6.9c, the optimal quasi-particle ansatz has the largest overlap with the states on the energy-momentum bands of special eigenstates closest to zero energy, thus reinforcing the above emergent quasi-particle picture.

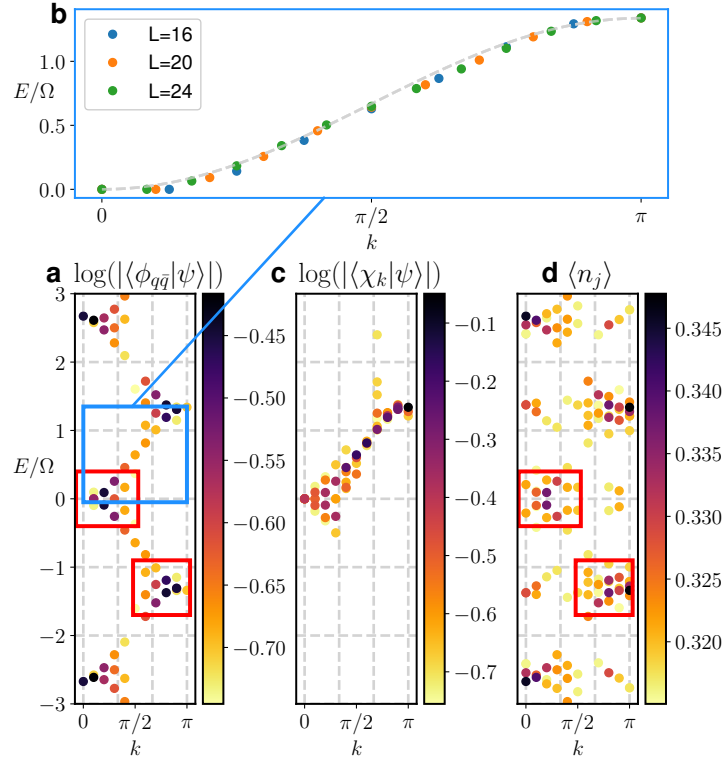


Figure 6.9: Emergent quasi-particle description of highly-excited states. **a**: Largest overlaps of the initial state  $|\phi_{e^+e^-}\rangle$  with a localized defect in a charge-density wave configuration of the Rydberg-atom chain with the energy eigenstates  $|\psi\rangle$  of the FSS Hamiltonian ( $\delta = 0, L = 20$ ) in Eq. (6.2), as a function of their corresponding momentum and energy. Within the gauge-theory description, the initial state corresponds to having a localized particle-antiparticle pair  $e^+e^-$ . **b**: The eigenstates with the largest overlaps display a regular functional dependence of energy on momentum that is remarkably close to a simple cosine band. **c**: The largest overlaps of the optimal matrix-product state quasi-particle ansatz  $|\chi_k\rangle$  built on an exact eigenstate with zero energy (see the main text) accurately reproduce the corresponding emergent quasi-particle band of panel **a**. **d**: Anomalous (non-thermal) expectation values of a local observable in energy eigenstates. The red boxes highlight the correspondence between the most relevant eigenstates building up  $|\phi_{e^+e^-}\rangle$  (panel **a**) and the most non-thermal eigenstates (panel **d**). The emergent spectral structure illustrated in this picture underlies the clean ballistic spreading of particle-antiparticle pairs displayed in Fig. 6.7.

### 6.3.5 Tuning the topological $\theta$ -angle in Rydberg experiments

So far, our discussion has focused exclusively on the relation between Rydberg experiments and the Schwinger model with topological angle  $\theta = \pi$ . A natural question to ask is whether, within the present setting, it is possible to realize genuinely confining theories, i.e., generic values of the topological angle  $\theta \neq \pi$ .

This is possible within the strong coupling limit upon introducing a linear term in the electric field. With reference to the lattice Schwinger model introduced in Sec. 6.3.2 and notations therein, we see that the two lowest degenerate energy states of the local electric field for  $\theta = \pi$  (i.e.  $L_{j,j+1} = 0, +1$ ) are split when  $\theta$  deviates from  $\pi$ , with an energy gap  $\Delta = J|\theta/\pi - 1|$ . In order to keep the structure of the Hilbert space compatible with the FSS model, one requires this  $\Delta$  to be much smaller than the gaps with the other states, which are of the order of  $J$ . This implies that, within the QLM formulation, we can only access very small deviations from  $\theta = \pi$ : this is not a limiting factor, and we will show how this simple setting already allows to witness the effects of confinement in the dynamics. The confining nature of the potential can be intuitively understood as follows: starting from the bare vacuum (the “string” state in Fig. 6.2), creating and separating a particle-antiparticle pair at a distance  $\ell$  entails the creation, between the two, of a string of length  $\ell$  with opposite electric field. The corresponding energy cost is proportional to  $\ell\Delta$ , signalling the confining nature of the potential. Accordingly, the lattice Schwinger model with strong  $J \gg \Omega, m, \Delta$  and with a topological angle  $\theta = \pi(1 \pm \Delta/J)$  is efficiently approximated by the QLM with an additional term linear in the electric field and proportional to  $\Delta$ .

In turn, within the exact mapping outlined in Sec. 6.2 and illustrated in Fig. 6.2, this  $\theta$ -angle term corresponds to an additional staggered field in the FSS model, leading to the Hamiltonian:

$$\hat{H}_{\text{Ryd}} = \sum_{j=1}^L (\Omega \hat{\sigma}_j^x + \delta \hat{\sigma}_j^z) + \sum_{j=1}^L (-1)^j \frac{\Delta}{2} \sigma_j^z. \quad (6.6)$$

The new term can be experimentally realized, e.g., by utilizing a position dependent AC Stark shift or, alternatively, a space-dependent detuning on the transition between ground and Rydberg states (it was realized, for example, in a recent work reported in Ref. [206]).

In Fig. 6.10, we show the effect of the  $\theta$ -angle on the evolution of the total electric field in the QLM starting from a uniform string state. Also in this case, the dynamics observed can be understood using the bosonized field theory in Eq. (6.5). As explained in Sec. 6.3.2, the integrability breaking term which appears for  $m > 0$  has the effect of damping the oscillations. Moreover, from the same equation we can predict that the impact of a variation of the  $\theta$ -term on the dynamics is enhanced when we increase the mass,

as data clearly show. This enhancement of the  $\theta$ -dependence becomes more evident when we cross the transition point: while in the symmetric phase with  $m < m_c$ , the explicit symmetry breaking caused by the electric field energy imbalance leads to damping of the string inversions, in the broken-symmetry (chiral) phase with  $m > m_c$  the effect of confinement is dramatic, causing the persistence of the initial electric string, with small long-lived oscillations. Focusing on the latter phase, in Fig. 6.11 we show the dynamical evolution of a finite electric string generated by a particle-antiparticle pair (left panels), at the deconfined point  $\theta = \pi$  (top) and in the confined phase with  $\theta \neq \pi$  (bottom). The right panels show the same evolution as it would appear in terms of measurements of Rydberg atom excitations. While for  $\Delta = 0$  nothing prevents the initially localized bare particles to propagate along the chain (top panels), the presence of a linear confining potential proportional to  $\Delta$  between them stabilizes the electric string, leading to effective Bloch oscillations of the edges and to a surprisingly long lifetime [207] (bottom panels). This effect signals that confinement can dramatically affect the non-equilibrium dynamics, potentially slowing it down as observed in both gauge theories [208] and statistical mechanics models [207, 209, 210]. In this regime, the model shows the same qualitative signatures of confinement as the quantum Ising chain in transverse and longitudinal field, such as the long-lived coherent oscillations and the suppression of the light-cone spreading [209].

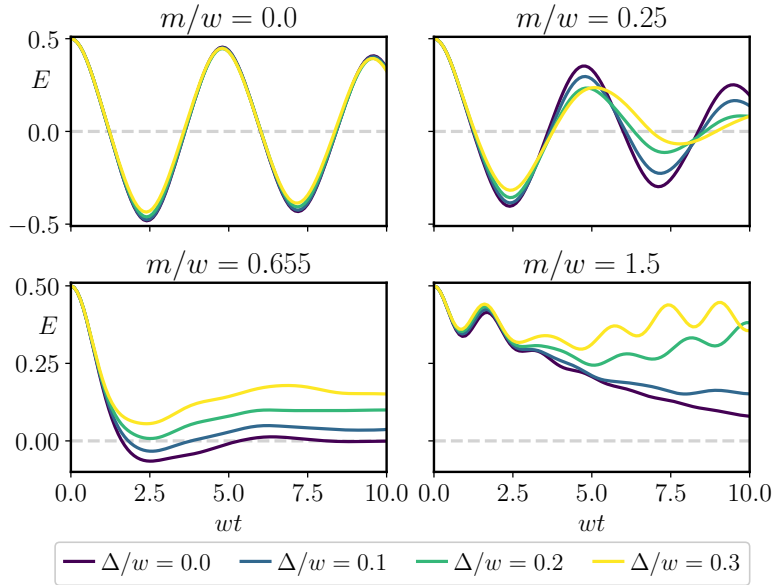


Figure 6.10: Effect of the  $\theta$ -angle on the dynamics of the electric field from uniform string states of the QLM. Data are shown for a chain of  $L = 28$  sites, for increasing values of the particle mass  $m/w$  and of the parameter  $\Delta$ , quantifying the deviation of the  $\theta$ -angle from  $\pi$  (see the main text). Dynamics for  $\Delta = 0$  correspond to the second column of Fig. 6.4.

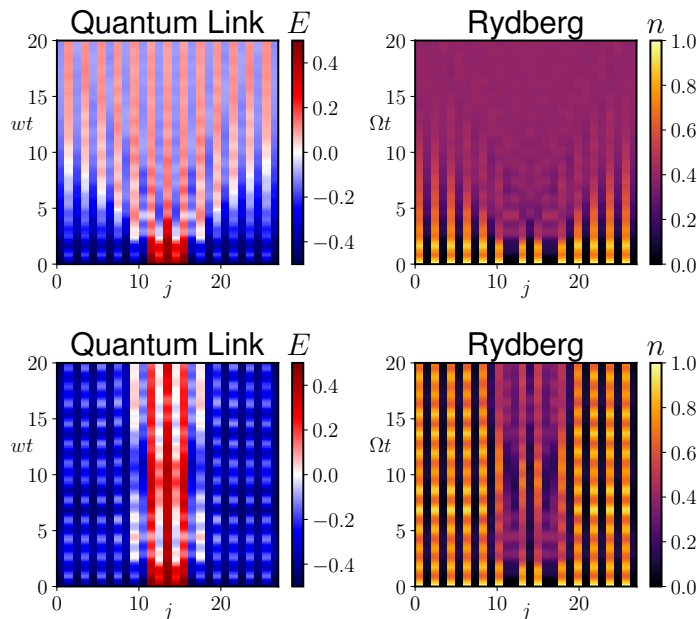


Figure 6.11:  $\theta$ -angle and string-breaking dynamics. Evolution of a bare particle-antiparticle pair state is displayed in terms of space- and time-dependent electric field in the QLM (left panels) and of the density of excited atoms in the Rydberg array (right panels), with  $m = -\delta = 1.5\Omega$  and  $L = 28$ . Simulations in the top row have  $\Delta = 0$ , corresponding to the deconfined field theory with  $\theta = \pi$ . Effects of confinement emerge in the second row, where a non-vanishing  $\Delta = 0.3\Omega$  stabilizes the electric string.

## 6.4 Conclusions

We proved that the large-scale quantum simulation of lattice gauge theories has already been achieved in state-of-the-art experiments with Rydberg atoms, as it can be realized by establishing a mapping between a  $U(1)$  gauge theory and Rydberg atom arrays. At the theoretical level, we showed that this novel interpretation provides additional insights into the exotic dynamics observed in experiments, linking it to archetypal phenomena in particle physics. Our field-theoretic description immediately implies the generality and applicability to a wide variety of model Hamiltonians within experimental reach, and among them we extensively discuss the example of the lattice Schwinger model in the Wilson formulation. We expect that future studies can further deepen the connection between the statistical mechanics description of such behaviour and its gauge-theoretic interpretation, for instance, elucidating the effects of non-thermal states [47, 48, 52, 105] and emergent integrability [69, 81], and the role of confinement in slowing down the dynamics [207–211]. At the experimental level, our findings immediately motivate further experiments along this direction, that can probe different

aspects of gauge theories, such as the decay of unstable particle-antiparticle states after a quench, and might be combined with other quantum information protocols [212]. We show how by tuning the  $\theta$ -angle – a possibility that is already available with current technologies – the different dynamical regimes expected from the field theory can be accessed. A particularly interesting perspective in this direction is the possibility of dynamically probing confinement via quantum quenches starting from a string embedded in the (bare) vacuum, a prototypical *gedanken* experiment in particle physics [190].

The quantum-simulation strategy we propose is based on the elimination of the matter degrees of freedom by exploiting Gauss law: This method does not rely on the specific formulation of the model and is in principle applicable to other lattice gauge theories (for a recent work along these lines see for example Ref. [213]). An intriguing future extension is represented by theories with non-Abelian gauge symmetries, an example of which can be found in Ref. [169], where links with finite-dimensional Hilbert spaces are utilized. The integration of matter degrees of freedom is equally well suited for higher dimensions, and Rydberg atoms are a promising platform for pursuing this direction [121, 214]. After the present analysis, the experiments performed in Ref. [46] represent a step-stone toward the ambitious realization of non-Abelian gauge theories in three spatial dimension, which remains an outstanding quest [129, 174].



# Chapter 7

## Non-Abelian lattice gauge theories with alkaline-earth-like atoms

Starting from early theoretical proposals [150, 153–155, 158, 158–160, 160–164, 172, 173] and from the pioneering trapped ion experiments of Ref. [166], the quantum simulation of Abelian lattice gauge theories (LGTs) has already been shown to scale beyond simple building blocks to regimes where classical simulations are challenging, if not prohibitive (see e.g Chapter 6). Instead, no scalable non-abelian LGTs quantum simulators exist to date<sup>1</sup>. The main roadblock for quantum simulating non-Abelian models stems from the fundamentally more complex nature of non-Abelian Gauss law in terms of quantum engineering: in particular, it is extremely challenging to constrain the dynamics of a quantum simulator in such a way that only gauge invariant states are populated. Presently, there exist only a few proposals that have addressed this [151–153, 155, 164, 215, 216], focusing on conceptual aspects of such challenge.

Here, we pursue a different approach. Building on impressive experimental developments over the last five years in harnessing quantum gases of alkaline-earth-like atoms, we present a proposal for the quantum simulation of  $SU(N) \times U(1)$  that combines a new conceptual framework to engineer gauge invariant dynamics, with an *ab initio* description of the physical setup. This combined approach has two key advantages: firstly, it allows us to immediately identify potential challenges in terms of microscopic constraints related to the quantum hardware (e.g., inability to realize the desired background potentials, etc.), that are known to be particularly relevant in the context of quantum engineering of LGTs; and secondly, it enables us to make precise predictions in terms of energy scale of the quantum simulator, and to properly frame the theoretical issues of imperfections in realizing

---

<sup>1</sup>Digital schemes have instead been already demonstrated in small scale experiments in Ref. [168, 180]

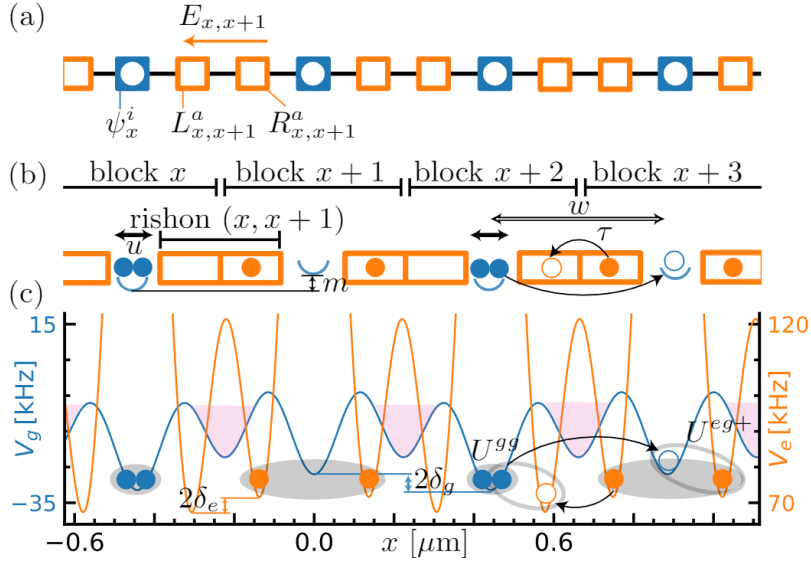


Figure 7.1: (a) Schematic of the 1D  $SU(N) \times U(1)$  LGT with both matter ( $\psi$ ) and gauge fields ( $L^a$ ,  $R^a$ ).  $E$  is the  $U(1)$  electric field on a link. (b) Schematic of corresponding QLM with one gauge boson per link. Its descriptive Hamiltonian is Eq. (7.2). (c) Corresponding setup of the 1D quantum simulator using cold  $^{173}\text{Yb}$  in an optical lattice.  $g$  atoms (blue) directly simulate matter and anti-matter fermions on sites  $x$ , while  $e$  atoms (orange) simulate the state of the gauge fields on the links: the rishons. Purple-shaded wells are never populated by the gauge-preserving dynamics. The key process in the QLM is the gauge-assisted hopping illustrated on the right of both (b) and (c). Before and after the hopping, each pair of particle on each block is a spin singlet (gray ellipses).

gauge invariant dynamics.

The setup we propose is depicted in Fig. 7.1. We propose to use cold  $^{173}\text{Yb}$  in their stable  $^1S_0 \equiv g$  and metastable  $^3P_0 \equiv e$  states, with hyperfine spin sublevels satisfying a  $SU(6)$  symmetry [217, 218]. We select  $N \leq 6$  of these six hyperfine states when initializing the system<sup>2</sup>. Only these  $N$  spin states are involved in the dynamics due to the global  $SU(6)$  symmetry leading to an effective  $SU(N)$  symmetry. The atoms are placed in an optical bipartite lattice (we call the two sublattices *even* and *odd*) and confined. Minima of the  $g$  atoms correspond to matter sites of the effective gauge theory. Each pair of nearest-neighbour  $g$  sites is separated by a double well for the  $e$  atoms (cf Fig. 7.1), which encode the gauge variable on the corresponding link. We define a *block* as the ensemble of one  $g$  site and its closest  $e$  sites (i.e., the closest side of a double well on each adjacent link). A staggered potential is superimposed: this potential introduces an energy

<sup>2</sup>This can be achieved, e.g., via optical pumping techniques, that have already been experimentally demonstrated at LENS and in Kyoto.

shift  $2\delta_g$  ( $2\delta_e$ ) between the  $g$  ( $e$ ) sites of even and odd blocks.

The strategy to build the simulator consists in making all gauge-invariant particle configurations in each block resonant with each others. The selected resonant configurations verify the number of atoms per block  $G_x = N$ <sup>3</sup> (the U(1) local charge) and total spin per block  $G_x^a = 0$  (the SU( $N$ ) local charge), with

$$G_x^a = \psi_x^{i\dagger} \lambda_{ij}^a \psi_x^j + \sum_{\hat{k}} c_{x,\hat{k}}^{i\dagger} \lambda_{ij}^a c_{x,\hat{k}}^j \quad (7.1a)$$

$$G_x = \psi_x^{i\dagger} \psi_x^i + \sum_{\hat{k}} c_{x,\hat{k}}^{i\dagger} c_{x,\hat{k}}^i. \quad (7.1b)$$

The matrices  $\lambda_{ij}^a$ ,  $a = 1, \dots, N$ , are the Pauli matrices for  $N = 2$  or their generalization for SU( $N$ ) such that  $\text{Tr} \lambda^a \lambda^b = 2\delta^{ab}$ . We used  $\psi_x^{i\dagger}$  (resp.  $\psi_x^i$ ) as the creation (resp. annihilation) operator of a  $g$  particle of SU( $N$ ) spin  $i = 1, \dots, N$  in the  $g$  well at the center of block  $x$ .  $c_{x,\hat{k}}^{i\dagger}$  is the creation operator of an  $e$  particle on the  $e$  well of block  $x$  closest to block  $x + \hat{k}$  (cf Fig. 7.1).  $\hat{k}$  are the vectors transforming  $x$  to one of its nearest neighbors. In 1D,  $L_{x,x+1}^a = c_{x+1}^{i\dagger} \lambda_{ij}^a c_{x+1}^j$  and  $R_{x,x+1}^a = c_{x+1,-1}^{i\dagger} \lambda_{ij}^a c_{x+1,-1}^j$ . All states satisfying  $G_x = N$ , and  $G_x^a = 0$  for all  $a$  (called Gauss' laws) make the gauge invariant subspace. The parameters are tuned such that all non-gauge-invariant configurations are off-resonant: in this way, resonant interactions between blocks are gauge-invariant by construction.

The effective Hamiltonian of the system in the resonant subspace corresponds to the SU( $N$ ) $\times$ U(1) QLM Hamiltonian for massive staggered fermions (see [174] for a review)

$$\begin{aligned} H_{\text{QLM}} = & m \sum_x s_x \psi_x^{i\dagger} \psi_x^i + \frac{w}{2} \sum_{x,\hat{k}} \psi_x^{i\dagger} \psi_x^i \psi_{x+\hat{k}}^{j\dagger} \psi_{x+\hat{k}}^j \\ & - \frac{\tau}{2} \sum_{x,\hat{k}} \left( \psi_{x+\hat{k}}^{i\dagger} U_{x+\hat{k},x}^{ij} \psi_x^j + \text{H.c.} \right) + \sum_x \frac{u_x}{2} \psi_x^{i\dagger} \psi_x^i (\psi_x^{j\dagger} \psi_x^j - 1) \end{aligned} \quad (7.2)$$

with  $s_x = +1$  ( $-1$ ) for even (odd) sites, and summation over repeated indices. The matter/anti-matter particles have mass  $m$ ; they interact with on-site interaction amplitude  $u_x$  and a nearest-neighbor interaction  $w$ . The gauge assisted-hopping, of amplitude  $\tau$ , is mediated by the SU( $N$ ) parallel transporter  $U_{x+\hat{k},x}^{ij} = c_{x,\hat{k}}^i c_{x+\hat{k},-\hat{k}}^{j\dagger}$ , according to the *rishon* formulation of QLM [174]: in this formulation, the gauge field is represented by fermionic particles (rishons) that sit on the left and right ends of the links. We work in the representation with  $\mathcal{N} \equiv c_{x,\hat{k}}^{i\dagger} c_{x,\hat{k}}^i + c_{x+\hat{k},-\hat{k}}^{i\dagger} c_{x+\hat{k},-\hat{k}}^i = 1$  rishon per link: the corresponding experimental setup has exactly one  $e$  particle per double well, avoiding 2-body  $e - e$  losses.

<sup>3</sup>The definition of  $G_x$  differ from the usual definition in the literature (such as Refs. [174]) by an unimportant locally conserved integer constant.

## 7.1 *Ab initio* derivation of the lattice model

We now elaborate on the derivation of Eq. (7.2) when starting from the lattice discretization of the atomic Hamiltonian. The continuous optical lattice Hamiltonian for alkaline-earth atoms is the standard [217]

$$\begin{aligned}
\mathcal{H} = & \sum_{\alpha i} \int d^3\mathbf{r} \Psi_{\alpha i}^\dagger(\mathbf{r}) \left( -\frac{\hbar^2}{2M} \nabla^2 + V_{\alpha i}(\mathbf{r}) \right) \Psi_{\alpha i}(\mathbf{r}) \\
& + \hbar\omega_0 \int d^3\mathbf{r} (\rho_e(\mathbf{r}) - \rho_g(\mathbf{r})) \\
& + \frac{g_{eg}^+ + g_{eg}^-}{2} \int d^3\mathbf{r} \rho_e(\mathbf{r}) \rho_g(\mathbf{r}) \\
& + \sum_{\alpha, i < j} g_{\alpha\alpha} \int d^3\mathbf{r} \rho_{\alpha i}(\mathbf{r}) \rho_{\alpha j}(\mathbf{r}) \\
& + \frac{g_{eg}^+ - g_{eg}^-}{2} \sum_{ij} \int d^3\mathbf{r} \Psi_{gi}^\dagger(\mathbf{r}) \Psi_{ej}^\dagger(\mathbf{r}) \Psi_{gj}(\mathbf{r}) \Psi_{ei}(\mathbf{r}),
\end{aligned} \tag{7.3}$$

with  $\Psi_{\alpha i}^\dagger$  the field creation operator at  $\mathbf{r}$  in the state  $\alpha = g, e$  with  $SU(N)$  spin  $i$  and  $\rho_\alpha(\mathbf{r}) = \sum_i \rho_{\alpha, i}(\mathbf{r}) = \sum_i \Psi_{\alpha i}^\dagger \Psi_{\alpha i}$ .  $M$  is the mass of  $^{173}\text{Yb}$ ,  $V_{\alpha i}$  is the lattice potential,  $\hbar\omega_0$  is the transition frequency between  $g$  and  $e$ ,  $g_{\alpha\alpha} = 4\pi\hbar^2 a_{\alpha\alpha}/M$ ,  $g_{eg}^\pm = 4\pi\hbar^2 a_{eg}^\pm/M$  and  $a_{\alpha\alpha}$ ,  $a_{eg}^\pm$  are the 2-body contact interaction scattering lengths.

The lattice version of the Hamiltonian is derived by decomposing  $\Psi_{\alpha i}$  into series of maximally localized Wannier functions [219, 220] from the populated  $s$  bands of the lattices only, separated by the gap  $\Delta_g$  and  $\Delta_e$  from the unpopulated bands (see Appendix B.4 for details). The lattice formulation of Eq. (7.3) involving only block  $x$  is

$$\begin{aligned}
h_x^0 = & \mu_x^g n_x + \frac{U_x^{gg}}{2} n_x (n_x - 1) \\
& + \sum_{\hat{k}} \left[ \mu_x^e n_{x, \hat{k}} + \frac{U_x^{eg+} + U_x^{eg-}}{2} n_x n_{x, \hat{k}} \right. \\
& \quad \left. + \frac{U_x^{eg+} - U_x^{eg-}}{2} \psi_x^{i\dagger} c_{x, \hat{k}}^{j\dagger} \psi_x^j c_{x, \hat{k}}^i \right] \\
& + \sum_{\hat{k}_1 \neq \hat{k}_2} t_{x, \hat{k}_1 \hat{k}_2}^e (c_{x, \hat{k}_1}^{i\dagger} c_{x, \hat{k}_2}^i + \text{H.c.}) + \dots,
\end{aligned} \tag{7.4}$$

with  $n_x = \psi_x^{i\dagger} \psi_x^i$  and  $n_{x, \hat{k}} = c_{x, \hat{k}}^{i\dagger} c_{x, \hat{k}}^i$ . We consider that the  $e$  double wells are separated by a large barrier, such that all hoppings  $t_e$  and the omitted density-assisted hoppings that change the number  $\mathcal{N}$  of rishons per link are suppressed.

## 7.2 Resonance conditions

We say that a process is resonant when it connects degenerate eigenstates of  $H_0 = \sum_x h_x^0$ . To induce the desired gauge-invariant dynamics, we require the gauge-assisted hopping to be resonant between compatible<sup>4</sup> gauge-invariant states. For example for  $N = 2$ , the spectrum of  $h_x^0$  in Table 7.1 and resonance of the gauge-assisted hopping impose

$$E_x^{gg} + E_{x+1}^{geS} = E_x^{geS} + E_{x+1}^{gg}, \quad (7.5a)$$

$$E_x^{eeS} + E_{x+1}^{gg} = E_x^{geS} + E_{x+1}^{geS}, \quad (7.5b)$$

$$E_x^{geS} + E_{x+1}^{geS} = E_x^{gg} + E_{x+1}^{eeS}, \quad (7.5c)$$

$$E_x^{geS} + E_{x+1}^{eeS} = E_x^{eeS} + E_{x+1}^{geS}, \quad (7.5d)$$

with the notations of Table 7.1. For example, the hopping in Fig. 7.1 is resonant if Eq. (7.5d) is verified. Taking  $\mu_x^\alpha = \mu^\alpha + s_x \delta_\alpha$ ,  $\alpha = g, e$ , and  $U_x^{ge+} = U^{ge+} + s_x \epsilon$ , the conditions Eqs. 7.5 impose (i)  $\delta_g + \epsilon = \delta_e$  and (ii)  $U_x^{gg} = 2U_x^{eg+}$ <sup>5</sup>. Small deviations from these resonance conditions contribute as gauge-invariant terms in Eq. (7.2). The mass is  $m = \delta_g - \delta_e + \epsilon$  and the amplitude of the on-site density interaction is  $u_x = U_x^{gg} - 2U_x^{eg+}$ . Extra correction to  $m$  and  $u_x$  and  $w$  in Eq. (7.2) are obtained from the interaction between neighbouring blocks projected onto the gauge-invariant subspace, as reported in Appendix B.5. As shown in the same Section, the reasoning generalizes for all  $N$ .

## 7.3 Off-resonance conditions

Conversely, all terms which would break gauge invariance are made off-resonant. Eigenspaces with  $G_x \neq N$  are off-resonant for large  $\mu^g$  and  $\mu^e$ . Simple hoppings of  $g$  or  $e$  particles between neighbouring blocks are suppressed by the staggering  $\delta_{g,e}$  in the chemical potentials. The gauge-breaking  $g - e$  magnetic multiplet state (triplet for  $N = 2$ ) with energy  $E_x^{geM}$  is off-resonant when  $U_x^{eg-} \neq U_x^{eg+}$ . When  $g$ -wells can be empty of particles, like in 1D for  $N = 2$ , the gauge-breaking  $e - e$  multiplet states have the same energy  $E_x^{eeM}$  as the  $e - e$  gauge-invariant singlet state ( $E_x^{eeS}$ ) such that the two belong to the same resonant subspace. However, the hybridization between the two types of states is suppressed as no on-block or nearest-block interactions resonantly connect the two ensembles. For  $N > 2$  in 1D or  $N > 3$  in 2D hexagonal lattice, the available multiplet states always contain at least one  $g$  particle, such that they are driven off-resonance by  $U_x^{eg-}$ .

<sup>4</sup>“Compatible” means that the configurations considered must all satisfy Gauss’ laws simultaneously. This includes having exactly one  $e$  particle on each link at all times.

<sup>5</sup>Note that a global offset in the chemical potentials for  $g$  atoms or  $e$  atoms is unimportant as the total number of  $g$  and  $e$  atoms is conserved.

Antisymmetric nuclear spin singlet (S)	
Electronic state (sym.)	Energy
$ g, g\rangle$	$E_x^{gg} = 2\mu_x^g + U_x^{gg}$
$\frac{1}{\sqrt{2}} \left(  g, e\hat{k}\rangle +  e\hat{k}, g\rangle \right)$	$E_x^{geS} = \mu_x^g + \mu_x^e + U_x^{eg+}$
$\frac{1}{\sqrt{2}} \left(  e\hat{k}_1, e\hat{k}_2\rangle +  e\hat{k}_2, e\hat{k}_1\rangle \right)$	$E_x^{eeS} = 2\mu_x^e$
Symmetric nuclear spin multiplet (M)	
Electronic state (antisym.)	Energy
$\frac{1}{\sqrt{2}} \left(  g, e\hat{k}\rangle -  e\hat{k}, g\rangle \right)$	$E_x^{egM} = \mu_x^g + \mu_x^e + U_x^{eg-}$
$\frac{1}{\sqrt{2}} \left(  e\hat{k}_1, e\hat{k}_2\rangle -  e\hat{k}_2, e\hat{k}_1\rangle \right)$	$E_x^{eeM} = 2\mu_x^e$

Table 7.1: The two particles eigenstates and eigenenergies of a single block  $x$  for  $N = 2$ . “ $e\hat{k}$ ” designate a state with one  $e$  particle from block  $x$  on the link between  $x$  and  $x + \hat{k} = x \pm 1$ . Only the singlet states satisfy gauge invariance ( $G_x^a = 0$  for all  $a$ ).

## 7.4 1D lattice setup and parameters

The 1D optical lattice potential displayed in Fig. 7.1(c) can be realized by interfering laser beams at three different wavelengths  $\lambda_0$ ,  $\lambda_1$  and  $\lambda_S$ , creating sinusoidal potentials along the  $x$ -direction with amplitude  $V_\alpha^0$ ,  $V_\alpha^1$ , and  $V_\alpha^S$ , and periodicity  $a_0$ ,  $a_0/2$ , and  $2a_0$ , respectively. In addition, a tight transverse confinement can be obtained by creating an optical lattice with spacing  $d$  and potential strengths  $V_\alpha^\perp$  along the transverse  $y$  and  $z$  directions. These lattices add together to give the optical potential  $V_\alpha$  in Eq. (7.3):

$$\begin{aligned}
 V_\alpha(\mathbf{r}) = & V_\alpha^0 \sin^2 \left( \frac{\pi x}{a_0} + \frac{\pi}{2} \right) + V_\alpha^1 \sin^2 \left( \frac{2\pi x}{a_0} + \frac{\pi}{2} \right) \\
 & + V_\alpha^S \sin^2 \left( \frac{\pi x}{2a_0} \right) + V_\alpha^\perp \left[ \sin^2 \left( \frac{\pi y}{d} \right) + \sin^2 \left( \frac{\pi z}{d} \right) \right].
 \end{aligned} \tag{7.6}$$

The resonance conditions are imposed by acting on the amplitude of the lattice potentials: the condition (i) is most sensitive to the superlattice potential  $V_\alpha^S$ , the condition (ii) is mainly tuned by adjusting the confining potential  $V_\alpha^\perp$  that modifies the widths  $\ell_{g/e}$  of the Wannier functions in the  $y$  and  $z$  directions (the interactions are enhanced by increasing the confinement)<sup>6</sup>. The realistic values of the experimental parameters chosen for  $N = 2$  in  $^{173}\text{Yb}$ , and the corresponding computed amplitudes are

<sup>6</sup>In a realistic setting, the three resonance conditions [the condition (i), and the con-

summarized in Tab. 7.2. Considering  $a_0 \simeq 0.44 \mu\text{m}$ , a possible set of laser wavelengths is  $\lambda_0 \simeq 0.44 \mu\text{m}$ ,  $\lambda_1 \simeq 0.64 \mu\text{m}$  and  $\lambda_S \simeq 0.69 \mu\text{m}$ .

$M$	$172.93 \text{ u}$	$a_0$	$\sim 0.44$	$\Delta_g$	$3.6962$
$g_{gg}$	$7.748 \text{ Hz } \mu\text{m}^3$	$V_g^0$	$-6.99$	$\Delta_e$	$31.3337$
$g_{eg}^+$	$72.97 \text{ Hz } \mu\text{m}^3$	$V_g^1$	$-20.02$	$\delta_g$	$-2.0720$
$g_{eg}^-$	$8.536 \text{ Hz } \mu\text{m}^3$	$V_g^S$	$-4.42$	$\delta_e$	$-2.0990$
$m$	$2.8 \cdot 10^{-5}$	$V_e^0$	$178.16$	$t_e$	$-3.0 \cdot 10^{-5}$ $-2.5 \cdot 10^{-5}$
$\tau$	$-0.00311$	$V_e^1$	$125.15$	$U^{eg+}$	$1.2321$
$u$	$< 10^{-6}$	$V_e^S$	$-7.45$	$U^{eg-}$	$0.1441$
$w$	$1.497 \cdot 10^{-4}$	$\ell_g$	$0.0578$ $0.0565$	$U^{gg}$	$2.4186$ $2.3307$
		$\ell_e$	$0.0235$ $0.0455$		

Table 7.2: Upper left: parameters of the  $^{173}\text{Yb}$  in Eq. (7.3) [218, 221, 222]. Lower left: *ab initio* parameters of Eq. (7.2) for the 1D setup, with  $N = 2$ . Center: parameters of the optical lattices. Right: corresponding values of the lattice Hamiltonian Eq. (7.4). Energies are in kHz and lengths are in  $\mu\text{m}$ . A cell has two values when the corresponding quantity is different for odd and even sites within significant digits.

The time scale of the dynamic of the effective QLM Hamiltonian is  $|\tau|^{-1} \sim 300 \text{ ms}$  and is within the resolution of the experiment. The gauge-breaking term  $t_e$  is two orders of magnitude smaller than the leading amplitudes. Changing slightly the amplitude of the potentials in the experiment allows exploration of the phase diagram around the competing regime of  $m$ ,  $\tau$ ,  $w$ , and  $u_x$ .

## 7.5 Generalization to $N > 2$ and 2D lattice setup

The strategy generalizes to larger  $N$  and higher dimensions. In Appendix B.6, we report the data for the  $U(3)$  QLM in one spatial dimension. In this case, three body losses of  $g$  atoms are present but the rates are much

---

dition (ii) for both  $x$  even and odd] are all affected by the potentials, and tuning  $V_\alpha^S$  and  $V_\alpha^\perp$  independently is not sufficient to meet them. However, the conditions can still be satisfied by tuning the laser amplitudes, simply because the number of conditions is smaller than the number of free parameters.

smaller than the characteristic frequencies of the relevant dynamic (the loss rate is of the order of  $5 \cdot 10^{-5}$  kHz).

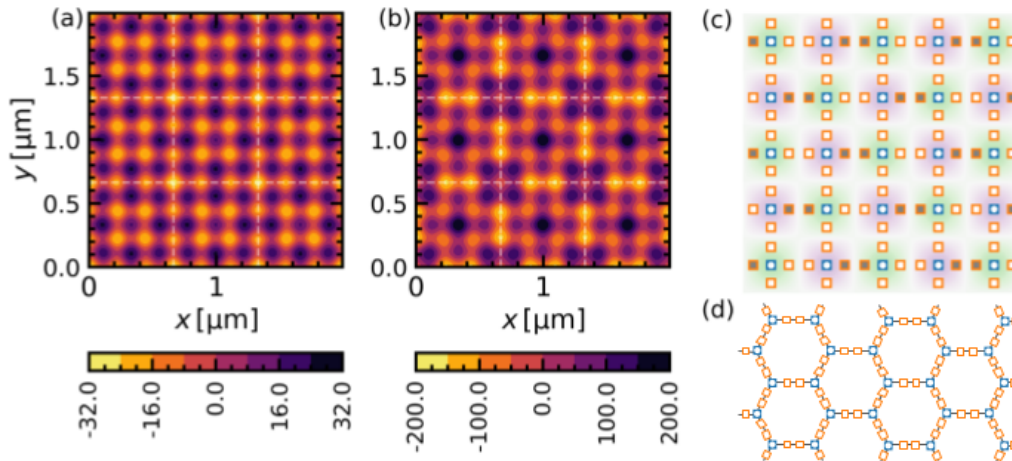


Figure 7.2: Optical lattice for the two-dimensional QLM: the  $g$  potential (a) has minima in the vertices of the lattice, the  $e$  potential (b) has two minima on each link. (c) The brickwall lattice is realized with the same potential of the square lattice ( $g$  sites (blue) correspond to matter, the  $e$  sites (orange) to rishons): the double wells represented as gray boxes are initialized with no  $e$  atoms, such that no gauge variable is present on the corresponding link. The superlattice shifts even and odd blocks (in green/purple). (d) The brickwall lattice is equivalent to the honeycomb lattice.

In Fig. 7.2(a,b) we show the profile of an optical lattice that can be used to simulate a QLM in a two-dimensional square lattice. An extra superlattice potential ensures the staggering. The amplitudes are tuned such that the resonance conditions (i) and (ii) are satisfied. In addition to the terms of Eq. (7.2), the effective Hamiltonian will contain plaquette terms generated in second order perturbation theory: second order terms can be comparable in amplitude to the leading first order terms for both one-dimensional and two-dimensional systems.

The same optical lattice can be used to realize a brickwall lattice (equivalent to a honeycomb lattice) QLM: it is sufficient to initialize the system in a state with “empty” links as in Fig. 7.2(c). The brickwall lattice has a non-trivial matter-gauge dynamics with  $N = 2$ , unlike the square lattice that does not host  $g$  atoms for  $G_x = 2$  and  $\mathcal{N} = 1$ .

## 7.6 Preparation of the initial state

In order to experimentally prepare initial states within the gauge invariant subspace one can exploit the spectroscopic resolution of the clock transition to resolve two-particle states with different electronic wavefunctions.

In particular,  $N = 2$  gauge-invariant (spin singlet) states can be created starting from a band insulator of  $g$ -state atoms in the lattice potential with periodicity  $a_0$ , and transferring each on-site  $|g, g\rangle$  (singlet) state into one of the states given in the top part of Table 7.1. This can be achieved by only employing global clock laser pulses after turning on the short lattice with  $a_0/2$  period.

## 7.7 Discussion and conclusion

In this work, we proposed an *ab initio* scalable experimental setup of an  $SU(N)\times U(1)$  lattice gauge theory quantum simulator in 1D and 2D. The experiment uses ultra-cold alkaline-earth-like fermionic atoms in an optical superlattice. The system is restricted to evolve within the resonant gauge-invariant subspace set by the initial state, while gauge-breaking states are off-resonant.

We perform an *ab initio* calculation that allows to estimate the energy scales involved in an experimental implementation. The time scales that characterize the effective gauge invariant dynamics can be as short as  $|\tau|^{-1} \sim 300$  ms, and are reachable by realistic experiments.

The main advantage of this setup is the immediate scalability: the system size is set by the size of the optical lattice, and can already reach hundreds of sites in available experiments. Therefore, this setup would allow for the first large-scale quantum simulation of a non-Abelian lattice gauge theory.

Another significant advantage is the possibility of realizing two-dimensional lattice gauge theories, whose quantum simulation has so far proven to be prohibitively challenging. In particular, our setup uses fermionic atoms to represent fermionic matter, allowing for a simpler implementation (that does not require Jordan-Wigner strings) in models with more than one dimension. This could pave the way to the study of novel phases of matter and quantum spin liquids.



## Part III

# Non-equilibrium dynamics of lattice gauge theories



## Chapter 8

# Confinement: physical mechanism and consequences on non-equilibrium

Confinement of elementary particles is renowned as a fundamental mechanism for our understanding of fundamental interactions of nature. The prototypical example of this phenomenon is quark confinement in quantum chromodynamics [139] which is a ruling principle of strong interactions: quarks cannot be isolated at low-energy and they are only found in composite particles called hadrons such as baryons and mesons. Indeed, the mass of ordinary matter is in an overwhelming majority in the binding energy of protons and neutrons rather than in the masses of truly elementary particles such as quarks and electrons.

Confinement of excitations is a relevant phenomenon also in condensed matter physics, as theoretically proposed in the late seventies [223, 224] and directly verified in the last decade in a number of experiments with inelastic neutron scattering or other spectroscopic probes [225–231]. To date, confinement has been found and studied in great details in many one-dimensional and quasi-one-dimensional magnetic insulators, with Ising-like [223, 224, 232–234] or Heisenberg-like [235–241] interactions. In all these cases, the spin-1/2 excitations (kinks or spinons) not only form bound states with integer spin, as a consequence of an (even weak) attractive interaction, but they cannot be observed as free particles at low energy, exactly like quarks in high energy physics. Following the pioneering work by McCoy and Wu [223], confinement has been studied with various analytical and numerical methods in the ground state of these many-body systems as well as in thermal equilibrium [167, 208, 233, 242–254]. In very recent times, it has been proposed that many quantitative aspects of confinement (such as the masses of the bound states) can be accessed very effectively following the non-equilibrium real time dynamics [209], a protocol which is routinely exploited in ultracold atoms and trapped ions experiments. This observation started an intensive theoretical activity on the

subject [6, 198, 207, 210, 255–261] that lead to direct experimental implementation of a quantum simulator with trapped ions [262], as well as several new theoretical and experimental ideas to understand lattice gauge theories in real time [4, 166, 187, 192, 263, 264].

This chapter is structured as follows: in Section 8.1 we introduce the concept of confinement and we illustrate the general physical mechanism (for a thorough discussion of the topic see, e.g., [265]); in Section 8.2 we discuss the specific case of one-dimensional (and quasi-one-dimensional) ferromagnets and antiferromagnets; in Section 8.3 we demonstrate the effect of confinement on the non-equilibrium dynamics of quantum many-body systems; finally in Section 8.4 we discuss possible future research directions.

## 8.1 What is confinement?

The idea of confinement was first introduced in the context of quantum chromodynamics (QCD) as the phenomenon that traps quarks into composite particles (called mesons and baryons): as a consequence, free quarks cannot be observed in nature. Quarks are held together by gluons (i.e., the quanta of the non-Abelian gauge field of QCD), which induce an effective interaction between them. At short distances, this interaction between quarks resembles the well-known Coulomb forces of quantum electrodynamics, with a potential  $V(r) \sim 1/r$ . At large distances, instead, the interaction between quarks is qualitatively different from Coulomb-like forces. The interaction potential has the form

$$V(r) = \sigma r, \quad (8.1)$$

where the constant  $\sigma$  is called *string tension*, to recall the presence of a *string* of gluon field lines that stick the quarks together. While the strength of Coulomb-like interactions decreases with distance, the linear potential in Eq. (8.1) grows indefinitely. To understand the difference between the two cases, it is useful to consider the quantum-mechanical problem of two particles interacting with a potential  $V(r)$ , and solve the Schroedinger equation for the relative distance  $r$  (see Fig. 8.1) for the Coulomb-like and the linear potential<sup>1</sup>.

In both cases, the lowest levels are bound states, and the corresponding wavefunctions decay exponentially with  $r$ . However, in the first case, if we give the system sufficient energy, such that it exceeds the threshold  $E = 0$ , it is excited to a delocalized state: for example, an hydrogen atom can be ionized, and the opposite charges (the electron and the proton) can be separated by an arbitrary distance. Electrons and protons are found in

---

<sup>1</sup>Note that this argument is not only valid for the case of one spatial dimension, but it also works in three dimensions: in the latter case, the effective potential contains an additional term  $L^2/2\mu r^2$ , where  $L$  is angular momentum and  $\mu$  is the reduced mass; this term does not affect the properties of the potential at large  $r$ , so the conclusions are still valid.

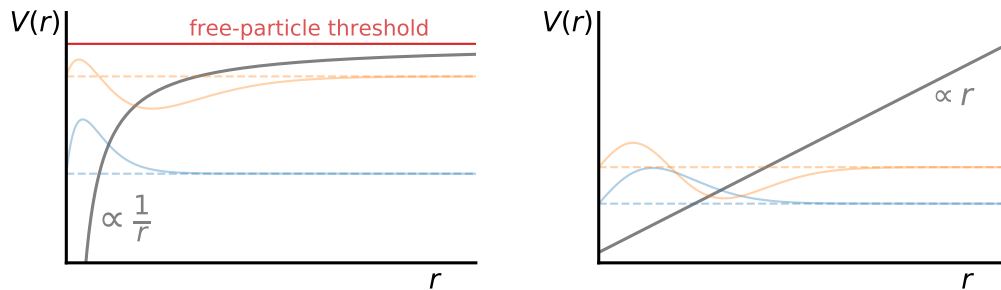


Figure 8.1: Left: Coulomb-like potential. At low energies, two particles form a bound state; at high energies, they are free. Right: linear potential. The two particles are always confined in bound states.

neutral atoms but they also exist as free particles. In the second case, we can never separate the two charged particles, irrespective of how much energy we inject in the system. All the eigenstates are neutral bound states and the spectrum is discrete. As we will see in the following, these bound states of the simple two-body problem correspond to excitations in a many-body system, called *mesons*. In contrast with the two-body case, in a many-body system the spectrum is discrete only up to the energy threshold of two-meson states. Nevertheless, all these states are neutral: the property that no charged particles can be isolated remains valid in the many-body context, and is the hallmark of confinement.

### 8.1.1 Confinement and gauge flux lines

We have so far explained why a linear effective potential between charges leads to confinement, i.e., to the fact that no isolated charged particles can exist. We now want to show how a confining (or non-confining) potential can emerge in a quantum field theory or in a many-body system: To do so, we need to use the language of gauge theories.

Gauge fields are the mediators of interaction between charges: this means that the effective potential that we studied in the previous paragraph can be equivalently seen as the energy of the gauge field. A simple example of this idea is well-known in classical electrodynamics, where the energy of a charge distribution can be equally expressed solely as the energy  $U \propto \int d\mathbf{r} E^2(\mathbf{r})$  of the electric field. With this equivalence, we can then understand the presence of a confining linear potential as the emergence of an electric *flux tube* (or *string*) between two charged particles: imagine that, for some reason, the electric field assumes a finite value in a cylinder that extends between the two charges, and that both this value and the radius of the cylinder do not depend on the distance  $r$  between the charges. Then, the resulting electrostatic energy is proportional to the volume of the cylinder and grows linearly in  $r$ , leading to confinement (see Fig. 8.2).

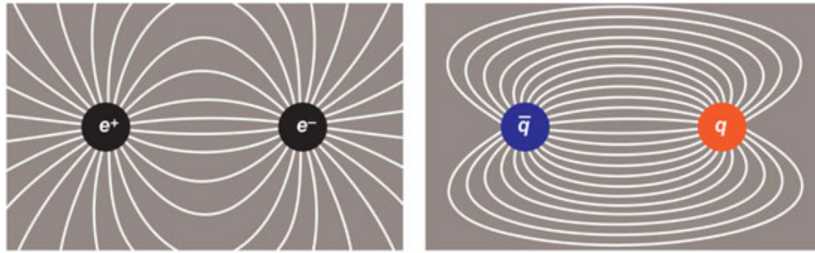


Figure 8.2: Left: in electromagnetism, the field generated by two charges spreads everywhere in space. Right: for a quark-antiquark pair, the field is concentrated around the line that connects the two (*flux tube*). Picture from [266].

How the flux tubes emerge in QCD or in a many-body system is typically a very complicated problem, that requires computationally-expensive Monte Carlo simulations on lattice models. An illustration of flux tubes emerging in simulations of this type is shown in Fig. 8.3.

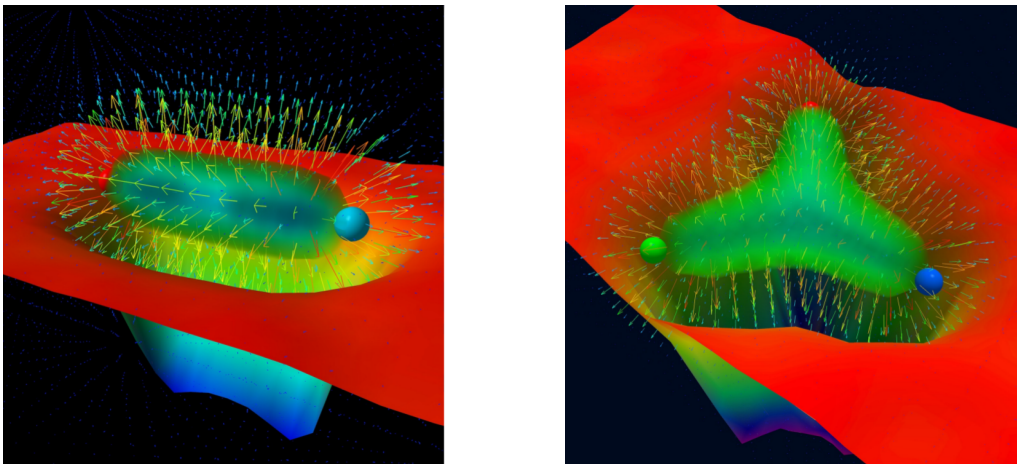


Figure 8.3: Left: simulation of the separation of a meson. As the quark and the antiquark are separated, a flux tube extends between them. Right: a simulation of the separation of a baryon. Credits: Derek Leinweber, Centre for the Subatomic Structure of Matter (CSSM) and Department of Physics, University of Adelaide, 5005 Australia.

### 8.1.2 String breaking

We have so far shown that, because of the emergence of flux tubes, in a confined theory the interaction energy between two charges grows indefinitely with their distance. However, this picture is not completely correct. Imagine having two static charges that are kept at a distance  $r$  and letting your system reach equilibrium in this configuration. When the distance  $r$

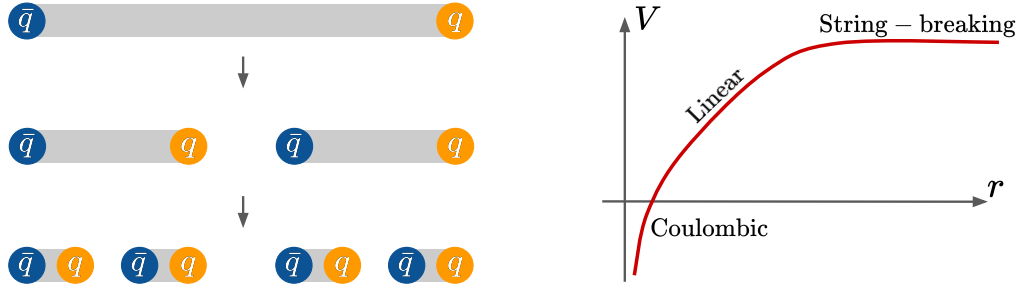


Figure 8.4: Left: String breaking by quark-antiquark pair production. Right: effective potential between two quarks.

is large enough, it may be energetically more convenient to create two new particles that "break" the flux tube and screen the interaction potential. This phenomenon, known as *string breaking* takes place when the energy  $\sigma r$  associated with the flux tube exceeds the energy  $E = 2m$  needed to create two particles (of mass  $m$ ) out of the vacuum. Therefore, the effective two-body potential  $V(r)$  that grows linearly for intermediate  $r$ , saturates for large  $r$  to a value  $V \sim 2m$ . The qualitative dependence of the interaction potential between two quarks at distance  $r$  is shown in Fig. 8.4

## 8.2 Confinement in one-dimensional ferromagnets and antiferromagnets

In condensed matter physics, many examples of confinement have recently been investigated. The equivalent of quarks can be represented by various types of charged excitations (where "charged" means that they transform non-trivially under a certain symmetry). For example, confined states of spinons have been studied in one-dimensional (or quasi-one-dimensional) ferromagnets or antiferromagnets [223, 228, 232, 234, 234, 238, 239, 242, 243, 249, 251, 252, 263, 267–271]; they have been detected in neutron scattering experiments on  $\text{CaCu}_2\text{O}_3$  and on  $\text{CoNb}_2\text{O}_6$  [226, 228]. Confinement of kinks has also been observed in long-range interacting spin chains, simulated with trapped ions [262].

To illustrate how confinement emerges in quantum spin chains, we consider the quantum Ising chain in transverse and longitudinal field, which represents the simplest example. The concepts that we are going to explain here can be easily generalized to other one-dimensional ferromagnets and anti-ferromagnets subject to an external magnetic field.

### 8.2.1 The quantum Ising chain in transverse and longitudinal field

We consider a chain of  $L$  spin-1/2 variables, described by the following Hamiltonian

$$H = -J \sum_{j=1}^{L-1} \sigma_j^z \sigma_{j+1}^z - h \sum_{j=1}^L \sigma_j^z - g \sum_{j=1}^L \sigma_j^x. \quad (8.2)$$

The operators  $\sigma_j^\alpha$  are Pauli matrices at site  $j$  and the coupling  $J > 0$  is ferromagnetic.

Let us first focus on the case  $h = 0$ . In this case, the model has a  $\mathbb{Z}_2$  symmetry associated with the global spin flip transformation  $X = \prod_{j=1}^L \sigma_j^x$ . At temperature  $T = 0$ , the symmetry is spontaneously broken for  $|g| < J$ : the system is a ferromagnet with local magnetization  $\langle \sigma_j^z \rangle = \pm M$ , with  $M = [1 - (g/J)^2]^{1/8}$ . The excitations on top of the ferromagnetic ground state can be computed by mapping the Hamiltonian to a model of free fermions. The excitations correspond to kinks, which interpolate between domains of opposite magnetization. The kinks can propagate freely in the system, so they are "deconfined".

For  $h \neq 0$ , the longitudinal field introduces an effective interaction between the kinks. In analogy with flux tubes of quantum chromodynamics, the domains that are anti-aligned with the longitudinal field acquire an energy proportional to their lengths, inducing a linear interaction between the kinks at their edges. As proven by McCoy and Wu in a seminal paper in 1978 [223], the model is confined. Kinks cannot propagate freely and are bound into mesons. While kinks are topological excitations with a non-zero  $\mathbb{Z}_2$  charge, mesons are neutral: they represent the new elementary excitations of the model.

### 8.2.2 The quantum Ising chain as a lattice gauge theory

As anticipated in Section 8.1.1, gauge theories are a useful framework for studying confinement. To illustrate this with a concrete example, we now show that the Ising chain introduced in Eq. 8.2 can be mapped exactly to a  $\mathbb{Z}_2$  lattice gauge theory [6, 272, 273]. This mapping allows to make explicit the identification of kinks with particles and of spins with gauge fields that mediate the interactions between them. To this end, fictitious fermionic matter degrees of freedom are introduced on the sites of the dual chain (i.e., on the bonds of the original chain [140, 274]): they represent  $\mathbb{Z}_2$ -charged particles. We therefore define the fermionic creation operators  $c_j^\dagger$ , and the following Hamiltonian [6, 275]

$$H_{\mathbb{Z}_2} = m \sum_j c_j^\dagger c_j + \frac{\tau}{2} \sum_j \sigma_{j+1/2}^z + w \sum_j (c_j^\dagger - c_j) \sigma_{j+1/2}^x (c_{j+1} + c_{j+1}^\dagger), \quad (8.3)$$

where  $m$  is the fermion mass,  $\tau$  is the string tension of the gauge field, and  $w$  is the interaction strength of fermions, mediated by gauge fields (the corresponding terms describe hopping and pair creation/annihilation of fermions). This Hamiltonian has a local  $\mathbb{Z}_2$  symmetry generated by the operators

$$G_j = \sigma_{j-1/2}^z \sigma_{j+1/2}^z (1 - 2n_j), \quad [H_{\mathbb{Z}_2}, G_j] = 0. \quad (8.4)$$

The Gauss law  $G_j \equiv 1$  is the local constraint that restricts the Hilbert space to the "neutral" or "gauge invariant" sector: the allowed configurations are those in which fermions sit on all the bonds where a kink is present in the gauge field configuration.

All matrix elements of the Hamiltonian (8.3) between two classical configurations coincide with the corresponding matrix elements of the quantum Ising chain [Eq. (8.2)] in the  $\sigma^z$ -basis, upon identifying  $m = 2J$ ,  $\tau = -2h$ ,  $w = -g$ , and up to an overall energy shift (see Appendix C.1.1 for details). Within this LGT picture, the longitudinal field  $h$  in the quantum Ising chain plays the role of the electrostatic string tension  $\tau$ , leading to particle confinement.

### 8.3 Non-equilibrium dynamics

While in the previous sections we introduced confinement as a static property, related to the effective interaction between charges and to the nature of the excitations of a system, we here want to show how it manifests itself in the real-time dynamics after a quantum quench (Fig. 8.5).

Following Ref. [209], we will focus on the Ising chain introduced in Section 8.2.1. The system is prepared in the ground state of the Hamiltonian Eq. (8.2); at  $t = 0$  the parameters  $h$  and  $g$  are suddenly changed and the time evolution is monitored from that moment. We first consider the case  $h = 0$  and  $|g| < J$ . The quench in  $g$  corresponds to the creation of pairs of kinks with opposite momenta. The kinks are generated at the same position, and then propagate freely in opposite directions. This fact can be observed in the time evolution of the two point connected correlators  $\langle \sigma_1^z \sigma_{1+m}^z \rangle_c$  (Fig. 8.6, top left panel): the spreading of the correlators in time follows a light-cone shape, indicating that kinks propagate freely, with velocities determined by their dispersion relation.

In the presence of a small longitudinal field  $h \neq 0$ , the light cone is seen only at very short times: then, the kinks are deviated by their linear interaction and the two point correlators seem to extend only up to a finite distance<sup>2</sup>. This effect signals the confinement of the pairs of kinks into mesons: the residual oscillations in time of the correlators can be interpreted

<sup>2</sup>A residual light cone is seen when zooming to smaller values of the correlators. This light cone is caused by pairs of mesons that propagate with opposite momenta. For small quenches, however, this effect is very weak. Note that, since  $|g| < J$ , correlations extend up to a distance that is smaller than the typical length for string breaking.

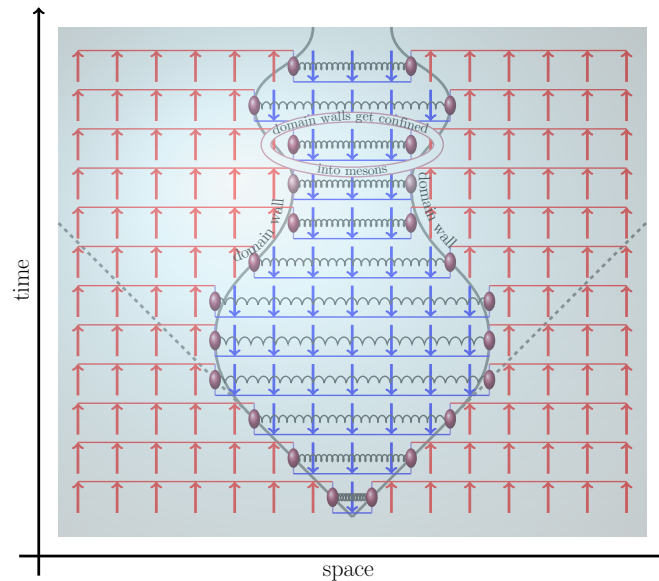


Figure 8.5: Illustration of the real-time dynamic following a quantum quench: a pair of domain walls created in the quench bounce back and forth because of confining interactions. Figure from [209].

as oscillations of the relative distance  $r$  between the kinks composing the mesons (Bloch oscillations). The suppression of the spreading of correlator signals that the eventual relaxation to thermal equilibrium would require extremely long time. This fact is also observed in the time evolution of the bipartite entanglement entropy [209]: the growth is linear for  $h = 0$ , while for  $h \neq 0$  it is significantly reduced and seems to saturate, with residual fluctuations due to the aforementioned Bloch oscillations.

## 8.4 Outlook

The non-equilibrium dynamics of systems with confinement is a topic that has recently witnessed growing interest from different communities and offers numerous prospects for future investigations.

On one side, many questions about the role of confinement in thermalization are still open. In Chapter 9 we estimate two lower bounds for the time scales involved in the dynamics. Does confinement inhibit the process which leads to thermal equilibrium, or do confined systems ultimately thermalize, but only after these very long times? One of the scenarios that has been proposed is that confinement in the quantum Ising model leads to nonthermal eigenstates, in both continuum and lattice theories, in one and two dimensions [210, 255]. The authors of these works claim that single meson states persist above the two-meson threshold, that they do not hybridize with the continuous spectrum and are analogous to quantum scars. The possibility of having scars induced by confinement is a fascinating one;

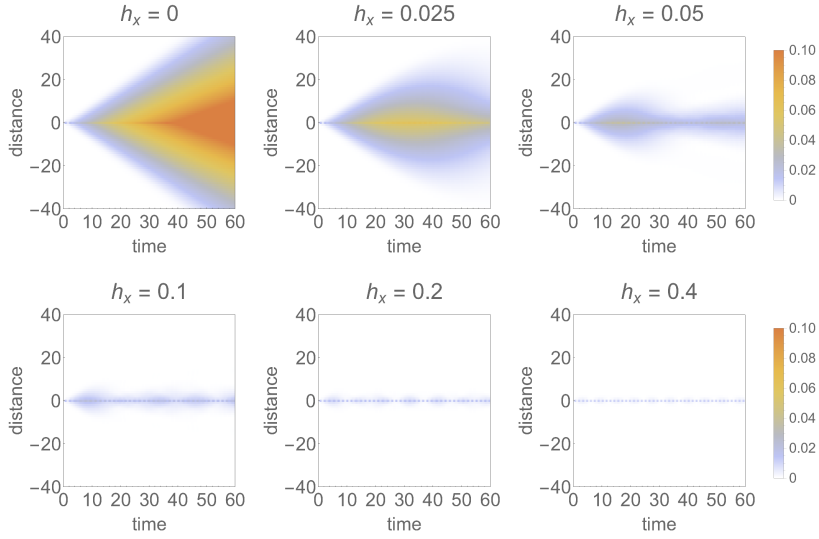


Figure 8.6: Connected correlators  $\langle \sigma_1^z \sigma_{1+m}^z \rangle_c$  after a quench from  $g = h = 0$  to the ferromagnetic phase with  $g = 0.25$  and with varying  $h = 0, 0.025, 0.05, 0.1, 0.2, 0.4$  ( $h_x$  corresponds to  $h$  in our notation). When  $h$  is increased, the light cone disappears and the spreading of correlations is suppressed. Figure from [209].

further studies on different confined models could help shed some light on this question.

On another side, an increasing effort is being put into studying confinement with quantum simulators. Since quantum simulators are particularly advantageous for studying real-time evolution, the dynamical properties of confinement make it an ideal physical phenomenon to investigate with these tools. Various experimental platforms can naturally support confined dynamics and can thus be used for quantum-simulation purposes. Trapped ions, for example, are one of the most suitable: there, confinement is intrinsically generated by long-range interactions, even in the absence of a longitudinal field [256, 262]. Another convenient platform is represented by Rydberg atoms, as demonstrated in Section 6.3.5.

Quantum simulators may be used to study the properties of mesons and baryons. For example, the masses of mesons can be measured with good accuracy from the power spectrum of one-point functions, with the so-called "quench spectroscopy" [209]. Moreover, the collisions of these composite objects are particularly interesting since they can lead to the generation of new particles via inelastic processes [7, 276, 277]. In Chapter 10 we show how scattering amplitudes can be computed in the quantum Ising chain and how they can be measured in general with a quantum simulator. Other non-equilibrium phenomena amenable to quantum simulation are related to the string-breaking effect introduced in Section 8.1.2 and include, for example, the decay of a metastable "false vacuum" state (see Chapter 11),

a phenomenon of primary interest in physical cosmology.

Notably, confinement is not the only physical phenomenon that leads to anomalous dynamics in lattice gauge theories: as discussed in Chapter 13, another mechanism, associated with the presence of static charges in the system, has been shown to induce MBL-like dynamics [10, 11, 208].

Finally, an important perspective for future research is represented by confinement and non-equilibrium dynamics in higher-dimensional systems. As shown in Chapter 12, quasi-one-dimensional systems already support a richer variety of confined excitations. For truly two-dimensional and three-dimensional systems, however, very little is known so far: on one side, extensive numerical simulations become prohibitive in more than one dimension; on the other side, the emergence of confinement in two or three dimensions is much less intuitive than in one dimension, and theoretical advances are significantly more difficult. In this context, quantum simulators could play a key role in helping us understand the emergence of confinement in higher dimensions and the real-time dynamics associated with it.

## Chapter 9

# Quasilocalized dynamics from confinement of quantum excitations

Several recent numerical studies of one-dimensional lattice gauge theories and quantum spin chains have found that confinement may give rise to anomalous real-time dynamics [4, 167, 187, 188, 190, 192, 193, 198, 207, 209, 211, 213, 254, 256, 264, 278–281] and spectral properties [210, 255, 261] at finite energy density above the ground state, in contrast with the generically expected thermalization [14, 19–21, 282–285]. The signatures of these phenomena include extraordinary long-lived coherent oscillations of local observables [190, 193, 209, 256, 278–280, 286], suppression of the light-cone spreading of quantum correlations [209, 256] and of the entanglement growth [192, 209, 256], and persistent inhomogeneities [4, 167, 188, 190, 192, 207, 211, 213, 281]. While these observations suggest that confinement is related to a suppression of thermalization, the nature of this connection has not yet been clarified.

In this work we investigate the relationship between the aforementioned dynamical effects of confinement and prototypical aspects of the localization of interacting particles [27–30, 287–303]. We demonstrate that confinement causes quasilocalized dynamics of states with dilute excitations. In fact, the route towards thermalization involves the decay of these states into entropically favored many-particle states: the energy stored in confining strings has to be converted into mass via the creation of new pairs of excitations from the vacuum. We show that these processes can become dramatically slow, in close analogy with the Schwinger effect, and with the suppressed decay of false vacua in quantum electrodynamics [304]. In this regime, fast spatial propagation of excitations is prevented by their Stark localization [305] in the mutual confining potentials. Remarkably, these two phenomena stabilize nonthermal behavior and low entanglement for extremely long times in a thermodynamically relevant portion of the many-body Hilbert space. This fact is illustrated in Fig. 9.1 for the case of the quantum Ising chain in

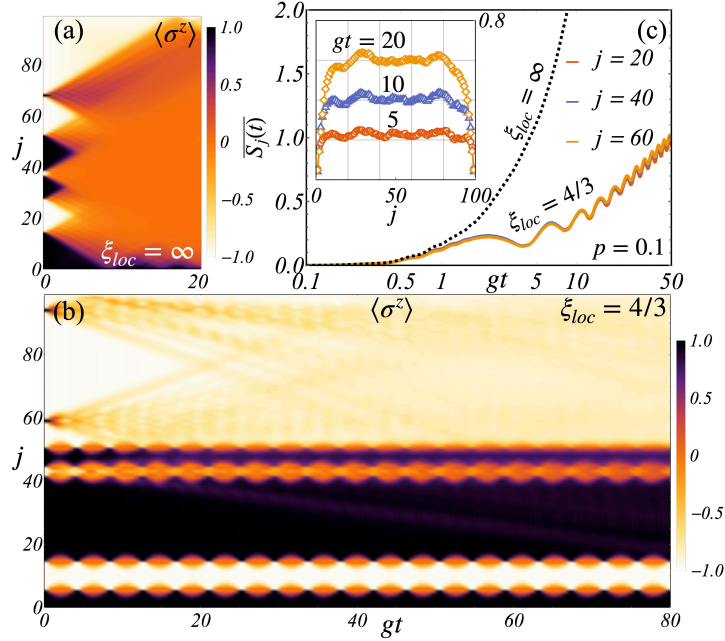


Figure 9.1: **Effects of confinement:** nonequilibrium evolution of the magnetization profile [panels (a) and (b)] and of entanglement (c) in a quantum Ising chain.  $L = 100$  spins are initialized in a random product state with a density  $p = 0.1$  of longitudinal domain-walls. The quantum evolution is simulated via the time-evolving block-decimation algorithm on matrix-product states with maximum bond dimension  $D=300$  [306]. The dynamics are generated by  $H$  in Eq. (9.1) with  $J = 5g$ , and (a)  $h = 0$ , (b)  $h = 0.75g$ . Panel (c): dynamics of the von Neumann entanglement entropy  $S_j(t)$  for different position  $j$  of the bipartition cut, averaged over 500 initial states.  $S_j(t)$  grows linearly in the deconfined limit (a),  $\xi_{loc} = \infty$  and logarithmically in the presence of confinement (b),  $\xi_{loc} = 4/3$ , as also emphasized by the inset. These qualitative features are unaltered upon varying the localization length  $\xi_{loc}$  while keeping  $p \lesssim 1/(2\xi_{loc})$  and  $J \gg |g|, |h|$ .

transverse and longitudinal field, introduced in Section 8.2.1, whose Hamiltonian we report here for convenience:

$$H = -J \sum_{j=1}^{L-1} \sigma_j^z \sigma_{j+1}^z - h \sum_{j=1}^L \sigma_j^z - g \sum_{j=1}^L \sigma_j^x, \quad (9.1)$$

In the absence of confinement ( $h = 0$ , Fig. 9.1 (a)), domain walls freely propagate, smoothening out all spatial inhomogeneities; in the presence of a confining potential ( $h \neq 0$ , Fig. 9.1 (b)), bound states of closeby domain walls diffuse (upper half of the plot), while isolated domain walls are Stark-localized by linear confining potentials, and perform coherent Bloch oscillations of spatial amplitude  $\xi_{\text{loc}} = g/h$  (lower half of the plot). In the following, we aim at characterizing this behaviour in a quantitative way and connecting it with the dynamics of the von Neumann entanglement entropy (Fig. 9.1 (c,d)).

## 9.1 Exponential suppression of string breaking

To illustrate the dynamics associated with string breaking in the quantum Ising chain, it is useful to exploit the exact mapping to a  $\mathbb{Z}_2$  lattice gauge theory explained in Section 8.2.2 (see Fig. 9.2). We report here the Hamiltonian:

$$H_{\mathbb{Z}_2} = m \sum_j c_j^\dagger c_j + \frac{\tau}{2} \sum_j \sigma_{j+1/2}^z + w \sum_j (c_j^\dagger - c_j) \sigma_{j+1/2}^x (c_{j+1} + c_{j+1}^\dagger), \quad (9.2)$$

where  $m = 2J$  is the fermion mass,  $\tau = -2h$  is the string tension of the gauge field, and  $w = -g$  is the interaction strength of fermions, mediated by gauge fields. Because of Gauss' law ( $G_x = \sigma_{j-1/2}^z \sigma_{j+1/2}^z (1 - 2n_j) = 1$ ), when two particles in the vacuum are adiabatically separated at a distance  $d$ , a gauge-field string has to extend between them. The energy  $E(d) \sim \tau d$  associated with the string grows proportionally to  $d$  and eventually overcomes the threshold  $E_{\text{min}} \sim 2m$  for the creation of a new pair.

We argue that the *dynamical* breaking of strings after a quench of the interactions takes anomalously long times for large values of the mass. The mechanism for this suppression may be essentially understood as a tunneling process across a high energy barrier. In fact, the decay process which converts the large amount of potential energy stored in long gauge-field strings into the energy of additional particle-antiparticle pairs is energetically allowed and entropically favorable, because a string state is very atypical compared to many-particle states with the same total energy. Accordingly, thermalization requires string breaking. However, due to the energy conservation, the created particle and antiparticle of a pair must be separated at such a distance  $d$  that the energy  $\tau d$  they subtract from the broken string portion equals their mass, i.e.,  $\tau d \sim 2m$ . If the string tension  $\tau$  is small

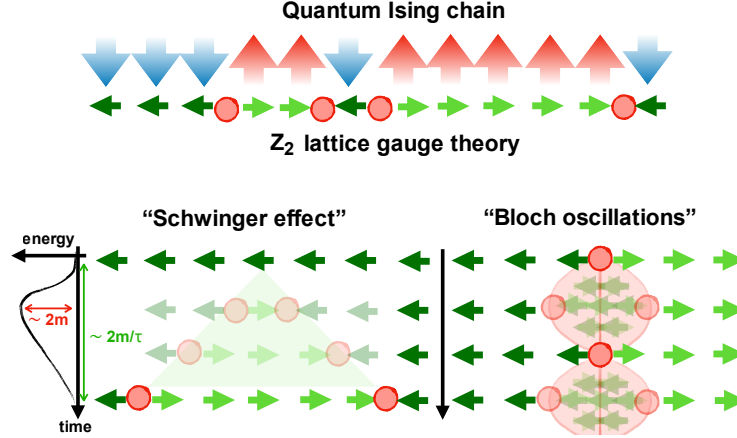


Figure 9.2: **Mapping between a quantum spin chain and a LGT:** Cartoon of the mapping of the quantum Ising chain in Eq. (9.1) onto the  $1 + 1$ -dimensional  $\mathbb{Z}_2$  lattice gauge theory in Eq. (9.2) (top), and of the two key mechanisms which render the resulting dynamics slow: suppression of false vacuum decay for weak coupling ("Schwinger effect", bottom left), and Stark-localization of particles in a linear potential ("Bloch oscillations", bottom right).

compared to the particle mass  $m$ , local pair creation is not possible, virtual particles have to tunnel across a distance  $d \sim 2m/\tau \gg 1$  in order for the string to decay — see the bottom left panel of Fig. 9.2 for an illustration (here the lattice spacing is the unit length). This occurs through increasingly high-order processes in the interactions, and hence the decay is extremely slow.

### 9.1.1 Perturbative construction

The above qualitative picture is made quantitative by constructing the effective Hamiltonian in perturbation theory in  $1/m$ . We formally split the Hamiltonian into the mass term (which corresponds to  $H_0 = -J \sum_j \sigma_j^z \sigma_{j+1}^z$  for the quantum Ising chain), possessing highly-degenerate blocks, and the rest  $V$ , which involves gauge field and interactions.  $H_0$  defines sectors of the Hilbert space labelled by the number of particles and well-separated in energy.  $V$  may contain block-diagonal matrix elements  $H_1$ , describing particle energy and motion, and block-off-diagonal ones  $R_1 = V - H_1$ , corresponding to particle pair creation or annihilation. The latter processes are eliminated through a unitary transformation  $e^{S_1}$ . For the quantum Ising chain, the resulting effective Hamiltonian is

$$H_{\text{eff}}^{(1)} = -J \sum_j \sigma_j^z \sigma_{j+1}^z - h \sum_j \sigma_j^z - g \sum_j (P_{j-1}^\dagger \sigma_j^x P_{j+1}^\dagger + P_{j-1}^\dagger \sigma_j^x P_{j+1}^\dagger), \quad (9.3)$$

where  $P_j^\uparrow$  ( $P_j^\downarrow$ ) projects onto the "up" ("down") state of the  $j$ -th spin along  $z$ .

This standard procedure [307–309] (often termed Schrieffer-Wolff transformation) can be carried out to any arbitrary order  $n$  in perturbation theory: One introduces higher-order terms  $S_2, S_3, \dots$  in the generator of the unitary transformation  $e^{S_{\leq n}}$ , with  $S_{\leq n} = -S_{\leq n}^\dagger = S_1 + S_2 + \dots + S_n$ . These terms are determined order by order in such a way that the transformed Hamiltonian commutes with  $H_0$  up to the  $n + 1$ -th power of the perturbation strength, i.e.,

$$H' = e^{S_{\leq n}} H e^{-S_{\leq n}} = H_{\text{eff}}^{(n)} + V_{>n}, \quad H_{\text{eff}}^{(n)} \equiv H_0 + H_1 + \dots + H_n, \quad (9.4)$$

with  $[H_j, H_0] = 0$  (see Appendix C.2 for details). The effective Hamiltonian  $H_{\text{eff}}^{(n)}$  preserves the block-diagonal structure of  $H_0$  and accounts for all transitions within each sector of  $H_0$  occurring through up to  $n$  intermediate transitions involving states in different blocks (*virtual* particle pairs). The perturbative series generated by this transformation are generally divergent at finite energy density, pointing to an asymptotic hybridization of the various blocks and hence thermalization. However, by adapting the rigorous theory in Ref. [310], one finds that by truncating the series at an "optimal order"  $n^*$  that scales linearly with the particle mass  $m$ , the rest  $V_{>n^*}$  can be made *exponentially* small in  $m$ . Consequently, the effect of the latter can be neglected for exponentially long times. Denoting  $H_{\text{eff}}^{(n^*)} \equiv H_{\text{eff}}$  and  $S_{\leq n^*} \equiv S$ , the nonequilibrium evolution of the system is accurately described by

$$|\Psi(t)\rangle \simeq e^{-S} e^{-itH_{\text{eff}}} e^S |\Psi(t=0)\rangle. \quad (9.5)$$

### 9.1.2 Time scale

Within this transformed picture, the number of particles is exactly conserved by  $H_{\text{eff}}$ , and hence it is approximately conserved by  $H$  in the original picture at least for exponentially long times. This implies that the bulk of a long gauge string is stable against pair creation, since the "string-breaking" (or "vacuum-decay") time scale is exponentially long in  $m$ . In Appendix C we provide the details of the construction of  $H_{\text{eff}}$  in general and for the specific case of the quantum Ising chain. For that model, for  $J \gg |g|, |h|$  the estimates adapted from Refs. [310–313] lead to the quasiconservation of the spatial density of domain-walls at times  $t \ll T_{\text{sb}}$ , where

$$T_{\text{sb}} \geq |g|^{-1} \exp\left(\text{const} \times J/\sqrt{h^2 + g^2}\right), \quad (9.6)$$

and the constant is independent of the parameters (see Appendix C.2).

This bulk stability persists in the continuum limit [232], and, within the mapping to a LGT, it is reminiscent of the Schwinger effect in quantum electrodynamics [304], in that the decay rate  $\Gamma(\mathcal{E})$  per unit volume of a

false vacuum in the presence of a background electric field  $\mathcal{E}$  into particle pairs, is exponentially small in the ratio between the electron mass  $m$  and the electrostatic energy  $|e\mathcal{E}| \times 1/m$  contained within a Compton length, i.e.,  $\Gamma(\mathcal{E}) \propto (e\mathcal{E})^2 \exp\left(-\frac{\pi m^2}{|e\mathcal{E}|}\right)$ , where  $e$  is the electron charge and  $\hbar = c = 1$  [304, 314].

## 9.2 Prethermalization and Stark localization

The nonequilibrium dynamics starting from a generic initial state may be expected to undergo *prethermalization* to the Gibbs ensemble  $e^{-\beta H_{\text{eff}}}/Z$  defined by the effective (nonintegrable) Hamiltonian  $H_{\text{eff}}$  discussed above, at the inverse temperature  $\beta$  uniquely determined by the energy density of the initial state [205, 310]. Contrarily to this expectation, we demonstrate that the combination of confinement and lattice effects leads to a dramatic slowdown of prethermalization in a thermodynamically significant portion of the many-body Hilbert space. This phenomenon is due to the Stark localization of particles [305] in their mutual linear confining potential, which suppresses spatial propagation and energy transport for *arbitrary* interaction strength  $g$ .

We consider below many-particles states, with a diluteness parameter  $p$ , i.e., with an average separation of  $1/p$  lattice sites between consecutive particles. To disentangle the effect of having a finite particle mass — leading to exponentially slow pair creation — from the intrinsic slow dynamics of  $H_{\text{eff}}$ , we analyze the nonequilibrium dynamics generated by the latter truncated at the lowest order. The effective picture consists of a system of hopping hardcore particles in a constant electric field, subject to interactions. Higher-order terms in  $H_{\text{eff}}$  do not alter the physics qualitatively, as they just renormalize the hopping amplitudes with small longer-range terms (see Appendix C.2).

### 9.2.1 Two-body effective model and delocalization time

In the extremely dilute limit  $p \ll 1$  the system consists of isolated particles moving in a linear potential, a so-called Wannier-Stark ladder. This problem can be solved exactly [315]: eigenstates are product states of localized orbitals with equispaced energy levels  $\mathcal{E}_n \propto n$ . For the  $\mathbb{Z}_2$  LGT in Eq. (9.2),  $\mathcal{E}_n = \tau n$  and the localized wavefunction centered around the site  $n$  has the form  $\mathcal{J}_{n-j}(2w/\tau)$ , where  $\mathcal{J}_\nu$  is the Bessel function of order  $\nu$ . The tails of this localized orbitals decay faster than exponentially for  $|n-j| \gg g/h = 2w/\tau \equiv \xi_{\text{loc}}$ . If the distance between consecutive particles is much larger than  $\xi_{\text{loc}}$ , transport and thermalization are suppressed, and particles perform coherent (Bloch) oscillations around their initial position, with spatial amplitude  $\xi_{\text{loc}}$  and temporal period  $\pi/h$  [207].

Delocalization gradually occurs as  $\ell = 1/p$  is made comparable with twice the localization length  $2\xi_{\text{loc}}$ . To understand this phenomenon and the associated time scales, we consider an isolated string with a particle at site  $j_1$  and another particle at site  $j_2 > j_1$ .

The effective Hamiltonian in the two-particle sector reads

$$H_{2\text{-body}} = \sum_{j_1 < j_2} \tau(j_2 - j_1) |j_1, j_2\rangle \langle j_1, j_2| + w \left( |j_1 + 1, j_2\rangle \langle j_1, j_2| + |j_1, j_2 + 1\rangle \langle j_1, j_2| + \text{H.c.} \right).$$

This Hamiltonian is the lowest-order effective model in the limit of infinite particle mass  $m^1$ .

The meson wavefunctions and dispersion relations can be solved explicitly [6, 316] by switching to the center-of-mass and relative variables,  $s = j_1 + j_2$ ,  $r = j_2 - j_1 > 0$ . Substituting the ansatz

$$|\psi_k\rangle = \sum_{j_1 < j_2} \psi_k(j_1 + j_2, j_2 - j_1) |j_1, j_2\rangle \quad \psi_k(s, r) = e^{iks} \phi_k(r) \quad (9.7)$$

into the Schroedinger equation, we get a Wannier-Stark equation for the reduced wavefunction  $\phi_k(r)$ ,

$$\tilde{w}_k [\phi_k(r + 1) + \phi_k(r - 1)] + \tau r \phi_k(r) = \mathcal{E} \phi_k(r) \quad (9.8)$$

with an effective hopping  $\tilde{w}_k = 2w \cos k$  and, crucially, the boundary condition  $\phi_k(0) \equiv 0$  due to Pauli exclusion. This equation is equivalent to the recursion relation of the Bessel functions:

$$\phi_k(r) = \mathcal{J}_{r-\mathcal{E}/\tau}(2\tilde{w}_k/\tau). \quad (9.9)$$

The boundary condition  $\mathcal{J}_{-\mathcal{E}/\tau}(2\tilde{w}_k/\tau) = 0$  yields the quantization rule

$$\mathcal{E} = \mathcal{E}_\ell(k) = \tau \nu_\ell(2\tilde{w}_k/\tau) \equiv -\tau \times \{\ell\text{-th zero of } x \mapsto \mathcal{J}_x(2\tilde{w}_k/\tau)\} \quad (9.10)$$

for  $\ell = 1, 2, \dots$ . Therefore, the solution consists of a discrete sequence of two-particle bound states ("mesons") labelled by  $\ell = 1, 2, \dots$  with dispersion relations  $\mathcal{E}_\ell(k)$ . The meson wavefunctions are thus

$$\psi_{\ell,k}(s, r) = e^{iks} \mathcal{J}_{r-\nu_\ell}(2\tilde{w}_k/\tau). \quad (9.11)$$

<sup>1</sup>A large but finite fermion mass  $m$  only produces a perturbative dressing of the vacuum and of mesons, which can be explicitly computed order by order via the Schrieffer-Wolff transformation in Section 9.1.1 and in Appendix C.2 (for instance, the first correction involves next-nearest-neighbor fermion hopping with amplitude  $w^2/2m$ ). Using this approach, the large- $m$  analysis of meson dynamics can be systematically modified to achieve the desired accuracy for large but finite  $m$ . Thus, for simplicity, here we will focus on the limit of large fermion mass; for more details on finite- $m$  effects, see also C.6.

The wavefunctions with  $\ell \gg 2\xi_{\text{loc}}$  are localized far away from the boundary  $r = 0$ : they are hardly affected by it, and hence their energy  $\mathcal{E}_\ell = \tau\ell$  is independent of  $k$ . This implies that spatially extended bound states have asymptotically flat bands: the two particles perform uncorrelated Bloch oscillations at the edges of the string connecting them, while the quantum diffusion of their center of mass is suppressed. On the contrary, for bound states with an extension comparable to that of the Bloch oscillations, the presence of the boundary bends the dispersion relation  $\mathcal{E}_\ell(k)$ . The correction  $\delta\mathcal{E}_\ell(k)$  in the dilute regime  $\ell \gtrsim 2\xi_{\text{loc}}$  is found to be approximately (see Appendix C.3)

$$\delta\mathcal{E}_\ell(k) \simeq -2|w| \cos k \mathcal{J}_\ell(2\xi_{\text{loc}} \cos k) \mathcal{J}_{\ell-1}(2\xi_{\text{loc}} \cos k). \quad (9.12)$$

From the spreading velocities  $v_\ell^{\text{max}} = \text{Max}_k |\partial_k \mathcal{E}_\ell(k)|$  of bound states of quantum number  $\ell$ , we can then estimate the delocalization time scale  $T_{\text{dloc}}(\ell, \xi_{\text{loc}})$ . For large  $\ell \gtrsim \xi_{\text{loc}}^2$ , one has

$$T_{\text{dloc}}(\ell, \xi_{\text{loc}}) \sim |w|^{-1} (\ell!)^2 \ell^{-3/2} \xi_{\text{loc}}^{-2\ell+1}. \quad (9.13)$$

As a result of the rapid increasing of  $T_{\text{dloc}}$  with  $\ell$ , pairs of distant particles take an extremely long time to delocalize. The typical delocalization time scale is thus state-dependent via the diluteness parameter  $p$  (unlike the string-breaking time scale  $T_{\text{sb}}$  in Eq. (9.6)). We stress that the above equations are nonperturbative in  $2w/\tau = g/h = \xi_{\text{loc}}$  and hence valid for arbitrarily large values of this ratio.

### 9.3 Slow entanglement growth

The scenario outlined above sheds light on the effects of confinement on the nonequilibrium evolution of entanglement. While the entanglement entropy  $S(t)$  is expected to increase linearly in time in generic quantum many-body systems which dynamically relax to equilibrium [317–323], the quasilocalization discussed above is expected to cause a severe suppression of the growth of  $S(t)$  despite the finite energy density, in analogy with disordered and glassy quantum systems [30, 208, 287, 288, 290, 295, 298–300, 324, 325]. This expectation is confirmed by numerical simulations using the time-evolving-block-decimation (TEBD) algorithm on matrix-product states [306], with maximum bond dimension  $D = 300$ . In particular, we initialize a quantum Ising chain of  $L = 100$  spins in nonentangled product states with a spatial density  $p$  of domain-walls: in Fig. 9.1 these states are drawn from a thermal ensemble  $\rho_0 = e^{-\mu H_0}/Z$  of the "unperturbed" classical Ising chain with  $p = [1 - \tanh(\mu J)]/2$ . (Similar dilute states with tuneable  $p$  can be experimentally realized via the quantum Kibble-Zurek mechanism [103, 326]). The numerical results reported in Fig. 9.1 are compatible with a logarithmic growth of the bipartite entanglement entropy  $S_j(t)$  superimposed to

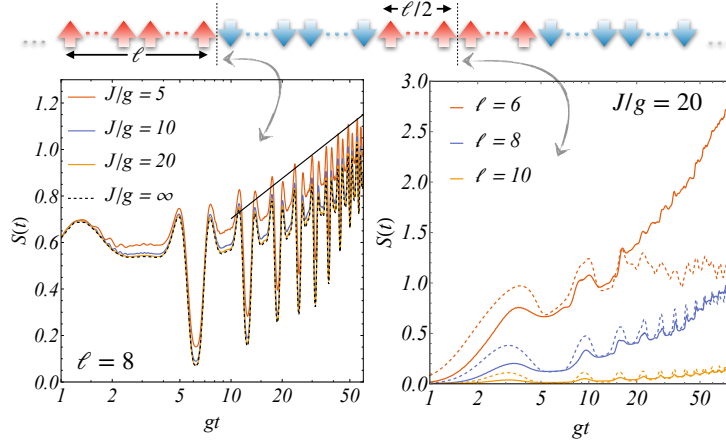


Figure 9.3: **Signatures of slow dynamics:** growth of the von Neumann entanglement entropy  $S(t)$  in the nonequilibrium dynamics of the quantum Ising chain in Eq. (8.2), numerically simulated via the TEBD algorithm, starting from a state with equally spaced domain-walls at a distance  $\ell$ ; the cartoon above the plots indicates the position of the bipartition cuts along the chain. Left:  $S(t)$  exhibits pronounced coherent oscillations with frequency  $2h$  superimposed to a slow growth (the straight line is a guide for the eye). Right: The growth of  $S(t)$  slows down upon increasing the diluteness. Dotted lines represent the growth of  $S(t)$  in the evolution of a single isolated string formed by the two domain-walls adjacent to the cut. The latter can be obtained analytically (see Appendix C.3), is upper-bounded by  $\log \ell + \text{const}$ , and reaches its maximum around the time  $T_{\text{dloc}}$ , cf. Eq. (9.13). Parameters:  $\xi_{\text{loc}} = 2$ ,  $L = 120$ .

coherent oscillations of period  $\pi/h$ , ascribed to Bloch oscillations. In Fig. 9.3, instead, regularly arranged initial states are considered with equispaced domain-walls at a distance  $\ell = 1/p$  and  $L = 120$ . The fast convergence of  $S(t)$  to that generated by the effective Hamiltonian  $H_{\text{eff}}$  upon increasing  $J$  (Fig. 9.3, left panel) leads us to rule out the hypothesis that the slow vacuum decay is responsible for the entanglement growth. Furthermore, the bottom right panel of Fig. 9.3 shows that the initial growth of  $S(t)$  is captured by the delocalization of individual strings described in Eq. (9.13) above; however, at longer times, many-particle effects lead to a slow unbounded growth.

## 9.4 Outlook

In the framework of localization phenomena in disorder-free quantum systems [292–303, 327, 328], this work establishes the role of confinement as a robust mechanism capable of dramatically slowing down the approach to equilibrium [4, 198, 207–209, 256, 264, 281, 325, 329]. It is interesting to

highlight the connection with the recently proposed "Stark many-body localization" [87, 98, 302, 303], in that the effective dynamics of the systems considered in the present work may be viewed as that of interacting particles in a constant field. Our preliminary numerical results suggest that rare high-density regions embedded in dilute systems do *not* thermalize the rest of the system within the relevant time scales in this work; however, a complete analysis of this problem and of the various stages of the dynamics [257] calls for further investigations which we leave to future studies.

Our discussion applies to generic one-dimensional lattice models with confined excitations, including Abelian and non-Abelian LGTs [139, 192, 330]. The extension of our work to confining theories in higher dimensions stands as a challenging direction for future work, inasmuch as their real-time dynamics has hardly been explored in the framework of nonequilibrium statistical mechanics.

# Chapter 10

## Scattering of mesons

A challenging problem in high-energy physics is simulating collisions of complex composite particles. In quantum chromodynamics (QCD), a first-principle estimation of the distribution of particles produced by hadron scattering would facilitate the search for new physics beyond the Standard Model; moreover, heavy-ion collisions provide fundamental information on the deconfinement transition and on the early Universe evolution [331]. Although simulating higher-dimensional non-Abelian gauge theories represents a long-term goal, it is of great interest to understand whether quantum simulators are already capable of studying the scattering of composite particles in a strong-coupling regime, at least in simplified settings. Lower-dimensional gauge theories [189, 332] exhibit a tractable version of particle confinement leading to an analog of quark-antiquark bound states (*mesons*). Real-time dynamics of variants of these models witnessed recent developments in both classical [192, 333] and quantum [4, 166, 179, 262] simulations, opening the door to investigations of the simplest instances of collisions between complex structured objects arising from confinement.

In this Chapter, we demonstrate that present-day quantum simulators allow to investigate selected meson collisions in  $1 + 1$ -dimensional Abelian lattice gauge theories (LGTs), as sketched in Fig. 10.1, mimicking scattering experiments with particle accelerators. Quantum simulators offer unprecedented access to full real-time resolution of a complex collision event and to the quantum correlations thereby generated. Here, we particularly focus on the production of new mesonic species, i.e., *inelastic* events redistributing internal and kinetic energies of mesons emerging from the collision. We propose protocols to experimentally observe this with current facilities, and provide a benchmark theoretical study of scattering amplitudes. While we consider a controlled regime where exact numerical simulations can be pushed and compared with analytical results, quantum simulators may explore conditions inaccessible to traditional methods, including the continuum limit of quantum field theories.

The Chapter is organized as follows. In Sec. 10.1, we introduce the  $\mathbb{Z}_2$ -LGT analyzed throughout, and discuss particle confinement and the re-

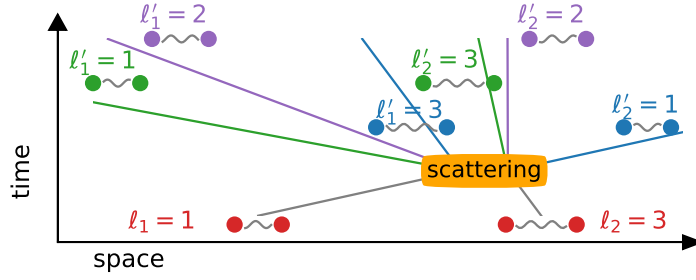


Figure 10.1: Sketch of a scattering event: The collision of two incoming mesons with internal quantum numbers  $\ell_1, \ell_2$  generates a superposition of several possible outcomes, labelled by the quantum numbers of outgoing mesons.

sulting mesonic spectra and wavefunctions in the regime of large particle mass. In Sec. 10.2, we present a theoretical study of meson-meson scattering amplitudes, based on an exact solution of the Schrödinger equation. We discuss elastic and inelastic processes, and benchmark the results against numerical simulations. Finally, in Sec. 10.3, we propose concrete protocols to prepare, simulate and observe meson scattering with present-day quantum simulators (e.g., Rydberg-atom arrays). Appendix C contains various additional details on the discussion and computations in this Chapter: in Section C.4 we consider the effective model in the 4-particle sectors and we describe a method to construct the solutions of the scattering problem in the limit of large fermion mass; in Section C.5 we derive the analytic expression of the meson current, we discuss its physical meaning and we prove the associated continuity equation; in Section C.6 we summarize and discuss the effects of having a finite fermion mass.

## 10.1 Confinement and mesons

In this work we will be concerned with  $(1 + 1)$ -dimensional models with confinement of the type discussed in Section 8.2. For the sake of definiteness, we will focus on the  $\mathbb{Z}_2$ -LGT in Eq. (8.3). For convenience, we report here the Hamiltonian and we summarize the main properties of the model:

$$H = m \sum_j c_j^\dagger c_j + \frac{\tau}{2} \sum_j \sigma_{j+1/2}^z + w \sum_j (c_j^\dagger - c_j) \sigma_{j+1/2}^x (c_{j+1} + c_{j+1}^\dagger). \quad (10.1)$$

In this equation,  $c_j^\dagger$  and  $c_j$  denote creation and annihilation operators of spinless fermions of mass  $m > 0$  on the sites  $j \in \mathbb{Z}$  of a one-dimensional lattice, and  $\sigma_b^{x,y,z}$  denote spin-1/2 operators (Pauli matrices) acting on the bonds  $b \in \mathbb{Z} + 1/2$  of the lattice, representing a gauge field with string tension  $\tau$ . Interactions, with coupling strength  $w$ , are such that all the local operators  $G_j = \sigma_{j-1/2}^z \sigma_{j+1/2}^z (1 - 2c_j^\dagger c_j)$  are conserved, i.e.,  $[G_j, H] = 0$ .

These operators satisfy  $G_j^2 \equiv 1$  and thus generate local  $\mathbb{Z}_2$  symmetries. Here we focus on the neutral gauge sector, i.e., the subspace characterized by  $G_j|\psi\rangle = |\psi\rangle$  for all  $j$ .

The LGT in Eq. (10.1) exhibits particle confinement for  $m > 2|w|$ ,  $\tau \neq 0$ . By gauge invariance, a string of excited gauge field extends between two charges created out of the vacuum, inducing a confining potential  $V(r) \propto r$  that grows unbounded at large distances  $r$ . Thus, the excitations form a discrete tower of *neutral*<sup>1</sup> bound states (termed *mesons*, in analogy with QCD), labelled by their internal quantum number  $\ell = 1, 2, \dots$  and their center-of-mass momentum  $k$ .

As shown in Section 9.2.1, in the large- $m$  limit, mesonic spectra  $\mathcal{E}_\ell(k)$  and wavefunctions  $\psi_{\ell,k}(j_1, j_2)$  can be determined exactly by solving the reduced two-body problem, governed by the projection of  $H$  in Eq. (10.1) onto the two-fermion sector spanned by states  $\{|j_1 < j_2\rangle\}$  (labelled by the positions of the two fermions along the chain). For definiteness, we assume  $\tau > 0$  from now on. The exact solution [6, 316] yields the quantized mesonic spectra

$$\mathcal{E}_\ell(k) = \tau \nu_\ell(2\tilde{w}_k/\tau) \quad (10.2)$$

with  $\ell = 1, 2, \dots$ ,  $\tilde{w}_k = 2w \cos k$ ,  $k \in [-\pi/2, \pi/2)$ , and  $\nu_\ell(x)$  is the  $\ell$ -th (real) zero of the map  $a \mapsto \mathcal{J}_a(x)$ , where  $\mathcal{J}_a(x)$  is the Bessel function<sup>2</sup>. The associated mesonic wavefunctions read

$$\psi_{\ell,k}(s, r) = e^{iks} \mathcal{J}_{r-\nu_\ell(2\tilde{w}_k/\tau)}(2\tilde{w}_k/\tau). \quad (10.3)$$

As an example, Fig. 10.3-(a) reports a plot of the lowest mesonic spectra  $\ell = 1, 2, 3$  for  $w/\tau = 0.6$ .

## 10.2 Scattering amplitudes

We first provide a theoretical analysis of meson-meson scattering. We present an exact solution of the problem in the regime of large fermion mass  $m$ . The predictions of elastic and inelastic cross section peaks, together with our numerical simulations, provide a non-trivial benchmark for quantum simulations. While our solution is valid for arbitrary coupling strength  $w/\tau$  and arbitrary incoming states, quantum simulations turn out to be easiest for  $w/\tau \approx 1$  and low mesonic quantum numbers, as discussed below.

Armed with the mesonic spectra  $\mathcal{E}_\ell(k)$ , we consider the scattering of two incoming mesons with quantum numbers  $\ell_{1,2}$ , approaching each other with

<sup>1</sup>Note that the  $\mathbb{Z}_2$ -charge is defined modulo 2, i.e., particle and antiparticle are the same object, so a two-fermion bound state is neutral.

<sup>2</sup>The momenta  $k$  and  $k + \pi$  generate the same solution up to a phase: Since  $\mathcal{J}_\alpha(-z) = e^{i\pi\alpha} \mathcal{J}_\alpha(z)$ , when  $k \mapsto k + \pi$  the wavefunction  $\Psi$  gets multiplied by  $(-)^s e^{i\pi(r-\nu_n)} = e^{-i\pi\nu_n} (-)^{2j_2} = e^{-i\pi\nu_n}$ , i.e., a global phase.

definite momenta  $k_{1,2}$ . The open elastic and inelastic scattering channels can be found by a kinematic analysis, which consists in determining the set of the outgoing quantum numbers  $\{(\ell'_1, k'_1), (\ell'_2, k'_2)\}$  compatible with the incoming ones by conservation of total energy and momentum:

$$\begin{cases} E \equiv \mathcal{E}_{\ell_1}(k_1) + \mathcal{E}_{\ell_2}(k_2) = \mathcal{E}_{\ell'_1}(k'_1) + \mathcal{E}_{\ell'_2}(k'_2), \\ K \equiv k_1 + k_2 = k'_1 + k'_2 \pmod{\pi}. \end{cases} \quad (10.4)$$

For all choices of incoming states, there always exist two elastic solutions, called *transmitted* and *reflected*, having  $(\ell'_1, \ell'_2) = (\ell_2, \ell_1)$  and  $(\ell_1, \ell_2)$  respectively. The existence of inelastic channels, instead, is not guaranteed for generic incoming states<sup>3</sup>.

The conservation of the number of fermions allows to derive a continuity equation, which defines an associated mesonic current, as derived in C.5. The conservation of the total current across the collision yields a constraint on the scattering amplitudes of open channels. The fraction associated with each outgoing asymptotic solution has the physical meaning of a total cross section, as it can be identified with the probability  $P_{\ell'_1, \ell'_2}$  of detecting that particular scattering outcome in the asymptotic future [334].

Determining the scattering amplitudes and cross sections requires solving the four-fermion Schrödinger equation. We thus consider the effective Hamiltonian  $H_{4\text{-body}}$  for the four-body problem, i.e., Eq. (10.1) projected to the four-fermion subspace spanned by the states  $\{|j_1 < j_2 < j_3 < j_4\rangle\}$ . This consists of the hopping terms of amplitude  $w$  for the four particles, and the two diagonal confining pairwise potentials  $\tau(j_2 - j_1)$  and  $\tau(j_4 - j_3)$ . We formulate the ansatz  $\psi_{\ell_1, q}(s_1, r_1)\psi_{\ell_2, K-q}(s_2, r_2)$ , where  $r_{1,2}, s_{1,2}$  are the relative distance and the center-of-mass position for the two mesons, the single-meson wavefunctions  $\psi$  are defined as in Eq. (10.3), but, crucially, the momentum  $q \in \mathbb{C}$  is allowed to span the complex plane. The ansatz above represents an admissible asymptotic solution, provided  $q \in \mathbb{C}$  satisfies the *complex* energy condition

$$\nu_{\ell_1}(2\tilde{w}_q/\tau) + \nu_{\ell_2}(2\tilde{w}_{K-q}/\tau) = E/\tau, \quad (10.5)$$

where the total energy  $E$  and momentum  $K$  are determined by the incoming state  $\{(\ell_1, k_1 = q_{\text{in}}), (\ell_2, k_2 = K - q_{\text{in}})\}$ , with  $q_{\text{in}} \in \mathbb{R}$ , and  $\nu_{\ell}(w)$  is here a complex zero of the analytic function  $z \mapsto \mathcal{J}_z(w)$ , labelled by  $\ell \in \mathbb{N}$ . We index by  $\alpha \in \mathbb{N}$  all the triplets  $(\ell_1^\alpha, \ell_2^\alpha, q_\alpha)$  which satisfy Eq. 10.5. For a given incoming state, the exact solution  $\Psi$  of the scattering problem is expressed by a linear superposition including the incoming state and all compatible

<sup>3</sup>For intermediate ratios  $\tau/w$  (a condition that best suits experiments, see below), it can be seen that inelastic channels are favoured when at least one incoming meson is “heavy”, i.e.,  $\ell_2 > 1$ . The reason is that, for sufficiently small  $w/\tau$ , the sum of the quantum numbers  $\ell_1 + \ell_2$  is conserved in the scattering. This is a consequence of the conservation of the total energy and of the fact that  $\mathcal{E}(\ell, k) \simeq \tau\ell$  in this limit. The example in Fig. 10.3 comprises an inelastic channel  $(\ell_1, \ell_2) = (1, 3) \rightarrow (\ell'_1, \ell'_2) = (2, 2)$ .

*outgoing* (i.e., with outgoing currents) and *evanescent* (i.e., with  $\Im \mathbf{m}(q) < 0$ ) asymptotic solutions:

$$\begin{aligned} \Psi(s_1, r_1, s_2, r_2) &= \psi_{\ell_1, k_1}(s_1, r_1) \psi_{\ell_2, k_2}(s_2, r_2) \\ &+ \sum_{\alpha} A_{\alpha} \psi_{\ell_1, q_{\alpha}}(s_1, r_1) \psi_{\ell_2, K - q_{\alpha}}(s_2, r_2). \end{aligned} \quad (10.6)$$

The wavefunction  $\Psi$  solves the Schrödinger equation in the full region  $j_3 - j_2 = (s_2 - s_1 - r_1 - r_2)/2 > 0$ <sup>4</sup>. Due to Pauli exclusion at  $j_2 = j_3$ , the equation forces the boundary condition  $\Psi|_{s_2 - s_1 - r_1 - r_2 = 0} \equiv 0$ , which determines the coefficients  $A_{\alpha}$ , including the scattering amplitudes of open channels. In fact, this condition gives rise to an infinite set of inhomogeneous linear equations on varying  $r_{1,2} = 1, 2, \dots$  for the infinitely many unknowns  $A_1, A_2, \dots$ . The very nature of confinement, though, provides a natural truncation for this hierarchy: For  $q_{\alpha} \in \mathbb{R}$ , the meson wavefunctions are bound states, and thus fall off rapidly for large distances; for complex solutions  $q_{\alpha} \notin \mathbb{R}$ , the normalizability condition  $\Im \mathbf{m}(q) < 0$  guarantees exponential decay. Thus, asymptotic solutions with high mesonic quantum numbers  $\ell' \gg \ell_{1,2}$  have tiny amplitudes, and their contribution is effectively redundant. For more details, see C.4.

In Fig. 10.2 we plot the cross sections  $P_{\ell_1, \ell_2}$  computed as described above, as a function of the incoming momenta  $k_1, k_2$ , for the scattering  $(1, 3) \rightarrow (\ell'_1, \ell'_2)$  when  $w/\tau = 0.6$ .

The scattering amplitudes can be readily connected with the products of real-time wavepacket collisions. We verify this by numerically computing instances of the exact time evolution within the four-body subspace. We consider the example in Fig. 10.1: In a system with  $L = 36$  fermionic sites, we prepare two Gaussian wavepackets

$$\Psi(s_1, s_2, r_1, r_2; t = 0) = e^{-[(s_1 - s_1^0)^2 + (s_2 - s_2^0)^2]/8\sigma^2} \psi_{\ell_1, k_1^0}(s_1, r_1) \psi_{\ell_2, k_2^0}(s_2, r_2) \quad (10.7)$$

of the meson wavefunctions in Eq. (10.3) with  $\ell_1 = 1$ ,  $\ell_2 = 3$ , centered around momenta  $k_1^0 = 1.3$ ,  $k_2^0 = -0.4$  and positions  $s_1^0 = 24$ ,  $s_2^0 = 48$ , with envelopes of width  $\sigma = 3\sqrt{2}$  lattice sites. Time evolution from this initial state is generated by the four-body Hamiltonian  $H_{4\text{-body}}$  with  $\tau = 1$ ,  $w = 0.6$ . The final state at time  $t_f = 50$  is examined, when the wavepackets have collided and the products of the collision have not yet reached the boundary of the system. The energy and momentum of the incoming and outgoing states are represented in Fig. 10.3-(a). In Fig. 10.3-(b) and (c) we plot the joint probability distribution of the momenta  $k_1, k_2$  at times  $t = 0$  and  $t = t_f$ , respectively, obtained via the Fourier transform of  $\Psi(s_1, s_2, r_1, r_2; t)$  with respect to the center-of-mass positions  $s_{1,2}$ . While the initial state shows a single density peak at  $(k_1^0, k_2^0)$ , the final state gives three different

<sup>4</sup>The additional conditions  $j_2 - j_1 = r_1 > 0$ ,  $j_4 - j_3 = r_2 > 0$  are automatically satisfied by the ansatz.

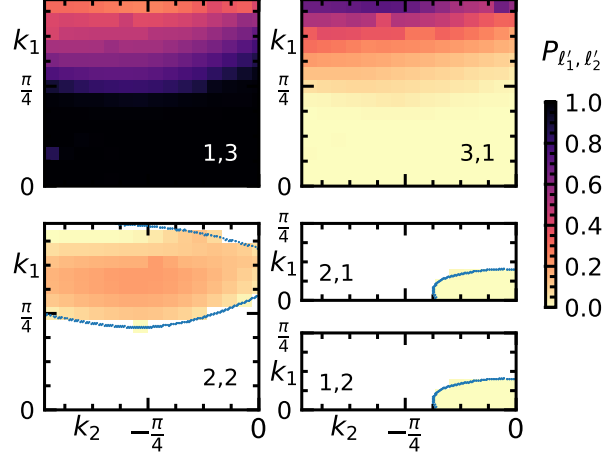


Figure 10.2: Probabilities of the various scattering channels  $(1, 3) \rightarrow (\ell'_1, \ell'_2)$  as a function of the incoming momenta, for  $w/\tau = 0.6$ . The blue lines delimit the regions where the inelastic channels  $(2, 2)$ ,  $(1, 2)$ ,  $(2, 1)$  are open. The probabilities of the channels plotted in the five panels sum up to one with good precision [small deviations from this value are shown in Fig. C.5-(b)].

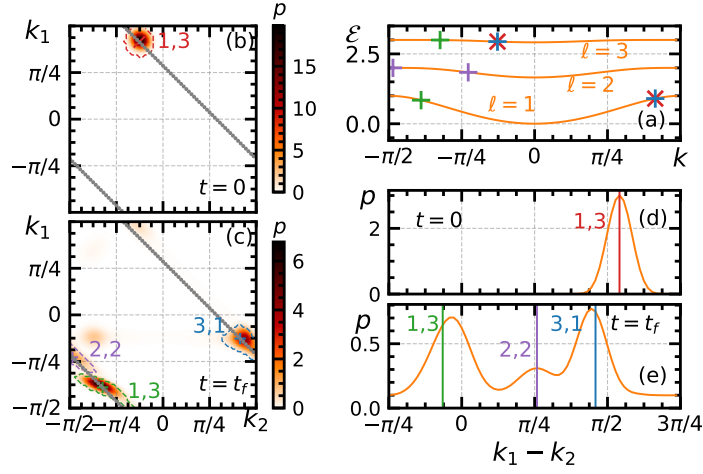


Figure 10.3: Mesonic wavepackets collision. (a) Spectra  $\mathcal{E}_\ell(k)$  of the lightest mesons for the  $\mathbb{Z}_2$ -LGT in Eq. (10.1) with  $\tau = 1$ ,  $w = 0.6$  and  $m \gg \tau$ . The crosses indicate the momenta and energies of the two mesons in the incoming (red) and outgoing (purple, blue, green) states. (b-e) Probability density of the meson momenta  $p(k_1, k_2)$  (b,c) and of the relative momentum  $p(k_1 - k_2)$  (d,e) at time  $t = 0$  (b,d) and  $t = t_f = 50$  (c,e). The dashed contours in panel (c) mark the regions  $p > 0.25$ .

density peaks, all lying on the line  $k_1 + k_2 = k_1^0 + k_2^0 \bmod \pi$ , demonstrating the conservation of total momentum. The three peaks correspond to the channels predicted from the kinematic analysis [the crosses in Fig. 10.3-(a)]:

one for the transmitted solution  $(\ell'_1, \ell'_2) = (3, 1)$  (with  $k_1 = -0.4$ ,  $k_2 = 1.3$ ), one for the reflected solution  $(1, 3)$  ( $k_1 \simeq -1.0$ ,  $k_2 \simeq -1.2$ ), and one for the inelastic solution  $(2, 2)$  ( $k_1 \simeq -1.5$ ,  $k_2 \simeq -0.7$ ). The peaks can be better resolved by plotting the distribution of the relative momentum  $k_1 - k_2$ , as done in Fig. 10.3-(e). The relative weights enclosed within the dashed contours in Fig. 10.3-(c),  $P_{13}^{\text{num}} \simeq 0.49$ ,  $P_{22}^{\text{num}} \simeq 0.1$ ,  $P_{31}^{\text{num}} \simeq 0.41$ , are compatible with the predicted cross sections  $P_{13} \simeq 0.47$ ,  $P_{22} \simeq 0.12$ ,  $P_{31} \simeq 0.41$ <sup>5</sup>.

## 10.3 Quantum simulation

The analysis above outlines a tractable regime where non-trivial meson scattering phenomena can be accessed and understood. We now discuss how to observe them — and possibly extend their scope — with a quantum simulator, which minimally requires: *i*) designing the desired Hamiltonian dynamics; *ii*) preparing the incoming state; *iii*) detecting the outgoing states.

Crucially, problem *i*) does not involve any experimental fine-tuning: the basic phenomena only rely on confinement, and are thus robust to any weak perturbation to the model. As a concrete example, we will focus on simulating the Hamiltonian in Eq. (10.1) by exploiting the equivalence with the quantum Ising chain in a tilted magnetic field (see Section 8.2.2):

$$H_{\text{qIc}} = \sum_j -\frac{m}{2} \sigma_{j-1/2}^z \sigma_{j+1/2}^z + \frac{\tau}{2} \sigma_{j+1/2}^z + w \sigma_{j+1/2}^x. \quad (10.8)$$

The mapping above is extremely advantageous for quantum simulations because it implements gauge invariance exactly, similarly to what done in Refs. [4, 166] for the Schwinger model. The dynamics governed by Eq. (10.8) can be experimentally realized both with optical lattices [335, 336] and Rydberg atoms trapped in optical tweezers [46, 337].

The preparation of the initial state *ii*) is subtle, as sharp meson wavepackets involve considerable entanglement between atoms, which is precluded to single-site optical manipulations. We present here an approach exploiting spatially inhomogeneous fields in Eq. (10.8) to filter meson wavepackets with sharply-defined momenta, at the price of moderately longer chains and a limited amount of post-selection. The numerical simulation in Fig. 10.4-(a) illustrates the core idea: when  $w/\tau \lesssim 1$ , a spatially localized spin flip in the left region mostly excites the lowest (and fastest) meson  $\ell = 1$  at all momenta; hence, a sharp spatial variation in the fields  $\tau(j)$ ,  $w(j)$  (inset) determines a corresponding change in the shape of mesonic bands [from that in panel (b) to that in (c)]; energy conservation (horizontal dashed lines)

<sup>5</sup>A smaller peak can be observed far from the momentum-conserving line  $k_1 + k_2 = k_1^0 + k_2^0$ , and corresponds to the reflection of the second meson on the boundary after scattering in the  $(3, 1)$  channel. The missing probability fraction outside the dashed contours in Fig. 10.3-(c) is due to such effects as well as to the arbitrary cutoff used to define the contours, and amounts to  $\approx 20\%$  here.

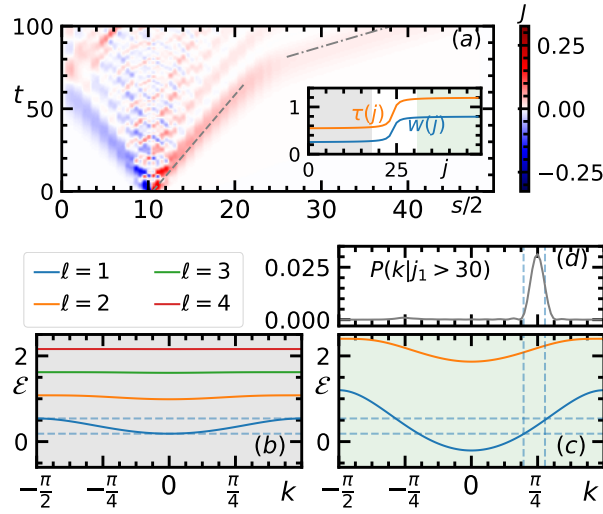


Figure 10.4: Manipulation of mesonic wavepackets by inhomogeneous fields. (a) Time evolution of the meson current density  $J(s, t)$  originating from a single spin flip (see the main text) at  $s/2 = (j_1 + j_2)/2 = 10.5$ , in the inhomogeneous field profiles shown in the inset, interpolating between  $\tau_L = 0.54$ ,  $w_L = 0.25$  (left) and  $\tau_R = 1.2$ ,  $w_R = 0.8$  (right). The slopes of the dashed and dashed-dotted lines correspond to the maximal velocity of the  $\ell = 1$  meson in the left and right regions, respectively. (b-c) Mesonic spectra in the left (b) and right (c) regions. The horizontal dashed lines indicate the range of allowed energies; the vertical lines define the range of momenta  $k^* \pm \delta k$  allowed in the right region. (d) Momentum distribution of the transmitted meson wavepacket.

selects a narrow momentum window  $k^* \pm \delta k$  (vertical dashed lines) for which rightward propagation is allowed. Panel (d) shows that at time  $t = 50$  the fraction of mesonic wavepacket filtered in the right region is  $\approx 20\%$  (the rest is reflected at the interface), and its momentum distribution has support within the selected window. An analogous preparation can be made on the opposite side of the chain for the desired incoming mesonic wavepacket from the right. Similarly, inhomogeneous fields can be used to accelerate mesons.

Finally, detecting the scattering products *iii*) is conceptually simple, as the mesons involved in the various possible outcomes of a collision have different velocities [cf. Fig. 10.1], so they can be resolved as spatially separate wavepackets. For implementations based on Eq. (10.8), the particle density  $c_j^\dagger c_j$  in Eq. (10.1) maps to the domain-wall density  $(1 - \sigma_{j-1/2}^z \sigma_{j+1/2}^z)/2$ : Thus, it is sufficient to measure the magnetization profile  $\langle \sigma_{j+1/2}^z(t_f) \rangle$  in the final state [46, 335–337] to reconstruct the momenta of the mesons from their positions, the quantum numbers from their extension, and the cross sections from their probabilities. We note that the required time and length scales estimated from the above discussion ( $50 \div 100$  lattice sites and units

of time) are within reach of present-day experiments: Ref. [46], for example, demonstrated state preparation and single-qubit readout in a chain of 51  $^{87}\text{Rb}$  atoms governed by Ising-type dynamics close to Eq. (10.8), with excellent coherence control over several tens of time units ( $2\pi/w$ ).

## 10.4 Outlook

The analysis of the meson scattering problem and the proposed strategies for quantum simulations presented here can be straightforwardly applied to any one-dimensional model exhibiting confinement, including Abelian and non-Abelian lattice gauge theories (e.g., quantum link models [4, 147]). They can also be extended to long-range interacting models, for which confinement effects [256, 281] have been recently experimentally investigated with trapped ions [262]. The novel theoretical approach and exact solution to the meson scattering problem presented here will provide the basic building block for understanding the non-equilibrium evolution in quantum spin chains with confinement of excitations [209, 256], particularly the recently reported lack of thermalization [6, 198, 207, 210, 254, 279–281].

Compared to real-world scattering experiments, quantum simulations naturally give access to full real-time resolution of the dynamics of a complex collision event, and to the pattern of quantum correlations and entanglement at the level of partons [338, 339], for which simplified lower-dimensional models such as the one discussed here could already provide deep insights. In future work, we plan to investigate this, as well as to optimize schemes for cold-atom platforms. Intriguingly, quantum simulators could allow to explore regimes beyond our theoretical analysis such as the continuum limit of quantum field theories [234, 271, 340–342]. This would represent a first step towards the ultimate goal of simulating realistic scattering problems in QCD such as heavy-ion collisions [193].



# Chapter 11

## False vacuum decay in quantum spin chains

The possibility that our universe, as it cooled down, may have settled into a metastable state (false vacuum) that may eventually decay was proposed by Coleman in 1977 and has been since then one of the most popularized ideas of physical cosmology [343–346]. The decay would happen through bubble nucleation, i.e., the formation of bubbles of true vacuum that rapidly expand: the probability for this process to occur is extremely small, and studying this phenomenon is notoriously challenging due to its intrinsic non-perturbative character.

As discussed in Chapter 5, the possibility of using tools from quantum technologies for studying problems of strongly coupled quantum field theories has recently attracted a lot of interest [128–130, 174]. On the one hand, tensor-network approaches are promising candidates for studying non-equilibrium properties that cannot be accessed with traditional Monte Carlo simulations. These approaches have been successfully applied to  $1 + 1$  and  $2 + 1$  dimensional lattice gauge theories [201, 203, 333, 347–351] but they suffer from limitations with dimensionality. Therefore, there has been an increasing interest in the toolbox of quantum simulators [4, 152, 153, 159, 166, 168, 216]. The hope is that controllable quantum systems in table-top experiments will help us understand difficult problems in quantum field theory, including, for example, the decay of the false vacuum [352–356]. In this context, one-dimensional quantum spin models represent the ideal framework for benchmarking quantum simulators: they can host particle confinement [223, 224], a property that can be observed in the non-equilibrium dynamics after a quantum quench [209, 256, 262]; it has also been suggested that their real-time evolution can reveal interesting phenomena including collisions of particles (see Chapter 10) and bubble nucleation [7, 276, 277, 342, 357, 358].

Here, we propose to study the decay of the false vacuum in quantum spin models using simulations of real-time dynamics after a quantum quench.

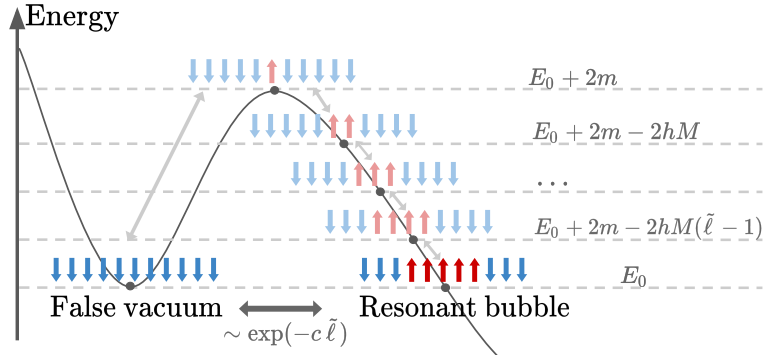


Figure 11.1: *Illustration of bubble formation* (false vacuum is in blue, true vacuum in red). The process that leads to the resonant bubble goes through  $O(\tilde{\ell})$  off-resonant states: a small bubble is (virtually) created and expanded until it reaches the resonant size  $\tilde{\ell}$ . As a consequence, the matrix element that drives the false vacuum decay is exponentially small in  $\tilde{\ell} \propto h^{-1}$ .

## 11.1 False vacuum decay

To illustrate the phenomenon of false vacuum decay we consider the prototypical model for confinement introduced in Section 8.2.1, the quantum Ising chain in transverse and longitudinal field. We report here the Hamiltonian, where we fix  $J = 1$ :

$$H(g, h) = - \sum_i (\sigma_i^z \sigma_{i+1}^z + g \sigma_i^x + h \sigma_i^z) . \quad (11.1)$$

Here  $\sigma_i^\alpha$  are Pauli operators, and the amplitudes  $g$  and  $h$  are the transverse and longitudinal field, respectively.

We remind the reader that for  $h = 0$  the model has a  $\mathbb{Z}_2$  symmetry that is spontaneously broken for  $|g| < 1$  (ferromagnetic phase). In this phase there are two ground states characterized by opposite magnetizations  $\langle \sigma_i^z \rangle = \pm M$ , with  $M = (1 - g^2)^{1/8}$  [359]. The model is diagonalized with a mapping to free fermions: the corresponding excitations in the ferromagnetic phase are kinks that interpolate between domains with opposite magnetization [360]. The kinks can propagate freely and have dispersion relation

$$\omega(\theta) = 2 (1 - 2g \cos \theta + g^2)^{1/2} . \quad (11.2)$$

For a longitudinal field  $h \neq 0$ , the  $\mathbb{Z}_2$  symmetry is explicitly broken and the degeneracy between the two ground states is split by an extensive quantity  $\sim 2hMN$ , where  $N$  is the number of sites in the chain: the state with magnetization aligned with the external field (the *true vacuum*) is the ground state of the model, while the one with opposite magnetization (the *false vacuum*) is a metastable state. As explained in Section 8.2.1, the nature of the excitations is also drastically modified: the longitudinal field induces a linear potential between the kinks, confining them into *mesons* [223].

The false vacuum is at high energy, so it can resonantly decay into the continuum of multi-meson states. While this decay is a very complicated process, the basic mechanism can be understood as the formation of bubbles of true vacuum in the system. Creating a bubble of size  $\ell$  requires the energy given by the masses of the two kinks lowered by  $2hM\ell$ . When this energy becomes zero, the bubble is resonantly excited. This bubble can then further decay through other resonant processes. However, for  $h$  sufficiently small, the phenomenon of bubble formation is very slow. This slowness can be understood by the following simple heuristic argument. A resonant bubble of size  $\tilde{\ell}$  results from the frequent creation of a small bubble (of size of order 1) that then should expand until it reaches the resonant size  $\tilde{\ell} \gg 1$  (see Fig. 11.1). This expansion is a high-order process in the perturbation theory in  $h$  and, as a consequence, the matrix element for exciting the resonant bubble is exponentially small in  $\tilde{\ell} \propto h^{-1}$ .

The decay of the metastable false vacuum in the Ising chain has been studied in Ref. [232], where the following expression of the decay rate per site was obtained <sup>1</sup>:

$$\gamma = \frac{\pi}{9} h M \exp\left(-\frac{q}{h}\right) \quad (11.3)$$

with  $q = |f(-i \ln g)|/M$  and  $f(\theta) = 2 \int_0^\theta \omega(\alpha) d\alpha$ . Note that  $q$  and  $M$  only depend on  $g$ . This rate  $\gamma$  can be interpreted as the number of resonant bubbles that are created per unit time divided by the number of sites. In agreement with the argument explained above, the decay is non-perturbative in the longitudinal field, with an exponential dependence on  $h^{-1}$ .

We note that an analogous mechanism drives the phenomenon known as *string breaking*. String breaking is typically understood as the saturation of the effective interaction between two static charges (or kinks, in this case) at large distance, due to the screening effects of other charges: in other words, the string that extends between the two static charges is broken by the creation of dynamical charges. In the model we are studying, the string corresponds to a false vacuum domain and the string breaking effect corresponds to the formation of a bubble in the domain. The dynamics of string breaking has been studied in this model, in other spin chains, and lattice gauge theories [3, 6, 160, 167, 187, 188, 192, 198, 200, 211, 213, 257, 264, 278, 330, 361], and similar expressions for the decay rate were found.

## 11.2 Quench protocol and methods

The goal of this Chapter is to show that a window of Hamiltonian parameters of the Ising spin chain  $(g, h)$  exists such that the false vacuum decay can be observed through numerical simulations of the non-equilibrium dynamics

---

<sup>1</sup>In Ref. [232], the rate  $\gamma$  contains an oscillatory term  $\tilde{g}(h)$ : we work here in the approximation  $\tilde{g}(h) \simeq 1$ , which is justified for  $h$  sufficiently far from 1.

after a quantum quench. The quench protocol is the following: i) we prepare the system in the ferromagnetic state with all the spins in the  $\sigma_i^z = 1$  direction; ii) we evolve the system in imaginary time with the Hamiltonian  $H(g, -h)$  using infinite volume time evolving block decimation (iTEBD) until we achieve a good convergence to the ground state; iii) we quench  $-h \rightarrow h$  and evolve in real time. Using this protocol, we are able to prepare the false vacuum of  $H(g, h)$  and study its evolution in real time using iTEBD. The state preparation ii) is obtained using a Trotter step  $\delta t = 10^{-3}$ , and the imaginary time evolution stops when the relative change of the energy density is smaller than  $10^{-16}$ . The real time evolution after the quench iii) is performed with a Trotter step  $\delta t = 10^{-2}$ . The bond dimension  $\chi$  is set to 512. We checked the stability of the numerical simulations with respect to changes in  $\chi$  and  $\delta t$ .

We stress that in our quench protocol the false vacuum decay drives the system toward a thermal state, that has a finite energy density with respect to the true vacuum. Only in the limit  $h \rightarrow 0$  this state tends to the true vacuum.

### 11.3 Time scales

Before embarking on the analysis of the numerical data, we should have a clear picture of all the time scales entering in the quench dynamics of our model. Starting from the false vacuum, the first process happening is the creation of off-resonant bubbles. During this (relatively) short-time transient, say up to time  $\tau_r$ , the system remains effectively frozen in the false vacuum until the resonant bubbles start being produced. However, here we are not interested in this transient but only in the growth of the resonant bubbles, because this is the process that leads to the false vacuum decay described by the rate (11.3). For the accurate measurement of this rate, we need a clear separation of this time scale from the successive ones. Indeed, at very late time, when most of the false vacuum decayed, since the system is at finite energy density, it starts thermalizing through the propagating states that originate from the decay of the resonant bubbles: the late time dynamics is governed by the thermal state corresponding to the energy of the pre-quench state (only for very small  $h$  this is close to zero temperature, i.e. the true vacuum). We denote with  $\tau_D$  the time scale for the onset of thermalization; unfortunately, we do not know how to estimate  $\tau_D$ , but its determination lies beyond the scope of this work.

We emphasize that Eq. (11.3) is expected to work well under the assumption of a clean separation of time scales, i.e.  $\tau_r \ll \gamma^{-1} \ll \tau_D$ . For the Hamiltonian (11.1), such separation of time scales is guaranteed in the regime  $h \ll 1$  and  $g$  not too close to 1. The requirement  $h \ll 1$  is obvious, since as  $h$  grows all the above time scales  $\tau_r, \gamma^{-1}, \tau_D$  become of order one and there cannot be any separation. Moreover, if  $g$  gets too close to 1, the

masses of the kinks become very small and the assumption that the false vacuum preferably decays into one-domain states (resonant bubbles) is no longer justified.

In conclusion, the false vacuum decay is expected to be described by Eq. (11.3) in the limit of small  $h$  and  $g$  not too close to 1. However, as the fields are reduced, the time scale  $\gamma^{-1}$  soon becomes extremely large (which is the reason why false vacuum decay is generically an elusive phenomenon, see also [362]). Thus the main difficulty of the numerical analysis is to find a window of the Hamiltonian parameters such that there is an optimal balance between a reasonable separation of times scales (to have a time range in which Eq. (11.3) describes something) and its numerical accessibility. We found that such balance is obtained for rather small  $h$  (of the order of  $10^{-2}$ ), but with  $g$  relatively large  $g \sim [0.7, 0.9]$ : a smaller  $g$  makes the decay time ( $\gamma^{-1}$ ) too long and a larger  $h$  destroys completely the time-scale separation.

## 11.4 Results

To estimate the decay rate, we analyze the following two observables

$$F(t) = \frac{\langle \sigma_i^z(t) \rangle + \langle \sigma_i^z(0) \rangle}{2\langle \sigma_i^z(0) \rangle}, \quad (11.4)$$

$$G(t) = 1 - \|\rho(t) - \rho(0)\|_1, \quad (11.5)$$

where  $\rho(t)$  is the two-site density matrix at time  $t$  and  $\|\rho(t) - \rho(0)\|_1$  is the trace distance between the two density matrices. Both quantities can be easily computed in iTEBD, and satisfy  $F(0) = G(0) = 1$ , while they vanish in the true vacuum. The time evolution of  $F(t)$  is fully encoded in the magnetization and, consequently, is expected to decay with a rate

$$\gamma_F \simeq \gamma_{\tilde{\ell}} = \frac{f(\pi)}{18} \exp\left(-\frac{q}{h}\right), \quad (11.6)$$

where the size of the resonant bubble is  $\tilde{\ell} = \frac{f(\pi)}{2hM\pi}$  (see Ref. [232]). Note that for small  $h$ , this rate is much larger than  $\gamma$ , so the time scale needed to observe the decay in our simulation is significantly reduced.

As an illustrative example for the determination of the decay rates of  $F$  and  $G$ , in Fig. 11.2 we report their evolution at fixed  $g = 0.8$  and different values of  $h$  on a semi-log scale. It is evident that after a short transient, all the data show a distinct exponential decay (linear behavior on semi-log scale).

For all the considered values of  $g$  and  $h$ , we performed an exponential fit  $O(t) = A_O e^{-\gamma_O t}$ , with  $O = F, G$ . The fit is done in a time range  $t_0 < t < t_1$  and then we check the stability of the fit for small variations of  $t_0, t_1$ .

The resulting decay rates  $\gamma_{F,G}$  are plotted in Fig. 11.3-a,b,c as functions of  $h^{-1}$  again on semi-log scale. The exponential dependence on  $1/h$ ,

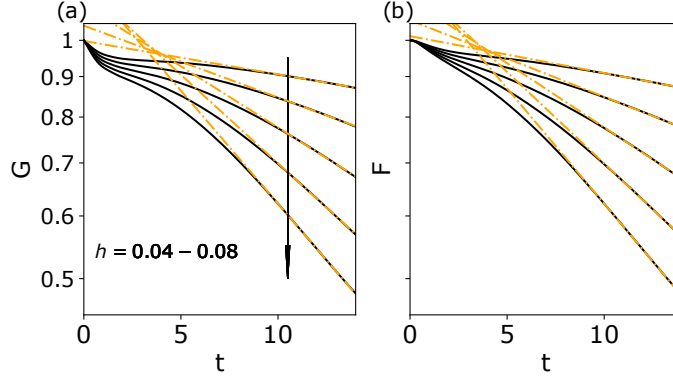


Figure 11.2: *False vacuum decay in the quantum Ising chain.* The time evolution of  $F(t)$  and  $G(t)$ , in Eqs. (11.4) and (11.5), is shown for  $g = 0.8$  and different values of  $h$  after the quench  $-h \rightarrow h$ . The dot-dashed lines are the exponential fits in the decay region performed to extract the decay rates  $\gamma_F$  and  $\gamma_G$ .

expected from Eq. (11.6), is very clear in the data. We fitted these rates with

$$\gamma_O = k_O e^{-q_O/h}, \quad O = F, G. \quad (11.7)$$

In Fig. 11.3-d we report the obtained coefficients  $q_F, q_G$ : they are compatible with each other and they both agree very well with the theoretical prediction  $q = |f(-i \ln g)|/M$  in the full range of  $g$  considered. The prefactors  $k_F$  and  $k_G$  in Eq. (11.7) turn out to be different from what is predicted by Eq. (11.6) (the data in Fig. 11.3-a,b,c are shifted compared to the dashed line). However, this shift is not surprising at all because we know that (i) the prefactor depends on the specific observable (e.g., compare Eqs. (11.3) and (11.6)), (ii) we expect it to be more affected by the approximations done in the derivation of Eq. (11.6).

## 11.5 XXZ ladder

To show the general validity of our analysis, we consider a second model presenting confinement of elementary excitations with Hamiltonian [9]

$$H(\Delta_{\parallel}, \Delta_{\perp}) = \frac{1}{2} \sum_{j=1}^L \sum_{\alpha=1,2} [\sigma_{j,\alpha}^x \sigma_{j+1,\alpha}^x + \sigma_{j,\alpha}^y \sigma_{j+1,\alpha}^y + \Delta_{\parallel} \sigma_{j,\alpha}^z \sigma_{j+1,\alpha}^z] + \Delta_{\perp} \sum_{j=1}^L \sigma_{j,2}^z \sigma_{j,1}^z \quad (11.8)$$

i.e., two XXZ spin-1/2 chains coupled along the longitudinal direction through an anisotropic Ising-like interaction (this model is studied in detail in Chapter 12). Compared to the Ising spin chain (11.1), the model possesses two

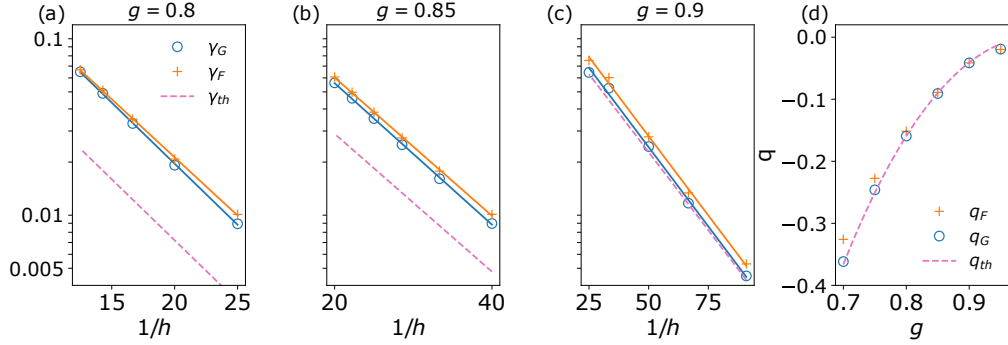


Figure 11.3: *Decay rates in the quantum Ising chain.* In panels (a),(b),(c) we show the decay rates  $\gamma_F, \gamma_G$ , obtained from the fits of  $F(t), G(t)$  as in Fig. 11.2. The continuous lines are the fits of the exponential dependence of the rates in  $1/h$ . The dashed line represents the theoretical prediction (11.6). From the fits the coefficients  $q_F$  and  $q_G$  are extrapolated and showed against the theoretical value  $q_{th} = |f(-i \ln g)|/M$  (dashed line) in panel (d).

interesting features. The first is that in the absence of the confining interaction ( $h$  and  $\Delta_\perp$ ), the Ising spin chain becomes a free model, while the decoupled XXZ chains constitute an interacting (integrable) spin model. The second one is that confinement is induced by the internal interaction between the chains, a built-in mechanism, instead of an external field. We work in the gapped anti-ferromagnetic phase, i.e.,  $\Delta_\parallel \in (1, +\infty)$  where the model for  $\Delta_\perp = 0$  has four degenerate antiferromagnetic ground states. The confining potential explicitly breaks the original  $\mathbb{Z}_2 \times \mathbb{Z}_2$  symmetry to a single  $\mathbb{Z}_2$  [9]: the four degenerate ground states at  $\Delta_\perp = 0$  are split in two doublets separated by an energy of the order  $\Delta_\perp L$ . The two lowest states (the true vacua) are now the stable ground states, while the other two (the false vacua) are metastable states at high energy and can decay in the continuum of the many-body spectrum.

In analogy with the Ising model, we prepare the false vacuum as the ground state at  $-\Delta_\perp$  and then we quench  $-\Delta_\perp \rightarrow \Delta_\perp$ . For several values of the interactions  $\Delta_\perp$  and  $\Delta_\parallel$ , we extract the decay rates  $\gamma_{F,G}$  for  $F(t), G(t)$  (here  $F$  in Eq. (11.4) is built with the staggered magnetization and  $G$  in Eq. (11.5) with the reduced density matrix of two adjacent rungs). In Fig. 11.4, a) and b), we show the time evolution of  $G$  after the quench for two values of  $\Delta_\parallel$ . Even though we do not have analytic predictions for this ladder, we expect that the underlying mechanism of the false vacuum decay is the same so we can fit the decay rate with Eq. (11.7) with the replacement  $h \rightarrow \Delta_\perp$ . The test of this scaling for  $\gamma_G$  is presented in Fig. 11.4 c) and d), showing a perfect agreement. The quality of the fit for  $\gamma_F$  is very similar, although in Fig. 11.4 we only report the final values for  $\gamma_F$  and not the data for  $F(t)$ .

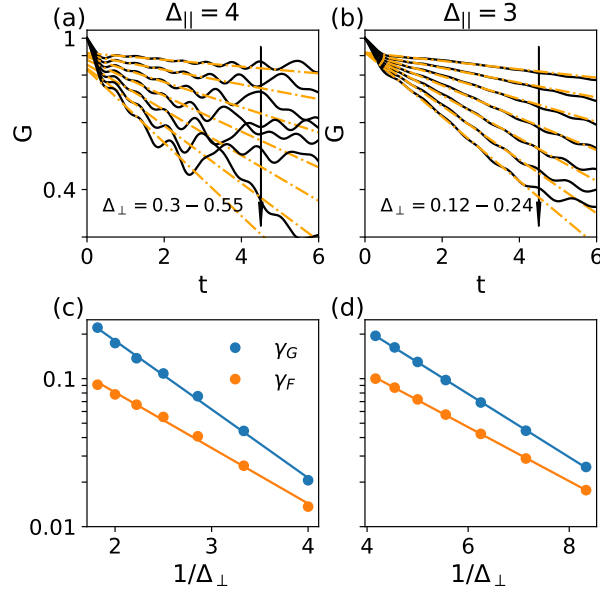


Figure 11.4: *False vacuum decay for the XXZ ladder.* Panels (a) and (b): Time evolution of  $G$  in Eq. (11.5) after a quench  $\Delta_{\perp} \rightarrow -\Delta_{\perp}$  with  $\Delta_{\parallel} = 4$  (a) and  $\Delta_{\parallel} = 3$  (b) with different values of  $\Delta_{\perp}$ . In (a)  $\Delta_{\perp} = 0.25, 0.3, 0.35, 0.4, 0.45, 0.5, 0.55$  while  $\Delta_{\perp} = 0.12, 0.14, 0.16, 0.18, 0.20, 0.22, 0.24$  in (b). The arrows indicate the growing direction of  $\Delta_{\perp}$ . Panels (c) and (d): decay rates extracted from the fits in (a) and (b), respectively, on semi-logarithmic scale. The continuous lines are fits of the decay rates performed according to Eq. (11.7)

## 11.6 Conclusions and outlook

In this Chapter we provided robust numerical evidence that for two one-dimensional spin models featuring confinement of elementary excitations it is possible to identify a range of physical parameters such that the rate of false vacuum decay is accessible in measurable time scales. The quench protocol that we described here is amenable to quantum simulation, for example with trapped ions or Rydberg atoms (both can simulate a system with confinement). For the false vacuum preparation, the imaginary time evolution used in the numerics can be replaced by an adiabatic preparation.

We conclude by briefly discussing how the the trapped-ion quench experiment of Ref. [262] (for the observation of domain wall confinement in real time) can be adjusted to measure the false vacuum decay. In this experiment, the ion dynamics is well captured by a long-range quantum Ising model in which the  $\mathbb{Z}_2$  symmetry is spontaneously (and not explicitly) broken. Hence, there are two degenerate real vacua and no false one. In order to get a phenomenology similar to our setup it is sufficient to slightly tilt the effective magnetic field (that in Ref. [262] is in the  $z$  direction) via a Rabi rotation, see the review [134]. This tilting provides a small component

of the magnetic field along the  $x$  axis that breaks the degeneracy of the two vacua with a real and a false one. Then the preparation of the system in the false vacuum and the following quench are done with the very same techniques exploited already in Ref. [262]. Finally one- and two-point functions of the spin can be measured, as already done in Ref. [262], giving access to  $F(t)$  and  $G(t)$  in Eqs. (11.4) and (11.5).



## Chapter 12

# Confinement in the spectrum of a Heisenberg-Ising spin ladder

In this work, we study and characterize accurately the spectrum of another model displaying confinement of elementary excitations. This system consists of two XXZ spin-1/2 chains coupled in an anisotropic manner, along the longitudinal (easy axis) direction via an Ising-like coupling. One of the motivations to study the effects of confinement in antiferromagnetic ladders lies in the fact that, in contrast to spin chains where confinement is triggered by a symmetry-breaking field or long-range interactions, in a ladder geometry the confining potential naturally emerges as the effect of the (even small) local interaction between the chains, as can be easily seen in a mean field treatment [233, 363–365]. Consequently, the external field is not required because the staggered magnetization of one chain provides an effective staggered field for the other. There are various possible ladders featuring confinement (e.g., those composed of Ising-like chains), but many of these require an external magnetic field which imposes difficulties in prospective cold atomic realizations (see however [335]). Here we focus instead on coupled Heisenberg-type spin chains in which no external field, either longitudinal or transverse, makes an appearance, making them suitable for cold atom experiments. For example, the two chains can be mapped by a Jordan–Wigner transformation to spinless fermions coupled by a density-density interaction. This model can be easily realized by freezing the spin degrees of freedom in real fermion gases, e.g., utilizing the techniques of Ref. [366] for Ytterbium atoms. Alternatively, one can use the true spin degrees of freedom and freeze the charge degree of freedom in spin-1/2 fermionic condensates.

Explicitly the Hamiltonian is given by

$$\begin{aligned}
H(\Delta_{\parallel}, \Delta_{\perp}) = & \frac{J}{2} \sum_{j=1}^L [\sigma_{j,1}^x \sigma_{j+1,1}^x + \sigma_{j,1}^y \sigma_{j+1,1}^y + \Delta_{\parallel} (\sigma_{j,1}^z \sigma_{j+1,1}^z + 1)] \\
& + \frac{J}{2} \sum_{j=1}^L [\sigma_{j,2}^x \sigma_{j+1,2}^x + \sigma_{j,2}^y \sigma_{j+1,2}^y + \Delta_{\parallel} (\sigma_{j,2}^z \sigma_{j+1,2}^z + 1)] \quad (12.1) \\
& + J \Delta_{\perp} \sum_{j=1}^L \sigma_{j,2}^z \sigma_{j,1}^z.
\end{aligned}$$

Here  $\sigma_{j,k}^{\alpha}$  denotes the Pauli spin operators at the  $j^{\text{th}}$  site of chain  $k \in \{1, 2\}$  and we impose periodic boundary conditions,  $\sigma_{L+1,k}^{\alpha} = \sigma_{1,k}^{\alpha}$ . The parameter  $J$  sets the energy scale, throughout the paper we set it to  $J = 1$ . We focus on the regime  $\Delta_{\parallel} \in (1, +\infty)$  for the anisotropy parameter of the chains which corresponds to their gapped antiferromagnetic phases. The last term couples the two spin chains with an Ising-like interchain interaction. Without losing generality, we set  $\Delta_{\perp} > 0$ , i.e., an antiferromagnetic coupling of the chains. The sign of  $\Delta_{\perp}$  can be reversed with a spin flip applied to one of the two chains, without altering the spectrum.

The model is highly symmetric. The  $z$  component of the total magnetization on each chain,  $M_k = \sum_j \sigma_{j,k}^z$ , is conserved, corresponding to two  $U(1)$  symmetries. For  $\Delta_{\perp} = 0$  there is a  $\mathbb{Z}_2 \times \mathbb{Z}_2$  symmetry associated with the spin flip  $\sigma_{j,k}^{y/z} \rightarrow -\sigma_{j,k}^{y/z}$  of each chain. The coupling  $\Delta_{\perp} \neq 0$  explicitly breaks this symmetry: the residual one is the global spin flip of both chains (a single  $\mathbb{Z}_2$ ). Moreover, there is an additional symmetry related to the swapping of the chains  $\sigma_{j,1}^{\alpha} \leftrightarrow \sigma_{j,2}^{\alpha}$ . Finally, due to translational invariance, the energy levels are organized as eigenstates of the total momentum  $P$ .

A recent work [251] studied the properties of bound states on an XXZ chain in the anti-ferromagnetic region with the confining potential provided by an external staggered field. This model can be interpreted as arising from a mean field treatment of the XXZ ladder in (12.1), with the staggered field encoding the mean field effect of one chain on the other [233, 363–365].

There is however a fundamental difference between confinement in ladders and chains with an external field. Indeed, since for the ladders one symmetry is spontaneously broken, there are (at least) two true ground states (vacua) and the neutral mesons with respect to the confined charge can interpolate between the same vacuum or between different ones. This feature leads to the existence of two types of neutral bound states which we dub intrachain (‘Type 1’) and interchain (‘Type 2’) mesons interpolating, respectively, between the same or different vacua.

Although such the mean-field treatment in [251] is rather accurate to capture an entire family of bound states, it completely misses another one. We go beyond this approximation, and study the full system in the strong anisotropy regime. As generally anticipated above, the main new theoretical

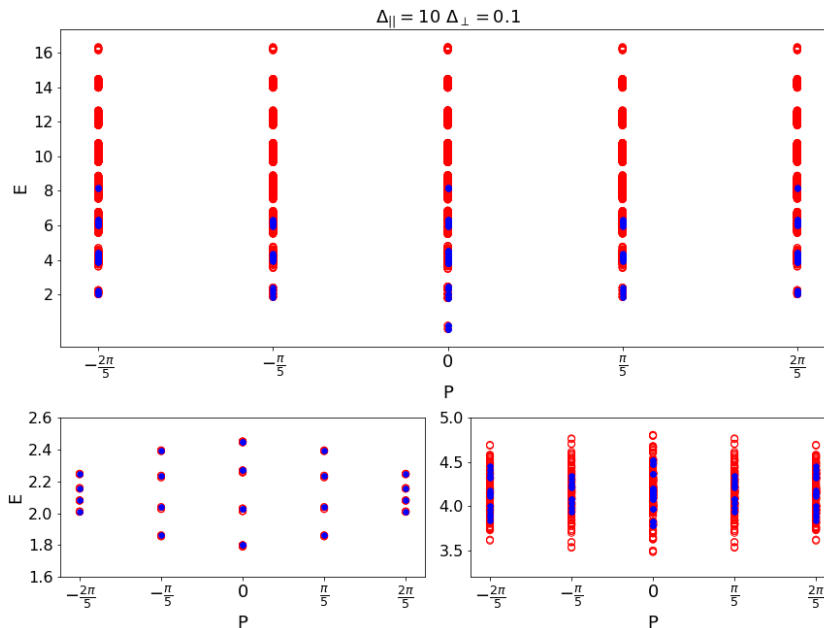


Figure 12.1: Spectrum of the Heisenberg-Ising ladder Hamiltonian (12.2) for  $\Delta_{\parallel} = 10$  and  $\Delta_{\perp} = 0.1$  (red circles) compared with the XXZ-chain in a staggered field (blue symbols), see Eq. (12.3). Both spectra are in the sector of zero magnetization. *Top*: Entire spectrum of both Hamiltonians for  $L = 10$ . For large enough  $\Delta_{\parallel}$ , the spectrum is organized in bands with fixed number of particles (kinks). The ladder has many more states than the corresponding chain. *Bottom*: Zooms of the two-particle and four-particle sectors close to energy  $E \sim 2$  and  $E \sim 4$  respectively. For the two-particle sector and even  $L$ , the spectra of the two models are in one-to-one correspondence (modulo a four-fold degeneracy which is resolved at higher order in  $\epsilon$ ). This is no longer the case for the four-particle sector (and for odd  $L$  in the two-particle sector).

insight is that beyond the already known (intrachain) mesons that also appear in the mean field approach, we identify another class of bound states that we dub interchain mesons.

The chapter is structured in the following way. In Section 12.1 we describe the elementary excitations (intrachain and interchain mesons) and study their spectrum in the strong anisotropy regime. In Section 12.2 we use a semiclassical approach to find a more accurate estimate of the spectrum in the regime of moderate anisotropy. In Section 12.3 we introduce an approximation to capture the spectrum of two-meson states. In Section 12.4 we discuss the nature of the first excited states and find a transition as a function of the anisotropy parameters. In Section 12.5 we draw our conclusions. In the Appendix C.7 we report some details about semiclassical quantization.

## 12.1 Elementary excitations in the strong anisotropy regime

The goal of this chapter is to provide an accurate description of the spectrum of the Heisenberg-Ising ladder in the regime with confining quasiparticles.

To set the problem, we report the entire spectrum of the Hamiltonian in the sector of zero magnetization for  $L = 10$ , calculated numerically by means of exact diagonalization. We consider  $\Delta_{\parallel} = 10$  and  $\Delta_{\perp} = 0.1$ . The spectrum is organized in bands of fixed even number of particles around the energies equal to this number (in units of  $\Delta_{\parallel}$ ). In the figure, together with the spectrum of the ladder, we report the numerically calculated spectrum of the XXZ spin-chain in a staggered field which is a mean field description of the ladder. As can be seen clearly, the ladder has many more states than the corresponding chain, which is obvious as the Hilbert space of the ladder is exponentially larger than that of the chain. In the bottom panels, we report zooms of the two-particle and four-particle sectors. Inside each band, there is a fine structure given by states with precise quantum numbers. Here, we are after an accurate characterization of this fine structure and of the effects of confinement. A first observation that will have a very simple explanation later is that the two-particle spectrum of the ladder is in one-to-one correspondence with that of the chain. This is true modulo a four-fold degeneracy that is a consequence of the discrete symmetries of the Hamiltonian (12.2) (spin flip and chain swap) and is lifted in higher perturbative order in  $\epsilon = 1/\Delta_{\parallel}$ . We then notice that the correspondence between the chain and the ladder is not valid for the four-particle sector, where there are many more states that we will describe in the following. We stress that the correspondence between the two-particle sectors in the ladder and in the chain does not hold for odd  $L$ .

In order to understand the structure of the elementary excitations, it is instructive to focus first on the parameter regime  $\Delta_{\parallel} \gg 1$ . In this Ising limit it is useful to rescale the Hamiltonian (12.1) by  $\Delta_{\parallel}$  [251], i.e.

$$\begin{aligned}
 H_{\text{I}}(\epsilon, \Delta_{\perp}) = & \sum_{\alpha=1,2} \sum_{j=1}^L \left[ \epsilon(\sigma_{j,\alpha}^+ \sigma_{j+1,\alpha}^- + \sigma_{j,\alpha}^- \sigma_{j+1,\alpha}^+) + \frac{1}{2}(\sigma_{j,\alpha}^z \sigma_{j+1,\alpha}^z + 1) \right] \\
 & + \epsilon \Delta_{\perp} \sum_{j=1}^L \sigma_{j,2}^z \sigma_{j,1}^z,
 \end{aligned} \tag{12.2}$$

where  $\epsilon = 1/\Delta_{\parallel}$ . We study this Hamiltonian perturbatively in  $\epsilon$ .

When  $\epsilon = 0$ , the two chains are decoupled and the hopping terms are absent. The Hamiltonian has four degenerate ground states given by the four possible combinations of the Néel  $|\Psi_1\rangle = |\uparrow\downarrow\uparrow\downarrow \dots\rangle$  and anti-Néel  $|\Psi_2\rangle = |\downarrow\uparrow\downarrow\uparrow \dots\rangle$  states of the two chains (here  $|\uparrow\rangle$  is chosen with quantization axis in the  $z$  direction, i.e.,  $\sigma_j^z|\uparrow\rangle = |\uparrow\rangle$ ). In the units of Eq. (12.2)

all these ground states have exactly zero energy for  $\epsilon = 0$ . The fundamental excitations of each chain are kinks  $|K_{\alpha\beta}(j)\rangle$  interpolating between the two vacua  $|\Psi_\alpha\rangle$  and  $|\Psi_\beta\rangle$  ( $\alpha, \beta \in \{1, 2\}, \alpha \neq \beta$ ) at the bond between sites  $j$  and  $j + 1$  (cf. Fig. 12.2). Note that the spin  $s$  and the parity of the site  $\rho = j \bmod 2$  on the chain  $\alpha \in \{1, 2\}$  are related by  $s = (-1)^\alpha(1/2 - \rho)$ . For  $0 < \epsilon \ll 1$  and  $\Delta_\perp = 0$ , the exactly known ground states of the chains are still almost Néel and anti-Néel states, but their degeneracy is lifted for finite  $L$  yielding exponentially small (in  $L$ ) splittings. Similarly, the hopping term hybridizes the kink states and lifts their extensive degeneracy. When  $\Delta_\perp > 0$ , two of the four 0-kink states in which the spins are anti-aligned along the rungs, gain extensive ( $\propto -\Delta_\perp L$ ) negative energy while the other two gain extensive positive energy ( $\propto \Delta_\perp L$ ). In the thermodynamic limit, the latter two become false vacua and together with all the formerly low lying excitations above them are pushed to finite energy density. On the ladder a single kink in one of the two chains toggles between a true and a false vacuum (illustrated in grey and red, respectively, in Fig. 12.2). This implies that the nature of the low-lying excitations change qualitatively when the coupling between the chains is turned on. The low energy sector only bears states with an even number of kinks since there must be a true vacuum both on the left and on the right of these states. Consequently, states made with two kinks become the elementary excitations in the spectrum. The energy acquired by the false vacuum between the two kinks induces an effective linear potential between them: the two kinks are confined in excitations that we call *mesons*, following a standard terminology in the literature. Because of the presence of two true vacua, we can distinguish between two classes of mesons. 'Type 1' mesons are interpolating between the same vacuum while 'Type 2' mesons are interpolating between two different vacua (see Fig. 12.2 to grasp the idea with a graphical representation).

We now illustrate more clearly the difference between these two mesons in terms of the symmetries of the model. For  $\Delta_\perp = 0$  the model has a  $\mathbb{Z}_2 \times \mathbb{Z}_2$  symmetry associated with the total spin flip along each chain. A kink on a given chain has a non-zero  $\mathbb{Z}_2$  charge for the spin-flip symmetry on that chain. When  $\Delta_\perp$  is turned on, the symmetry is explicitly broken and only one  $\mathbb{Z}_2$  symmetry is left (i.e., the global spin-flip of both chains). A charge  $Q$  can be assigned to the explicitly broken symmetry: this charge corresponds to the parity of the total number of kinks. As a consequence of confinement, the low-energy spectrum can harbour only neutral objects, while charged objects are pushed up in the spectrum. Both 'Type 1' and 'Type 2' mesons are neutral with respect to this symmetry, i.e. they have  $Q = 0$ . The remaining  $\mathbb{Z}_2$  symmetry is spontaneously broken in the ground state. Another charge  $q$  may be assigned to this different symmetry: 'Type 1' mesons correspond to  $Q = 0$  and  $q = 0$  while 'Type 2' to  $Q = 0$  and  $q = 1$ . Very importantly, since this second symmetry is not explicitly broken, low-energy states do not need to be neutral with respect to  $q$ . On the contrary, it is possible to have charged excitations ('Type 2' mesons) which are the sort

of composite kinks for the spontaneously broken global spin-flip symmetry. While at first, this phenomenon can sound rather peculiar, it is actually very similar to what happens for strong interactions: the mesons are neutral particles for the color charge but they are not for the electrical charge, related to another symmetry of nature.

In finite volume  $L$ , because of periodic boundary conditions, chains with an odd number of sites can host an odd number of kinks while chains with an even number of sites can host an even number of kinks. Namely, for  $L$  odd there are only  $q = 1$  states while for  $L$  even only  $q = 0$  states (the opposite holds for anti-periodic boundary conditions). Consequently, as long as  $\Delta_{\perp} \ll \Delta_{\parallel}$ , the lowest energy states are ‘Type 1’ mesons if  $L$  is even and ‘Type 2’ mesons if  $L$  is odd. In the following, we give a quantitative account of their dispersion relation both for an infinite system and for a ladder of finite size. The approach we exploit here is rather standard: we project the many-body Hilbert space onto the 2-kink sector yielding an effective two-body Hamiltonian which can be treated with elementary quantum mechanics techniques. As discussed above, the degeneracy of the ground and excited states gets lifted at the first order in  $\epsilon$ , thus the dispersion relation of the low-energy meson excitations, which correspond to the low lying many-body levels, can be well described by a first order perturbative analysis in  $\epsilon$  restricted to the two-kink sector.

### 12.1.1 ‘Type 1’ intrachain mesons

‘Type 1’ or intrachain mesons are formed by kinks on the same chain, as shown in Fig. 12.2. In the regime  $\Delta_{\perp} \ll \Delta_{\parallel} = \epsilon^{-1}$ , the interchain interaction can be studied in a mean field fashion [233, 363–365], by focusing on one of the chains and treating the spontaneous staggered magnetization  $\bar{\sigma}$  of the other chain as an effective external field:

$$\hat{H}_S(\epsilon, h) = \sum_{j=1}^L \left[ \epsilon (\sigma_j^+ \sigma_{j+1}^- + \sigma_j^- \sigma_{j+1}^+) + \frac{1}{2} (\sigma_j^z \sigma_{j+1}^z + 1) \right] + \epsilon h \sum_{j=1}^L (-1)^j \sigma_j^z. \quad (12.3)$$

where  $h = \bar{\sigma} \Delta_{\perp}$ . Here we assume that the other chain is in the approximate anti-Néel state; the Néel case follows by the global spin flip symmetry. In the limit  $\Delta_{\parallel} \gg 1$ , the staggered magnetization is  $\bar{\sigma} \approx 1$ . The excitations of the infinite antiferromagnetic chain (i.e., Hamiltonian (12.3) with  $L \rightarrow \infty$ ) and their confinement have been studied using various approximations in Ref. [251]. Here we extend the analysis of this work to finite chains.

We introduce the projector  $\hat{P}_2$  onto the 2-kink subspace spanned by the basis  $|K_{\alpha\beta}(j_1)K_{\beta\alpha}(j_2)\rangle$ . The action of the projected Hamiltonian  $\hat{H}_2 =$

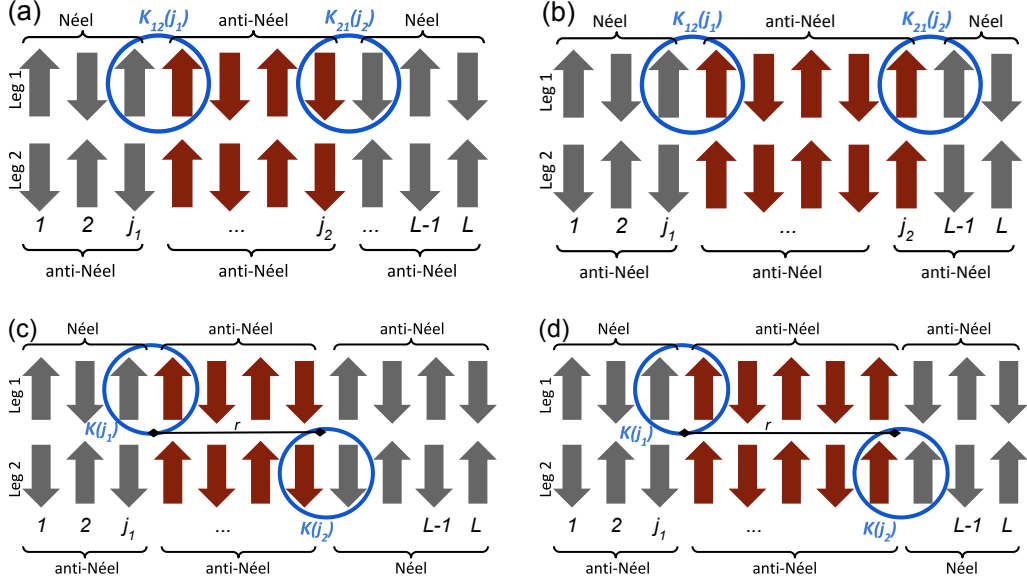


Figure 12.2: Schematic picture of the possible mesons in the ladder. In (a) and (b) we have ‘Type 1’ intrachain mesons built from two kinks on the same chain. Instead, in (c) and (d) we have ‘Type 2’ interchain mesons built from two kinks on the different chains. ‘Type 1’ mesons interpolate between the same kind of vacua, while ‘Type 2’ mesons interpolate between vacua of different kind. The coupling  $\Delta_{\perp}$  induces a linear potential between the kinks, because the energy cost scales with the distance of the kinks equal to the number of spins that have frustrated interchain links (shown in red). This distance is even for kinks of opposite spins (a,c) and odd for kinks of the same spin (b,d).

$\hat{P}_2 \hat{H}_S \hat{P}_2$  on 2-kink states is easily worked out as

$$\begin{aligned}
\hat{H}_2(\epsilon, \Delta_{\perp}) |K_{\alpha\beta}(j_1) K_{\beta\alpha}(j_2)\rangle = & \\
& [2 + (-1)^{\alpha} \epsilon h(L - 2j)] |K_{\alpha\beta}(j_1) K_{\beta\alpha}(j_2)\rangle \\
& + \epsilon \{ [|K_{\alpha\beta}(j_1 - 2) K_{\beta\alpha}(j_2)\rangle + |K_{\alpha\beta}(j_1) K_{\beta\alpha}(j_2 + 2)\rangle] (1 - \delta_{j,L-1})(1 - \delta_{j,L-2}) \\
& + [|K_{\alpha\beta}(j_1) K_{\beta\alpha}(j_2 - 2)\rangle + |K_{\alpha\beta}(j_1 + 2) K_{\beta\alpha}(j_2)\rangle] (1 - \delta_{j,1})(1 - \delta_{j,2}) \}, \tag{12.4}
\end{aligned}$$

where  $1 \leq j = j_2 - j_1 \leq L - 1$ . The first line gives the effective potential, while the second and third lines describe the hopping of the kinks by two sites. The Kronecker-delta factors encode the hard-core nature of the kinks.

Exploiting translational invariance by 2 sites, we are looking for the

energy eigenfunctions in the sector of total spin  $s$  in the form

$$|\Psi_n(s = \pm 1)\rangle = \sum_{j_1 = \frac{3-s}{2}}^{L - \frac{1+s}{2}} \sum'_{r=1}^{L-1} \psi_n^{(s)}(r|P) e^{iP(j_1+r/2)} |K_{12}(j_1)K_{21}(j_1+r)\rangle, \quad (12.5a)$$

$$|\Psi_n^{(o)}(s = 0)\rangle = \sum_{j_1=1}^{L-1} \sum'_{r=2}^{L-2} \psi_n^{(o)}(r|P) e^{iP(j_1+r/2)} |K_{12}(j_1)K_{21}(j_1+r)\rangle, \quad (12.5b)$$

$$|\Psi_n^{(e)}(s = 0)\rangle = \sum_{j_1=2}^L \sum'_{r=2}^{L-2} \psi_n^{(e)}(r|P) e^{iP(j_1+r/2)} |K_{12}(j_1)K_{21}(j_1+r)\rangle, \quad (12.5c)$$

where the primed sums run over odd or even integers, and the momentum of the center of mass  $P$  is quantized as  $P = k 2\pi/L$ ,  $k = -\lfloor \frac{L}{4} \rfloor, \dots, \lfloor \frac{L}{4} \rfloor$ . The limited range of the momentum reflects the doubling of the unit cell due to the staggered background field. The “o/e” superscripts refer to the odd and even sites on which the kinks are located. The parity of the distance  $r$  is fixed by the spin of the kinks:  $r = 2, 4, \dots, L-2$  if the total spin is 0 and  $r = 1, 3, \dots, L-1$  if the total spin is  $\pm 1$  (see Fig. 12.2).

Using these expressions, the eigenvalue problem of  $\hat{H}_2$  leads to the discrete Sturm–Liouville equation

$$(2 + 2\epsilon\Delta_\perp r) \psi_n^{(a)}(r) + 2\epsilon \cos(P) [\psi_n^{(a)}(r+2) + \psi_n^{(a)}(r-2)] = E_n^{(a)}(P) \psi_n^{(a)}(r), \quad (12.6)$$

for all relative wave functions  $\psi_n^{(a)}(r|P)$ ,  $a \in \{+1, -1, o, e\}$ . Here  $E_n$  are the excitation energies with respect to the ground state energy  $\mathcal{E}_{\text{GS}} = -\epsilon\Delta_\perp L$ . The boundary conditions are  $\psi_n^{(\pm 1)}(-1) = \psi_n^{(\pm 1)}(L+1) = 0$  and  $\psi_n^{(o/e)}(0) = \psi_n^{(o/e)}(L) = 0$ . The solutions can be written down exploiting the recurrence relation satisfied by the Bessel functions of the first  $J_{\nu+1}(z) + J_{\nu-1}(z) = 2\nu/z J_\nu(z)$  and similarly for and the second kind  $Y_\nu(z)$ , obtaining

$$\psi_n^{(a)}(r|P) = N_n^{(a)} \left[ J_{\nu_n^{(a)}(P)-r/2}(\Delta_\perp^{-1} \cos P) + A_n^{(a)} Y_{\nu_n^{(a)}(P)-r/2}(\Delta_\perp^{-1} \cos P) \right], \quad (12.7)$$

where  $N_n^{(a)}(P)$  is the normalization and  $\nu_n^{(a)}(P)$  and  $A_n^{(a)}(P)$  are determined by the boundary conditions. These solutions are labeled by the integer  $n$  and their energy eigenvalues are

$$E_n^{(a)}(P) = 2 + 4\epsilon\Delta_\perp \nu_n^{(a)}(P). \quad (12.8)$$

We plot the energy levels  $E_n(P)$  obtained by solving Eq. (12.6) (or equivalently Eq. (12.8)) for  $L = 10$  in the case of total spin  $s = 0$  in Fig. 12.3. These analytic predictions are compared to the exact diagonalization results

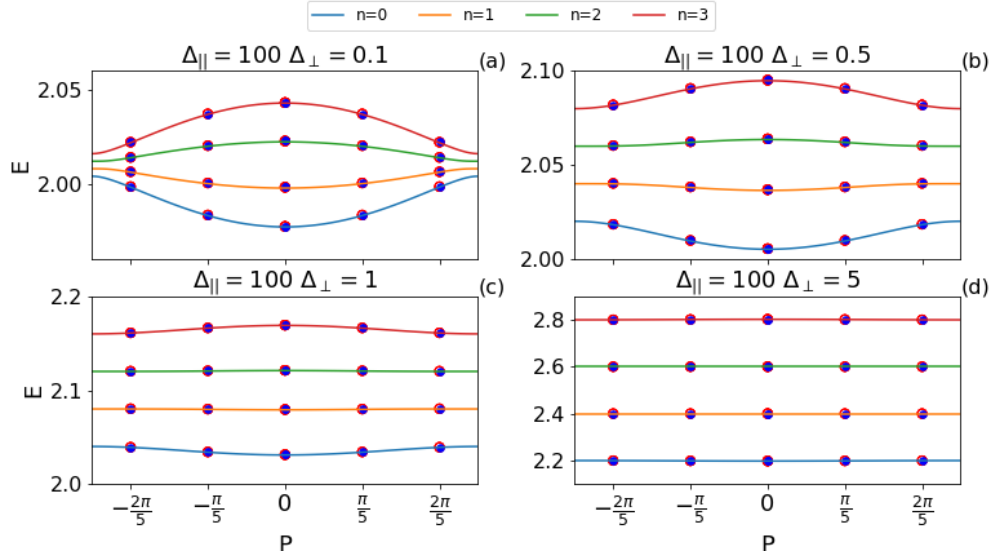


Figure 12.3: Low-lying part of the spectrum in the spin  $s = 0$  sector of the ladder in Eq. (12.2) (red circles) and of the staggered XXZ chain in Eq. (12.3) (blue dots) for  $L = 10$ ,  $\Delta_{\parallel} = 100$ , and  $\Delta_{\perp} = 0.1, 0.5, 1, 5$ . The numerical data have been obtained by exact diagonalization. The dispersion relations of the mesons in the 2-kink approximation (12.8) are shown in continuous lines, obtained by solving Eq. (12.6) numerically. The internal quantum number  $n$  of each curve is in the legend on top of the plot. In the strong anisotropy regime, and for even  $L$ , the ladder is equivalent to the staggered XXZ chain in the two-kink sector.

both for the ladder Hamiltonian (12.2) and for the staggered chain Hamiltonian (12.3) for  $\Delta_{\parallel} = 100$  and different values of the interchain coupling  $\Delta_{\perp}$ . For these couplings, the low energy part of the ladder spectrum matches perfectly the spectrum of the staggered XXZ chain. Moreover, both spectra are well captured by the 2-kink approximation.

In Fig. 12.4 we explore the robustness of this effective description as we move away from the strong anisotropic region by reporting a comparison with the numerical results from exact diagonalization for a ladder of length  $L = 10$  with  $\Delta_{\parallel} = 5$ . Even though the quantitative agreement is worse for  $\Delta_{\parallel} = 5$  than for  $\Delta_{\parallel} = 100$ , the effective two-kink Hamiltonian still represents a good qualitative description of the low energy states as long as the energy bands of different kink numbers are well separated. Indeed, the main qualitative effect is that as  $\Delta_{\perp}$  increases (at fixed  $\Delta_{\parallel}$ ), some high energy states, which are not captured by the mean-field staggered XXZ chain, come down to low energy and mix up (and at some point hybridize) with the part of the spectrum we are able to describe. At a more quantitative level, even for the smallest values of  $\Delta_{\perp}$  we observe deviations that anyhow were expected. Indeed, as  $\Delta_{\parallel}$  is decreased, the fundamental excitations interpolate between vacua that cannot be approximated by a Néel or an anti-Néel state.

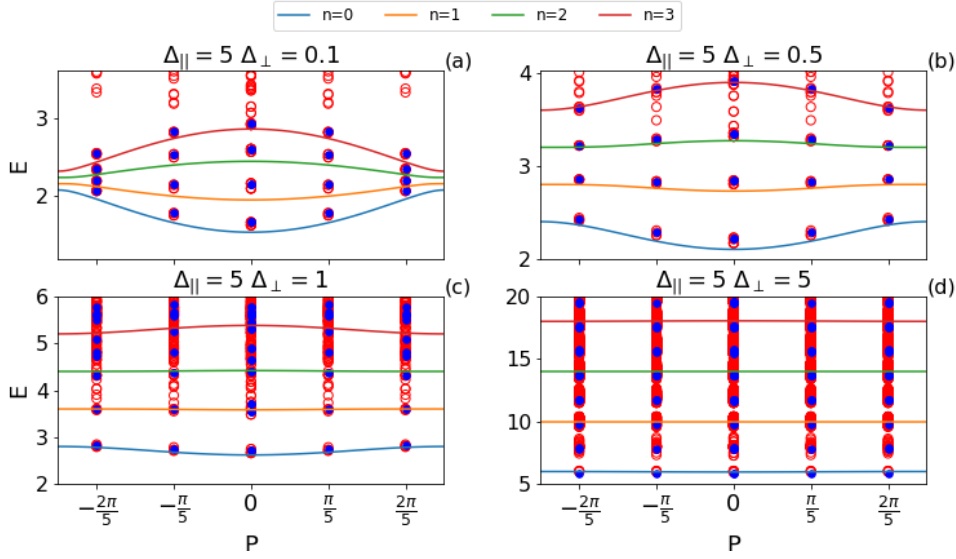


Figure 12.4: Low-lying part of the spectrum in the spin  $s = 0$  sector of the ladder in Eq. (12.2) (red circles) and of the staggered XXZ chain in Eq. (12.3) (blue dots) obtained by exact diagonalization for  $L = 10$ ,  $\Delta_{\parallel} = 5$ , and  $\Delta_{\perp} = 0.1, 0.5, 1, 5$ . The dispersion relations of the mesons in the 2-kink approximation are shown in continuous lines, obtained by solving Eq. (12.6) numerically. The internal quantum number  $n$  is in the legend on top of the plot.

Moreover, the nontrivial scattering properties of those excitations will start to play a role. Both effects will be investigated in the next section.

### 12.1.2 ‘Type 2’ interchain mesons

We now turn to the meson excitations that are formed by two kinks located on different chains (see Fig. 12.2). On a ladder with periodic boundary condition, these states can only exist for  $L$  odd, and they have no equivalent in a staggered XXZ chain.

We can follow steps very similar to those for intrachain mesons in the previous subsection. We first project onto states having one kink on each leg of the ladder. The main difference is that in this case there is no hardcore constraint for the kinks as they can cross by passing above/below each other and hence their wave function is

$$|\Psi_n(s)\rangle = \sum_{j_1=1}^L \sum_{r=0}^{L-1} \phi_n(r|P, s) e^{iP(j_1+r/2)} |K(j_1)\rangle_1 |K(j_1+r)\rangle_2, \quad (12.9)$$

where the subscripts 1, 2 label the legs of the ladder. The spins of the kinks should add up to  $s$ . The center of mass momentum  $P$  is quantized as  $P = k 2\pi/L$ ,  $k = -\lfloor \frac{L}{2} \rfloor, \dots, \lfloor \frac{L}{2} \rfloor$ .

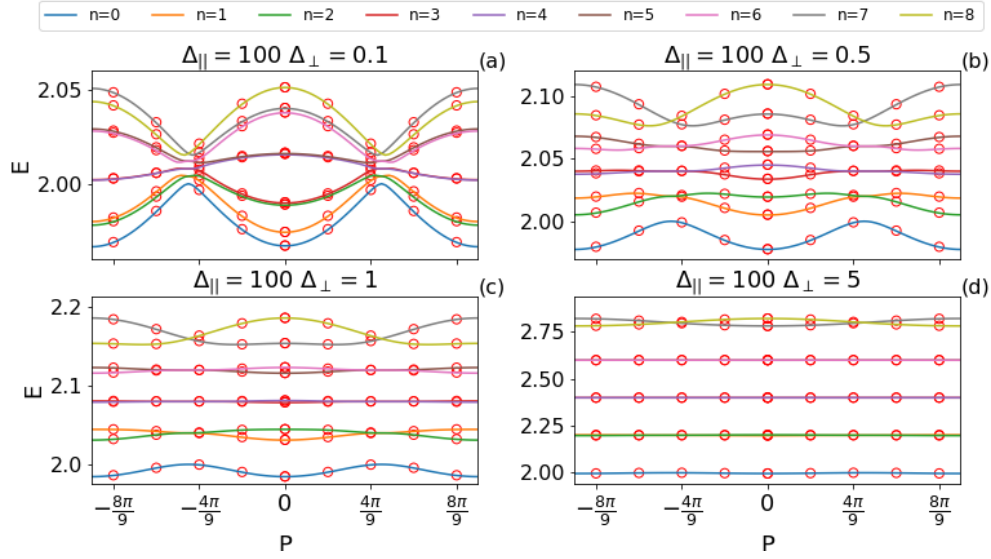


Figure 12.5: Low-lying part of the spectrum in the spin sector  $s = 0$  of the ladder (12.2) (red circles) for  $L = 9$ ,  $\Delta_{\parallel} = 100$ , and  $\Delta_{\perp} = 0.1, 0.5, 1, 5$ . The dispersion relations of the mesons in the 2-kink approximation (12.13) are shown in continuous lines, obtained by solving Eq. (12.10) numerically. The internal quantum number  $n$  is in the legend on top of the plot. Notice many qualitatively different features compared to the ladder of even length in Fig. 12.3.

The equation for the relative wave function in all spin sectors turns out to be

$$(2 + 2\epsilon\Delta_{\perp}\ell_s(r))\phi_n(r) + 2\epsilon\cos(P)[\phi_n(r+2) + \phi_n(r-2)] = E_n(P)\phi_n(r), \quad (12.10)$$

with  $r = 0, 1, \dots, L-1$ . The function  $\ell_s(r)$  is the length of the string between the kinks and is defined as

$$\ell_{s=0}(r) = \begin{cases} r & \text{if } r \text{ even} \\ L-r & \text{if } r \text{ odd,} \end{cases} \quad \ell_{s=\pm 1}(r) = \begin{cases} r & \text{if } r \text{ odd} \\ L-r & \text{if } r \text{ even.} \end{cases} \quad (12.11)$$

Note that swapping the chains corresponds to  $r \leftrightarrow L-r$  which also changes the parity of  $r$ , thus the definitions (12.11) are consistent with this symmetry. The boundary conditions are  $\phi_n(-2) = \phi_n(L-2)$ ,  $\phi_n(2) = \phi_n(L+2)$ , and  $\phi_n(-1) = \phi_n(L-1)$ ,  $\phi_n(1) = \phi_n(L+1)$ . The solutions are given by

$$\phi_n^{(\pm)}(r|P, s) = (\pm)^r N_n^{(\pm)}(P, s) \left[ J_{\nu_n^{(\pm)}(P, s) - \ell(r)/2}(\Delta_{\perp}^{-1} \cos P) + A_n^{(\pm)}(P, s) Y_{\nu_n^{(\pm)}(P, s) - \ell(r)/2}(\Delta_{\perp}^{-1} \cos P) \right], \quad (12.12)$$

where  $N_n^{(\pm)}(P, s)$  is the normalization,  $\nu_n^{(\pm)}(P, s)$  and  $A_n^{(\pm)}(P, s)$  are fixed by the boundary conditions which now relate the wave function at odd and even

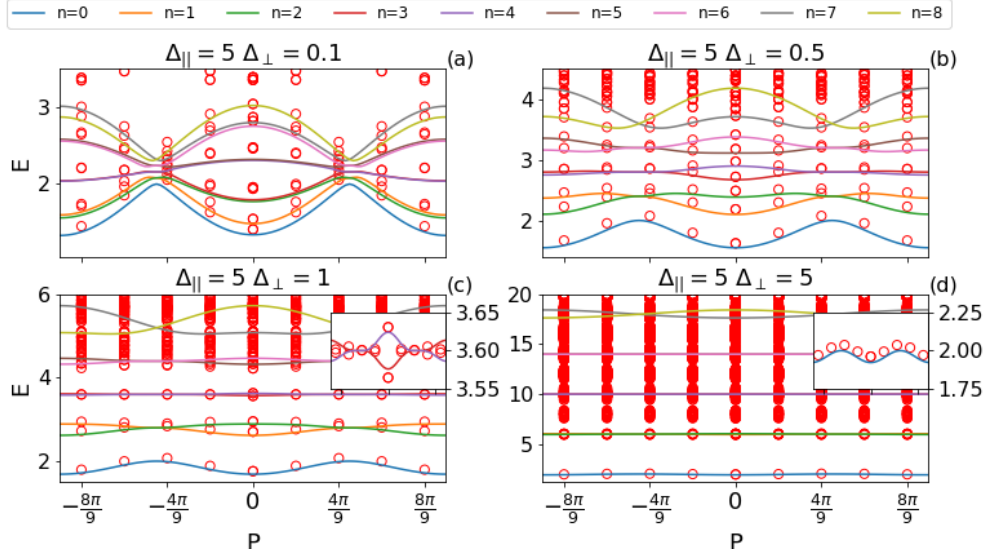


Figure 12.6: Low-lying part of the spectrum in the spin sector  $s = 0$  of the ladder (12.2) (red circles) for  $L = 9$ ,  $\Delta_{\parallel} = 5$ , and  $\Delta_{\perp} = 0.1, 0.5, 1, 5$ . The dispersion relations of the mesons in the 2-kink approximation (12.13) are shown as continuous lines, obtained by solving Eq. (12.10) numerically. The internal quantum number  $n$  is in the legend on top of the plot. The insets show the accuracy of our approximation in resolving the spectrum on a more refined scale.

sites. Notice that the four boundary conditions give only two independent equations.  $\phi_n^{(+)}(r)$  are symmetric, while  $\phi_n^{(-)}(r)$  are anti-symmetric under the exchange  $r \leftrightarrow L - r$ . The energies are given by

$$E_n^{(\pm)}(P, s) = 2 + 4\epsilon\Delta_{\perp} \nu_n^{(\pm)}(P, s). \quad (12.13)$$

In Fig. 12.5 we compare the levels obtained from Eq. (12.13) with the results of exact diagonalization of the ladder Hamiltonian for  $L = 9$  in the spin sector  $s = 0$  for  $\Delta_{\parallel} = 100$  and different values of the interchain coupling  $\Delta_{\perp}$ . Similarly to the intrachain mesons, the spectrum is very well captured by the effective 2-kink description. The figure also demonstrates the richer structure of the ‘Type 2’ interchain mesons as they have about twice as many internal excitations as the ‘Type 1’ intrachain mesons have.

In Fig. 12.6 the same comparison is shown for  $\Delta_{\parallel} = 5$  and various values of  $\Delta_{\perp}$ . Analogously to the case of ‘Type 1’ mesons, the overall structure of the spectrum is captured by the 2-kink approximation in the regions where the bands are well separated. The deviations of exact numerical results from the 2-kink approximation are more pronounced than for  $\Delta_{\parallel} = 100$ , because the dressing of the fundamental excitations becomes relevant for small  $\Delta_{\parallel}$ .

We conclude this section by mentioning that bound states between two coupled 1+1 dimensional models have been observed also in conformal field

theories [367], but in a very different context that does not lead to confinement.

## 12.2 A semiclassical approach for finite $\Delta_{\parallel}$

When approaching smaller values of the anisotropy parameter  $\Delta_{\parallel}$  at  $\Delta_{\perp} = 0$ , the ground state of the model and its fundamental excitations experience significant changes. The doubly degenerate ground states of both chains still have anti-ferromagnetic order but with a smaller average staggered magnetization. The latter is exactly known from the Bethe ansatz solution of the XXZ spin chain and it is given by

$$\bar{\sigma} = \prod_{n=1}^{\infty} \left( \frac{1 - e^{-2n\gamma}}{1 + e^{-2n\gamma}} \right)^2, \quad \Delta_{\parallel} = \cosh(\gamma). \quad (12.14)$$

As  $\Delta_{\parallel}$  decreases, the ground states with the above staggered magnetization are no longer well approximated by a Néel or an anti-Néel state. The elementary excitations are still topological quasi-particles that interpolate between the two vacua, but now they interact in a nontrivial way. In this section we describe how these properties affect the ‘Type 1’ intrachain mesons.

The most pragmatic way to treat the presence of a non-vanishing  $\Delta_{\perp}$  would be a perturbative expansion in small  $\Delta_{\perp}$  around the exact eigenstates at  $\Delta_{\perp} = 0$ . The latter approach is rather technical and involves a Bethe–Salpeter equation with a perturbative form factor expansion. Although less rigorous, here we follow another, more heuristic approach whose main advantage is having a straightforward physical interpretation. Following Ref. [246], the idea is to look for semi-classical bound states of the Hamiltonian

$$H(x_1, x_2, \vartheta_1, \vartheta_2) = \omega(\vartheta_1) + \omega(\vartheta_2) + f(|x_2 - x_1|), \quad (12.15)$$

where

$$f = 2\epsilon\Delta_{\perp}\bar{\sigma}^2, \quad (12.16)$$

is the ‘‘string tension’’ taking into account the average magnetization of both chains, and we introduced the continuum coordinates  $x_1, x_2 \in \mathbb{R}$  and their canonical conjugate momenta  $\vartheta_1, \vartheta_2$ . The function  $\omega(\vartheta)$  is the lattice dispersion relation of the kink quasi-particle obtained by a Bethe Ansatz approach [368]

$$\omega(\vartheta) = \frac{2\epsilon K(k)}{\pi} \sinh \gamma \sqrt{1 - k^2 \cos^2 \vartheta}, \quad (12.17)$$

where  $K(k)$  is the complete elliptic integral whose modulus  $k$  is related to the anisotropy through the relation  $K(\sqrt{1 - k^2})/K(k) = \gamma/\pi$ . The Hamiltonian (12.15) describes the classical motion of two particles experiencing a

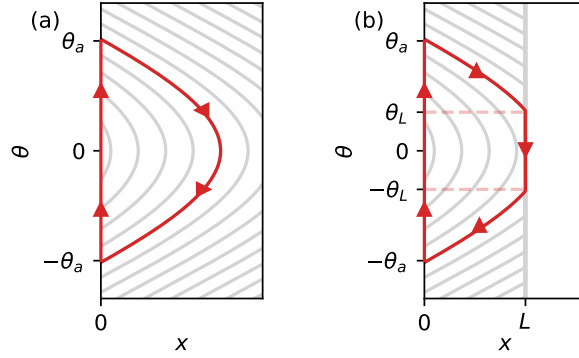


Figure 12.7: Classical trajectories in phase space  $(x, \theta)$  for the Bohr–Sommerfeld quantization. The grey lines are the various trajectories at fixed energy. In infinite volume, the trajectories are always like the red one depicted in (a). In finite volume  $L$  we have a hard cutoff that deforms some trajectories as reported in (b).

long range interaction with kinetic energy given by the exact kinetic energy of a kink of the XXZ chain. After a canonical transformation to center of mass and relative coordinates,

$$X = \frac{x_1 + x_2}{2}, \quad x = x_2 - x_1, \quad (12.18)$$

$$\Theta = \vartheta_1 + \vartheta_2, \quad \vartheta = \frac{\vartheta_2 - \vartheta_1}{2}, \quad (12.19)$$

the Hamiltonian reads

$$H(X, \Theta; x, \vartheta) = \varepsilon(\vartheta|\Theta) + f|x|, \quad (12.20)$$

with  $\varepsilon(\vartheta|\Theta) = \omega(\Theta/2 - \vartheta) + \omega(\Theta/2 + \vartheta)$ . In these new variables, the equations of motion are

$$\dot{X} = \frac{\partial \varepsilon}{\partial \Theta}, \quad \dot{\Theta} = 0, \quad (12.21)$$

$$\dot{x} = \frac{\partial \varepsilon}{\partial \vartheta}, \quad \dot{\vartheta} = -f \operatorname{sgn}(x). \quad (12.22)$$

The total momentum  $\Theta$  is an integral of motion as well as the energy

$$E = \varepsilon(\vartheta|\Theta) + f|x|. \quad (12.23)$$

The bound state energies can be obtained via the Bohr–Sommerfeld quantization condition which reads as

$$\oint \vartheta dx = 2\pi(n + \delta), \quad n = 0, 1, 2, \dots, \quad (12.24)$$

where the integral is taken over the closed path in the  $(\vartheta, x)$  classical phase space, and  $\delta$  is a phase shift discussed below. In principle, the energies obtained from this equation become more and more accurate with increasing  $n$ . For simplicity, we restrict the analysis to the case when  $\varepsilon(\vartheta|\Theta)$  has a single minimum at  $\vartheta = 0$  which holds for  $\Theta < \Theta_c = \arccos\left(\frac{1-\sqrt{1-k^2}}{1+\sqrt{1-k^2}}\right)$  [251]. The path is an arc in the  $x > 0$  half plane (see Fig. 12.7-a) parameterized using Eqs. (12.23) and (12.22) starting from  $x(0) = 0^+$ ,  $\vartheta(0) = \vartheta_a$  :

$$x(t) = \frac{E - \varepsilon(\vartheta(t)|\Theta)}{f}, \quad (12.25)$$

$$\vartheta(t) = \vartheta_a - ft, \quad (12.26)$$

where  $\vartheta_a$  satisfies  $E = \varepsilon(\vartheta_a|\Theta)$ . The turning point is at

$$x_{\max} = \frac{E - \varepsilon(0|\Theta)}{f}, \quad (12.27)$$

and is reached at time  $t_{\max} = \vartheta_a/f$ . After another  $t_{\max}$  time elapses, the two kinks scatter at  $x(2t_{\max}) = 0$  which abruptly flips the sign of  $\vartheta$ , so the phase space path is closed by a straight segment at  $x = 0$  connecting  $-\vartheta_a$  with  $\vartheta_a$ . These phase space paths are reported in Fig. 12.7-a. The left hand side of Eq. (12.24) reads

$$\begin{aligned} \oint \vartheta dx &= - \int_{-\vartheta_a}^{\vartheta_a} d\vartheta \vartheta \frac{dx(\vartheta)}{d\vartheta} = -\frac{1}{f} \int_{-\vartheta_a}^{\vartheta_a} d\vartheta \vartheta \dot{x}(\vartheta) \\ &= \frac{1}{f} \int_{-\vartheta_a}^{\vartheta_a} d\vartheta \vartheta \frac{\partial \varepsilon(\vartheta|\Theta)}{\partial \vartheta} = \frac{1}{f} \left( 2E\vartheta_a - \int_{-\vartheta_a}^{\vartheta_a} d\vartheta \varepsilon(\vartheta|\Theta) \right), \end{aligned} \quad (12.28)$$

where Eq. (12.22) was used to trade the time derivative for a derivative with respect to  $-\vartheta$ .

The phase shift  $\delta$  receives two kinds of contributions. First, at the regular turning point there is a  $\pi/2$  phase shift ( $\delta = 1/4$ ). Second, at  $x = 0$  we have to take into account the scattering phase shift of the particles. In the Ising regime  $\Delta_{\parallel} \gg 1$ , the kinks behave as free hard core particles, so their scattering phase shift is simply  $\pi$ . This is equivalent to enforcing that the relative wave function vanish at the origin, and leads to  $\delta = 1/2$ , the same as for a particle suffering a hard reflection. Away from the Ising limit the kinks have a nontrivial, momentum-dependent scattering phase shift  $\phi_{\eta}(p_1, p_2)$  that can be obtained via Bethe ansatz (see Appendix C.7 for its detailed expression). The index  $\eta$  accounts for the spins of the kinks and will be dropped from now on to simplify the notation. This phase needs to be added to the left hand side of Eq. (12.24), which leads to

$$2E(\vartheta_a) - \int_{-\vartheta_a}^{\vartheta_a} dq \varepsilon(\vartheta|\Theta) = 2\pi f \left( n + \frac{3}{4} \right) + f \phi \left( \frac{\Theta}{2} - \vartheta_a, \frac{\Theta}{2} + \vartheta_a \right). \quad (12.29)$$

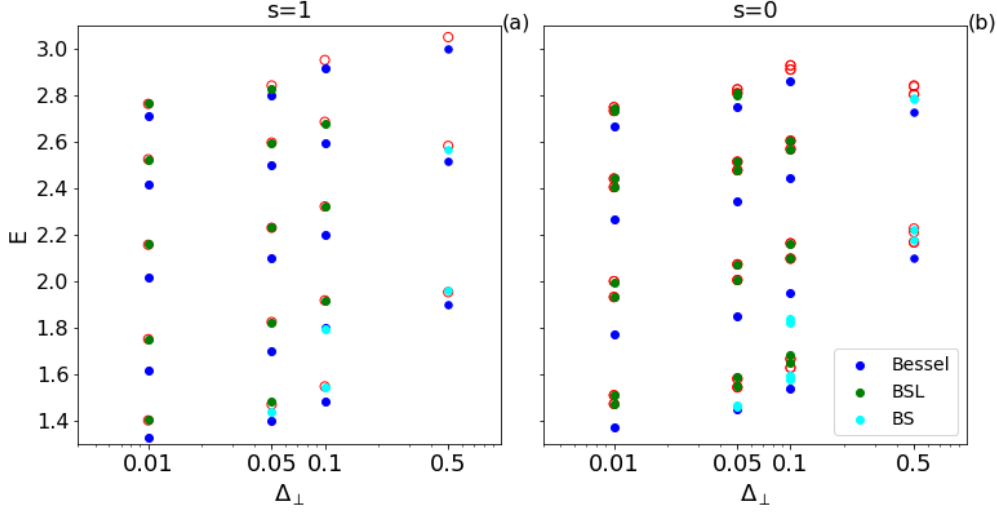


Figure 12.8: Comparison of various approximations for the intrachain meson energies at  $\Delta_{\parallel} = 5$  in the sectors with spin  $s = 0$  (right) and  $s = 1$  (left), both with total momentum  $P = 0$ . The exact diagonalization results are shown in red empty circles. The full symbols correspond to the 2-kink approximation of Sec. 12.1.1 (“Bessel”), the infinite volume semiclassical (“BS”) and the finite volume semiclassical (“BSL”) results according to the color code shown in the legend.

The procedure has to be modified in finite volume, when the maximum separation  $x_{\max}$  can become larger than the system size  $L$ . There are two possible cases depending on the value of  $x_{\max}$ . If  $x_{\max} < L$ , then the energy levels are given by the solutions of Eq. (12.29), while for  $x_{\max} > L$  the system does not reach the turning point but experiences another scattering at  $x = L$ . The integration paths in phase-space are shown for the two cases in Fig. 12.7-b.

Let us denote by  $\vartheta_L$  the momentum right before the reflection at  $x = L$ . Then the momentum  $\vartheta$  jumps from  $\vartheta_L$  to  $-\vartheta_L$  so the arc in the phase space is chopped to have a flat part at  $x = L$ . As a consequence, the new quantization equation reads

$$\begin{aligned}
 & 2f\vartheta_L L + 2E(\vartheta_a - \vartheta_L) - 2 \int_{\vartheta_L}^{\vartheta_a} dq \varepsilon(q|\Theta) \\
 & = 2\pi f(n+1) + f\phi\left(\frac{\Theta}{2} - \vartheta_a, \frac{\Theta}{2} + \vartheta_a\right) + f\phi\left(\frac{\Theta}{2} - \vartheta_L, \frac{\Theta}{2} + \vartheta_L\right),
 \end{aligned} \tag{12.30}$$

together with the conditions  $\varepsilon(\vartheta_a|\Theta) = E$  and  $\varepsilon(\vartheta_L|\Theta) = E - fL$ .

We compare the predictions for the intrachain meson energies with spin  $s = 0$  at  $P = \Theta = 0$  (meson mass gaps) of the 2-kink effective equation



Figure 12.9: Schematic pictures of 4-kink states for a ladder of even length: (a) a 4-kink state composed of two intrachain mesons and (b) a 4-kink state composed of two interchain mesons.

(12.6) and those of the semiclassical quantization (12.29), (12.30) with exact diagonalization data of the ladder at  $\Delta_{\parallel} = 5$  in Fig. 12.8. The plot clearly shows that while the 2-kink approximation with hard-core kinks breaks down, the (finite volume) semiclassical approximation yields an excellent agreement with the exact diagonalization results. Thanks to the spin-dependent phase shift, this approximation also predicts the energy splitting for the case  $s = 0$ , which partially lifts the degeneracy of the spectrum (from four-fold to two-fold) in the thermodynamic limit and cannot be captured with the first approach. Remarkably, even though the semiclassical method is supposed to work well for high energy bound states with large quantum numbers, it gives accurate results even for the lowest lying mesons.

## 12.3 Composite excitations

We recall that in the regime  $\Delta_{\parallel} \gg 1$  and  $\Delta_{\parallel} \gtrsim \Delta_{\perp}$ , the energy spectrum of the Hamiltonian (12.1) is organized in bands of states with a given number of kinks, as shown in Fig. 12.1. In the previous two sections, we developed an effective systematic description for the low lying 2-kink states. Here, we introduce a more heuristic treatment to grasp the nature of some of the higher excited states. We focus on the case of even  $L$  and zero magnetization in both chains, i.e.,  $M_1 = M_2 = 0$ .

The first class of states lying above the 2-kink ones are obviously the four-kink states. For even  $L$ , the latter can either be a combination of two intrachain (Fig. 12.9-a) or of two interchain mesons (Fig. 12.9-b). Notice that for odd  $L$  we instead have only combinations of one intrachain and one interchain meson, a situation that we do not describe here. In the zeroth order approximation in which we neglect the interaction between mesons, the energy levels of the four-kink states is just the sum of the dispersion relations obtained in the preceding sections for the single mesons, i.e.,

$$E(n_1, n_2, p, P) = \frac{1}{2} \left[ E_{n_1} \left( \frac{P}{2} + p \right) + E_{n_2} \left( \frac{P}{2} - p \right) + \{n_1 \leftrightarrow n_2\} \right], \quad (12.31)$$

where  $n_1$  and  $n_2$  collectively label the internal states of the mesons,  $p = (p_1 - p_2)/2$  is the relative momentum and  $P = p_1 + p_2$  is the total momentum

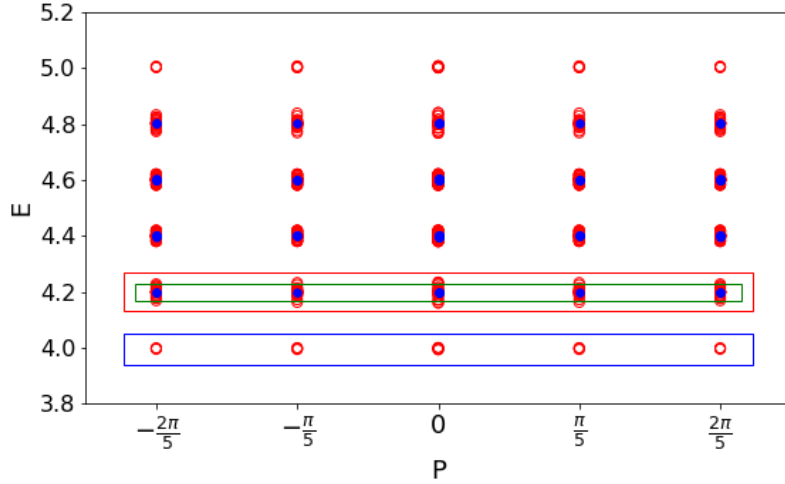


Figure 12.10: Spectrum of the ladder (red circles) and the staggered XXZ chain (blue dots) for energies in the interval  $E \in [4, 5]$  where four-kink states lie for large  $\Delta_{\parallel}$ . We report data for the zero magnetization sector in both chains  $M_1 = M_2 = 0$ . We work at  $\Delta_{\perp} = 5$ ,  $\Delta_{\parallel} = 100$ , and  $L = 10$ . The blue, red, and green rectangles are the regions that are magnified in Fig. 12.11.

of the mesons. The labels  $n_{1,2}$  are assigned from the less energetic to the most energetic internal states at  $P = 0$ . Since we are treating the two mesons as non-interacting particles, we have some strong constraints on the allowed values of the relative momentum  $p$ . First, the finite-volume quantization of  $p$  is affected by the reduced effective volume where the kinks can move freely due to the constraint that they cannot overlap. Accordingly, the relative momentum is quantized as  $p = m\pi/L_{\text{eff}}$  with  $m$  integer. The effective available volume is  $L_{\text{eff}} = L - 2$  for two interchain mesons (two kinks on each chain) and  $L_{\text{eff}} = L - 4$  for two intrachain mesons (the four kinks are all on the same chain). Moreover, since they cannot overlap, the states with  $p = 0$  are forbidden. These two reasonable assumptions will be justified also a posteriori by the correct description of the relevant part of the energy spectrum.

The approximation of non-interacting mesons works for large enough  $\Delta_{\perp}$  and in the limit  $\Delta_{\parallel} \gg 1$ . Indeed, when  $\Delta_{\perp}$  becomes too small, the internal oscillations of each meson become so wide that the 4-kink states cannot be interpreted as a composition of separate mesons. Furthermore, this approximation is not expected to be effective for large  $n_{1,2}$  because higher meson states have a more extended wave function (as it can be immediately deduced by looking at the spreading of the Bessel functions with respect to their index).

We compare the spectra of the ladder and of the staggered XXZ chain in Figs. 12.10 and 12.11. In the former figure we report all states in the

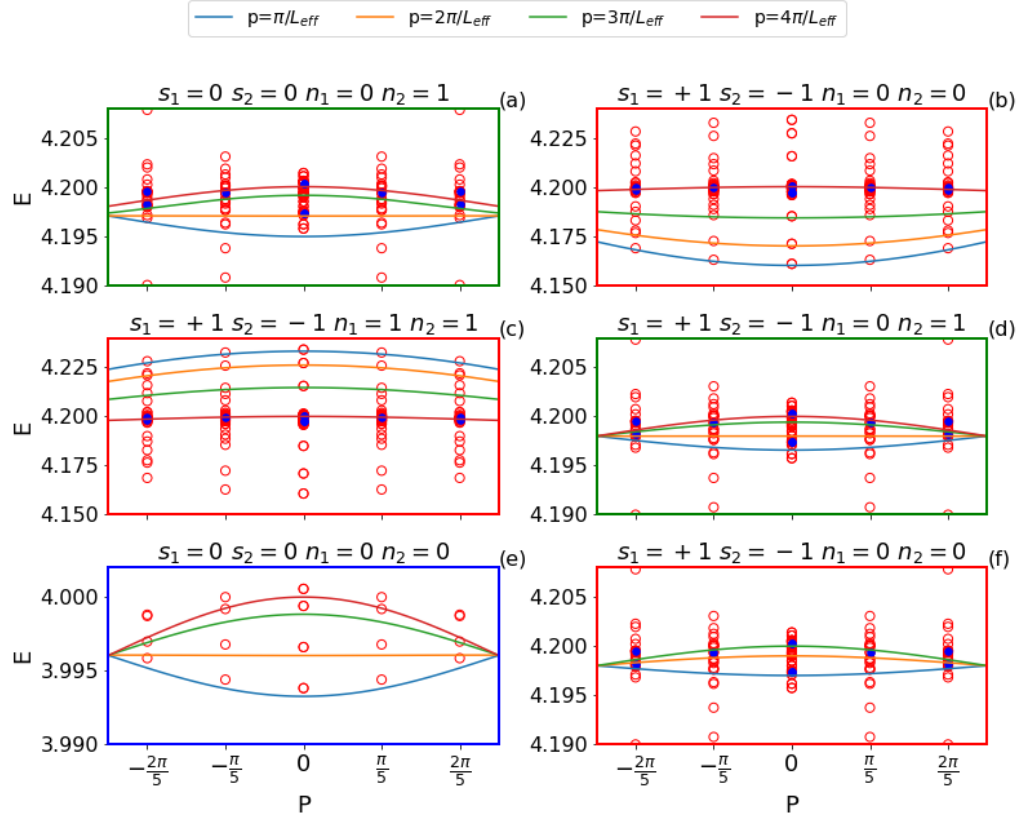


Figure 12.11: Zooms of the marked areas in Fig. 12.10. The different symbols are the numerical data. The frame colors (red, green, and blue) correspond to the colors of the rectangles in Fig. 12.10. The green area is a further zoom of the red one. The continuous lines correspond to the noninteracting two-meson approximation (12.31) for interchain ‘Type 2’ (a,b,c,d,e) and intrachain ‘Type 1’ (f) mesons. Each panel shows these approximate energy levels for fixed values of the spins and internal labels of the mesons corresponding to the quantum numbers reported above each panel. The different lines correspond to different values of the relative momentum  $p$  reported in the legend on top of the plot.  $L_{\text{eff}} = L - 2$  or  $L_{\text{eff}} = L - 4$  for interchain and intrachain mesons, respectively.

energy interval  $[4, 5]$  and identify some smaller windows (indicated by large rectangles) that are analyzed in detail in the latter figure. The first simple fact evident in both figures is that there are many more 4-kink states in the ladder than in the chain, reflecting the presence of interchain mesons which do not exist on the chain. Hence, for the 4-kink states, the mean-field treatment does not predict much.

We present a more quantitative analysis in Fig. 12.11. Here we zoom in the regions within the colored rectangles in Fig. 12.10. The spectrum in these windows is compared with the energy levels computed with Eq. (12.31). Notice that the red rectangle appears three times and the green

one twice, where the green area is a further zoom of the red one. We make this choice because we plot the dispersion relation with different quantum numbers that cannot be put on the same graph in a clear manner. On top of each panel we report the quantum numbers corresponding to the spin and the internal energy levels of the mesons that are displayed in the plot.

Despite the roughness of the approximation, it is remarkable that Eq. (12.31) captures some features of the spectrum. For example, the four dispersions plotted in the frames (b) and (c) very neatly describe families of states that are well separated from each other. Also in panel (f), the intrachain states (that exist also for the staggered chain but with different momentum quantization, as it is clear from the fact that they alternate) are well captured by our approximation. Instead, resolving the states within the green frames in Figs. 12.11 is beyond the purpose of our approximation. It is a dense region where the separation of the states is comparable to higher perturbative orders in  $\epsilon$  that are neglected in our description. On the other hand, all the states that are sufficiently isolated in the spectrum (on an energy scale of order  $\epsilon$ ), are well captured by this approximation. We remark that while, in virtue of confinement, the single-meson bands described in Sec. 12.1 remain discrete and well separated in energy when  $L$  goes to infinity, the two-meson bands become denser and fall in the continuum part of the spectrum.

## 12.4 A transition for the first excited states

We have already shown in Sec. 12.1 that, in the limit of large  $\Delta_{\parallel}$  and moderate  $\Delta_{\perp}$ , the low-lying excitations of a ladder with even  $L$  in the sector of zero magnetization are well captured by an effective model of a spin chain in staggered field; the lowest excitations are intrachain ('Type 1') mesons, confined bound states of kinks. Decreasing the value of  $\Delta_{\parallel}$ , we observe that the nature of the first excited states changes qualitatively. This can be understood from a simple classical argument. The lowest lying intrachain meson (Fig. 12.12-a) has energy  $E_{\text{intra}} \simeq 2 + 4\Delta_{\perp}/\Delta_{\parallel}$ , while the least energetic interchain meson (Fig. 12.12-b) has  $E_{\text{inter}} \simeq 2$ . Despite being less energetic, we cannot find this interchain excitation in the low-energy spectrum in the zero-magnetization sector, because, as discussed in Sec. 12.1.2, a single meson of this type carries magnetizations  $s_{1,2} = \pm 1/2$  on the two chains and it is only compatible with odd  $L$ . However, when  $\Delta_{\parallel}$  is sufficiently small, the energy of the first intrachain meson becomes so large that it is comparable with the energy  $2E_{\text{inter}} \simeq 4$  of a two-meson state of 'Type 2' (Fig. 12.12-c). This happens when  $2E_{\text{inter}} = E_{\text{intra}}$ , i.e. for  $\Delta_{\parallel} \sim 2\Delta_{\perp}$ .

We illustrate this transition in Fig. 12.13 for  $\Delta_{\parallel} = 100$  and  $\Delta_{\parallel} = 5$  by showing all the numerically calculated zero-momentum eigenstates in the relevant energy range as functions of  $\Delta_{\perp}$ , for  $\Delta_{\perp}$  around  $\Delta_{\parallel}/2$ . The blue

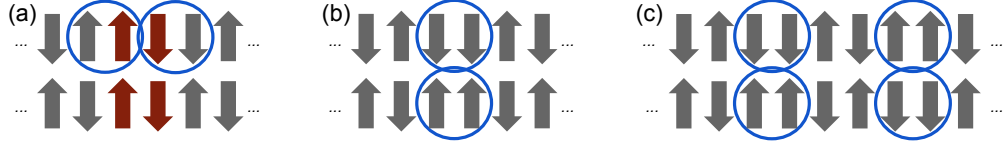


Figure 12.12: Schematic pictures of the lowest-lying (a) intrachain and (b) interchain mesons. For  $\Delta_{\perp} \lesssim 2\Delta_{\parallel}$  the intrachain meson (a) represents the first excited state. In the regime  $\Delta_{\perp} \gtrsim 2\Delta_{\parallel}$  the low-energy sector is made of states with pairs of interchain mesons (c).

dots represent the ‘Type 1’ intrachain single meson states of the staggered XXZ chain. As expected, when  $\Delta_{\perp} \approx \Delta_{\parallel}/2$ , the two kinds of states become nearly degenerate. At this point, the single meson and the 2-meson states hybridize. As the interchain two-meson states are invariant under the chain swap transformation, they only hybridize with intrachain meson states that are also invariant under chain swapping.

The observed phenomenon is not a quantum phase transition as it does not concern the ground state but the excited states. As a matter of fact, similar “transitions” take place already for smaller  $\Delta_{\perp}$  at higher energy levels involving states with more kinks and mesons. Nonetheless, the change in the nature of the low-energy sector has important physical consequences. It can be observed, for example, in the non-equilibrium dynamics after a quantum quench, where the spreading of correlations is determined by the quasiparticle excitations. While in the absence of confinement excitations can propagate freely, in the presence of an attractive potential quasiparticles get confined into mesons and hence the spreading of entanglement and correlations is suppressed. This is what we expect when  $\Delta_{\parallel} \gtrsim 2\Delta_{\perp}$ . Conversely, for  $\Delta_{\parallel} \lesssim 2\Delta_{\perp}$ , the low-energy sector is a continuum of two-meson states: while kinks are still confined in mesons, the spreading of correlation is not suppressed because the pairs of mesons are free to move with opposite momenta. Therefore, in a quench a dramatic difference between the two regimes is likely to emerge.

## 12.5 Conclusions

In this manuscript we systematically characterized the spectrum of the Heisenberg-Ising ladder with Hamiltonian (12.1) in the region of parameters presenting confinement, i.e. in the ordered antiferromagnetic phase of the two chains for  $\Delta_{\parallel} > 1$ . Our main result is that we find two kinds of quasiparticle excitations, which we dub intrachain and interchain mesons, that correspond to bound states of kinks within the same chain or between different ones, respectively. Very importantly, intrachain mesons can be also obtained by means of a mean field treatment mapping the Hamiltonian to a staggered chain. Interchain mesons are genuine features of the

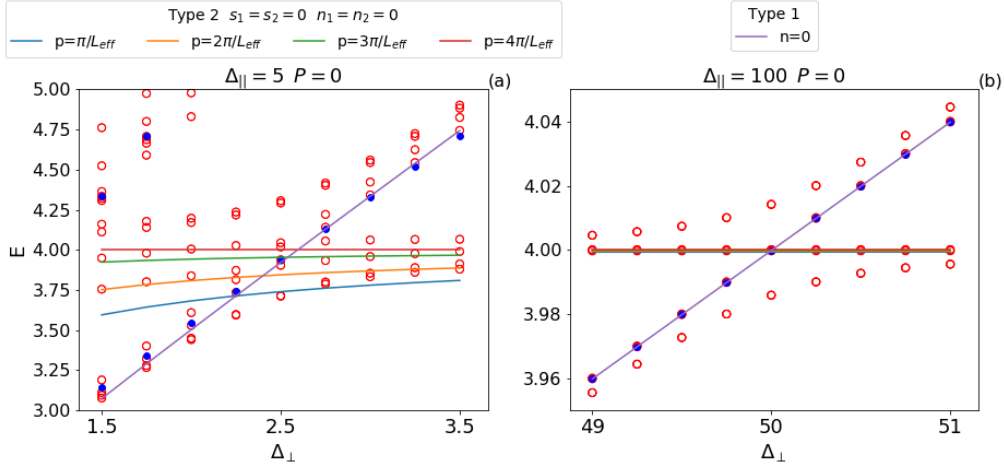


Figure 12.13: Spectrum on the ladder (red circles) and on the staggered chain (blue dots) around the level crossing near  $\Delta_{||} \approx 2\Delta_{\perp}$ . The violet solid line shows the numerical prediction for the first level of intrachain mesons computed using Eq. (12.6). The other lines are extracted from Eq. (12.31) for two interchain mesons with  $s_1 = s_2 = 0$  and  $n_1 = n_2 = 0$  like in Fig. 12.11-e. The corresponding quantum numbers are shown in the legend.

ladder and they were not known by other means. They are expected to be a common characteristic of ladders with Ising-like rung interactions that lead to confinement. In fact, their existence is a consequence of the spontaneous breaking of one symmetry. Hence, there are two equivalent true vacua and neutral mesons can interpolate between the same or different ones. One-particle intrachain (interchain) mesons are present only when the total ladder has even (odd) length. Conversely, two-particle states of interchain mesons are present also for even  $L$ .

We quantitatively characterize the meson states. First, in the limit of large  $\Delta_{||}$  we find the one-particle meson dispersion by projecting on the two-kink subspace. We release the condition of very large anisotropy exploiting semiclassical quantization. We also describe the four-kink (two mesons) states in the dilute approximation, i.e., treating the two mesons as non-interacting particles. Finally, we point out an interesting transition for the first excited state in even length ladders. At fixed  $\Delta_{||}$ , the first excited state is a one-particle intrachain meson state for small  $\Delta_{\perp}$ , but as the latter is increased it crosses over to a two interchain meson state.

We finally discuss some lines of future research. A first question concerns the physics of more than two coupled chains (e.g., three for a start). Are there new kinds of bound states that can emerge from the enlarged local Hilbert space? It would be interesting to investigate also the case of anisotropic Heisenberg-like (XXZ) interchain coupling which is more relevant to experiments on spin-chain compounds. Another interesting question concerns the influence of these bound states on the non-equilibrium quench

dynamics, a subject that, as mentioned in the introduction, is nowadays under intense scrutiny. We plan to address this interesting topic in a future work.



# Chapter 13

## Breakdown of ergodicity in disordered $U(1)$ lattice gauge theories

Ergodicity is one of the pillars of statistical mechanics. In the quantum regime, the ergodic hypothesis and the corresponding eigenstate thermalization hypothesis (ETH) [19, 20] provide a sensible justification for the use of microcanonical and canonical ensembles *in lieu* of their Hamiltonian dynamics to compute long term averages of observables (see Section 1.1). An established mechanism to circumvent thermalization is provided by Anderson localization [27]. The latter describes how non-interacting systems can feature a dynamical phase in which diffusion (and hence transport) and ergodicity are suppressed without any need to fine-tune the Hamiltonian to an integrable one. Remarkably, this mechanism has been shown to survive the introduction of interactions at the perturbative level [28, 369], a phenomenon dubbed many-body localization (MBL) [16, 17, 370, 371]. However, owing to the fundamentally more complex nature of many-body theories, establishing the breakdown of ergodicity and characterizing the ergodic/non-ergodic transition in generic, interacting microscopic models has proven challenging. At the practical level, this is due to the fact that quantum chaos (which underlies ETH) is ultimately linked to the full spectral content of a theory [372], where the applicability of analytical techniques is less established compared to low-energy studies [28, 369, 373–380].

An archetypal example in this field has been the one-dimensional (1D) Heisenberg model with random fields [31], where, in the absence of  $SU(2)$  symmetry [381–384], first signatures of the breakdown of ergodicity were established at finite volume. Despite a follow-up impressive numerical effort [34, 385–389], the precise location of the localization transition in this and similar microscopic models is still actively debated. A systematic drift of the would-be critical disorder strength was noticed already as early as in Ref. [31]. The finite-size scaling theory close to the phase transition is also still far from being satisfactory, with the numerically extracted critical

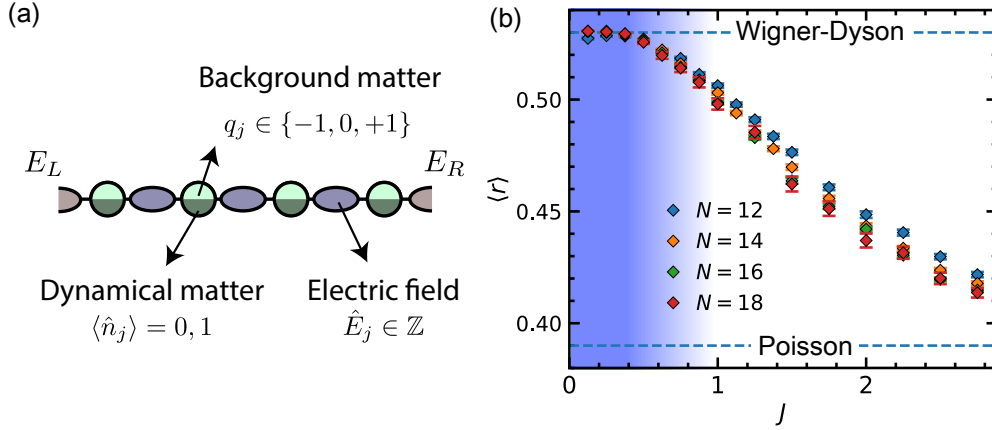


Figure 13.1: (a) Schematics of  $U(1)$  lattice gauge theories. The  $U(1)$  gauge field lives on links between the sites of the chain. Dynamical matter (dark green) is a fermionic variable living on the sites, while static charges (light green) are random integers which take values  $0, \pm 1$ . (b) Average level spacing ratio (see Eq. (13.5)) as a function of the gauge coupling  $J$  for different  $N$  (see text). The shaded region represents the estimated ergodic phase.

exponents [34, 387, 390] at odds with strong disorder renormalization group predictions [391, 392], and not compatible with the Harris criterion [393, 394]. A recent analysis based on a different finite-size scaling ansatz was proposed where the transition point drifts *linearly* with system sizes [395], which however seems to apply, at small sizes, also to models where localization is demonstrated on solid grounds [396, 397]. On top of this, a recent analysis discussed how large a system size one should analyze to go beyond the transient behavior in numerical or experimental studies [398]. The challenge is thus to identify generic mechanisms where, oppositely to the case of spin chains, interactions and disorder can cooperate (rather than compete) in establishing ergodicity breaking, potentially leading to completely novel scenarios in terms of finite-size scaling relevant to exact simulations and experiments [399, 400].

In this work, we show how lattice gauge theories (LGTs) provide a framework within which the transition between ergodic and non-ergodic behavior can be studied using conventional, well controlled numerical methods. The key element of this observation is the *cooperative* effect of disorder and Coulomb law, which leads to a localization phenomenon that - as we show below - is parametrically different from that observed in other models. Specifically, we illustrate this mechanism in the context of the 1D lattice Schwinger model - quantum electrodynamics in 1D, illustrated schematically in Fig. 13.1(a). A sample of our results is depicted in Fig. 13.1(b), which shows the average level spacing ratio, as a function of the gauge coupling. The results display a sharp departure from Wigner-Dyson expectations, and, crucially, the transition point from the corresponding plateau

is unaffected by finite-volume effects. This behavior reflects into a modified functional form of the spectral form factor, which is not compatible with ergodicity.

Before entering into the details of our treatment, we find useful to illustrate a qualitative reasoning why 1D gauge theories may be an ideal candidate to display a smoother behavior in terms of finite volume effects, and a clearer breakdown of ergodicity. In the typical Basko-Aleiner-Altshuler (BAA) scenario [28], interactions open up channels for delocalization by allowing a series of local rearrangements to create a resonance between two quantum states. This leads to a competition between disorder and interactions. In the presence of one-dimensional Coulomb law, interactions cannot be introduced perturbatively and therefore a BAA-like analysis does not work. This is because a local rearrangement of the degrees of freedom (spins or particle occupation numbers) leads to a large (even extensive) change in energy, therefore suppressing the amplitude of having a resonant process. This behavior is unrelated to the case of non-confining long range interactions (e.g., which decay like  $1/r^\alpha$ ,  $\alpha > 0$ , see Ref. [401–403]), and is reflected in finite-volume properties observed in previous numerical studies [208, 404, 405], that focused on quench dynamics and local observables. More quantitatively, the relative strength of the interaction term w.r.t. the hopping term scales as  $L^{-\alpha}$ , hence for  $\alpha > 0$  the effect of disorder in the charge distribution would not be enhanced but suppressed.

## 13.1 Model Hamiltonian

We focus here on the 1D version of quantum electrodynamics, namely the Schwinger model [189] in its Kogut-Susskind lattice regularized version [141] introduced in Section 5.1.1. The two components of a Dirac spinor (electron and positron) sit on even and odd sites. The corresponding Hamiltonian on an open chain of  $N$  sites reads:

$$\begin{aligned}
 H = & -iw \sum_{n=1}^{N-1} (\psi_n^\dagger e^{i\varphi_{n,n+1}} \psi_{n+1} - h.c.) \\
 & + J \sum_{n=0}^N (L_{n,n+1} - \theta/2\pi)^2 + m \sum_{n=1}^N (-1)^n \psi_n^\dagger \psi_n \quad (13.1)
 \end{aligned}$$

Matter and gauge degrees of freedom are, respectively,  $N$  spinless fermions  $\psi_n$  living on the sites and  $N + 1$  unbounded bosons  $L_{n,n+1}$  living on the links.  $L$  and  $\varphi$  stand for electric field and vector potential, and they are conjugate variables:  $[L, \varphi] = -i$ ;  $\theta$  is the lattice version of a topological angle, that we used below to tune between confined ( $\theta \neq \pi$ ) and deconfined ( $\theta = \pi$ ) regimes [144]. Physical states  $|\Psi\rangle$  in the Hilbert space satisfy Gauss law:  $(L_{n+1,n} - L_{n,n-1} - \psi_n^\dagger \psi_n + \frac{1}{2}[1 - (-1)^n]) |\Psi\rangle = q_n |\Psi\rangle$ . The  $\{q_n\}$  are

numbers representing the static charge distribution. We set  $m = 0$  and  $w = 1$  in what follows (the mass term is not essential for the phenomenon we describe).

Disorder-free many-body localization dynamics in this system has been reported in Ref. [208]. There, the idea was to use superselection sectors in a clean system as an effective source of correlated disorder. Other signatures of MBL in the presence of disordered on-site potentials were reported in Ref. [405]. Here, instead, we study the system properties to the presence of random, static background charges, that we randomly choose in the set  $q_j = \{0, \pm 1\}$  with equal probability.

The Hamiltonian Eq. (13.1) can be mapped into a spin-1/2 chain with standard techniques (see Section 5.3). We define  $\sigma^\alpha$  as the standard Pauli matrices. The resulting Hamiltonian reads:

$$H_0 = H_{\text{Hop}} + JH_{\text{Int}} + JH_{\text{Dis}} \quad (13.2)$$

where  $H_{\text{Hop}}$  is just the hopping term  $H_{\text{Hop}} = -\sum_{n=1}^{N-1} (\sigma_n^+ \sigma_{n+1}^- + \text{h.c.})$ , while the second and third terms read

$$H_{\text{Int}} = \frac{1}{2} \sum_{n=1}^{N-2} \sum_{\ell=n+1}^{N-1} (N - \ell) \sigma_n^z \sigma_\ell^z, \quad (13.3)$$

$$H_{\text{Dis}} = \frac{1}{2} \sum_{n=1}^{N-1} \left( \sum_{\ell=1}^n \sigma_\ell^z \right) \left[ 2 \sum_{j=1}^n q_j + \frac{(-1)^n - 1}{2} - \frac{\theta}{\pi} \right] \quad (13.4)$$

and describe the Coulomb interaction between dynamical charges (both terms), and the interaction between dynamical and static ones (the last term). Note that the parameter  $J$  measures at the same time disorder and interaction strength. The intimate relation between these two quantities is a natural consequence of the existence of Coulomb law: in any local theory in 1D, local background charges will inevitably generate a sink (or source) of the electric field, and thus their effect on the system is tied to the gauge coupling.

Below, we consider only static charge distributions such that  $\sum_n q_n = 0$  and  $q_n = 0, \pm 1$ . We set the left boundary electric field  $L_{0,1} = 0$  and restrict to charge neutrality,  $\sum_n \psi_n^\dagger \psi_n = 0$ . In order to avoid spurious effects close to  $J = 0$  due to the system becoming non-interacting, we add a next-to-nearest-neighbor interaction of the form  $H_\epsilon = \epsilon \sum_{n=1}^{N-2} \sigma_n^z \sigma_{n+2}^z$  and set  $\epsilon = 0.5$ .

## 13.2 Spectral diagnostics: average level spacing ratio

To capture the breakdown of ergodicity, we focus on spectral properties. We study the Hamiltonian in Eq. (13.2) by full diagonalization in the Hilbert

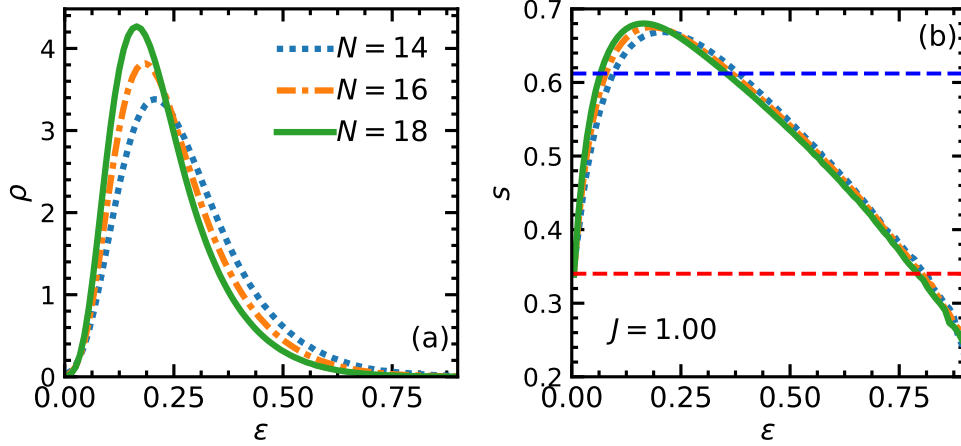


Figure 13.2: Spectral density (a) and entropy per site (b) of the Hamiltonian Eq. (13.1) for different  $N$  and  $J = 1$  as a function of the rescaled energy  $\varepsilon = (E - E_{\min})/(E_{\max} - E_{\min})$ . The blue dashed lines cut the spectrum keeping only the eigenvalues  $E$  s.t.  $s(E)/s_{\max} > A$ . We employed  $A = 0.5$  for the computation of the level statistics  $r$  (red) and  $A = 0.9$  for the computation of the spectral form factor (blue).

space sector with zero total spin along  $z$ . In the gauge theory picture, this means zero dynamical total charge. We define the ratio between nearby gaps as

$$r_{\alpha} = \frac{\text{Min}\{\Delta E_{\alpha}, \Delta E_{\alpha+1}\}}{\text{Max}\{\Delta E_{\alpha}, \Delta E_{\alpha+1}\}} \quad (13.5)$$

here  $\alpha$  labels the eigenvalues of  $H$  for a given disorder realization. We average  $r$  over a spectral window centered on the most-likely eigenvalue, and over 1000 and 100 disorder realizations for  $N < 18$  and  $N = 18$  respectively.

As illustrated in Fig. 13.2 (a), the Coulomb interaction makes the eigenvalue distribution  $\rho$  strongly asymmetric, due to the super-linear scaling of the largest eigenvalues in the spectrum. We thus cut the tails of the spectral density  $\rho$  by monitoring the thermodynamic entropy per site:  $s = \log \rho/L$ . To compute the level statistics  $r$  we keep only the eigenvalues  $E$  for which  $s(E)/s_{\max} > 0.9$  (blue dashed line in Fig. 13.2 (b)). This is illustrated in Fig. 13.3(a), where the energy resolved  $r$ -value is plotted as a function of gauge coupling and energy density<sup>1</sup>. Considering the full spectrum does not lead to quantitative changes in the transition region.

The resulting scaling of  $r$  versus  $J$  is plotted in Fig. 13.1. The results illustrate how compatibility with a Wigner-Dyson distribution of the energy levels breaks down at around  $J \simeq 0.5$ ; contrary to the Heisenberg model case (where the critical disorder strength increases by 50% when comparing

<sup>1</sup>Similar behavior occurs in the Bose-Hubbard model [406]

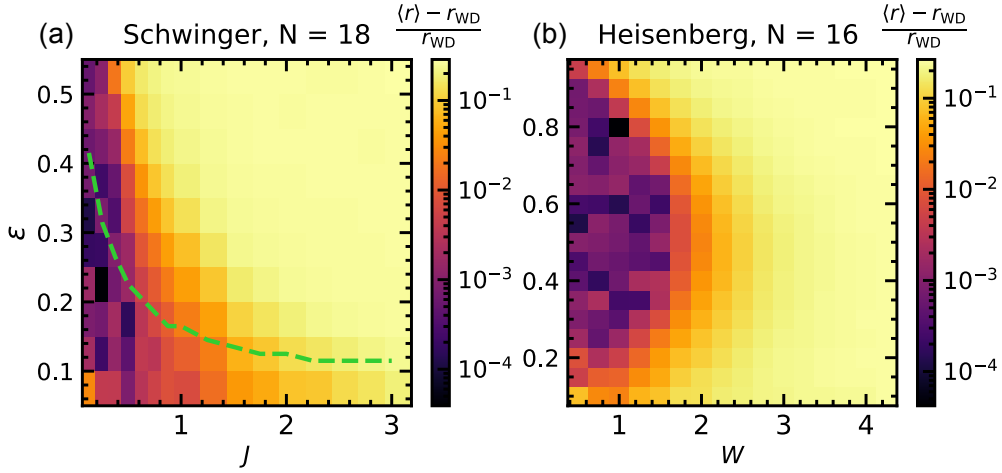


Figure 13.3: Energy-resolved  $r$  as a function of the rescaled energy  $\varepsilon$ , and gauge coupling  $J$  in the lattice gauge theory (a) and disorder strength  $W$  in the Heisenberg model (b). The green dashed line indicates the position of the maximum of the spectral density.

$N = 12$  and  $N = 18$ ), there is no appreciable finite-volume drift. We note that this behavior is fully compatible with the energy-resolved pattern of  $r$  plotted in Fig. 13.3(a): indeed, only states very close to the ground state are not localized, and as such, the global value of  $r$  is dominated by the vast majority of states that is localized (note that the vertical axis in Fig. 13.3(a) is limited to  $\varepsilon \in [0.05, 0.55]$  for the sake of clarity). The ergodic region (shaded) is followed by a regime where  $\langle r \rangle$  takes intermediate values: while it is not possible to reliably distinguish between emergent integrability (denoted by Poisson statistics) and an intermediate value of  $r$ , there is a clear finite-size trend toward the former for  $J > 1$ . Within statistical errors, we do not observe a clear crossing: longer chains routinely have smaller  $r$  values with respect to shorter chains. Finally, let us note that our diagnostics may actually underestimate the extent of the non-ergodic regime, as there exist random-matrix models [407] where ergodicity is broken even in regimes where  $r$  is compatible with GOE.

### 13.3 Spectral diagnostics: form factor

As a further evidence of breakdown of ergodicity, we analyze spectral correlations which go beyond nearby eigenvalues via the spectral form factor (SFF), defined as

$$K(\tau) = \frac{1}{Z} \left| \sum_{\alpha} g(\tilde{E}_{\alpha}) e^{i2\pi\tau\tilde{E}_{\alpha}} \right|^2 \quad (13.6)$$

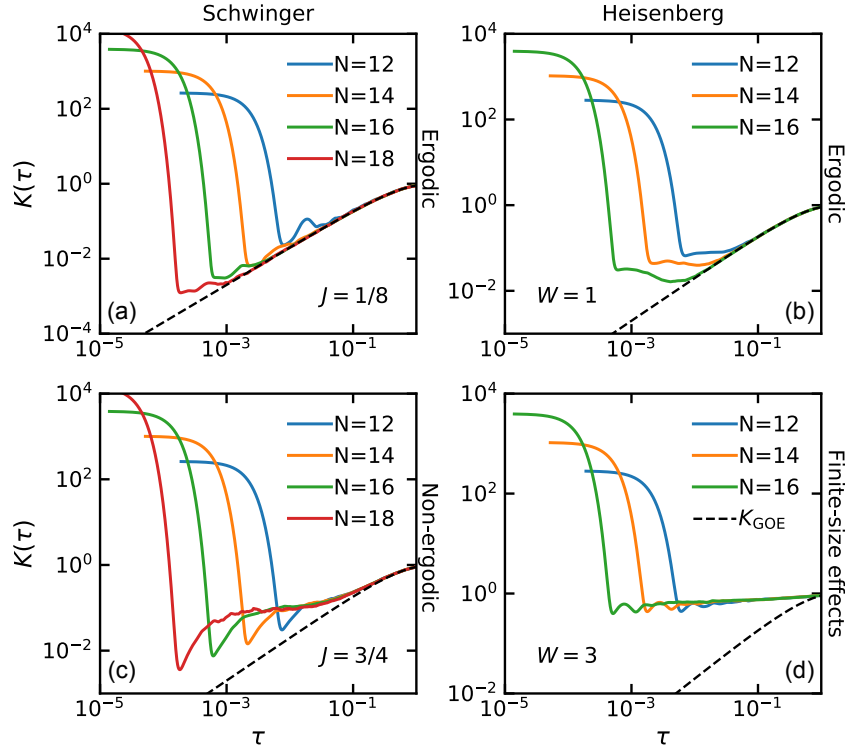


Figure 13.4: Comparison between the SFF of the Hamiltonian Eq. (13.2) (a,c) and of the Heisenberg model with on-site disorder (b,d). In the deep ergodic region (a,b) the SFF approaches the GOE prediction at times which decrease exponentially with the size of the system. For  $J = 3/4$  in the LGT (c) the bulk of the spectrum is non-ergodic and the SFF deviates from the GOE prediction at intermediate times. For  $W = 3$  in the Heisenberg chain (d) the level statistics is still flowing to WD, however the small effective localization length prevents accessing ergodic properties of thermodynamic limit.

where  $\tilde{E}_\alpha$  are the unfolded eigenvalues. In order to smooth the effects due to boundaries of the spectrum, we apply a gaussian filter  $g(x) = e^{-\frac{(x-\mu)^2}{2(\eta\sigma)^2}}$ , with  $\mu$  and  $\sigma$  the average and variance of the disorder realization of the unfolded spectrum.  $\eta$  quantifies the strength of the filter, and we take  $\eta = 0.3$  in what follows.  $\mathcal{Z} = \sum_\alpha |g(\tilde{E}_\alpha)|^2$  is a normalization s.t.  $K(\tau) \simeq 1$  for large  $\tau$ . Before applying the filter, we cut the edges of the spectrum according to  $s(E)/s_{\max} > 0.5$ , which means we take a fraction of eigenvalues larger than 0.9. Upon unfolding, the Heisenberg time  $t_H$ , corresponding to the timescale beyond which the discrete nature of the spectrum manifest itself and thus non-universal features kick in, is set to unity. The SFF in Eq. (13.6) is computed for each disorder realization for  $\tau \in [0, 1]$  and an average over disorder is performed for each value of  $\tau$ .

The analysis of  $K(\tau)$  allows to probe if the system is ergodic [395, 396,

408]. This can be done by comparing the averaged SFF with the SFF expected from an ensemble of orthogonal random matrices with gaussian entries (GOE),  $K_{\text{GOE}} = 2\tau - \tau \log(1 + 2\tau)$ . We call  $t_{\text{GOE}}$  the time at which the averaged SFF approaches the GOE prediction. If the system is ergodic [396], this corresponds to the Thouless time, and one has  $t_{\text{GOE}}/t_{\text{H}} \rightarrow 0$  in the thermodynamic limit (specifically, the Thouless time shall increase algebraically with  $N$ ).

In Fig. 13.4(a,b), we plot the spectral form factor in the Schwinger model and Heisenberg model in their ergodic regions: in both cases, the Thouless time is clearly decreasing with system size, further confirming the ergodic nature of the phase. The results in Fig. 13.4(c) correspond to a regime of gauge couplings whose  $r$  value departs from GOE: such departure is indeed confirmed by the fact that the  $t_{\text{GOE}}/t_{\text{H}}$  is not decreasing with system size, and oppositely, the SFF seems to collapse on a finite linear region, which implies  $\ln t_{\text{GOE}} \sim N$ ; this timescale directly indicates that the system is not ergodic, and it is suggestive of an emergent localization even at this value of the coupling. We note that, in this parameter regime, we do not observe saturation of the Thouless time, which is instead evident in spin models (see Fig. 13.4(d) and Ref. [395]).

Finally, we comment on the consequences of our numerical observations on transport properties. In the region  $J < 0.5$ , our numerical data are consistent with a power-law scaling. Transport properties in this regime are thus expected to be qualitatively similar to the case of the Heisenberg model in random fields. Oppositely, for larger values of the disorder, the fact that the ratio  $t_{\text{GOE}}/t_{\text{H}}$  is size independent suggests that the suppression of transport is related to a size-independent scale, a very different scenario compared to what is observed in Heisenberg models, characterized instead by anomalous transport properties [409–412]: while it is not possible to immediately connect this mechanism to confinement, we naturally expect this emergent scale to be connected with the string tension, as the latter is size-independent and is the only parameter needed to characterize Coulomb interactions at large scales.

## 13.4 Origin of ergodicity breaking

We conjecture that the origin of ergodicity breaking in lattice gauge theories stems from the fact that Coulomb law - which is acting at all energy scales - further constrains the system dynamics, and thus acts as an amplifier of any background disorder. In fact, for increasing system sizes, a larger fraction of the states of the spectrum will feature regions with a large accumulation of charge: as a consequence, the electrostatic energy (which is locally unbounded) becomes dominant and the effect of Coulomb interactions is enhanced. The presence of an unbounded energy density, which contrasts with the usual behaviour of spin models, does not affect low-energy

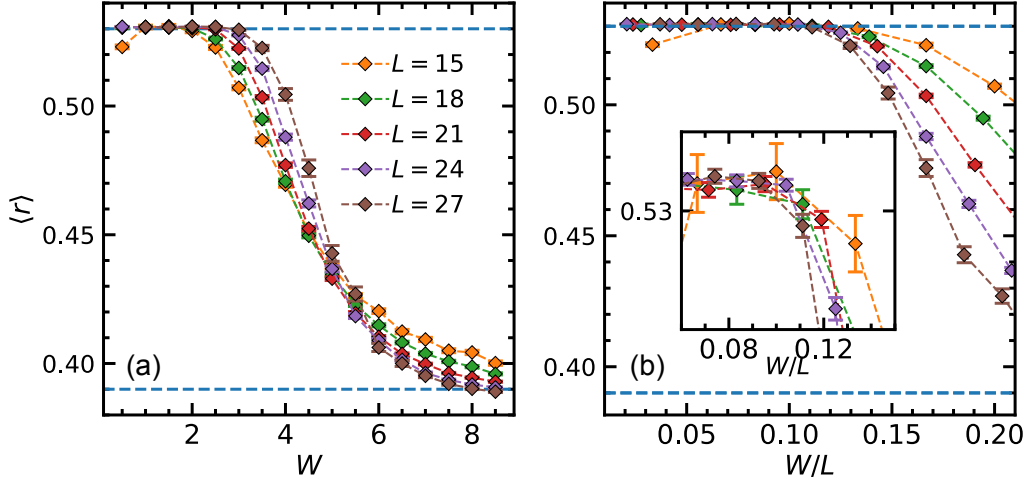


Figure 13.5: Average level spacing ratio for the constrained spin model  $H_{QLM}$ , corresponding to the Schwinger model with truncated gauge fields. The finite-size scaling of  $\langle r \rangle$  exhibits the same phenomenology as in the Heisenberg chain:  $\langle r \rangle$  vs  $W$  (a) shows a crossing point drifting on the right for increasing  $N$ ,  $\langle r \rangle$  vs  $W/N$  (b) gives a good data collapse for  $W/N < 0.1$ .

states, but has important consequences on the rest of the spectrum: for instance, it systematically reduces the number of available resonances when size is increased. In order to substantiate this statement, we studied (1) the Schwinger model in its deconfined regime,  $\theta = \pi$ , and (2) a quantum link version of the model with truncated gauge fields, where Coulomb law is washed out by the truncation. We do not observe any difference in our data between confining and deconfining regimes in the Schwinger model. We note that the fact that (de)confinement is not crucial here is not unexpected, as the latter is a phenomenon that only dictates the dynamics in the vicinity of the vacuum state. See Appendix C.8 for an analysis of the effect of the topological angle in the Schwinger model.

In Fig. 13.5(a-b), we instead show  $r$  versus the disorder strength  $W$  in a quantum link model in the presence of a background disorder [160]. The model considered is a constrained spin model of the form  $H_{QLM} = \sum_i (W_i n_i - \sigma_i^x)$ ,  $n_i n_{i+1} = n_i n_{i+2} = 0$ , where  $n = (1 - \sigma^z)/2$  (i.e. it is a PXP model with nearest and next-nearest neighbour blockade). By applying the mapping of Chapter 6, the system dynamics can be mapped into a quantum link model with strong nearest-neighbor interactions. We attempted a collapse scaling following [34], and assuming finite transition point  $W_c$  and correlation length critical exponent  $\nu$ . The best fitting  $W_c$  and  $\nu$  seem to increase linearly with size. The scaling of  $r$  follows rather closely the functional form proposed in Ref. [395]. These two observations indicate that, even in this model, the available system sizes are not sufficient to determine whether ergodicity is broken in the thermodynamic limit [398]. Overall, the

findings on these two models support our conjecture above.

## 13.5 Conclusions and outlook

We have provided numerical evidence for the breakdown of ergodicity in disorderd  $U(1)$  lattice gauge theories. Our results do not immediately indicate if localization kicks in right after such a breakdown, or if an intermediate non-ergodic, delocalized regime occurs. Further studies based on localization-specific diagnostics and transport properties may elucidate this aspect. The dynamical consequences of our results are immediately testable on quantum simulation platforms, where many-body dynamics of  $U(1)$  lattice gauge theories has been recently realized [4, 46, 166], and might be extended to Yang-Mills theories.

Part IV  
Appendix



# Appendix A

## Non-equilibrium dynamics in constrained quantum systems

Here we provide additional information on the results presented in Chapters 2 and 3.

### A.1 Properties of the PXP and the other constrained models

In this section, we summarize the properties of the spectrum of the PXP ( $\alpha = 1$ ) and the other constrained model with  $\alpha > 1$  of their perturbations. For any  $\alpha \geq 1$ , the Hamiltonian  $H_0^\alpha$  and the perturbation  $V^\alpha$  commute with the space reflection symmetry  $I$  and anticommute with the particle-hole symmetry  $C_{ph} = \prod_i \sigma_i^z$ . This fact has some important consequences, that hold for any Hamiltonian with these symmetries:

- all the eigenstates with  $E \neq 0$  are found in pairs of opposite energies (*doublets*), related by particle-hole symmetry ( $C_{ph} |E\rangle = |-E\rangle$ );
- states with  $E = 0$  can be classified as eigenstates of  $C_{ph}$  (*singlets*);
- the subspace of zero-energy eigenstates is exponentially large in  $L$ ;
- the singlets have same eigenvalue with respect to  $C_{ph}$  and  $I$ : this means that the zero-energy space is the direct sum of two subspaces with  $C_{ph} = I = \pm 1$ ;
- if  $|\psi\rangle$  and  $|\phi\rangle$  are two singlet eigenstates of  $H_0$ , then  $\langle\phi|V|\psi\rangle = 0$ . This holds even if  $\langle\phi|\psi\rangle \neq 0$  (or even if  $|\psi\rangle = |\phi\rangle$ ).

#### A.1.1 Scars

Here we report the properties of the scars under the action of  $I$  and  $C_{ph}$ . For the PXP model ( $\alpha = 1$ ), they satisfy:

$$I |\Gamma_{12}\rangle = (-1)^{L/2-1} |\Gamma_{12}\rangle \quad (\text{A.1})$$

$$I |\Gamma_{11}\rangle = (-1)^{L/2} |\Gamma_{11}\rangle \quad (\text{A.2})$$

$$C_{ph} |\Gamma_{11}\rangle = (-1)^{L/2} |\Gamma_{11}\rangle \quad (\text{A.3})$$

$$I |\Gamma_{21}\rangle = (-1)^{L/2-1} |\Gamma_{21}\rangle \quad (\text{A.4})$$

$$I |\Gamma_{22}\rangle = (-1)^{L/2} |\Gamma_{22}\rangle \quad (\text{A.5})$$

$$C_{ph} |\Gamma_{22}\rangle = (-1)^{L/2} |\Gamma_{22}\rangle. \quad (\text{A.6})$$

The scars defined in Section 2.3.3 for  $\alpha > 1$  and  $L = (\alpha + 2)n + 3$  satisfy

$$I |\psi_\alpha^{(\pm 3)}\rangle = (-1)^n |\psi_\alpha^{(\pm 3)}\rangle \quad (\text{A.7})$$

$$C_{ph} |\psi_\alpha^{(\pm 3)}\rangle = |\psi_\alpha^{(\mp 3)}\rangle. \quad (\text{A.8})$$

## A.2 Stability to other perturbations

We report here the data of the fidelity susceptibility of the scars and of a generic thermal eigenstate in the PXP model for a different perturbation  $V'$ , defined as

$$V' = \sum_{i=2}^{L-3} P_{i-2} \sigma_{i-1}^+ \sigma_i^- \sigma_{i+1}^+ P_{i+2} + \text{H.c.} \quad (\text{A.9})$$

The perturbation is again chosen in such a way to have the same properties under symmetry transformations as the PXP Hamiltonian  $H_0$ , i.e.  $IV'I = V$ ,  $C_{ph}V'C_{ph} = -V'$ . The results in Fig. A.1 show the same behaviour that we observed for the perturbation  $V$  in Chapter 3: the fidelity susceptibility grows exponentially with system size for the states  $|\Gamma_{th}\rangle$ ,  $|\Gamma_{21}\rangle$  and linearly for the state  $|\Gamma_{th}\rangle$ .

## A.3 Exact scars in the PXP model – properties of the edges

In this section we recall some properties of the scars of Eq. (2.5) and (2.7), and we comment on the profile of the energy density. As was noticed in Ref. [52], the PXP Hamiltonian can be written as a sum of two parts: a part which contains two-body interactions between blocks, and one with single-block terms only. The two-body terms annihilate the scars (we refer to the appendix of Ref. [52] for the proof), while the remaining terms are

$$H' = \sum_b [ |10\rangle \langle 00| + |01\rangle \langle 00| + h.c. ]_b. \quad (\text{A.10})$$

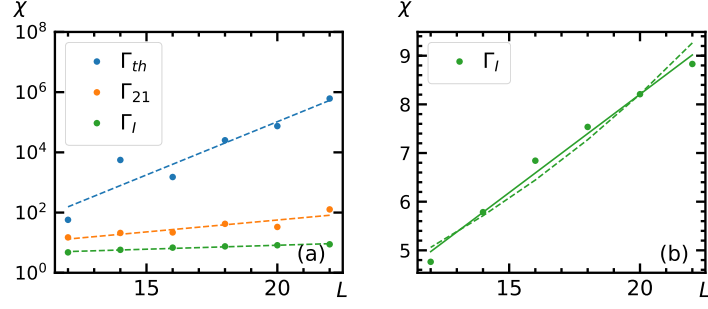


Figure A.1: Scaling of the fidelity susceptibility with system size, for the perturbation  $V'$ . The results shown refer to the states (a)  $|\Gamma_{th}\rangle$ ,  $|\Gamma_{21}\rangle$  and (b)  $|\Gamma_I\rangle$  with open boundary conditions. Dashed lines are obtained from fits with an exponential scaling, solid lines with linear scaling. Similarly to the results for the perturbation  $V$  shown in Fig. 2.2, also in this case the scaling is exponential for the states  $|\Gamma_{th}\rangle$ ,  $|\Gamma_{21}\rangle$  (in agreement with ETH) and is linear for the state  $|\Gamma_I\rangle$ .

A more convenient expression is obtained by defining the states

$$|\pm\rangle = \frac{1}{2}(|01\rangle + |10\rangle + \sqrt{2}|00\rangle), \quad (\text{A.11})$$

$$|\mathbf{0}\rangle = \frac{1}{\sqrt{2}}(|10\rangle - |01\rangle). \quad (\text{A.12})$$

The Hamiltonian  $H'$  has the form

$$H' = \sqrt{2} \sum_b (|+\rangle \langle +| - |-\rangle \langle -|). \quad (\text{A.13})$$

This expression is useful to interpret the profile of the energy density of the scars. After this change of basis and a gauge transformation with the unitary matrix  $V = \frac{1}{\sqrt{2}} \begin{pmatrix} 1 & 1 \\ 1 & -1 \end{pmatrix}$ , the new matrices have the form

$$A^+ = V \frac{1}{2} (A^{01} + A^{10} + \sqrt{2}A^{00}) V^{-1} = \begin{pmatrix} 0 & \sqrt{2} \\ 0 & 0 \end{pmatrix}, \quad (\text{A.14})$$

$$A^- = V \frac{1}{2} (A^{01} + A^{10} - \sqrt{2}A^{00}) V^{-1} = \begin{pmatrix} 0 & 0 \\ \sqrt{2} & 0 \end{pmatrix}, \quad (\text{A.15})$$

$$A^{\mathbf{0}} = V \frac{1}{\sqrt{2}} (A^{10} - A^{01}) V^{-1} = \begin{pmatrix} 1 & 0 \\ 0 & 1 \end{pmatrix}, \quad (\text{A.16})$$

and the new boundary vectors are

$$v'_1 = V v_1 = \begin{pmatrix} 1 \\ 0 \end{pmatrix}, \quad (\text{A.17})$$

$$v'_2 = Vv_2 = \begin{pmatrix} 0 \\ 1 \end{pmatrix}. \quad (\text{A.18})$$

Now each block can be interpreted as a spin-1 variable with states  $+$ ,  $\mathbf{0}$ ,  $-$  indicating the  $S_z$  component, and the Hamiltonian  $H'$  corresponds to the magnetization in the  $z$  direction. The form of the matrices  $A^+$ ,  $A^-$ ,  $A^0$ , allows to easily see which are the non-zero components in the local  $S_z$  basis: they are the ones with the structure of a "dilute antiferromagnet", i.e. with alternating  $+$  and  $-$  and an arbitrary number of  $\mathbf{0}$ s in between. This structure is a renowned feature of the AKLT state, whose relation with the MPS scars has been already pointed out in Ref. [52]. In open boundary conditions, the boundary vectors fix the sign of the first non-zero spin: on the left  $v'_1$  ( $v'_2$ ) constrains it to be in a  $+$  ( $-$ ) state and viceversa for the vector on the right. Therefore, the components of the state  $\Gamma_{12}$  have a number of  $+$ s that exceeds the number of  $-$ s by one, so its energy is  $E = \sqrt{2}$  (and viceversa for  $\Gamma_{21}$ , with  $E = -\sqrt{2}$ ). The states  $\Gamma_{11}$  and  $\Gamma_{22}$ , on the other hand, have the same number of  $-$ s and  $+$ s, so they have energy  $E = 0$ . The energy density profiles reported in Ref. [52] can be understood as well from this construction: they correspond to the magnetization profile of the dilute antiferromagnet. In the bulk, the local magnetization averages to 0, while on the boundary it is affected by the choice of the boundary vector.

## A.4 Exact scars with $E = \sqrt{3}$ – Proof

In this section we prove that the following state is an exact scar with energy  $E = \sqrt{3}$

$$|\psi_\alpha^{(3)}\rangle = \sum_{\vec{s}} \left[ (1, 0)^T \cdot N^{s_1} M^{s_2} \dots M^{s_{2n}} N^{s_{2n+1}} \cdot (0, 1) \right] |\vec{s}\rangle \quad (\text{A.19})$$

where  $s_1, s_2, \dots, s_{2n+1}$  label the states of the blocks and

$$M^s = \begin{cases} 1 & \text{if } s = 00 \dots 00 \\ 0 & \text{otherwise,} \end{cases} \quad (\text{A.20})$$

$$N^0 = \begin{pmatrix} 0 & \sqrt{3} \\ 0 & 0 \end{pmatrix}, \quad N^L = \begin{pmatrix} 0 & 1 \\ 0 & 1 \end{pmatrix}, \quad (\text{A.21})$$

$$N^C = \begin{pmatrix} 1 & 1 \\ 0 & -1 \end{pmatrix}, \quad N^R = \begin{pmatrix} -1 & 1 \\ 0 & 0 \end{pmatrix}. \quad (\text{A.22})$$

The indices  $0, L, C, R$  are the state of three-site block, with the following notation:  $|0\rangle = |000\rangle$ ,  $|L\rangle = |100\rangle$ ,  $|C\rangle = |010\rangle$ ,  $|R\rangle = |001\rangle$ .

The matrices in Eqs. A.21 and A.22 satisfy

$$N^R N^L = 0, \quad (N^0 + N^L)(N^R + N^0) = 0. \quad (\text{A.23})$$

The first equation implies that the state satisfies the blockade constraint. We can split the Hamiltonian in two parts:  $H = H_M + H_N$  where  $H_M$  ( $H_N$ ) flips only sites in the  $M$  ( $N$ ) blocks.

We first prove that  $H_M |\psi_\alpha^{(3)}\rangle = 0$ . Consider a single term  $P_{i-\alpha} \dots P_{i-1} X_i P_{i+1} \dots P_{i+\alpha}$  where  $i$  belongs to a block of type  $M$ : if  $i$  is not the first or last site of the block, it can only be flipped if both neighbouring  $N$  blocks are in the state 0. However, this never happens because  $N^0 M^s N^0 = 0$ . If  $i$  is the first site of the blocks, these two conditions must hold for it to be flippable: (i) the previous block must be in state 0; (ii) the following block must be either in state 0 or  $R$ . But  $N^0 M^s N^0 = N^0 M^s N^R = 0$ , so this Hamiltonian term annihilates the state. Similarly, using  $N^0 M^s N^0 = N^L M^s N^0 = 0$ , we find that the last site of the block cannot be flipped. This means that the sites in the  $M$  blocks are all "frozen" in the 0 state and concludes the proof that  $H_M |\psi_\alpha^{(3)}\rangle = 0$ .

We now consider  $H_N$ :

$$H_N |\psi_\alpha^{(3)}\rangle = \sum_b \left[ (|0\rangle \langle R|)_b (1 - |L\rangle \langle L|)_{b+1} + (1 - |R\rangle \langle R|)_{b-1} (|0\rangle \langle L|)_b + (|0\rangle \langle R|)_b + h.c. \right] |\psi_\alpha^{(3)}\rangle \quad (\text{A.24})$$

where  $b = 1, \dots, n+1$  labels the blocks of type  $N$ . From the relations  $N^R N^L = N^0 N^L + N^R N^0 = 0$ , we find that all the terms involving more than one block cancel and we are left with

$$H_N |\psi_\alpha^{(3)}\rangle = H' |\psi_\alpha^{(3)}\rangle. \quad (\text{A.25})$$

$$H' = \sum_b \left[ |0\rangle ( \langle R| + \langle C| + \langle L| ) + h.c. \right]_b. \quad (\text{A.26})$$

Now, to prove that  $H' |\psi_\alpha^{(3)}\rangle = \sqrt{3} |\psi_\alpha^{(3)}\rangle$ , it is useful to change basis and define:

$$|\pm\rangle = \frac{|L\rangle + |C\rangle + |R\rangle \pm \sqrt{3}|0\rangle}{\sqrt{6}}, \quad (\text{A.27})$$

$$|l\rangle = \frac{|C\rangle - |L\rangle}{\sqrt{2}}, \quad |r\rangle = \frac{|C\rangle - |R\rangle}{\sqrt{2}}. \quad (\text{A.28})$$

In this new basis the matrices have the form

$$N^+ = \begin{pmatrix} 0 & \sqrt{6} \\ 0 & 0 \end{pmatrix}, \quad N^- = 0, \quad (\text{A.29})$$

$$N^l = \begin{pmatrix} 1/\sqrt{2} & 0 \\ 0 & -\sqrt{2} \end{pmatrix}, \quad N^r = \begin{pmatrix} \sqrt{2} & 0 \\ 0 & -1/\sqrt{2} \end{pmatrix}. \quad (\text{A.30})$$

and the Hamiltonian  $H'$

$$H' = \sum_b \left[ \sqrt{3}|+\rangle \langle +| - \sqrt{3}|-\rangle \langle -| \right]_b \quad (\text{A.31})$$

$H'$  is diagonal in the new basis  $\{|+\rangle, |-\rangle, |l\rangle, |r\rangle\}$ . It is now sufficient to prove that all the non zero-components of  $|\psi\rangle$  in the new basis have a one and only one block in  $|+\rangle$  and all the others are in  $|l\rangle$  or  $|r\rangle$ . This can be understood from the fact that (i)  $N^+ N^{\alpha_1} \dots N^{\alpha_p} N^+ = 0$  (for any string in between) and that (ii) any string of matrices without  $N^+$  is diagonal, so it annihilates when contracted with the boundary vectors  $(1, 0)^T, (0, 1)$ . The energy density profile of this state is then easy to understand in these basis: all the three-site blocks have the same energy density, because the '+' can be located anywhere in the chain, while the other sites have energy density 0. This contrasts with the MPS scars found in Ref. [52]: while there the energy density is localized on the edges because of the structure of dilute antiferromagnet, here the construction resembles a spin wave with a delocalized excitation.

## A.5 Exact scars with $E = \sqrt{2}$ , $\alpha = 3$

We now consider the case  $\alpha = 3$  and construct exact eigenstates with  $E = \pm\sqrt{2}$  as matrix product states with finite bond dimensions. They are constructed by assembling position dependent matrices in a periodic pattern, illustrated in Fig. A.2.



Figure A.2: Structure of an MPS for  $L = 24$ . The blocks are made of two sites. Empty dots are sites in the state 0. The structure of the state for generic system sizes is based on the periodic repetition of the pattern 0BC0CA0 (highlighted in the picture).

The matrices  $A, B, C$  are defined on two-site blocks and have bond dimension 2. The dots represent empty sites. The pattern (0BC0CA0) that is repeated periodically consists of 11 sites. The first and last two sites of the open chain have to be in a block of type A or B. Therefore we have 4 possible states, labelled by the first and last block:

- $|\phi_{AB}^{(2)}\rangle$ , for  $L = 6 + 11n$ ;
- $|\phi_{BA}^{(2)}\rangle$ , for  $L = 9 + 11n$ ;
- $|\phi_{AA}^{(2)}\rangle$  and  $|\phi_{BB}^{(2)}\rangle$ , for  $L = 13 + 11n$ .

The matrices for the eigenvalue  $E = \sqrt{2}$  are defined as

$$A^{00} = \begin{pmatrix} 0 & 1/\sqrt{2} \\ 0 & 1 \end{pmatrix}, \quad A^{10} = \begin{pmatrix} 1/\sqrt{2} & 1/2 \\ 0 & 0 \end{pmatrix}, \quad (\text{A.32})$$

$$A^{01} = \begin{pmatrix} -1/\sqrt{2} & 1/2 \\ 0 & 0 \end{pmatrix} \quad (\text{A.33})$$

$$B^{00} = \begin{pmatrix} 1 & 1/\sqrt{2} \\ 0 & 0 \end{pmatrix}, \quad B^{10} = \begin{pmatrix} 0 & 1/2 \\ 0 & 1/\sqrt{2} \end{pmatrix}, \quad (\text{A.34})$$

$$B^{01} = \begin{pmatrix} 0 & 1/2 \\ 0 & -1/\sqrt{2} \end{pmatrix} \quad (\text{A.35})$$

$$C^{00} = \begin{pmatrix} 0 & 0 \\ 1 & 0 \end{pmatrix}, \quad C^{10} = \begin{pmatrix} 0 & 1/\sqrt{2} \\ 0 & 0 \end{pmatrix}, \quad (\text{A.36})$$

$$C^{01} = \begin{pmatrix} 0 & -1/\sqrt{2} \\ 0 & 0 \end{pmatrix} \quad (\text{A.37})$$

The boundary vectors are obtained by contracting the extremal matrices with  $(1, 0)^T$  on the left and  $(0, 1)$  on the right. The states  $|\phi_{rs}^{(\pm 2)}\rangle = C_{ph} |\phi_{rs}^{(2)}\rangle$  ( $r, s = A, B$ ) are other exact scars with energy  $E = -\sqrt{2}$ .

These scars satisfy the following properties:

$$I |\phi_{AB}^{(\pm 2)}\rangle = -|\phi_{AB}^{(\pm 2)}\rangle \quad (\text{A.38})$$

$$I |\phi_{BA}^{(\pm 2)}\rangle = -|\phi_{BA}^{(\pm 2)}\rangle \quad (\text{A.39})$$

$$I |\phi_{AA}^{(\pm 2)}\rangle = |\phi_{BB}^{(\pm 2)}\rangle \quad (\text{A.40})$$

$$I |\phi_{BB}^{(\pm 2)}\rangle = |\phi_{AA}^{(\pm 2)}\rangle. \quad (\text{A.41})$$

### A.5.1 Proof

We first prove that the state above satisfies the constraints. The conditions are:  $B^r C^s = C^r A^s = 0$  for  $r = 01, 10$  and  $s = 01, 10$ ,  $C^{01} C^{01} = C^{01} C^{10} = C^{10} C^{10} = 0$ , and  $A^{01} B^{10} = 0$ . It is straightforward to check that all of them are satisfied by the matrices  $A, B$  and  $C$ .

We now define the local Hamiltonian term  $h_i = P_{i-3} P_{i-2} P_{i-1} X_i P_{i+1} P_{i+2} P_{i+3}$  and prove that  $h_i |\psi_{\alpha=3}\rangle = 0$  when  $i$  is one of the sites between two  $C$  blocks. To prove this, we note that  $C^{00} C^{00} = 0$ , which immediately implies  $P_{i-2} P_{i-1} P_{i+1} P_{i+2} |\psi_{\alpha=3}\rangle = 0$ . Similarly, we can prove that  $h_i |\psi_{\alpha=3}\rangle = 0$  when  $i$  is one of the sites between an  $A$  and a  $B$  block by noting that  $A^{00} B^{00} = 0$  so the projectors in  $h_i$  annihilate the state  $|\psi_{\alpha=3}\rangle$ .

The next step is proving  $h_i |\psi_{\alpha=3}\rangle = 0$  for  $i$  belonging to the  $C$  blocks. To set the notation, we label the two-site blocks (of types  $A, B, C$ ) in the chains with indices  $b = 0, 1, 2, \dots, N_b$  from left to right. We define  $\Gamma_A$  as the set of integers  $b$  such that the  $b$ -th block is of type  $A$ , and similarly for  $\Gamma_B$  and  $\Gamma_C$ . We also define the operator  $P_b^s$  which projects the block  $b$  in the state  $|s\rangle$ .

With this notation, we obtain the following equation

$$\begin{aligned} \sum_{b \in \Gamma_C} \sum_{i \in b} h_i = & \sum_{b, b+1 \in \Gamma_C} P_{b-1}^{00} |00\rangle_b (\langle 10| + \langle 01|)_b P_{b+1}^{00} \\ & + P_b^{00} |00\rangle_{b+1} (\langle 10| + \langle 01|)_{b+1} P_{b+2}^{00} \\ & + P_{b-1}^{00} (|10\rangle + |01\rangle)_b \langle 00|_b P_{b+1}^{00} \\ & + P_b^{00} (|10\rangle + |01\rangle)_{b+1} \langle 00|_{b+1} P_{b+2}^{00}. \end{aligned} \quad (\text{A.42})$$

The sum in the right hand side runs over the indices such that both  $b$  and  $b+1$  are blocks of type  $C$ . The first two terms of the sum annihilate  $|\psi_{\alpha=3}\rangle$  because  $C^{01} + C^{10} = 0$ , the last two terms because  $C^{00}C^{00} = 0$ .

From the observations we made so far, we have now obtained that

$$H |\psi_{\alpha=3}\rangle = \sum_{b \in \Gamma_A \cup \Gamma_B} \sum_{i \in b} h_i |\psi_{\alpha=3}\rangle. \quad (\text{A.43})$$

We can rewrite the action of these terms as

$$\sum_{b \in \Gamma_A \cup \Gamma_B} \sum_{i \in b} h_i |\psi_{\alpha=3}\rangle = (H_{non-int} - H_{int}) |\psi_{\alpha=3}\rangle. \quad (\text{A.44})$$

The Hamiltonian  $H_{non-int}$  contains the terms

$$\begin{aligned} H_{non-int} = & \sum_{b \in \Gamma_A} P_{b-1}^{00} [|00\rangle (\langle 10| + \langle 01|) + h.c.]_b \\ & + \sum_{b \in \Gamma_B} [|00\rangle (\langle 10| + \langle 01|) + h.c.]_b P_{b+1}^{00}, \end{aligned} \quad (\text{A.45})$$

where, for the sake of brevity, in our notation for the boundary terms we choose to define  $P_{-1}^{00} \equiv 1$ ,  $P_{N_b+1}^{00} \equiv 1$ . The Hamiltonian  $H_{int}$  reads

$$\begin{aligned} H_{int} = & \sum_{\substack{b \in \Gamma_A \\ b+1 \in \Gamma_B}} P_{b-1}^{00} [|00\rangle \langle 01| + h.c.]_b P_{b+1}^{10} \\ & + P_b^{01} [|00\rangle \langle 10| + h.c.]_{b+1} P_{b+2}^{00}. \end{aligned} \quad (\text{A.46})$$

By noting that  $A^{01}B^{10} = 0$  and  $C^{00}(A^{00}B^{10} + A^{01}B^{00})C^{00} = 0$ , we find that  $H_{int} |\psi_{\alpha=3}\rangle = 0$ .

To conclude our proof, we now have to demonstrate that  $H_{non-int} |\psi_{\alpha=3}\rangle = \sqrt{2} |\psi_{\alpha=3}\rangle$ . We define the states

$$|e\rangle = \frac{|10\rangle + |01\rangle}{\sqrt{2}}, \quad |o\rangle = \frac{|10\rangle - |01\rangle}{\sqrt{2}}, \quad (\text{A.47})$$

$$|\pm\rangle = \frac{|00\rangle \pm |e\rangle}{\sqrt{2}}, \quad |0\rangle = |00\rangle. \quad (\text{A.48})$$

We now perform the following changes of basis: on the  $A$  and  $B$  blocks, we use the (non-orthogonal) states  $|+\rangle$ ,  $|o\rangle$ ,  $|0\rangle$ , such that the new matrices of the MPS have the form

$$\tilde{A}^+ = \begin{pmatrix} 0 & 1 \\ 0 & 0 \end{pmatrix}, \quad \tilde{A}^o = \begin{pmatrix} 1 & 0 \\ 0 & 0 \end{pmatrix}, \quad (\text{A.49})$$

$$\tilde{A}^0 = \begin{pmatrix} 0 & 0 \\ 0 & 1 \end{pmatrix} \quad (\text{A.50})$$

$$\tilde{B}^+ = \begin{pmatrix} 0 & 1 \\ 0 & 0 \end{pmatrix}, \quad \tilde{B}^o = \begin{pmatrix} 0 & 0 \\ 0 & 1 \end{pmatrix}, \quad (\text{A.51})$$

$$\tilde{B}^0 = \begin{pmatrix} 1 & 0 \\ 0 & 0 \end{pmatrix}, \quad (\text{A.52})$$

while on the  $C$  blocks we use  $|0\rangle$ ,  $|e\rangle$  and  $|o\rangle$ , with the matrices

$$\tilde{C}^0 = \begin{pmatrix} 0 & 0 \\ 1 & 0 \end{pmatrix}, \quad \tilde{C}^e = 0, \quad \tilde{C}^o = \begin{pmatrix} 0 & 1 \\ 0 & 0 \end{pmatrix}. \quad (\text{A.53})$$

We now merge the pairs of consecutive  $C$  blocks. The only non-zero matrices for the superblock are

$$\tilde{G}^{0,o} = \begin{pmatrix} 0 & 0 \\ 0 & 1 \end{pmatrix}, \quad \tilde{G}^{o,0} = \begin{pmatrix} 1 & 0 \\ 0 & 0 \end{pmatrix}. \quad (\text{A.54})$$

The components of  $|\psi_{\alpha=3}\rangle$  now have the form

$$|\psi_{\alpha=3}\rangle = \sum_{\vec{s}=(s_0,\dots,s_{N_b})} c_{\vec{s}} |s_0\rangle \otimes |s_1\rangle \cdots \otimes |s_{N_b}\rangle \quad (\text{A.55})$$

where the sum runs over the three new states of the basis for each component  $s_b$  and

$$c_{\vec{s}} = (1 \ 0) \left( \dots \tilde{B}^{s_{b-1}} \tilde{G}^{s_b, s_{b+1}} \tilde{A}^{s_{b+2}} \tilde{B}^{s_{b+3}} \dots \right) \begin{pmatrix} 0 \\ 1 \end{pmatrix}. \quad (\text{A.56})$$

From the simple structure of the matrices, it is now easy to see that the only cases that give  $c_{\vec{s}} \neq 0$  are the ones where the product of matrices in parentheses is a sequence of  $\tilde{A}^o$ ,  $\tilde{B}^0$ ,  $\tilde{G}^{o,0}$ , followed by a single matrix  $\tilde{A}^+$  or  $\tilde{B}^+$  and then by a sequence of  $\tilde{A}^0$ ,  $\tilde{B}^o$ ,  $\tilde{G}^{0,o}$ . Consider now a state  $\vec{s}$  that satisfies this condition and let  $b^*$  be the index that corresponds to the  $\tilde{A}^+$  or  $\tilde{B}^+$  matrix. All the terms in  $H_{non-int}$  annihilate  $|\vec{s}\rangle$ , except for the one with  $b = b^*$ : to prove this, it is sufficient to note that, for  $b \in \Gamma_A$  if (i)  $b < b^*$  then  $s_{b-1} = o$  and hence  $P_{b-1}^0 |s_{b-1}\rangle = 0$ , while if (ii)  $b > b^*$  then  $s_b = o$  and  $[[00] (\langle 10| + \langle 01|) + h.c.]_b |s_b\rangle = 0$ ; similarly, if (i)  $b < b^*$  then  $s_b = o$  and  $[[00] (\langle 10| + \langle 01|) + h.c.]_b |s_b\rangle = 0$ , while if (ii)  $b > b^*$  then  $s_{b+1} = o$  and  $P_{b+1}^0 |s_{b+1}\rangle = 0$ . The term of  $H_{non-int}$  with  $b = b^*$ , on the

other hand gives a non-zero term: if  $b^* \in \Gamma_A$ , then  $s_{b^*-1} = 0$  and  $s_{b^*} = +$ , so  $P_{b^*-1}^0[|00\rangle (\langle 10| + \langle 01|) + h.c.]_b |\vec{s}\rangle = \sqrt{2} |\vec{s}\rangle$ , while if  $b^* \in \Gamma_B$ , then  $s_{b^*+1} = 0$  and  $s_{b^*} = +$ , so  $[|00\rangle (\langle 10| + \langle 01|) + h.c.]_b P_{b^*+1}^0 |\vec{s}\rangle = \sqrt{2} |\vec{s}\rangle$ . Therefore, we conclude that for each  $\vec{s}$  such that  $c_{\vec{s}} \neq 0$   $H_{non-int} |\vec{s}\rangle = \sqrt{2} |\vec{s}\rangle$ , and using Eq. (A.55), we have  $H_{non-int} |\psi_{\alpha=3}\rangle = \sqrt{2} \psi_{\alpha=3}$ .

## A.6 Spectra of QLRN

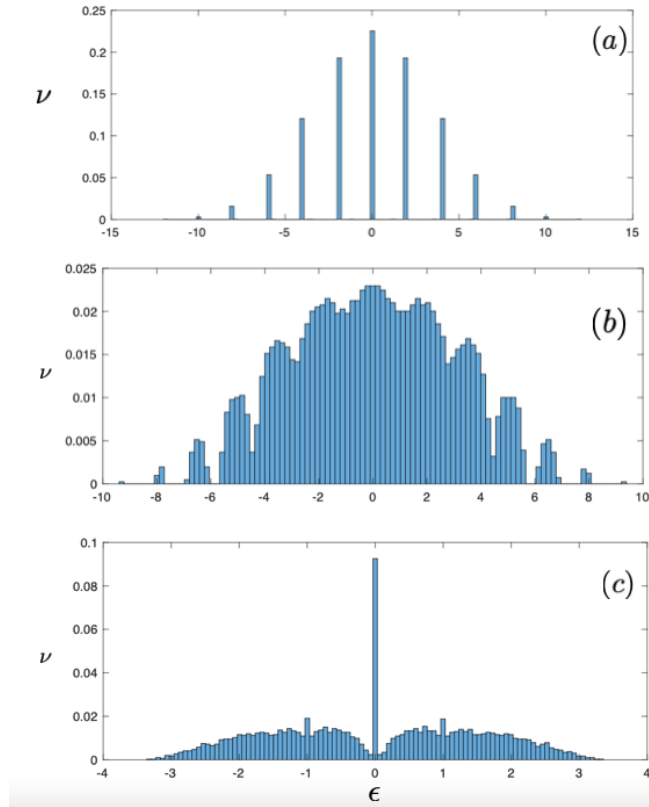


Figure A.3: Histograms of the density of states  $\nu$  vs. energy  $\epsilon$  of the eigenstates for a QLRN with  $N = 12$  and  $p = 1$  (panel a),  $p = 0.75$  (panel b), and  $p = 0.15$  (panel c).

Let us consider the spectra of QLRN as a function of  $p$  as shown in Fig. (A.3) for  $N = 12$ . When  $p = 1$  all states that can be connected by a single spin flip are connected and the Hamiltonian is  $H = \sum_i \sigma_i^x$ : the resulting spectrum is therefore trivial, highly degenerate with eigenvalues  $\epsilon_i = N - 2i$ , with  $i = 0, \dots, N$ , and degeneracy  $D_i = \binom{N}{i}$  (see Fig. (A.3-a)). Introducing a slight stochasticity in the selection of edges splits the degeneracies leading to a characteristic spectrum similar to that shown in Fig. (A.3-b) for  $p = 0.75$ . A further reduction of  $p$  leads to a fragmentation of the Hilbert space: in the network representation one observes a giant

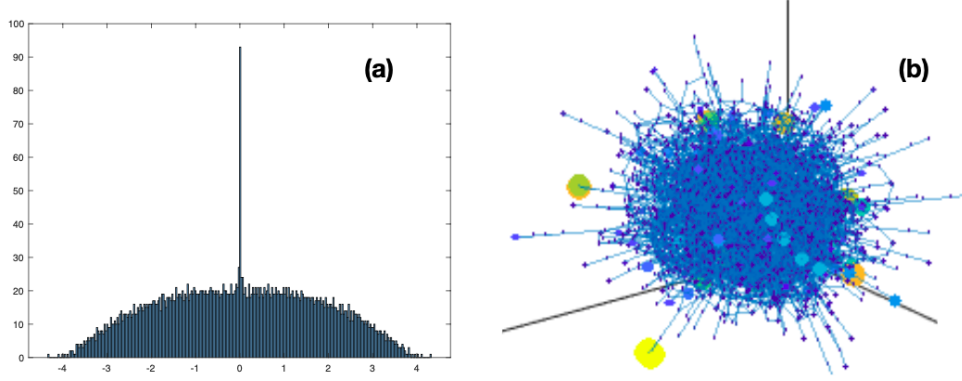


Figure A.4: (a) Histogram representation of the spectrum of the giant connected component for a QLRN with  $N = 12$  and  $p = 0.25$ . The peak at  $\epsilon = 0$  is still visible and is associated to wavefunctions mainly localized on the periphery of the network as shown in panel (b).

connected component and a few disconnected nodes associated to a peak at  $\epsilon = 0$  as well as, for sufficiently small  $p$  (Fig. (A.3-c) for  $p = 0.15$ ), pairs of nodes connected by an edge (peaks at  $\pm 1$  in Fig. (A.3-c) in the histogram of the eigenvalues )

Localization is expected to occur when  $p$  is sufficiently small. Of course there is a *trivial* localization related to wave functions completely localized in small disconnected components which will contribute to the peaks at  $\epsilon = 0$  and  $\epsilon = \pm 1$  in Fig. (A.3-c). A much more interesting type of localization is however happening in the giant connected component of the network that contains most of the nodes: as shown in Fig. (A.4) the peak at  $\epsilon = 0$  persists also in this case. A visualization of the weights of the corresponding wave functions in the network, shows that these localized states are associated to wave functions with large amplitudes on nodes at the boundaries of the network. Qualitatively similar results are obtained for different  $N$ .

## A.7 Generalized QLRN

The notion of QLRN can be generalized to encompass situations in which either the elementary degrees of freedom are not spin 1/2 or the number of spins flipped locally is larger than one, as in Ref. [86, 98], maintaining locality and constrained dynamics.

For concreteness, let us consider the set of sequences  $\{\sigma_i\}$ , where  $i = 1, \dots, N$  and  $\sigma_i = \{0, \dots, q\}$ , ( $q$  is a positive integer). Two nodes  $\{\sigma_i\}$  and  $\{\sigma'_i\}$  are connected with probability  $0 \leq p \leq 1$  if: *i*) - the string  $\{\sigma_i - \sigma'_i\}$  has nonzero entries only locally, i.e. in a compact interval of finite size  $L_0 \leq N$  and *ii*) - the distance  $\sum_i |\sigma_i - \sigma'_i| \leq S_0$ . The random

local Hamiltonian associated to this network is then its adjacency matrix and the resulting ensemble of Hamiltonians will be denoted as  $\mathcal{H}_p(L_0, S_0)$ . Note that if  $S_0 \geq 2$  in general the Hamiltonian does not anticommute with the total parity. It is evident that if  $q = 1$ ,  $L_0 = 1$  and  $S_0 = 1$  we have the special case discussed in Chapter 3 and that the PXP Hamiltonian is just one of the realizations in  $\mathcal{H}_p(1, 1)$ . Networks with larger local Hilbert space  $q$ ,  $S_0 > 1$  and more complex spin flips  $L_0 > 1$  are naturally related for example to spin-1 models [86] or fermionic models [98], whose analysis is left for future work.

## A.8 Participation ratio and system size

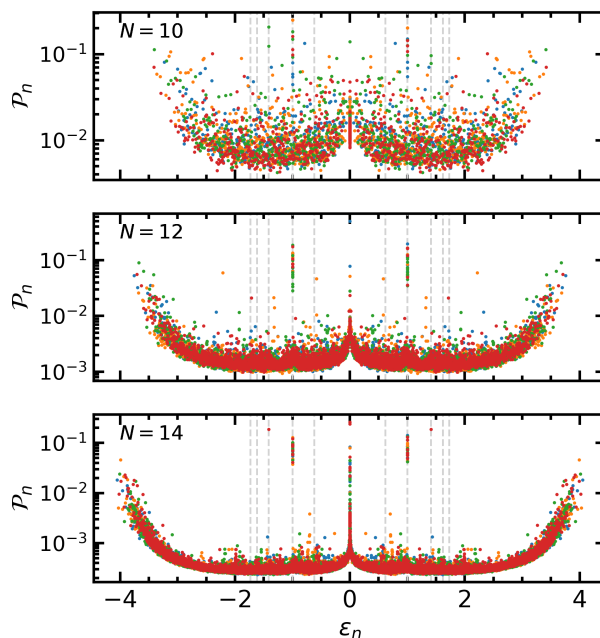


Figure A.5: Participation ratio  $\mathcal{P}_n$  of the eigenstates for  $p = 0.2$  and different system sizes  $N$ .

In Fig. (A.5) we plot the participation ratio of the eigenstates for different values of the system size  $N$ . We note that, as  $N$  is increased, the majority of the eigenstates get closer to a smooth dependence of  $\mathcal{P}$  on the energy  $\epsilon$  (the thermal cloud). Statistical scars, instead, remain well isolated, with strongly non-thermal values.

## A.9 Centrality and degree of statistical scars

The characterization of the localization of stochastic and statistical scars done in Chapter 3 with the participation ratio  $\mathcal{P}_n$  and the betweenness  $B_n$

can be done using other figures of merit such as the degree and the centrality of the eigenstates, defined as

$$\langle k \rangle_n = \sum_i |c_n(\{\sigma\})|^2 k(\{\sigma\}), \quad (\text{A.57})$$

$$\langle C \rangle_n = \sum_i |c_n(\{\sigma\})|^2 C(\{\sigma\}). \quad (\text{A.58})$$

As shown in Fig. (A.6), statistical scars are characterized by anomalously small values of both quantities.

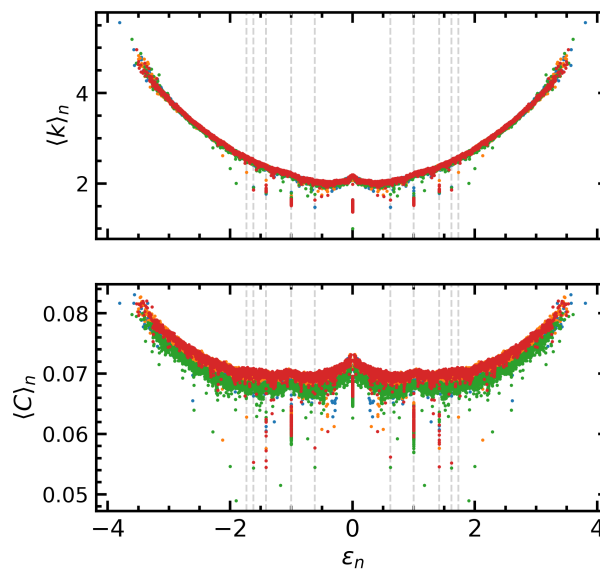


Figure A.6: Degree  $\langle k \rangle_n$  and centrality  $\langle C \rangle_n$  of the eigenstates as a function of their energy  $\epsilon_n$ . Different colors refer to different realizations of the network. Statistical scars are characterized by small values of both  $\langle k \rangle_n$  and  $\langle C \rangle_n$ .

## A.10 Eigenstate phase transition at different $\epsilon^*$

In Chapter 3, we discussed for the presence of an eigenstate phase transition based on the degeneracy of statistical scars at  $\epsilon^* = 1$ . It is possible to extend this picture to all network-predicted values of quantized energies.

In Fig. A.7, we show the degeneracy scaling versus system size for four additional values of  $\epsilon^*$ . For  $p < 0.2$ , we consistently observe that degeneracy is increasing with system size (due to the absence of a decade of sizes, we refrain from commenting on the precise scaling function). For  $p = 0.2$ , we observe few degeneracies, and the data seem consistent with a decreasing

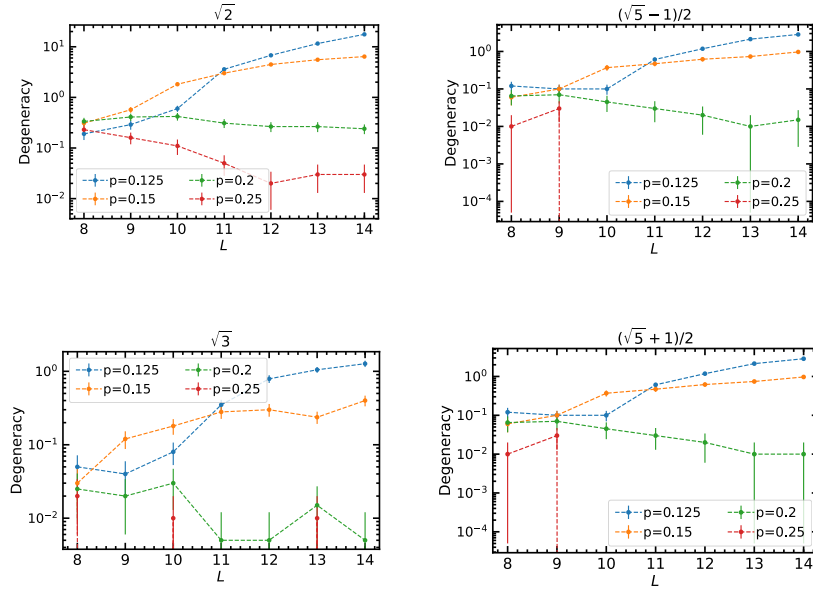


Figure A.7: Degeneracy of statistical scars vs. system size  $N$  for different  $p$ . Statistical scars show qualitatively, though less clearly, the same behaviour as those with  $\epsilon^* = 1$ : up to  $p \simeq 0.2$  their number appears to grow with system size while for larger  $p$  one observes saturation.

degeneracy for all  $\epsilon^*$ . For  $p = 0.25$ , we observe a similar behavior, modulo the fact that for several data sets, we do not observe any degeneracy at all.

The overall picture seems to suggest that an eigenstate transition occurs for all values of  $\epsilon^*$ , and that the transition point, for all cases, is located between  $0.15 < p < 0.2$ . Larger system sizes and more comprehensive numerics will be needed to determine whether all transitions happen at the same critical value of  $p$ , or if they are energy-dependent.

# Appendix B

## Quantum simulation of lattice gauge theories

In this Appendix, we provide additional information on the results of Chapters 6 and 7.

### B.1 Entanglement evolution in the FSS model

We consider the FSS model defined in Eq. (6.2) and we investigate the time evolution of the bipartite entanglement entropy  $S(t)$  of the chain. We consider as initial state the CDW, which is equivalent to considering the QLM evolving from one of the two uniform string configurations, see Fig. 6.2. In order to determine  $S$ , we compute the time-dependent reduced density matrix  $\hat{\rho}_R(t)$  of a subsystem consisting of  $L/2$  consecutive sites of the chain, by tracing out the degrees of freedom of the remaining complementary  $L/2$  sites. In these terms, the von Neumann entanglement entropy is defined by  $S(t) = -\text{Tr}[\hat{\rho}_R(t) \ln \hat{\rho}_R(t)]$ .

Figures B.1a and B.1b show the evolution of  $S$  for various values of the mass  $m$  and of the chain length  $L$ , respectively. Information spreading is directly tied to particle production: it is fast at the critical point  $m = m_c$  (green curve in Fig. B.1a, with  $m_c/w = 0.655$ , see Section 6.3) or above it  $m > m_c$  (red curve), where particles are not confined. For  $m < m_c$  (yellow and blue curves), instead, it slows down considerably, as was already observed in the spin-1 QLM [192]. For  $m/\omega = 0$  the change in the original slope of the curve which occurs around  $t\omega \simeq 12$  is due to a finite-volume effect, as demonstrated in Fig. B.1b, where such a change progressively disappears upon increasing  $L$ . In all cases, the fast oscillations correspond to different stages of pair production.

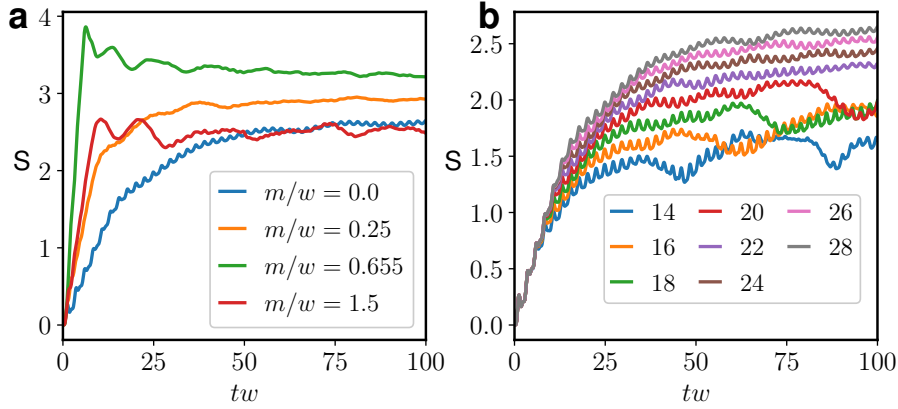


Figure B.1: Growth of entanglement entropy in the FSS model. **a:** Growth of the half-chain entanglement entropy for different values of the particle mass  $m$ . Initial state is CDW/string, and  $L = 28$ . **b:** Growth of entanglement entropy for different sizes  $L$ . Initial state is CDW/string, and  $m = 0$ .

## B.2 Spectral properties of the FSS model

*Robustness of the spectral structure* — As shown in Section 6.3.4, the FSS model for  $m = 0$  features the emergence of regular structures in the middle of the spectrum in terms of energy-momentum bands. We here show that these structures are generically present for sufficiently small values of  $|m/w|$ . Figure B.2 shows the energy-momentum relation of the eigenstates which have largest overlaps with the inhomogeneous state  $|\phi_{e^+e^-}\rangle$  defined in Section 6.3.4. For  $m/w = 0.1$  and  $m/w = -0.2$ , similar dispersion relations to the case  $m/w = 0$  are observed, the main difference being an overall energy shift.

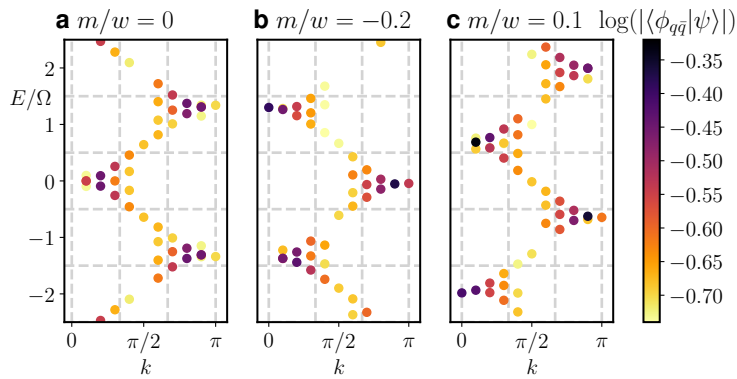


Figure B.2: Robustness of the spectral structure. Energy-momentum relation of eigenstates around  $E = 0$  for  $L = 20$ . For each eigenstate  $|\psi\rangle$ , the colour indicates the value of  $\log_{10}(|\langle\psi|\phi_{e^+e^-}\rangle|)$  (eigenstates with smallest overlaps are not plotted). The dispersion observed for  $m/w = 0$  (panel **a**) is shifted but persists when we introduce a non zero mass (panels **b** and **c**).

*Quasi-particle ansatz for emergent excitations* — In order to obtain physical intuition on the emergence of regular energy-momentum bands in highly-excited states which govern the non-equilibrium evolution of localized defects, we propose the following wavefunction

$$|\chi_k\rangle = \sum_{j=1}^L e^{-ikj} \hat{O}_{j-1,j,j+1} |\Phi_{k=0}\rangle, \quad (\text{B.1})$$

where  $|\Phi_{k=0}\rangle$  is the exact eigenstate found in Ref. [52] with momentum  $k = 0$  and energy 0, and  $\hat{O}_{j-1,j,j+1}$  is a three-site operator depending on a number of variational parameters. Due to the constraints, the space where this operator acts is reduced from dimension  $2^3$  to 5. The inversion symmetry with respect to site  $j$  reduces the number of free variational parameters in  $\hat{O}_{j-1,j,j+1}$  to 11. We choose a basis of operators  $\{\hat{M}_{j-1,j,j+1}^\alpha\}_{\alpha=1}^{11}$  for parameterizing  $\hat{O}_{j-1,j,j+1}$  and define

$$|\phi_k^\alpha\rangle = \sum_{j=1}^L e^{-ikj} \hat{M}_{j-1,j,j+1}^\alpha |\Phi_{k=0}\rangle. \quad (\text{B.2})$$

For each  $k$ , we minimize the energy variance in the space spanned by the states  $|\phi_k^\alpha\rangle$ . To this aim, we compute the three matrices  $N_{\alpha\beta}^k = \langle \phi_k^\alpha | \phi_k^\beta \rangle$ ,  $P_{\alpha\beta}^k = \langle \phi_k^\alpha | \hat{H} | \phi_k^\beta \rangle$ ,  $Q_{\alpha\beta}^k = \langle \phi_k^\alpha | \hat{H}^2 | \phi_k^\beta \rangle$ . In order to prevent numerical issues in the minimization, we diagonalize the matrix of the norms  $N_k$  and we compute the (rectangular) matrix  $U^k$  whose columns are the eigenvectors of  $N^k$  having non-zero eigenvalues. We then find the vector  $\mathbf{c}_k = (c_k^1, \dots, c_k^m)$  that minimizes

$$\sigma_{\hat{H}}^2 = \frac{\mathbf{c}_k^\dagger U^{k\dagger} Q^k U^k \mathbf{c}_k}{\mathbf{c}_k^\dagger U^{k\dagger} N^k U^k \mathbf{c}_k} - \left( \frac{\mathbf{c}_k^\dagger U^{k\dagger} P^k U^k \mathbf{c}_k}{\mathbf{c}_k^\dagger U^{k\dagger} N^k U^k \mathbf{c}_k} \right)^2. \quad (\text{B.3})$$

Note that by introducing the matrix  $U^k$  we restrict the minimization to states with non-zero norms, thus further reducing the number of variational parameters to  $m(k) \leq 11$ . The optimal wavefunction is then obtained as

$$|\chi_k\rangle = \sum_{\alpha=1}^{11} \sum_{\beta=1}^m U_{\alpha\beta}^k c_k^\beta |\phi_k^\beta\rangle. \quad (\text{B.4})$$

## B.3 Continuum limit of the massive Schwinger model

The massive Schwinger model briefly introduced in Section 6.3.2 describes the quantum electrodynamics of fermions of mass  $m$  and charge  $e$  in  $1 + 1$  dimensions. Its Lagrangian density is

$$\mathcal{L} = -\frac{1}{4} F_{\mu\nu} F^{\mu\nu} + \bar{\psi}(i\not{\partial} - e\not{A} - m)\psi \quad (\text{B.5})$$

where  $F_{\mu\nu} = \partial_\mu A_\nu - \partial_\nu A_\mu$ . The indices  $\mu, \nu = 0, 1$  indicate respectively the time and space directions, and the slash notation indicates contraction with the Dirac matrices  $\gamma_\mu$ . This model can be formulated in terms of a bosonic field  $\phi$  [202]. We briefly recall here the main points of the derivation of the bosonic Hamiltonian obtained in Ref. [144].

In the Coulomb gauge ( $A_1 = 0$ ), the Euler-Lagrange equation for  $A_0$  yields

$$\partial_1^2 A_0 = -e j_0 \quad (\text{B.6})$$

where  $j_0 = \psi^\dagger \psi$  is the charge density. Integrating Eq. (B.6), we obtain the continuum version of Eq. (5.10),

$$F_{01} = -\partial_1 A_0 = e \partial_1^{-1} j_0 + F \quad (\text{B.7})$$

where  $F$  is a number, representing a classical background field. The Hamiltonian density obtained from the Lagrangian (B.5) has the form

$$\mathcal{H} = \bar{\psi}(i\gamma_1 \partial_1 + m)\psi + \frac{1}{2} F_{01}^2. \quad (\text{B.8})$$

The interacting Hamiltonian for the fermions can be formulated using Eq. (B.7) to integrate out the gauge fields. Integrating by parts in the zero charge sector, i.e.,  $\int dx j_0(x) = 0$ , we obtain

$$H = \int dx \bar{\psi}(i\gamma_1 \partial_1 + m)\psi - \frac{e^2}{4} \int dx dy j_0(x) j_0(y) |x - y| - eF \int dx x j_0(x). \quad (\text{B.9})$$

Similarly to the lattice version of this model [cf. Eqs. (5.9) and (5.12)], the resulting Hamiltonian contains the energy of massive free fermions, the Coulomb interaction between charges (which increases linearly in one spatial dimension) and the interactions between the charges and the background field.

The method of bosonization can be applied, by noting that in  $1 + 1$  dimensions the conserved vector field  $j^\mu = \bar{\psi} \gamma^\mu \psi$  can be written as the curl of a scalar field  $\phi$

$$j_\mu = \pi^{-1/2} \epsilon_{\mu\nu} \partial^\nu \phi. \quad (\text{B.10})$$

By substituting in Eq. (B.7) we get

$$F_{01} = e\pi^{-1/2} \phi + F, \quad (\text{B.11})$$

and, from the results obtained for a free massive Dirac field [413], we know

$$\bar{\psi}(i\gamma_1 \partial_1 + m)\psi \rightarrow N_m \left[ \frac{1}{2} \Pi^2 + \frac{1}{2} (\partial_1 \phi)^2 - cm^2 \cos(2\pi^{1/2} \phi) \right]. \quad (\text{B.12})$$

where  $c = e^\gamma/(2\pi)$ ,  $\gamma \simeq 0.577$  is the Euler constant and  $N_m$  indicates normal ordering with respect to the mass  $m$ . Inserting Eqs. (B.11) and (B.12) in Eq. (B.8), the Hamiltonian density reads

$$\mathcal{H} = N_m \left[ \frac{1}{2}\Pi^2 + \frac{1}{2}(\partial_1\phi)^2 - cm^2 \cos(2\pi^{1/2}\phi) + \frac{e^2}{2\pi} \left( \phi + \frac{\pi^{1/2}F}{e} \right)^2 \right]. \quad (\text{B.13})$$

By shifting the field  $\phi \rightarrow \phi - \pi^{1/2}F/e$  and defining a new normal ordering with respect to the mass  $\mu = \pi^{-1/2}e$ , we finally obtain

$$\mathcal{H} = N_\mu \left[ \frac{1}{2}\Pi^2 + \frac{1}{2}(\partial_1\phi)^2 - cm\mu \cos(2\pi^{1/2}\phi - \theta) + \frac{\mu^2}{2}\phi^2 \right] \quad (\text{B.14})$$

where  $\theta = 2\pi F/e$ . The latter form connects with the discussion in Section 6.3.2.

## B.4 Non-Abelian lattice gauge theories with alkaline-earth-like atoms: derivation of the lattice Hamiltonian

In this Section we remind the key steps and approximations to obtain the discrete lattice Hamiltonian from Eq. 7.3. The main step is the decomposition of the field operators in the standard Wannier function basis [220, 414]. The centers of the Wannier functions of  $g$  states constitute the bipartite lattice of interest.

We take

$$\Psi_{gi}(\mathbf{r}) = \sum_{x \text{ even}} w_g^A(\mathbf{r} - \mathbf{R}_x) \psi_x^i + \sum_{x \text{ odd}} w_g^B(\mathbf{r} - \mathbf{R}_x) \psi_x^i, \quad (\text{B.15})$$

where  $\psi_x^i$  are the annihilation operator of the  $g$  atom on site  $x$  of spin  $i$  introduced at Eq. 7.1. The  $A/B$  labels indicate the functions with centers on the even/odd sublattice. Similarly, for the  $e$  lattice we take

$$\Psi_{ei}(\mathbf{r}) = \sum_{x \text{ even}, \hat{k}} w_{e,\hat{k}}^A(\mathbf{r} - \mathbf{R}_{x,\hat{k}}) c_{x,\hat{k}}^i + \sum_{x \text{ odd}, \hat{k}} w_{e,\hat{k}}^B(\mathbf{r} - \mathbf{R}_{x,\hat{k}}) c_{x,\hat{k}}^i. \quad (\text{B.16})$$

We now discuss how the expression of Wannier functions are obtained, and then provide the expression of the various amplitudes in Eqs. 7.4 using these Wannier functions.

### B.4.1 Localized Wannier functions

The Wannier functions are obtained as linear combinations of the Bloch functions which diagonalize the non-interacting part of the Hamiltonian in

Eq. (7.3). To obtain the Bloch functions, we consider the following single particle Hamiltonian for the two species  $\alpha = g, e$  (we dropped the term proportional to  $\hbar\omega_0$ , because it contributes as an overall constant)

$$H_{\text{non-int}}^\alpha = -\frac{\hbar^2}{2M}\nabla^2 + V_{\alpha i}(\mathbf{r}). \quad (\text{B.17})$$

The dependence of the potential in the (selected) hyperfine level  $i$  of the atoms is negligible, so  $V_\alpha(\mathbf{r}) \equiv V_{\alpha i}(\mathbf{r})$  and the eigenfunctions do not depend on  $i$ . The potential  $V_\alpha(\mathbf{r})$  is of the form

$$V_\alpha(\mathbf{r}) = \begin{cases} V_\alpha^\parallel(x) + V_\alpha^\perp(y, z) & \text{for 1D lattices,} \\ V_\alpha^\parallel(x, y) + V_\alpha^\perp(z) & \text{for 2D lattices.} \end{cases} \quad (\text{B.18})$$

For this type of potentials, the Wannier functions factorize as a function of transverse variables (orthogonal to the line/plane) and a function of longitudinal variables (along the line/plane). As the trapping potential  $V_\alpha^\perp$  is deep, it is well approximated by an harmonic oscillator such that the transversal dependence of the Wannier function is a gaussian. In 1D we find

$$w_\alpha(\mathbf{r}) = (\pi\ell_{\alpha y}\ell_{\alpha z})^{-1/2} \exp\left(-\frac{y^2}{2\ell_{\alpha y}^2} - \frac{z^2}{2\ell_{\alpha z}^2}\right) \varphi_\alpha(x) \quad (\text{B.19})$$

where  $\alpha$  is a multi-index that labels both the sublattice  $A, B$  and the site  $g, e, \hat{k}$ . The widths of the gaussians are obtained as<sup>1</sup>  $\ell_{y/z\alpha}^2 = \hbar d / \sqrt{2\pi^2 V_\alpha^{y/z} M}$  and  $\varphi_\alpha(x)$  is a function of the longitudinal continuous variable  $x$ . And similarly, in 2D

$$w_\alpha(\mathbf{r}) = (\sqrt{\pi}\ell_\alpha)^{-1/2} \exp\left(-\frac{z^2}{2\ell_\alpha^2}\right) \varphi_\alpha(x, y). \quad (\text{B.20})$$

To obtain the functions  $\varphi_\alpha$  we use the procedure discussed in Ref. [415]. In 1D, we compute the Bloch functions for both the  $g$  and the  $e$  potential, and we find the Wannier functions as the eigenfunctions of the projection of the position operator on a single band (if well isolated from the others) or a set of bands.

The lowest bands in the spectrum of the  $g$  and  $e$  lattice for the values in Tab. 7.2 of the main text are represented Fig. B.3. For  $g$ , the gaps  $\delta_g$  and  $\Delta_g$  are much larger than the bandwidths of the two lowest band. Therefore we can compute the Wannier functions for the two lowest  $s$  bands (the only two susceptible to be populated), without hybridization. From each band we obtain the Wannier function of one of the sublattices.

<sup>1</sup>In our numerical estimate in 1D we assume that  $\ell_{y/z\alpha}$  depends on the sublattice  $A/B$ . While this is not possible for a separable potential, as the one described here, we expect this to be possible in the true experimental setup, where the beams are positioned at an angle with respect to the  $x$  direction. To simplify our numerical estimate, we use the approximation of factorized Wannier functions and we assume then that  $\ell_{y/z\alpha}$  can be tuned independently for the  $A$  and  $B$  sublattices.

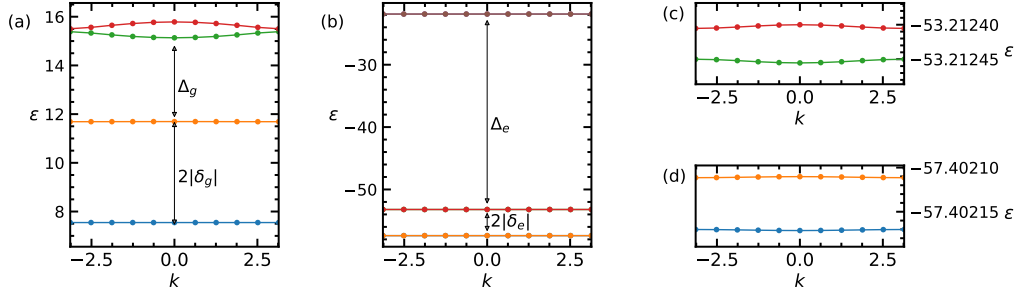


Figure B.3: Lowest bands of the (a)  $g$  and (b)  $e$  lattice. In (a), the first and the second bands are both well isolated from the rest. The gap between the two lowest bands is  $\sim 2|\delta_g|$ , the gap between the second and the third is what we define as  $\Delta_g$ . In (b) the first four bands form two doublets: they correspond to the pairs of sites  $e\pm$  on sublattice  $A$  and  $e\pm$  on sublattice  $B$ . The separation between the pairs is  $\sim 2|\delta_e|$ , and we define  $\Delta_e$  as the gap between the fourth and the fifth band. (c,d) Each pair of bands has separation  $\sim 2|t_e|$ .

On the other hand, for the  $e$  state the two lowest bands and the third and fourth bands are very close in energy (the splitting is  $\sim 2|t_e|$ ), so the hybridized Wannier functions are obtained by constructing the position operator on each pair. From each pair we obtain the Wannier functions of the sites  $e+$  and  $e-$  on each sublattice.

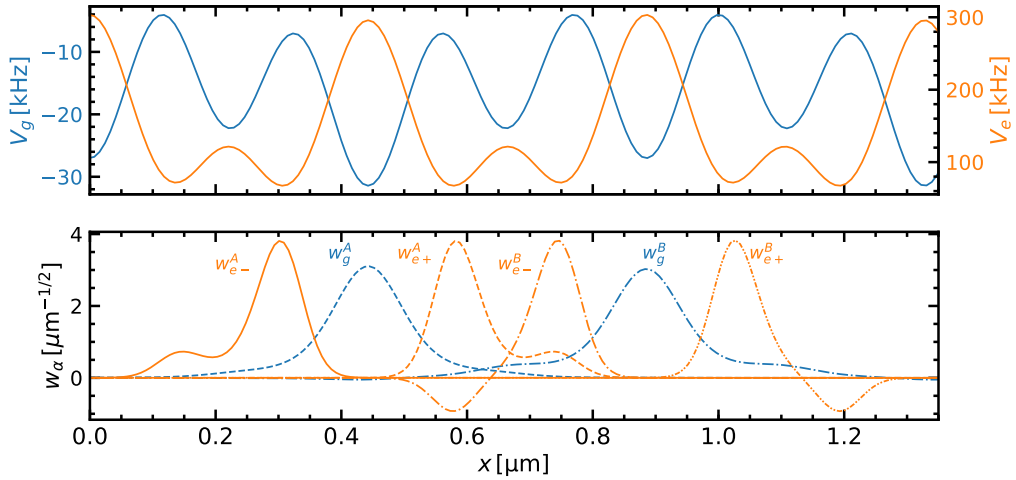


Figure B.4: Top: Lattice potential for the  $g$  and  $e$  lattice. The values of the amplitudes are the ones in Tab. 7.2. Bottom: Wannier functions of  $A$  and  $B$  blocks.

The Wannier functions obtained for the lattice amplitudes of Tab. 7.2 are plotted in Fig. B.4.

We remark that other choices of Wannier functions are possible: for example, one can hybridize the two lowest bands for the  $g$  states, and the

four lowest bands for the  $e$  states, thus obtaining the maximally localized ones. Both choices give a complete basis for the two/four lowest bands of the  $g/e$ , so the spectral properties of the lattice model are completely equivalent. However, we consider the other choice described above, because in that basis the hopping between sites in an even block and an odd block are 0 by construction. This choice is typically disadvantageous because it results in larger interaction terms between different sites: in our case, instead, this effect is beneficial because it enhances both the interaction terms needed to impose gauge invariance (namely  $U^{ge\pm}$ ) and the gauge-assisted hopping. Therefore, we find that this choice of basis is the most useful to encode the matter and gauge variables.

### B.4.2 Amplitude formulae

Once the Wannier functions are obtained, the expressions of all amplitudes in the single block Hamiltonian  $h_x^0$  Eqs 7.4 follows. We report here the equations. The amplitudes and the Wannier functions depend on the parity of the block, so all the following equations are intended for one of the two sublattices,  $A$  (even) or  $B$  (odd): we drop the sublattice index to simplify the notation.

$$\mu_e = \int dx w_{e+}(x) \left( -\frac{\hbar^2}{2M} \frac{d^2}{dx^2} + V_e(x) \right) w_{e+}(x) \quad (\text{B.21})$$

$$= \int dx w_{e-}(x) \left( -\frac{\hbar^2}{2M} \frac{d^2}{dx^2} + V_e(x) \right) w_{e-}(x), \quad (\text{B.22})$$

$$\mu_g = \int dx w_g(x) \left( -\frac{\hbar^2}{2M} \frac{d^2}{dx^2} + V_g(x) \right) w_g(x), \quad (\text{B.23})$$

$$t_e = \int dx w_{e+}(x) \left( -\frac{\hbar^2}{2M} \frac{d^2}{dx^2} + V_e(x) \right) w_{e-}(x), \quad (\text{B.24})$$

$$U^{gg} = \frac{g_{gg}}{2\pi\ell_g^2} \int dx [w_g(x)]^4, \quad (\text{B.25})$$

$$U^{eg\pm} = \frac{g_{eg}^\pm}{\pi(\ell_g^2 + \ell_e^2)} \int dx [w_g(x)]^2 [w_{e+}(x)]^2. \quad (\text{B.26})$$

## B.5 Resonance condition and derivation of QLM Hamiltonian

In this Section, we derive the Quantum Link Model Hamiltonian from the lattice Hamiltonian of Section B.4. We first define and prove the conditions which make the gauge-invariant subspace resonant. Then we show how these conditions bring (almost all) gauge-variant states off-resonant. Lastly, we derive the QLM Hamiltonian by projecting the lattice Hamiltonian on the resonant subspace.

### B.5.1 Resonance condition

We now demonstrate the resonance conditions for all  $N$  and all dimensions. We want to prove that all states with  $G_x = N$ ,  $G_x^a = 0$  are degenerate eigenstates of  $H_0 = \sum_x h_x^0$ , provided that these two conditions hold: (i)  $\delta_g + (N - 1)\epsilon = \delta_e$  and (ii)  $U_x^{gg} = 2U_x^{eg+}$ .

For  $G_x = N$ , the single block Hamiltonian  $h_x^0$  reads

$$h_x^0 = \mu_x^g n_x + \mu_x^e (N - n_x) + \frac{U_x^{gg}}{2} n_x (n_x - 1) + U_x^{ge+} n_x (N - n_x) - \frac{U_x^{eg+} - U_x^{eg-}}{4} S_x^a G_x^a. \quad (\text{B.27})$$

When (i) and (ii) are satisfied, we get

$$h_x^0 = \mu_x^e N + (\mu^g - \mu^e + U^{ge+} N) n_x - \frac{U_x^{eg+} - U_x^{eg-}}{4} S_x^a G_x^a, \quad (\text{B.28})$$

with  $S_x^a = \psi_x^{i\dagger} \lambda_{ij} \psi_x^j$ . For gauge-invariant states,  $G_x^a = 0$ , so the Hamiltonian  $H_0$  restricted to the gauge invariant space reads:

$$H_0 = \sum_x \mu_x^e N + (\mu^g - \mu^e + U^{ge+} N) \sum_x n_x. \quad (\text{B.29})$$

Since the total number of  $g$  particles  $\sum_x n_x$  is conserved, we find that the Hamiltonian  $H_0$  projected on the gauge-invariant space is proportional to the identity.

### B.5.2 Off-resonance condition

We now discuss what are the mechanisms which forbid the occupation of gauge variant states in the dynamics. The first requirement is that the number of rishons per link  $\mathcal{N} = 1$  is conserved. This is simply enforced by the huge barrier between different double wells. The next requirement is the Abelian constraint  $G_x = N$ , which imposes that the number of atoms per blocks is conserved. This is achieved by introducing the shifts  $\delta_g$  and  $\delta_e$  between blocks of different parity. The shifts make the hoppings between neighbouring blocks off-resonant, but they do not prevent longer-range hoppings between blocks of the same parity. We assume (and check, for our choice of realistic experimental parameters) that longer-range hoppings are small and can be safely neglected. When this is satisfied, the number of particles per block is conserved. The last condition to enforce is the non-Abelian constraint. As can be evinced from Eq. (B.28), the off-resonance condition  $U_x^{eg+} \neq U_x^{eg-}$  is enough to bring all states with  $G_x = N$ ,  $\mathcal{N} = 1$ , but  $G_x^a \neq 0$  off resonance as long as  $\sum_a (S_x^a)^2 \neq 0$ , i.e. as long as  $n_x \neq 0$ . The energy cost for these states depends on the antisymmetric representation  $\mathcal{R}_g$  of the  $n_x$   $g$  atoms, the representation  $\mathcal{R}_e$  of the  $N - n_x$   $e$  atoms,

and the representation  $\mathcal{R}_{ge}$  of all the  $N$  atoms on each site. Indeed,

$$S_x^a G_x^a = \frac{1}{2} \left( (S_x^a)^2 + \left( S_x^a + \sum_{\hat{k}} I_{x,\hat{k}}^a \right)^2 - \left( \sum_{\hat{k}} I_{x,\hat{k}}^a \right)^2 \right), \quad (\text{B.30})$$

$$= \frac{1}{2} (C_2(\mathcal{R}_g) + C_2(\mathcal{R}_{ge}) - C_2(\mathcal{R}_e)), \quad (\text{B.31})$$

with  $I_{x,\hat{k}}^a = c_{x,\hat{k}}^{i\dagger} \lambda_{ij} c_{x,\hat{k}}^j$  and  $C_2(\mathcal{R})$  the quadratic Casimir of the representation  $\mathcal{R}$ . When all atoms are in a singlet state (gauge-invariant),  $\mathcal{R}_e$  is the conjugate of  $\mathcal{R}_g$ , such that  $C_2(\mathcal{R}_g) = C_2(\mathcal{R}_e)$  and  $C_2(\mathcal{R}_{ge}) = 0$ : the states are always resonant.

States with no  $g$  atoms, such as the  $e - e$  triplets for  $N = 2$  in 1D, have  $C_2(\mathcal{R}_g) = 0$  and  $\mathcal{R}_{ge} = \mathcal{R}_e$ : they are also always resonant. However, because of the global  $SU(N)$  symmetry, for these states to be occupied the non-Abelian Gauss' law has to be simultaneously violated on at least two blocks: in one dimension this clearly cannot be achieved on two neighbouring blocks (because two subsequent  $e - e$  triplets do not satisfy the constraint  $\mathcal{N} = 1$ ), so the terms which violate Gauss' law will involve blocks with distance 2 or larger. These longer range terms are generally negligible.

When  $N \geq 3$  in 1D,  $S_x^a G_x^a \geq C_2(\mathcal{R}_{ge})/2$  for any possible set of representation, which is strictly positive when the state is not a singlet: the states are always off-resonant. For higher dimensions, all set of compatible representation must be considered: a gauge breaking state is resonant if it cancels Eq. B.31.

### B.5.3 Projected Hamiltonian in 1D

We now consider only resonant terms obtained from the interaction between neighbouring blocks: in other words we project all the terms on the eigenspace of  $H_0$  to which the initial state belongs (i.e. the gauge invariant sector with one rishon per link). We call  $P$  the projector on this space. We immediately exclude all the terms that have clearly no component on the gauge-invariant space and we are left with the following

$$H' = H_0 + P \sum_x h_{x,x+1}^1 P \quad (\text{B.32})$$

$$\begin{aligned}
Ph_{x,x+1}^1 P &= \left[ \frac{g_{eg}^+ - g_{eg}^-}{2} - \frac{1}{N} \frac{g_{eg}^+ + g_{eg}^-}{2} \right] J \left( \psi_{x+1}^{i\dagger} c_{x,+}^{j\dagger} \psi_x^j c_{x+1,-}^i + \text{H.c.} \right) \\
&+ g_{gg} K \left( 1 - \frac{1}{N} \right) n_x n_{x+1} \\
&+ \left[ \frac{g_{eg}^+ + g_{eg}^-}{2} - \frac{1}{N} \frac{g_{eg}^+ - g_{eg}^-}{2} \right] (I_x n_{x+1,-} n_x + I_{x+1} n_{x,+} n_{x+1}) \\
&+ \left[ \frac{g_{eg}^+ + g_{eg}^-}{2} - \frac{1}{N} \frac{g_{eg}^+ - g_{eg}^-}{2} \right] (L_x n_{x+1,+} n_x + L_{x+1} n_{x,-} n_{x+1})
\end{aligned} \tag{B.33}$$

where

$$J = \frac{2}{\pi \ell_{gA} \ell_{gB} \ell_{eA} \ell_{eB} (\ell_{gA}^{-2} + \ell_{gB}^{-2} + \ell_{eA}^{-2} + \ell_{eB}^{-2})} \int ds w_g^A(s) w_{e+}^A(s) w_{e-}^B(s - a_0) w_g^B(s - a_0) \tag{B.34}$$

$$K = \frac{1}{\pi(\ell_{g,A}^2 + \ell_{g,B}^2)} \int ds [w_g^A(s)]^2 [w_g^B(s - a_0)]^2 \tag{B.35}$$

$$I_x = \begin{cases} \frac{1}{\pi(\ell_{g,A}^2 + \ell_{e,B}^2)} \int ds [w_g^A(s)]^2 [w_{e-}^B(s - a_0)]^2 & \text{if } x \text{ is even} \\ \frac{1}{\pi(\ell_{g,B}^2 + \ell_{e,A}^2)} \int ds [w_g^B(s)]^2 [w_{e-}^A(s - a_0)]^2 & \text{if } x \text{ is odd} \end{cases} \tag{B.36}$$

$$L_x = \begin{cases} \frac{1}{\pi(\ell_{g,A}^2 + \ell_{e,B}^2)} \int ds [w_g^A(s)]^2 [w_{e+}^B(s - a_0)]^2 & \text{if } x \text{ is even} \\ \frac{1}{\pi(\ell_{g,B}^2 + \ell_{e,A}^2)} \int ds [w_g^B(s)]^2 [w_{e+}^A(s - a_0)]^2 & \text{if } x \text{ is odd} \end{cases} \tag{B.37}$$

We obtain

$$\begin{aligned}
H' &= H_0 - \tau \sum_x \left( \psi_{x+1}^{i\dagger} c_{x+1,-}^i - c_{x,+}^{j\dagger} \psi_x^j + \text{H.c.} \right) + \tilde{w} \sum_x n_x n_{x+1} \\
&+ \sum_x \frac{\tilde{u}_x}{2} n_x (n_{x+1,-} + n_{x-1,+}) + \sum_x \frac{\tilde{v}_x}{2} n_x (n_{x+1,+} + n_{x-1,-}), \tag{B.38}
\end{aligned}$$

where  $\tau$ ,  $w$ ,  $u_x$  and  $v_x$  are defined as

$$\tau = \left[ \frac{g_{eg}^+ - g_{eg}^-}{2} - \frac{1}{N} \frac{g_{eg}^+ + g_{eg}^-}{2} \right] J, \quad \tilde{w} = g_{gg} K \left( 1 - \frac{1}{N} \right), \tag{B.39}$$

$$\tilde{u}_x = 2 \left[ \frac{g_{eg}^+ + g_{eg}^-}{2} - \frac{1}{N} \frac{g_{eg}^+ - g_{eg}^-}{2} \right] I_x, \quad \tilde{v}_x = 2 \left[ \frac{g_{eg}^+ + g_{eg}^-}{2} - \frac{1}{N} \frac{g_{eg}^+ - g_{eg}^-}{2} \right] L_x. \quad (\text{B.40})$$

### B.5.4 Correction to the resonance condition

The projected Hamiltonian in Eq. (B.38) has the disadvantage that the amplitude  $\tau$  is typically much smaller than  $\tilde{u}_x$ , because the centers of the Wannier functions that are involved in its integral are more distant. This large difference in energy scale makes the model trivial and “freezes” the dynamics. To avoid this, we will now show how the large interaction terms that compete with the gauge-assisted hopping can be included in the Hamiltonian  $H_0$ , and how this modifies the resonance condition.

We can use the fact that we have one rishon per link and  $N$  atoms per block to rewrite

$$n_x(n_{x+1,-} + n_{x-1,+}) = n_x(2 - n_{x,+} - n_{x,-}) = n_x(2 + n_x - N), \quad (\text{B.41})$$

$$\begin{aligned} n_x(n_{x+1,+} + n_{x-1,-}) &= n_x(N - n_{x+1,-} - n_{x+1,+} + N - n_{x-1,+} - n_{x-1,-}) \\ &= 2Nn_x - n_x(n_{x+1} + n_{x-1}) - n_x(n_{x+1,-} + n_{x-1,+}). \end{aligned} \quad (\text{B.42})$$

The last two terms in Eq. (B.38) become

$$\begin{aligned} &\sum_x \left[ \frac{\tilde{u}_x}{2} n_x (n_{x+1,-} + n_{x-1,+}) + \frac{\tilde{v}_x}{2} n_x (n_{x+1,+} + n_{x-1,-}) \right] \\ &= \sum_x \left[ -\frac{\tilde{v}_x + \tilde{v}_{x+1}}{2} n_x n_{x+1} + \frac{\tilde{u}_x - \tilde{v}_x}{2} n_x (n_x - 1) \right. \\ &\quad \left. + \left( N\tilde{v}_x + \frac{\tilde{u}_x - \tilde{v}_x}{2} (3 - N) \right) n_x \right] \\ &\equiv \sum_x \left( -\frac{\tilde{v}_x + \tilde{v}_{x+1}}{2} n_x n_{x+1} \right) + \tilde{H}_0. \end{aligned} \quad (\text{B.43})$$

In this new form, these terms give an additional contribution to the interaction  $\tilde{w}$  between neighbouring matter sites, to the on-site interaction  $U_x^{gg}$  and to the chemical potential  $\mu_x^g$ . The terms in  $\tilde{H}_0$  can then be included in  $H_0$ , resulting in the following resonance conditions

$$\delta_g + N\chi + \frac{\eta - \chi}{2} (3 - N) + (N - 1)\epsilon \simeq \delta_e \quad (\text{B.44})$$

$$U_x^{gg} + \tilde{u}_x - \tilde{v}_x \simeq 2U_x^{eg+} \quad (\text{B.45})$$

where  $\tilde{u}_x = \tilde{u} + s_x \eta$ ,  $\tilde{v}_x = \tilde{v} + s_x \chi$ . We then define  $w = \tilde{w} - (\tilde{v}_x + \tilde{v}_{x+1})/2$ , while  $m$  and  $u_x$  are defined as small deviations from the resonance conditions

$$m = \delta_g + N\chi + \frac{\eta - \chi}{2} (3 - N) + (N - 1)\epsilon - \delta_e, \quad (\text{B.46})$$

$$u_x = U_x^{gg} + \tilde{u}_x - \tilde{v}_x - 2U_x^{eg+}. \quad (\text{B.47})$$

We finally obtain the new projected Hamiltonian

$$\begin{aligned} H' &= H_0 + \tilde{H}_0 + w \sum_x \psi_x^{i\dagger} \psi_x^i \psi_{x+1}^{j\dagger} \psi_{x+1}^j - \tau \sum_x \left( \psi_{x+1}^{i\dagger} c_{x+1,-}^i - c_{x,+}^j \psi_x^j + \text{H.c.} \right) \\ &= H_{res} + m \sum_x s_x \psi_x^{i\dagger} \psi_x^i + w \sum_x \psi_x^{i\dagger} \psi_x^i \psi_{x+1}^{j\dagger} \psi_{x+1}^j \\ &\quad - \tau \sum_x \left( \psi_{x+1}^{i\dagger} c_{x+1,-}^i - c_{x,+}^j \psi_x^j + \text{H.c.} \right) + \sum_x \frac{u_x}{2} \psi_x^{i\dagger} \psi_x^i (\psi_x^{j\dagger} \psi_x^j - 1) \end{aligned} \quad (\text{B.48})$$

with  $H_{res}$  constant on the gauge invariant subspace.

## B.6 *Ab initio* values: additional data

In Tab. B.1 we report realistic values for an experimental implementation of a one-dimensional  $\text{SU}(3) \times \text{U}(1)$  QLM using  $^{173}\text{Yb}$ .

$a_0$   $\sim 0.44$	$\Delta_g$   3.6962	$\tilde{u}$   0.05666
$V_g^0$   7	$\Delta_e$   31.3583	$\tilde{v}$   $3 \cdot 10^{-6}$
$V_g^1$   -20.02	$\delta_g$   -2.0720	$\tilde{v}$   0.001019
$V_g^S$   4.40	$\delta_e$   -2.0731	$\beta_g$   $5 \cdot 10^{-5}$
$V_e^0$   -178.16	$t^e$   $-3.0 \cdot 10^{-5}$	$m$   $-4.43 \cdot 10^{-4}$
$V_e^1$   125.15	$t^e$   $-2.5 \cdot 10^{-5}$	$\tau$   -0.00494
$V_e^S$   7.36	$U^{eg+}$   1.2321	$u$   $< 10^{-6}$
$\ell_g$   0.0578	$U^{eg-}$   0.1441	$w$   $2.45 \cdot 10^{-4}$
$\ell_g$   0.0565	$U^{gg}$   2.4075	
$\ell_e$   0.0235	$U^{gg}$   2.3013	
$\ell_e$   0.0455		

Table B.1: First column: parameters of the  $^{173}\text{Yb}$  in Eq. (7.3) [218, 222]. Second column: *ab initio* parameters of Eq. 7.2 for the 1D setup with  $N = 3$ . Third and fourth columns: parameters of the optical lattices. Fifth to seventh columns: corresponding values of the lattice Hamiltonian Eq. 7.4. Energies are in kHz and lengths are in  $\mu\text{m}$ . A box has two values when the corresponding quantity is different for odd and even sites within significant digits.



# Appendix C

## Non-equilibrium dynamics of lattice gauge theories

Here we derive in detail the results presented in Part III of the main text. The chapter is organized as follows: in Section C.1 we show how to map the quantum Ising chain onto a  $U(1)$  or a  $\mathbb{Z}_2$  lattice gauge theory (LGT); in Section C.2 we discuss the general construction of the effective Hamiltonian and we report its analytic determination at the lowest order in perturbation theory in the quantum Ising chain; in Section C.3 we study the effective model in the two-particle sector in order to estimate the delocalization time of an isolated string and rationalize the observed entanglement growth; in Section C.4 we consider the effective model in the 4-particle sectors and we describe a method to construct the solutions of the scattering problem in the limit of large fermion mass; in Section C.5 we derive the analytic expression of the meson current, we discuss its physical meaning and we prove the associated continuity equation; in Section C.6 we summarize and discuss the effects of having a finite fermion mass; in Section C.7 we collect the exact expressions for the scattering phases which are used in the semiclassical quantization equations in Sec. 12.2; in Section C.8 we report the results on the spectral statistics of the Schwinger model in the case of a non-zero topological angle.

### C.1 Exact mapping between quantum spin chains and lattice gauge theories in one spatial dimension

In this Section, we provide the details of the mappings between quantum spin chains and one-dimensional LGTs. The correspondence is based on the elimination of matter degrees of freedom. A related construction was proposed in Chapter 6, which allows one to interpret strongly interacting Rydberg atom arrays as the realization of a spin-1/2  $U(1)$  LGT with stag-

gered fermionic matter. For the sake of illustration, we focus here on the quantum Ising chain given in Eq. (10.8), but analogous mappings may be constructed for similar one-dimensional quantum lattice models by (i) introducing additional “matter” degrees of freedom on the bonds, and (ii) defining gauge-invariant interactions in such a way that the Gauss law renders these newly introduced degrees of freedom actually redundant.

### C.1.1 The quantum Ising chain as a $\mathbb{Z}_2$ LGT

Here we illustrate the details of the mapping between the  $\mathbb{Z}_2$ -LGT in Eq. (8.3) and the quantum Ising chain in a tilted magnetic field, Eq. (8.2). This mapping was proposed in Ref. [6], and is connected with the one discussed in Ref. [275].

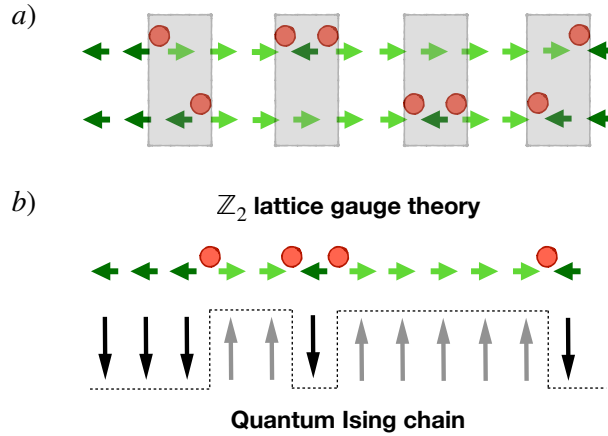


Figure C.1: (a) The two rows represent two gauge-neutral classical configurations of the matter and gauge fields in Eq. (8.3), i.e., simultaneous eigenstates of the operators  $n_j = c_j^\dagger c_j$  and  $\sigma_{j+1/2}^z$  for all  $j$ . Red spots denote the presence of a fermionic charge; horizontal green arrows denote the polarization of the gauge field: light, rightward for  $\sigma_{j+1/2}^z = +1$  and dark, leftward for  $\sigma_{j+1/2}^z = -1$ . By the Gauss law in Eq. (8.4), the gauge field varies only across sites that contain a charge. The grey-shaded rectangles highlight the possible local transitions, from the top to the bottom configuration, described by the interaction term in Eq. (8.3): from left to right, we have rightward fermion hop, pair annihilation, pair creation, leftward fermion hop. (b) Cartoon illustration of the exact mapping between the  $\mathbb{Z}_2$ -LGT in Eq. (8.3) in the neutral gauge sector defined by Eq. (8.4), and the quantum Ising chain in Eq. (8.2). The mapping hinges upon the elimination of the fermionic degrees of freedom, which are in one-to-one correspondence with gauge-field domain-walls by means of the Gauss law.

We consider the neutral sector, defined by the Gauss law, i.e.,  $G_j = \sigma_{j-1/2}^z \sigma_{j+1/2}^z (1 - 2n_j) \equiv 1$ , with  $n_j = c_j^\dagger c_j$  representing the number of fermions at site  $j$ . The essence of the mapping is the exact elimination

of the fermion degrees of freedom [169], as highlighted in Fig. C.1-(b). The latter are redundant due to the local constraints in Eq. (8.4): a classical configuration of the gauge field uniquely fixes the configuration of the fermionic matter via the Gauss law.

We present a formal proof of the equivalence. As a first step, we apply the Jordan-Wigner transformation to turn the fermions into hard-core bosons. To this aim, we introduce the spin-1/2 operators  $\tau_j^\alpha$ , for  $\alpha = +, -, z$ , defined as

$$\tau_j^- = \prod_{k<j} (1 - 2n_k) c_j, \quad \tau_j^+ = (\tau_j^-)^\dagger, \quad \tau_j^z = 2n_j - 1. \quad (\text{C.1})$$

As can be easily checked, the operators  $\tau_j^z$ ,  $\tau_j^x = \tau_j^+ + \tau_j^-$  and  $\tau_j^y = -i(\tau_j^+ - \tau_j^-)$  satisfy the usual commutation relations of spin operators. By applying this transformation, we get the Hamiltonian

$$H = m \sum_j \frac{1 + \tau_j^z}{2} + \frac{\tau}{2} \sum_j \sigma_{j+1/2}^z + w \sum_j \tau_j^x \sigma_{j+1/2}^x \tau_{j+1}^x, \quad (\text{C.2})$$

with the constraint

$$G_j = -\sigma_{j-1/2}^z \sigma_{j+1/2}^z \tau_j^z = 1. \quad (\text{C.3})$$

We now define a unitary transformation  $U$  that eliminates the matter degrees of freedom. In other words, we seek for a (gauge-variant) unitary  $U$  such that the transformed Gauss law  $G'_j = U G_j U^\dagger \equiv 1$  from Eq. (C.3) only depends on the matter degrees of freedom, whereas the transformed Hamiltonian  $H' = U H U^\dagger$  only involves the gauge degrees of freedom. This can be accomplished with

$$\begin{aligned} U &= \prod_j \exp \left[ \frac{i\pi}{2} (\tau_j^x - 1) \frac{1 - \sigma_{j-1/2}^z \sigma_{j+1/2}^z}{2} \right] \\ &= \prod_j \left[ \frac{1 + \sigma_{j-1/2}^z \sigma_{j+1/2}^z}{2} + \tau_j^x \frac{1 - \sigma_{j-1/2}^z \sigma_{j+1/2}^z}{2} \right]. \end{aligned} \quad (\text{C.4})$$

This transformation flips the spin  $\tau_j^z$  where the neighbouring gauge fields are anti-aligned and does nothing where they are aligned. We get  $U \tau_j^z U^\dagger = \tau_j^z \sigma_{j+1/2}^z \sigma_{j+1/2}^z$  and  $U \tau_j^x \sigma_{j+1/2}^x \tau_{j+1}^x U^\dagger = \sigma_{j+1/2}^x$ . The transformed constraint

$$G'_j = U G_j U^\dagger = -\tau_j^z \equiv 1 \quad (\text{C.5})$$

forces the  $\tau_j^\alpha$  spins to be polarized in the  $-\hat{z}$  directions. They enter the transformed Hamiltonian only via  $G'_j$ :

$$H' = m \sum_j \frac{1 - G'_j \sigma_{j-1/2}^z \sigma_{j+1/2}^z}{2} + \frac{\tau}{2} \sum_j \sigma_{j+1/2}^z + w \sum_j \sigma_{j+1/2}^x. \quad (\text{C.6})$$

Thus, in the neutral gauge sector, by Eq. (C.5) the spins  $\tau_j^\alpha$  are eliminated. Equation (C.6), which governs the dynamics within this sector, coincides with the quantum Ising chain in a tilted magnetic field reported in Eq. (8.2) (up to an irrelevant additive constant) upon identifying  $m = 2J$ ,  $\tau = -2h$ ,  $w = -g$ .

We note that, while in this derivation we used a non-local transformation to convert the fermions into hard-core boson, it is nevertheless possible to formulate a completely local mapping between the two Hamiltonians: in the neutral gauge sector, the Jordan-Wigner string can be completely reabsorbed using Gauss' law. To show that the mapping is local, it is sufficient to define the transformed spin operators

$$\tilde{\sigma}_{j+1/2}^x = (c_j^\dagger - c_j)\sigma_{j+1/2}^x(c_{j+1}^\dagger + c_{j+1}), \quad (\text{C.7})$$

$$\tilde{\sigma}_{j+1/2}^y = (c_j^\dagger - c_j)\sigma_{j+1/2}^y(c_{j+1}^\dagger + c_{j+1}), \quad (\text{C.8})$$

$$\tilde{\sigma}_{j+1/2}^z = \sigma_{j+1/2}^z. \quad (\text{C.9})$$

These operators satisfy the usual commutation relations of Pauli matrices and are related to the original spins by a local transformation. It is then immediate to write Eq. (8.3) in terms of the new spin operators, obtaining the quantum Ising chain in the neutral gauge sector:

$$H' = m \sum_j \frac{1 - \tilde{\sigma}_{j-1/2}^z \tilde{\sigma}_{j+1/2}^z G_j}{2} + \frac{\tau}{2} \sum_j \tilde{\sigma}_{j+1/2}^z + w \sum_j \tilde{\sigma}_{j+1/2}^x. \quad (\text{C.10})$$

### C.1.2 The quantum Ising chain as a U(1) LGT

The quantum Ising chain can equivalently be mapped to a  $U(1)$  lattice gauge theory. The correspondence is again based on the interpretation of the spin polarization operator  $s_j^z \equiv \sigma_j^z/2$  as a local "electric flux", and on the introduction of fictitious fermionic matter degrees of freedom on the sites of the dual chain. In this case, they represent "positrons" and "electrons". Crucially, one enforces local dynamical constraints that associate a kink (antikink) in the spin configuration with the presence of a positron (electron) on the corresponding bond, as described in Fig. C.2. These constraints are interpreted as implementing a discrete Gauss law and result from the  $U(1)$  gauge-invariance of matter-field interactions.

To make this construction explicit, we define two species of fermions, positively ( $p$ ) and negatively ( $e$ ) charged respectively, residing on the chain bonds (denoted as half-integer sites), with corresponding creation operators  $(c_j^{p,e})^\dagger$  and occupation numbers  $n_j^{p,e} = (c_j^{p,e})^\dagger c_j^{p,e}$ . We introduce a spin-1/2  $U(1)$ -quantum link model [145, 147],

$$H_{U(1)} = H_m + H_g + H_{\text{int}}, \quad (\text{C.11})$$

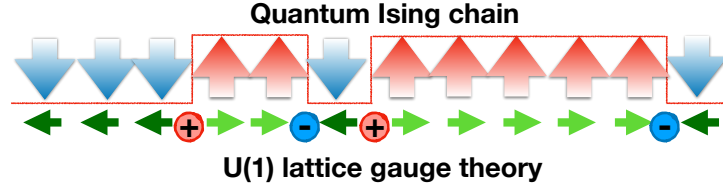


Figure C.2: **Mapping between a quantum spin chain and a LGT:** Cartoon of the mapping of the quantum Ising chain in Eq. (8.2) onto the  $1 + 1$ -dimensional  $U(1)$  lattice gauge theory in Eq. (C.11).

with

$$\begin{aligned}
 H_m &= m \sum_j (n_j^p + n_j^e) + U \sum_j n_j^p n_j^e, \\
 H_g &= \frac{\tau}{2} \sum_j \sigma_{j+1/2}^z, \\
 H_{\text{int}} &= w \sum_j \left\{ [(c_j^p)^\dagger + c_j^e] \sigma_{j+1/2}^+ [c_{j+1}^p + (c_{j+1}^e)^\dagger] + \text{h.c.} \right\},
 \end{aligned}$$

where  $\sigma_{j+1/2}^\pm = (\sigma_{j+1/2}^x \pm i\sigma_{j+1/2}^y)/2$  act as  $U(1)$  parallel transporters [140].  $H_m$  encodes the fermion mass and onsite Hubbard-like interaction, and  $H_g$  can be interpreted as the energy shift caused by a background field (or topological  $\theta$ -angle [4, 144]). In  $H_{\text{int}}$ , the various terms describe hopping and pair creation/annihilation of fermions. The  $U(1)$  gauge invariance of these interactions is expressed by the local symmetries  $[H, G_j] = 0$  with  $G_j = \sigma_{j+1/2}^z/2 - \sigma_{j-1/2}^z/2 - (n_j^p - n_j^e)$ . Accordingly, the complete Hilbert space decomposes into dynamically disconnected subspaces, labelled by the set of eigenvalues  $\{q_j = 0, \pm 1, \pm 2\}$  of  $\{G_j\}$ , interpreted as static background charges. Here we focus on the neutral gauge sector, i.e., on the space of the states  $|\psi\rangle$  for which the Gauss law  $G_j |\psi\rangle \equiv 0$  is satisfied at all sites  $j$ , i.e.,  $q_j \equiv 0$  [140]. This law asserts that the variation of the gauge field strength  $\sigma^z/2$  upon crossing a bond  $j$  equals the dynamical charge  $Q_j = n_j^p - n_j^e$  located on it.

In the presence of a strong Hubbard repulsion  $U \rightarrow \infty$ , each "classical configuration" of the gauge field (eigenstate of all  $\sigma_j^z$  operators) fully determines a unique configuration of the matter particles via the Gauss law. This allows one to eliminate the redundant matter degrees of freedom [4, 169] and write the model in terms of a *locally* self-interacting gauge field [144].<sup>1</sup> In this case, all matrix elements of the Hamiltonian (C.11) between two classical gauge-field configurations coincide with the corresponding matrix

<sup>1</sup>We observe that the converse elimination of the gauge field is also possible in one dimension, but the resulting model of interacting matter particles involves long-range Coulomb forces.

elements of the quantum Ising chain [Eq. (8.2)] in the  $\sigma^z$ -basis, upon identifying  $m = 2J$ ,  $\tau = -2h$ ,  $w = -g$ , and up to an overall energy shift.

It is interesting to finally comment on the gauge-integrated version of the above lattice gauge theory, where the gauge field is eliminated by solving the Gauss law [165, 167]. In one spatial dimension, the result of this procedure is a model of charges interacting via long-range Coulomb potentials. In the specific case of the  $U(1)$  LGT discussed above, the gauge-integrated model is equivalent to a model of charges subject to a constant electric field and to the constraint of sign alternation along the chain. The latter makes the particles interacting, as made explicit by the strong on-site Hubbard repulsion. The slow dynamics discussed in the Chapter 9 can thus be connected with the recently proposed "Stark many-body localization" of interacting charged particles in a strong field [302, 303].

## C.2 Construction of the effective Hamiltonian

We outline here the general procedure for the construction of the effective Schrieffer-Wolff Hamiltonian, following closely Refs. [309, 310, 312] to arbitrary order in perturbation theory. With the notation introduced in the Section 9.1.1,  $H_0$  denotes the "unperturbed" block-diagonal Hamiltonian given by the mass term, and the remaining terms are collected in  $V = H - H_0$ . As in Section 9.1.1, we introduce the generators  $S_1, \dots, S_n$  of the transformation which brings  $H$  to the desired block-diagonal form up to the various orders in perturbation theory.

Explicitly, the terms of the effective Hamiltonian and the generator of the unitary transformation are defined order by order in perturbation theory via the following recursive algorithm. We define  $V_1 \equiv V$  and for  $n \geq 2$ ,

$$V_n = \sum_{(k_1, \dots, k_p) \in [n]'} \frac{1}{p!} [S_{k_1}, [S_{k_2}, \dots, [S_{k_p}, H_0] \dots]] + \sum_{(k_1, \dots, k_p) \in [n-1]} \frac{1}{p!} [S_{k_1}, [S_{k_2}, \dots, [S_{k_p}, V] \dots]], \quad (\text{C.12})$$

where the summations run over the set  $[m]$  of the ordered partitions  $(k_1, \dots, k_p)$  of an integer  $m$ , i.e.,  $k_i \geq 1$  and  $\sum_{i=1}^p k_i = m$ , and the prime  $[m]'$  excludes the trivial partition  $(k_1 = m)$  with  $p = 1$ . The operator  $V_n$  represents the effective perturbation at the  $n$ -th order, i.e., the term of order  $n$  in the transformed Hamiltonian after eliminating all block-off-diagonal transitions up to the  $n - 1$ -th order, i.e.,  $H' = H_0 + \dots + H_{n-1} + V_n + V_{>n}$ . Just like in the first order, we split the perturbation into a block-diagonal and a block-off-diagonal term,  $V_n \equiv H_n + R_n$ . The former constitutes the  $n$ -th order correction to the effective Schrieffer-Wolff Hamiltonian  $H_{\text{eff}}$ , while the latter is eliminated by choosing  $S_n$  in such a way that  $[S_n, H_0] + R_n = 0$ .

This construction is algorithmic and may be carried out directly in the thermodynamic limit, as it involves only the commutation of local operators. However, manual derivations are limited to the first few orders because the combinatorial complexity of the calculation increases rapidly with the perturbative order  $n$ . The convergence properties of this kind of construction have been discussed in Ref. [310] in full generality, and later in Ref. [312] in a specific case. We observe that, differently from these works, the local density of the unperturbed Hamiltonian  $H_0$  need not be a single-site operator for our purposes (for example, in the quantum Ising chain,  $\sigma_j^z \sigma_{j+1}^z$  is not); however, the formal construction in the mentioned works may be adapted to the present case. It is rigorously shown therein that the relative magnitude of the “rest”  $V_{>n}$  compared to  $H_0$  has an upper bound proportional to  $n!$  times the perturbation strength to the power  $n$ . The perturbative series (presumably) diverges, pointing to an asymptotic mixing of the eigenstates among sectors and thermalization. However, truncation of the series to order  $n$  leads to a bound for the size of the effective perturbation at the  $n$ -th step. The optimal order  $n^*$  (the one which gives the tightest bound) scales as the inverse perturbation strength, which leads to an exponential bound. In the Section 9.1.2, we use this fact to prove that the effective Hamiltonian represents a good approximation for studying the dynamics up to times which become exponentially long upon increasing the inverse perturbation strength.

### C.2.1 Effective Hamiltonian of the quantum Ising chain

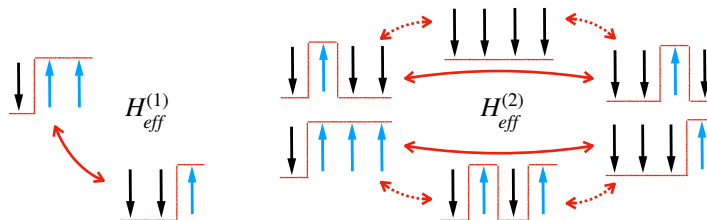


Figure C.3: Cartoon of the perturbative transitions described by the effective Hamiltonian  $H_{\text{eff}}^{(2)}$  of the quantum Ising chain up to the second order in  $1/J$ . At the first order, hopping of a kink/antikink by one lattice site is the only allowed transition. At the second order, one can either have hopping by one lattice site of a string/antistring of length one (top row) or hopping of two lattice sites of a kink/antikink (bottom row). Solid arrows show the block-diagonal transitions described by the effective Hamiltonian. The intermediate states mediating the processes, indicated by dashed arrows, involve “virtual” states belonging to a different block. The amplitudes of the second-order processes are proportional to  $g^2/J$ , see Eq. (C.15).

In order to show the structure of the effective Hamiltonian, we report its expression up to the third order for the quantum Ising chain in Eq. (8.2)

(using the notation introduced in Section 9.1.1):

$$H_0 = -J \sum_j \sigma_j^z \sigma_{j+1}^z, \quad (\text{C.13})$$

$$H_1 = -h \sum_j \sigma_j^z - g \sum_j (P_{j-1}^\dagger \sigma_j^x P_{j+1}^\dagger + P_{j-1}^\dagger \sigma_j^x P_{j+1}^\dagger), \quad (\text{C.14})$$

$$H_2 = +\frac{g^2}{4J} \sum_j \left[ + P_{j-1}^\dagger (\sigma_j^- \sigma_{j+1}^+ + \sigma_j^+ \sigma_{j+1}^-) P_{j+2}^\dagger + P_{j-1}^\dagger (\sigma_j^- \sigma_{j+1}^+ + \sigma_j^+ \sigma_{j+1}^-) P_{j+2}^\dagger \right. \\ \left. - P_{j-1}^\dagger (\sigma_j^+ \sigma_{j+1}^+ + \sigma_j^- \sigma_{j+1}^-) P_{j+2}^\dagger - P_{j-1}^\dagger (\sigma_j^+ \sigma_{j+1}^+ + \sigma_j^- \sigma_{j+1}^-) P_{j+2}^\dagger \right. \\ \left. - \sigma_j^z \sigma_{j+1}^z \right], \quad (\text{C.15})$$

$$H_3 = +\frac{hg^2}{8J^2} \sum_j \left[ -\sigma_j^z - \sigma_{j-1}^z \sigma_j^z \sigma_{j+1}^z \right. \\ \left. + P_{j-1}^\dagger (\sigma_j^+ \sigma_{j+1}^- + \sigma_j^- \sigma_{j+1}^+) P_{j+2}^\dagger - P_{j-1}^\dagger (\sigma_j^+ \sigma_{j+1}^- + \sigma_j^- \sigma_{j+1}^+) P_{j+2}^\dagger \right] \\ +\frac{g^3}{8J^2} \sum_j \left[ + P_{j-2}^\dagger (\sigma_{j-1}^+ \sigma_j^+ \sigma_{j+1}^+ + \sigma_{j-1}^- \sigma_j^- \sigma_{j+1}^- + \sigma_{j-1}^+ \sigma_j^- \sigma_{j+1}^+ + \sigma_{j-1}^- \sigma_j^+ \sigma_{j+1}^-) P_{j+2}^\dagger \right. \\ \left. + P_{j-2}^\dagger (\sigma_{j-1}^+ \sigma_j^+ \sigma_{j+1}^+ + \sigma_{j-1}^- \sigma_j^- \sigma_{j+1}^- + \sigma_{j-1}^+ \sigma_j^- \sigma_{j+1}^+ + \sigma_{j-1}^- \sigma_j^+ \sigma_{j+1}^-) P_{j+2}^\dagger \right. \\ \left. - P_{j-2}^\dagger (\sigma_{j-1}^+ \sigma_j^+ \sigma_{j+1}^- + \sigma_{j-1}^- \sigma_j^- \sigma_{j+1}^+ + \sigma_{j-1}^+ \sigma_j^- \sigma_{j+1}^- + \sigma_{j-1}^- \sigma_j^+ \sigma_{j+1}^+) P_{j+2}^\dagger \right. \\ \left. - P_{j-2}^\dagger (\sigma_{j-1}^+ \sigma_j^+ \sigma_{j+1}^- + \sigma_{j-1}^- \sigma_j^- \sigma_{j+1}^+ + \sigma_{j-1}^+ \sigma_j^- \sigma_{j+1}^- + \sigma_{j-1}^- \sigma_j^+ \sigma_{j+1}^+) P_{j+2}^\dagger \right. \\ \left. - P_{j-1}^\dagger \sigma_j^x P_{j+1}^\dagger - P_{j-1}^\dagger \sigma_j^x P_{j+1}^\dagger \right], \quad (\text{C.16})$$

while the generators  $S_1$  and  $S_2$  of the unitary transformation up to the second order in  $1/J$  are

$$S_1 = \frac{ig}{4J} \sum_j (P_{j-1}^\dagger \sigma_j^y P_{j+1}^\dagger - P_{j-1}^\dagger \sigma_j^y P_{j+1}^\dagger), \quad (\text{C.17})$$

$$S_2 = \frac{igh}{8J^2} \sum_j (-P_{j-1}^\dagger \sigma_j^y P_{j+1}^\dagger - P_{j-1}^\dagger \sigma_j^y P_{j+1}^\dagger) \quad (\text{C.18}) \\ +\frac{g^2}{8J^2} \sum_j \left[ + P_{j-1}^\dagger (\sigma_j^- \sigma_{j+1}^- - \sigma_j^+ \sigma_{j+1}^+) P_{j+2}^\dagger \right. \\ \left. + P_{j-1}^\dagger (\sigma_j^+ \sigma_{j+1}^- - \sigma_j^- \sigma_{j+1}^+) P_{j+2}^\dagger \right. \\ \left. + P_{j-1}^\dagger (\sigma_j^+ \sigma_{j+1}^+ - \sigma_j^- \sigma_{j+1}^-) P_{j+2}^\dagger \right. \\ \left. + P_{j-1}^\dagger (\sigma_j^- \sigma_{j+1}^+ - \sigma_j^+ \sigma_{j+1}^-) P_{j+2}^\dagger \right].$$

One realizes that higher-order terms have a twofold effect: they renormalize lower-order terms and introduce longer-range processes compatible with the

conservation of  $H_0$ . Note that the maximal range of these processes at order  $n$  is bounded by  $n + 2$ , as can be proven by induction. Transitions allowed up to the second order are sketched in Fig. C.3.

For the quantum Ising chain, the estimates of Refs. [310,312] yield

$$\frac{\|V_{\geq n}\|}{\|H_0\|} \leq \left( \text{const} \times n \frac{\sqrt{g^2 + h^2}}{J} \right)^n, \quad (\text{C.19})$$

where  $\|\cdot\|$  indicates the operator norm of the local density of the argument. Truncation of the series at the optimal order  $n^* \propto J/\sqrt{g^2 + h^2}$  leads to an exponential bound for the thermalization time, see Eq. (9.6).

The construction presented here is similar to that of Ref. [280] for the quantum Ising chain. However, while that study is concerned with the homogeneous dynamics of elementary quasiparticle excitations above the ground state, we are here interested in the effective dynamics of dilute domain-walls, corresponding to high-energy states of the model.

### C.3 Solution of the two-body problem

The two-body Hamiltonian for  $m \rightarrow \infty$  is obtained by projecting Eq. (8.3) onto the two-fermion subspace. It can be written in the basis of the fermion positions as

$$\begin{aligned} H_{2\text{-body}} &= \sum_{j_1 < j_2} \tau(j_2 - j_1) |j_1, j_2\rangle \langle j_1, j_2| \\ &+ w \left( |j_1 + 1, j_2\rangle \langle j_1, j_2| + |j_1, j_2 + 1\rangle \langle j_1, j_2| + \text{H.c.} \right), \end{aligned} \quad (\text{C.20})$$

where  $j_1 < j_2$  label the positions of the two fermions along the chain.

For  $\tau = 0$  the eigenstates are (antisymmetric combinations of) plane waves

$$\Psi_{k_1, k_2} = e^{ik_1 j_1 + ik_2 j_2} - e^{ik_2 j_1 + ik_1 j_2} \quad (\text{C.21})$$

with energy  $\mathcal{E}_{\text{free}}(k_1) + \mathcal{E}_{\text{free}}(k_2)$ , where  $\mathcal{E}_{\text{free}}(k) = 2w \cos k$ ,  $k \in [-\pi, \pi)$  is the free-fermion dispersion relation. For  $\tau \neq 0$ , however, a linear confining potential emerges between the two fermions, and the spectrum is nonperturbatively modified into a discrete tower of bound states (mesons) labelled by a quantum number  $\ell = 1, 2, \dots$ . Each meson has a different dispersion relation  $\mathcal{E}_\ell(k)$ , where  $k$  is the center-of-mass momentum of the bound state.

As shown in Section 9.2.1 the meson wavefunctions and dispersion relations can be solved explicitly [6,316] by switching to the center-of-mass and relative variables, yielding

$$\psi_{\ell, k}(s, r) = e^{iks} \mathcal{J}_{r-\nu_\ell}(2\tilde{w}_k/\tau), \quad (\text{C.22})$$

$$\nu_\ell(2\tilde{w}_k/\tau) \equiv -\tau \times \{ \ell\text{-th zero of } x \mapsto \mathcal{J}_x(2\tilde{w}_k/\tau) \}, \quad (\text{C.23})$$

with  $\tilde{w}_k = 2w \cos k$ . Note that  $k \in [-\pi/2, \pi/2)$ , because  $k$  and  $k+\pi$  generate the same solution up to a phase: Since  $\mathcal{J}_\alpha(-z) = e^{i\pi\alpha} \mathcal{J}_\alpha(z)$ , when  $k \mapsto k+\pi$  the wavefunction  $\psi$  gets multiplied by  $(-)^s e^{i\pi(r-\nu_\ell)} = e^{-i\pi\nu_\ell} (-)^{2j_2} = e^{-i\pi\nu_\ell}$ , i.e., a global phase.

The most important qualitative aspects of this exact solution are the following. For  $w \rightarrow 0$ , one finds energies  $\mathcal{E}_\ell(k) = \tau\ell$ , corresponding to a pair of fermions separated by a string of excited gauge fields of length  $\ell$ . In this limit, bound states are dispersionless (flat bands). As  $w$  increases, the lightest mesons progressively acquire mobility (band curvature). In particular, one can see that an effective hopping of the  $\ell$ -th meson appears at the  $2\ell$ -th order in perturbation theory in  $w/\tau$ , which gives rise to a band curvature (and hence a maximal velocity) of this order of magnitude. This can be confirmed by the exact solution above, as [416]

$$\nu_\ell(x) \underset{x \rightarrow 0}{\sim} \ell \left( 1 - \frac{x^{2\ell}}{(\ell!)^2} \right). \quad (\text{C.24})$$

Interestingly, the flat-band property of heavy mesons is a nonperturbative feature that persists to arbitrarily large values of the ratio  $w/\tau$ . As we are now going to show, for  $\ell \gg 4w/\tau$  the band curvature drops to zero faster than exponentially.

We can quantify the bending of the bands  $E_j(k)$  by making an estimate based on the Hellmann-Feynman theorem. Consider the model without the hard wall, and let  $u$  be the hopping amplitude between sites  $r = 0$  and  $r = 1$ , and  $\tilde{w}_k$  be the hopping amplitude on all the other links. For  $u = \tilde{w}_k$  the eigenenergies are  $\mathcal{E}_\ell(k) = \tau\ell$  and the eigenfunctions  $\phi_{k,\ell}^{u=\tilde{w}_k}(r) = \mathcal{J}_{\ell-r}(2\xi_{\text{loc}} \cos k)$ , with  $\xi_{\text{loc}} = g/h = 2w/\tau$ . On the other hand, if we adiabatically turn off the hopping amplitude between  $r = 0, 1$ , we obtain the eigenenergies  $\mathcal{E}_\ell(k)$  of the same model with the hard wall. From the Hellmann-Feynman theorem, we find that

$$\delta\mathcal{E}_\ell(K) = \mathcal{E}_\ell(k) - \tau\ell = 2 \cos k \int_{\tilde{w}_k}^0 [(\phi_{k,\ell}^u(0))^* \phi_{k,\ell}^u(1) + \text{h.c.}] du, \quad (\text{C.25})$$

where  $\phi_{k,\ell}^u(r)$  is the eigenfunction for a certain value of  $u$ .

We can estimate this integral by replacing the integrand with the average between the values at the two extrema. Since  $\phi_0^{(j,K)}(0) = 0$ , we find the correction to the dispersion relation

$$\delta\mathcal{E}_\ell(k) \simeq -2|w| \cos k \mathcal{J}_\ell(2\xi_{\text{loc}} \cos k) \mathcal{J}_{\ell-1}(2\xi_{\text{loc}} \cos k) \quad (\text{C.26})$$

$$\simeq -\frac{(2|w| \cos k)^{2\ell}}{\ell!(\ell-1)!|\tau|^{2\ell-1}}, \quad (\text{C.27})$$

where, in the last approximation, we used only the asymptotic behaviour of the eigenfunction for  $\ell \gg \xi_{\text{loc}}^2$  [417]. In Fig. C.4, these approximations are compared with numerical diagonalization of the one-kink problem with the

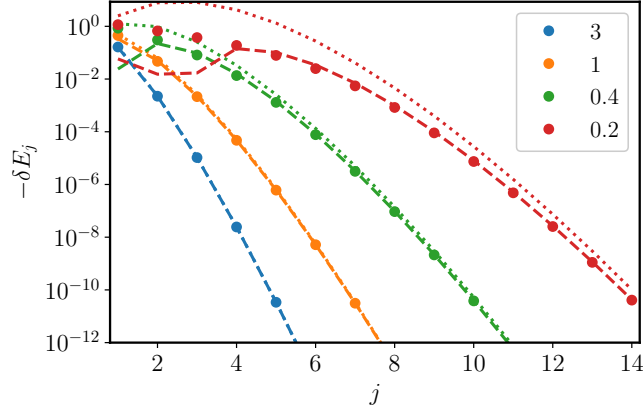


Figure C.4: Correction to the energy  $\mathcal{E}_j$  of the  $j$ -th eigenfunction, induced by the hard-wall potential. The dots correspond to the results of an exact diagonalization, the dashed line is the value estimated from Eq. (C.26) and the dotted line is the one obtained from Eq. (C.27). The energies are in units of  $g \cos k$  and the different colours refer to the different values of  $h$  reported in the legend.

hard wall: The first asymptotic estimate is found to be extremely accurate in the considered quasilocalized regime  $\ell \gtrsim 2\xi_{\text{loc}}$ . In a semiclassical picture, asymptotically exact for  $\ell \gg 1$ ,  $\xi_{\text{loc}} \gg 1$  and fixed  $\ell/\xi_{\text{loc}}$ , this regime corresponds to having the two particles at the edges of the string performing *non-overlapping* Bloch oscillations of amplitude  $\xi_{\text{loc}}$  each. We observe that the last asymptotic estimate in Eq. (C.27) agrees with the perturbation-theory argument for which nonvanishing corrections to the eigenenergy of the  $\ell$ -th bound state occur only at the  $2\ell$ -th order in  $\xi_{\text{loc}}$ ; we emphasize, however, that the equations above are valid for arbitrarily large localization lengths, provided the string length is even larger.

The result in Eq. (C.27) can be recovered from the exact single-string energy spectrum, expressed as a solution of the implicit equation

$$\mathcal{J}_{-\mathcal{E}_\ell/\tau}(2\xi_{\text{loc}} \cos k) = 0, \quad (\text{C.28})$$

first derived in Ref. [316]. From the series expansion [417]

$$\mathcal{J}_\nu(z) = \left(\frac{z}{2}\right)^\nu \sum_{p=0}^{\infty} \frac{(-1)^p}{\Gamma(p+1)\Gamma(p+1+\nu)} \left(\frac{z}{2}\right)^{2p} \quad (\text{C.29})$$

one readily realizes that the leading correction  $\delta\mathcal{E}_\ell(k)$  in  $z = 2\xi_{\text{loc}} \cos k$  to the flat band energy level  $\mathcal{E}_\ell(k) = \tau\ell$  is given precisely by Eq. (C.27).

From the above result, the maximal group velocity

$$v_\ell^{\text{max}} = \max_{k \in [0, \pi)} \left| \partial_k \delta\mathcal{E}_\ell(k) \right| \quad (\text{C.30})$$

of the  $\ell$ -th bound state can be computed. In particular, for  $\ell \gg \xi_{\text{loc}}^2$ , one finds

$$v_\ell^{\text{max}} \simeq \frac{|\tau| (2\ell)^{3/2}}{2 (\ell!)^2} \left(\frac{w}{\tau}\right)^{2\ell} e^{-1/2} = |h| \frac{(2\ell)^{3/2}}{(\ell!)^2} \left(\frac{g}{2h}\right)^{2\ell} e^{-1/2}. \quad (\text{C.31})$$

Note that these speeds dramatically drop to zero for  $\ell \gg |g/h|$ . The delocalization time in Eq. (9.13), is estimated by taking the inverse of  $v_\ell^{\text{max}}$ .

The fast increase of delocalization time with  $\ell$  is due to Wannier-Stark localization of particles in a linear potential: Single, isolated particles can be seen to perform a finite oscillatory motion (Bloch oscillations) with an amplitude of  $\xi_{\text{loc}} = g/h = 2w/\tau$  lattice sites. Correspondingly, their eigenstates are localized around each lattice site, with a localization length  $\xi_{\text{loc}}$ . When two particles are initialized at a distance much larger than  $2\xi_{\text{loc}}$ , they perform independent oscillations without touching each other, and the meson is thus immobile and localized. The mobility is provided by the hard-core interaction between the two kinks, which is suppressed as the overlap between the two localized wavefunction tails, corresponding to the estimate in Eq. (C.24) [6].

We observe that from the exact eigenvalues and eigenfunctions of the two-kink problem, one can obtain the dynamics of the entanglement entropy  $S(t)$  associated with a bipartition of the chain. The bottom right panel of Fig. 9.3 reports the growth of  $S(t)$  for the evolution of isolated strings, compared with the corresponding growth for initial dilute states with multiple strings. For an initial condition given by kinks located at sites  $i, j = n_{1,2}$  and bipartition cut at site  $r$ , the growth of  $S(t)$  turns out to approximately consist of a discrete sequence of "jumps", associated with the delocalization of the various components of the initial state on the eigenstates with quantum number  $\ell = 1, 2, \dots$ , their weight being maximal around  $\ell \approx |n_2 - n_1|$ . Eventually,  $S(t)$  converges to  $\log 2$  as  $t \rightarrow \infty$ , since the diffusing string will asymptotically be either entirely on the left or entirely on the right of the cut, with equal amplitude. Before this eventual saturation,  $S(t)$  can attain values larger than  $\log 2$ , caused by transient correlations between the two particles located on opposite sides of the cut. Using the fact that particles are confined, it is straightforward to formulate an upper bound for  $S(t)$ . In fact, for wavefunctions supported in the region  $|i - j| \leq d$ , i.e., with the two particles separated by no more than  $d$  lattice sites, the maximal von Neumann entanglement entropy is  $\log(d + 1)$ . For the considered initial condition, this bound holds with  $d \approx |n_2 - n_1| + 2\xi_{\text{loc}}$ .

We finally observe that there exist solutions of the Schroedinger equation (9.8) with complex momentum  $k$  and energy  $\mathcal{E}$ , with the same wavefunction (9.11) and the same (analytically continued) energy-momentum relation (9.10). Such solutions correspond to evanescent waves and are important in the scattering problem that will be analyzed below.

## C.4 Solution of the four-body problem

The four-body Hamiltonian for  $m \rightarrow \infty$  is obtained by projecting Eq. (8.2) onto the four-fermion subspace. It can be written in the basis of the fermion positions as

$$H_{4\text{-body}} = \sum_{j_1 < j_2 < j_3 < j_4} \left[ \tau(j_2 - j_1 + j_4 - j_3) |\vec{j}\rangle \langle \vec{j}| + w \sum_{n=1}^4 \left( |\vec{j} + \hat{e}_n\rangle \langle \vec{j}| + \text{H.c.} \right) \right] \quad (\text{C.32})$$

where  $\vec{j} = (j_1, j_2, j_3, j_4)$  and we defined the unit vectors  $\hat{e}_1 = (1, 0, 0, 0)$ ,  $\hat{e}_2 = (0, 1, 0, 0)$ , etc. The sum is constrained by Pauli exclusion.

The diagonal term  $\propto \tau$  can be viewed as the two confining potentials for the first and last pair of adjacent fermions. These potentials give rise to two bound states (mesons). These mesons experience no residual interactions; they only interact when they bump into each other, due to Pauli exclusion. For later convenience, we define the center-of-mass positions  $s_1 = j_1 + j_2$ ,  $s_2 = j_3 + j_4$  and relative distances  $r_1 = j_2 - j_1$ ,  $r_2 = j_4 - j_3$  for the two mesons.

We are interested in the problem of a scattering event with incoming mesons in states  $(\ell_1, k_1)$ ,  $(\ell_2, k_2)$ . This asymptotic state defines the total energy  $E \equiv \mathcal{E}_{\ell_1}(k_1) + \mathcal{E}_{\ell_2}(k_2)$  and the total momentum  $K \equiv k_1 + k_2 \bmod \pi$  of the system. Since meson-meson interactions are local, we formulate an ansatz in terms of the product state

$$\chi_{\ell'_1, k'_1, \ell'_2, k'_2}(s_1, r_1, s_2, r_2) = \psi_{\ell'_1, k'_1}(s_1, r_1) \psi_{\ell'_2, k'_2}(s_2, r_2), \quad (\text{C.33})$$

where  $\psi_{\ell'_{1,2}, k'_{1,2}}$  are eigenstates of the two-body problem with quantum numbers  $\ell'_{1,2}$  and generally complex momenta  $k'_{1,2} \in \mathbb{C}$ . For  $\Im \mathbf{m}(k'_1) \leq 0$ ,  $\Im \mathbf{m}(k'_2) \geq 0$ , the ansatz  $\chi_{\ell'_1, k'_1, \ell'_2, k'_2}$  is an asymptotic solution, and solves the Schrödinger equation in the full domain  $(s_2 - s_1 - r_1 - r_2)/2 = j_3 - j_2 > 0$  away from the scattering region (that is the hyperplane  $j_2 = j_3$ ).

To obtain the complete solution for given scattering data, we first need to determine the set of parameters  $\{(\ell_1^\alpha, k_1^\alpha), (\ell_2^\alpha, k_2^\alpha)\}_{\alpha=1,2,\dots}$  which simultaneously satisfy the conservation laws of total energy and momentum

$$E = \mathcal{E}_{\ell_1^\alpha}(k_1^\alpha) + \mathcal{E}_{\ell_2^\alpha}(k_2^\alpha), \quad (\text{C.34})$$

$$K = k_1^\alpha + k_2^\alpha \bmod \pi. \quad (\text{C.35})$$

Note that, while  $E$  and  $K$  are real,  $k_{1,2}^\alpha$  and  $\mathcal{E}_{\ell_{1,2}^\alpha}(k_{1,2}^\alpha)$  are generally complex. Solutions with real momentum and energy correspond to incoming or outgoing states, are only a finite number. The candidate scattering solution is a linear superposition of the form

$$\Psi(s_1, r_1, s_2, r_2) = \chi_{\ell_1, k_1, \ell_2, k_2} + \sum_{\alpha} A_{\alpha} \chi_{\ell_1^\alpha, k_1^\alpha, \ell_2^\alpha, k_2^\alpha}. \quad (\text{C.36})$$

The sum in Eq. (C.36) has to be restricted to the asymptotic solutions with outgoing current (see below) among those with real energy/momentum, and includes all the evanescent states that decay exponentially with the distance from the scattering region among those with complex energy/momentum.

The values of the coefficients  $A_\alpha$  are then obtained by imposing the continuity of the solution in the scattering region. More explicitly, we have to impose that  $\Psi \equiv 0$  on the hyperplane  $j_2 = j_3$ . We define  $S = (s_1 + s_2)/2$ ,  $R = s_2 - s_1$ , representing the global center-of-mass position and the distance between the two mesons, respectively. Hence, we have

$$\begin{aligned} \Psi(S, R, r_1, r_2) = & e^{iKS} \left[ e^{ipR} \phi_{\ell_1, K/2-p}(r_1) \phi_{\ell_2, K/2+p}(r_2) \right. \\ & \left. + \sum_{\alpha} A_{\alpha} e^{ip_{\alpha}R} \phi_{\ell_1^{\alpha}, K/2-p_{\alpha}}(r_1) \phi_{\ell_2^{\alpha}, K/2+p_{\alpha}}(r_2) \right] \end{aligned} \quad (\text{C.37})$$

where  $p = (k_2 - k_1)/2$ ,  $p_{\alpha} = (k_2^{\alpha} - k_1^{\alpha})/2$ , and  $\phi_{\ell, k}$  are the solutions to Eq. (9.8). The boundary condition applied to Eq. (C.37) reads

$$\sum_{\alpha} M_{(r_1, r_2), \alpha} A_{\alpha} = B_{(r_1, r_2)}, \quad (\text{C.38})$$

where

$$M_{(r_1, r_2), \alpha} = e^{ip_{\alpha}(r_1+r_2)} \phi_{\ell_1^{\alpha}, K/2-p_{\alpha}}(r_1) \phi_{\ell_2^{\alpha}, K/2+p_{\alpha}}(r_2), \quad (\text{C.39})$$

$$B_{(r_1, r_2)} = -e^{ip(r_1+r_2)} \phi_{\ell_1, K/2-p}(r_1) \phi_{\ell_2, K/2+p}(r_2). \quad (\text{C.40})$$

The coefficients  $A_{\alpha}$  are then obtained by solving the linear system in Eq. (C.38), truncated to a finite set of values of  $\alpha$  and  $r_{1,2} \leq r_{\max}$ . The truncation in  $\alpha$  can be safely performed: the open outgoing channels are only a finite number, and the evanescent states with increasingly high quantum numbers have large  $\Im(p_{\alpha})$ , resulting in negligible contributions. The truncation to  $r_1, r_2 \leq r_{\max}$  is also legitimate:  $B_{(r_1, r_2)}$  decays exponentially fast with  $r_1$  and  $r_2$ , thanks to the spatial decay of the mesonic wavefunctions  $\phi_{\ell, k}$ ; the coefficients  $M_{(r_1, r_2), \alpha}$  decay for the same reason when  $\alpha$  represents an outgoing solution with  $p \in \mathbb{R}$ , whereas the normalizability condition  $\Im(p) > 0$  guarantees the decay of the prefactor  $e^{ip_{\alpha}(r_1+r_2)}$  when  $\alpha$  represents an evanescent solution. In all the calculation presented in the Chapter 10, we have checked convergence with respect to these truncation cutoffs.

## C.5 Mesonic current

For sufficiently large  $m$  (see C.6), in a scattering process, the number of mesons is globally conserved. This conservation law is associated with a continuity equation. We now illustrate this continuity equation for the generic case of  $q$  mesons (i.e., in the  $2q$ -fermion sector) in limit  $m \rightarrow \infty$ . We define the density operator for the  $i$ -th meson at position  $x$

$$\chi_i(x) = \sum_{j_1 < j_2 < \dots < j_{2q}} \delta_{j_{2i-1}+j_{2i}, x} |\vec{j}\rangle \langle \vec{j}| \quad (\text{C.41})$$

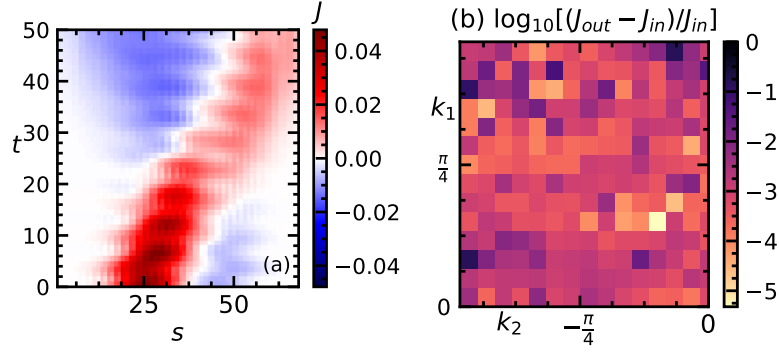


Figure C.5: (a) Profile of  $J(x, t)$  in a scattering event. The parameters of the simulation and the initial state are the same as in Fig. 10.3. (b) Violation of current conservation law in the analytical solution of the scattering problem. This quantity serves as a consistency check for the theory. Except for a small number of points (for which we attribute the inaccuracy to numerical instabilities in determining the set of solutions), the observed error in the current conservation is small.

with  $\vec{j} = (j_1, j_2, \dots, j_{2q})$ , and the total mesonic density

$$\rho(x) = \sum_{i=1}^q \rho_i(x) \equiv \sum_{i=1}^q \langle \Psi | \chi_i(x) | \Psi \rangle. \quad (\text{C.42})$$

The mesonic current is defined as  $J(x) = \sum_{i=1}^q J_i(x)$ , with

$$J_i(x) = -2w \sum_{j_1 < j_2 < \dots < j_{2q}} \delta_{j_{2i} + j_{2i+1}, x} \Im \left\{ \Psi^*(\vec{j}) \left[ \Psi(\vec{j} + \hat{e}_{2i}) + \Psi(\vec{j} + \hat{e}_{2i+1}) \right] \right\}, \quad (\text{C.43})$$

where  $\hat{e}_n$  is the unit vector along the direction of  $j_n$ . As an example, in Fig. C.5-(a) we plot the time-evolving profile of the meson current  $J(x, t)$  for the scattering event discussed in Fig. (10.3). The red (blue) color is associated to positive (negative) current, i.e., to a meson moving to the right (left).

The mesonic density and current satisfy the continuity equation

$$\partial_t \rho(x) = -J(x) + J(x-1). \quad (\text{C.44})$$

The proof of this equation is reported in the next section. We now derive the constraints imposed on the scattering solutions of the Schroedinger equation by the continuity equation.

Let us first consider the case of a single meson, with internal quantum number  $\ell$  and momentum  $k$ . The density current associated with it can be written in terms of its dispersion relation  $\mathcal{E}_\ell(k)$  and wavefunction  $\phi_{\ell,k}(r)$  as

$$\begin{aligned} J(x) &= -2w \Im \left\{ \sum_{r>0} \phi_{\ell,k}^*(r) e^{ik} [\phi_{\ell,k}(r+1) + \phi_{\ell,k}(r-1)] \right\} \\ &= \sum_{r>0} \phi_{\ell,k}^*(r) (-2w \sin k) [\phi_{\ell,k}(r+1) + \phi_{\ell,k}(r-1)] \\ &= \langle \phi_{\ell,k} | \partial_k H_k | \phi_{\ell,k} \rangle = \partial_k \mathcal{E}_\ell(k) = v_\ell(k). \end{aligned} \quad (\text{C.45})$$

where

$$H_k = \sum_{r>0} 2w \cos k (|r\rangle \langle r+1| + \text{H.c.}) + \tau r |r\rangle \langle r| \quad (\text{C.46})$$

is the reduced Hamiltonian for the internal coordinate of the meson with center-of-mass momentum  $k$  [see Eq. (9.8)]. We obtain that the mesonic current corresponds to the group velocity of the meson, in analogy with the case of a structureless quantum particle.

We now apply the continuity equation to the solution  $\Psi(s_1, r_1, s_2, r_2)$  of the stationary Schrödinger equation for the scattering problem discussed in Chapter 10. Equation (C.44) implies that  $J_R = J_L$ , where  $J_R$  and  $J_L$  are the currents on the right and on the left, very far from the scattering region. There, the density current can be easily computed as the sum of the currents of the isolated mesons. Since evanescent waves do not contribute far from the scattering region, only propagating waves (i.e., those with  $q_\alpha \in \mathbb{R}$ ) should be taken into account. Therefore, in a scattering process with incoming mesons of quantum numbers  $\ell_1$  and  $\ell_2$  and momenta  $k_1$  and  $k_2$ , the two currents read

$$J_L = v(\ell_1, k_1) + \sum_{\alpha|q_\alpha \in \mathbb{R}} |A_\alpha|^2 v(\ell_1^\alpha, k_1^\alpha) \quad (\text{C.47})$$

$$J_R = v(\ell_2, k_2) + \sum_{\alpha|q_\alpha \in \mathbb{R}} |A_\alpha|^2 v(\ell_2^\alpha, k_2^\alpha). \quad (\text{C.48})$$

where  $k_1^\alpha = q_\alpha$ ,  $k_2^\alpha = K - q_\alpha$  are the momenta of the outgoing mesons.

The condition  $J_R = J_L$  can be equivalently formulated as an equality between the incoming and outgoing currents  $J_{in} = J_{out}$ , defined as

$$J_{in} = v(\ell_1, k_1) - v(\ell_2, k_2) \quad (\text{C.49})$$

and

$$J_{out} = \sum_{\alpha} J_{\alpha} = \sum_{\alpha} |A_{\alpha}|^2 [-v(\ell_1^{\alpha}, k_1^{\alpha}) + v(\ell_2^{\alpha}, k_2^{\alpha})]. \quad (\text{C.50})$$

The equation  $J_{in} = J_{out}$  has an immediate physical interpretation as a conservation of probability: in a scattering event, at  $t = -\infty$  the two mesons are with probability 1 in the state  $\{(\ell_1, k_1), (\ell_2, k_2)\}$ ; at  $t = +\infty$ , the outgoing meson states  $\{(\ell_1^\alpha, k_1^\alpha), (\ell_2^\alpha, k_2^\alpha)\}$  have fractional probabilities  $P_\alpha = J_\alpha / J_{in}$ . Similarly to the scattering of structureless quantum particles, the probability of finding a certain scattering outcome (or total cross section) is proportional to the width of the wavepacket, which is determined by both the squared amplitude  $|A_\alpha|^2$  and the group velocity.

We stress that the sign of the total current defines outgoing states, characterized by  $-v(\ell_1^\alpha, k_1^\alpha) + v(\ell_2^\alpha, k_2^\alpha) > 0$ . In computing the amplitudes of a scattering event, one has to select the set of propagating asymptotic solutions according to this criterion, as anticipated in C.4 above.

We finally note that the conservation law  $J_{in} = J_{out}$  represents a consistency check on our results for the coefficients  $A_\alpha$  obtained from the truncation of the linear system in Eq. (C.38). In Fig. C.5-(b) we plot the relative violation of this conservation law, for the computations involved in Fig. 10.2.

### C.5.1 Proof of the continuity equation

We prove here the continuity equation (C.44).

In the sector with  $q$  mesons, we define the operators  $\Delta^+ = \sum_{i=1}^q \Delta_i^+$  where

$$\Delta_i^+ = \sum_{j_1 < j_2 < \dots < j_{2q}} \sum_{s=2i, 2i+1} w(1 - \delta_{j_{s+1}, j_s+1}) |\vec{j} + \hat{e}_s\rangle \langle \vec{j}|. \quad (\text{C.51})$$

The Hamiltonian can be written as  $H = \Delta^+ + \Delta^- + V$ , where  $\Delta^- = (\Delta^+)^\dagger$ ,  $V = \sum_i V_i$  and

$$V_i = \sum_{j_1 < j_2 < \dots < j_{2q}} \tau(j_{2i+1} - j_{2i}) |\vec{j}\rangle \langle \vec{j}|. \quad (\text{C.52})$$

The Heisenberg evolution of the meson density reads

$$\begin{aligned} \partial_t \rho(x) &= i \sum_{i=1}^q \langle \Psi | [H, \chi_i(x)] | \Psi \rangle \\ &= i \sum_{i=1}^q \langle \Psi | [\Delta_i^+ + \Delta_i^-, \chi_i(x)] | \Psi \rangle \\ &= 2 \sum_{i=1}^q \Im \langle \Psi | \chi_i(x) (\Delta_i^+ + \Delta_i^-) | \Psi \rangle. \end{aligned} \quad (\text{C.53})$$

By using the properties  $\Delta_i^- \chi_i(x) = \chi_i(x-1) \Delta_i^-$  and  $\langle \Psi | \Delta_i^- \chi_i(x) | \Psi \rangle = (\langle \Psi | \chi_i(x) \Delta_i^+ | \Psi \rangle)^*$  we get

$$\begin{aligned} \partial_t \rho(x) &= 2 \sum_{i=1}^m \Im \langle \Psi | \chi_i(x) \Delta_i^- + \chi_i(x) \Delta_i^+ | \Psi \rangle \\ &= 2 \sum_{i=1}^m \Im \langle \Psi | \chi_i(x) \Delta_i^- - \Delta_i^- \chi_i(x) | \Psi \rangle \\ &= 2 \sum_{i=1}^m \Im \langle \Psi | (\chi_i(x) - \chi_i(x-1)) \Delta_i^- | \Psi \rangle \\ &= -J(x) + J(x-1), \end{aligned} \quad (\text{C.54})$$

i.e., Eq. (C.44).

## C.6 Finite fermion mass

For the sake of simplicity, the discussion in Chapter 10 focuses on the limit  $m \rightarrow \infty$ . We compactly summarize here the effects of a finite fermion mass.

**Perturbative corrections to the exact spectra and scattering solution** – The main consequence of the finiteness of the fermion mass  $m$  is to produce a perturbative dressing of the vacuum and of the excitations.

These effects can be explicitly computed order by order via the Schrieffer-Wolff transformation introduced in Section C.2. The approximate Hamiltonian obtained by neglecting the higher-order remainder conserves the total fermion number, and exactly accounts for all perturbative  $n$ -th order transitions within each fermion-number sector occurring through up to  $n$  virtual transitions involving intermediate states in other sectors.

Upon restricting the transformed Hamiltonian to the  $2q$ -fermion sector, one ends up with higher-order corrections to  $H_{2q\text{-body}}$ . For example, the first correction involves next-nearest-neighbor particle hopping terms with amplitudes  $w^2/2m$ :

$$H_{2q\text{-body}}^{(1)} = \sum_{j_1 < \dots < j_{2q}} \left[ \tau \sum_{n=1}^{2q} (-)^n j_n |\vec{j}\rangle \langle \vec{j}| + w \sum_{n=1}^{2q} \left( |\vec{j} + \hat{e}_n\rangle \langle \vec{j}| + \text{H.c.} \right) - \frac{w^2}{2m} \sum_{n=1}^{2q} \left( |\vec{j} + \hat{2}e_n\rangle \langle \vec{j}| + \text{H.c.} \right) \right] \quad (\text{C.55})$$

with the understanding that

$$|j_1, \dots, j_n = j_{n+1}, \dots, j_{2q}\rangle \equiv 0, \quad (\text{C.56})$$

$$|j_1, \dots, j_n = j_{n+1} + 1, \dots, j_{2q}\rangle \equiv -|j_1, \dots, j_{n+1}, j_n, \dots, j_{2q}\rangle. \quad (\text{C.57})$$

Similarly, corrections of order  $w^r/m^{r-1}$  introduce new hopping terms of range  $r$  and renormalize shorter-range terms.

From the perturbatively corrected Hamiltonian, we can in principle derive the mesonic spectra, the scattering amplitudes and the mesonic currents to arbitrarily good accuracy, as long as  $m \gg |w|$ .

**Particle pair creation in high-energy collisions** – In the regime considered in this work, fermionic pair creation is energetically forbidden, because the fermion mass  $\sim m$  exceeds by far the kinetic bandwidth of excitations  $\sim w$ . However, this phenomenon becomes relevant when  $m \simeq 2|w|$ . This can be inferred from the exact spectrum of the free fermions for  $\tau = 0$ , obtained from the equivalence with the solvable transverse-field Ising chain [359]:

$$\mathcal{E}_{\text{free}}(k) = m \sqrt{1 + \frac{4w^2}{m^2} + 4\frac{w}{m} \cos k}. \quad (\text{C.58})$$

When  $m$  approaches  $2|w|$  (from above), the renormalized mass  $\mu \equiv \min_k \mathcal{E}(k) = m - 2|w|$  of fermionic particles decreases to small values, and the bandwidth is  $\sim 2m$ . Thus, if a weak string tension  $\tau \neq 0$  is considered, the kinetic energy of mesons can reach values much larger than their rest mass  $\sim 2\mu$ , and thus high-energy collisions could generate extra mesons. This phenomenon goes beyond the theoretical analysis presented in Section 10, but could be accessed with quantum simulators.

**Decay of heavy mesons** – A finite fermion mass may also trigger the instability of heavy mesons, which can decay into two or more lighter mesons when their gauge field string is sufficiently extended (*string breaking*). The lifetime of unstable mesons is (at least) exponentially long in the ratio  $m/|w|$ , as discussed in Section 9.1.1; James et al. [210] have argued that it may even be infinite, based on numerical evidence. Thus, this phenomenon is not relevant in the regime studied in Chapter 10. The instability threshold is instead relevant when approaching the continuum limit  $m \searrow 2|w|$ , where the model exhibits an emergent Lorentz invariance. In this regime, the lifetimes of mesons with mass  $M > 4\mu$  is only perturbative  $\sim \tau^3$ , as computed by Rutkevich [234].

## C.7 Kink scattering phases

In the gapped antiferromagnetic phase of the XXZ chain, in the absence of external magnetic fields, the elementary excitations are spin-1/2 topological excitations,  $|K_{\alpha\beta}(\vartheta)\rangle_s$  interpolating between the two degenerate vacua  $\alpha, \beta$ . Their momenta and  $z$  spin component are labeled by  $\vartheta$  and  $s$ , respectively. Their dispersion relation can be parameterized by the so-called rapidity variable  $\lambda \in [\pi/2, \pi/2]$  as [418]

$$\vartheta(\lambda) = \frac{\pi}{2} - \text{am}(2K\lambda/\pi, k), \quad (\text{C.59a})$$

$$\omega(\lambda) = \frac{2K}{\pi} \sinh(\gamma) \text{dn}(2K\lambda/\pi, k), \quad (\text{C.59b})$$

where  $K = K(k)$  is the complete elliptic integral of modulus  $k$  with

$$\frac{K(\sqrt{1-k^2})}{K(k)} = \frac{\gamma}{\pi}, \quad (\text{C.60})$$

and  $\text{am}(x, k)$  and  $\text{dn}(x, k)$  are the Jacobi amplitude and delta amplitude. The parameterization (C.59) is equivalent to the form (12.17) in the main text.

These particles are interacting which is manifested in their nontrivial scattering properties. In the total spin zero channel, corresponding to the scattering of a  $s = 1/2$  and a  $s = -1/2$  particle, the scattering matrix is diagonalized by the combinations

$$|K_{\alpha\beta}(\vartheta_1)K_{\beta\alpha}(\vartheta_2)\rangle_{\pm} = \frac{1}{\sqrt{2}} \left( |K_{\alpha\beta}(\vartheta_1)K_{\beta\alpha}(\vartheta_2)\rangle_{\frac{1}{2}, -\frac{1}{2}} \pm |K_{\alpha\beta}(\vartheta_1)K_{\beta\alpha}(\vartheta_2)\rangle_{-\frac{1}{2}, \frac{1}{2}} \right). \quad (\text{C.61})$$

The scattering phases are defined as

$$|K_{\alpha\beta}(\vartheta_1)K_{\beta\alpha}(\vartheta_2)\rangle_{ss} = w_0(\vartheta_1, \vartheta_2) |K_{\alpha\beta}(\vartheta_2)K_{\beta\alpha}(\vartheta_1)\rangle_{ss}, \quad (\text{C.62a})$$

$$|K_{\alpha\beta}(\vartheta_1)K_{\beta\alpha}(\vartheta_2)\rangle_{\pm} = w_{\pm}(\vartheta_1, \vartheta_2) |K_{\alpha\beta}(\vartheta_2)K_{\beta\alpha}(\vartheta_1)\rangle_{\pm}. \quad (\text{C.62b})$$

They were obtained in Ref. [368] using Bethe ansatz with the result

$$w(\vartheta_1, \vartheta_2) = -e^{i\phi_\eta(\vartheta_1, \vartheta_2)}, \quad (\text{C.63})$$

$$\phi_\eta(\vartheta_1, \vartheta_2) = \Phi_\eta(\lambda_1 - \lambda_2), \quad (\text{C.64})$$

$$\Phi_0(\lambda) = -\lambda - \sum_{n=1}^{\infty} \frac{e^{-n\gamma} \sin(2\lambda n)}{n \cosh(n\gamma)}, \quad (\text{C.65})$$

$$\Phi_\pm(\lambda) = \Phi_0(\lambda) + \chi_\pm(\lambda), \quad (\text{C.66})$$

$$\chi_+(\lambda) = -i \ln \left( -\frac{\sin[(\lambda - i\gamma)/2]}{\sin[(\lambda + i\gamma)/2]} \right), \quad (\text{C.67})$$

$$\chi_-(\lambda) = -i \ln \left( \frac{\cos[(\lambda - i\gamma)/2]}{\cos[(\lambda + i\gamma)/2]} \right) \quad (\text{C.68})$$

with  $\vartheta_k = \vartheta(\lambda_k)$  as in Eq. (C.59a). The scattering phases  $\phi_\eta(\vartheta_1, \vartheta_2)$  are the ones that appear in Eqs. (12.29) and (12.30) with  $\eta$  chosen according to the the total spin of the particles.

## C.8 Spectral statistics for non-zero topological angle

We report here the average level statistics for the Schwinger model (Eq.13.2) with  $\theta \neq 0$ . In Fig. C.6. we show  $r$  versus  $J$  for two other values. Within error bars, we do not observe any difference between confining and deconfining regimes: in both cases, ergodicity breaks down in the same coupling window.

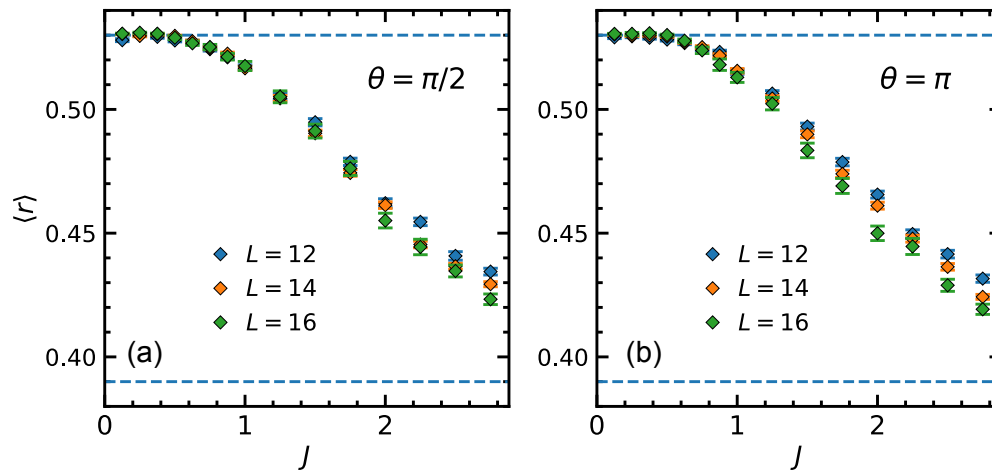


Figure C.6: Average level spacing ratio for the Schwinger model with non-zero topological angle  $\theta = \pi/2$  (a) and  $\theta = \pi$  (b). A non-zero  $\theta$  does not change the outcome w.r.t.  $\theta = 0$  (see Fig.13.1 (b)), not even in the deconfined regime  $\theta = \pi$ .



# Bibliography

- [1] F.M. Surace, M. Votto, E.G. Lazo, A. Silva, M. Dalmonte and G. Giudici, *Exact many-body scars and their stability in constrained quantum chains*, *Phys. Rev. B* **103** (2021) 104302.
- [2] F.M. Surace, M. Dalmonte and A. Silva, *Quantum local random networks and the statistical robustness of quantum scars*, [2107.00884](#).
- [3] F.M. Surace, G. Giudici and M. Dalmonte, *Weak-ergodicity-breaking via lattice supersymmetry*, *Quantum* **4** (2020) 339.
- [4] F.M. Surace, P.P. Mazza, G. Giudici, A. Lerose, A. Gambassi and M. Dalmonte, *Lattice Gauge Theories and String Dynamics in Rydberg Atom Quantum Simulators*, *Phys. Rev. X* **10** (2020) 021041.
- [5] F.M. Surace, P. Fromholz, F. Scazza and M. Dalmonte, *A scalable, ab initio protocol for quantum simulating  $SU(N)\times U(1)$  Lattice Gauge Theories with alkaline-earth like atoms, to appear* .
- [6] A. Lerose, F.M. Surace, P.P. Mazza, G. Perfetto, M. Collura and A. Gambassi, *Quasilocalized dynamics from confinement of quantum excitations*, *Phys. Rev. B* **102** (2020) 041118.
- [7] F. Surace and A. Lerose, *Scattering of mesons in quantum simulators*, *New Journal of Physics* **23** (2021) 062001.
- [8] G. Lagnese, F.M. Surace, M. Kormos and P. Calabrese, *False vacuum decay in quantum spin chains*, [2107.10176](#).
- [9] G. Lagnese, F.M. Surace, M. Kormos and P. Calabrese, *Confinement in the spectrum of a Heisenberg–Ising spin ladder*, *J. Stat. Mech.* **2009** (2020) 093106.
- [10] G. Giudici, F.M. Surace, J.E. Ebot, A. Scardicchio and M. Dalmonte, *Breakdown of ergodicity in disordered  $U(1)$  lattice gauge theories*, *Phys. Rev. Research* **2** (2020) 032034.

- [11] A. Russomanno, S. Notarnicola, F.M. Surace, R. Fazio, M. Dalmonte and M. Heyl, *Homogeneous Floquet time crystal protected by gauge invariance*, *Phys. Rev. Research* **2** (2020) 012003.
- [12] A. Offei-Danso, F.M. Surace, F. Iemini, A. Russomanno and R. Fazio, *Quantum clock models with infinite-range interactions*, *Journal of Statistical Mechanics: Theory and Experiment* **2020** (2020) 073107.
- [13] P. Sierant, G. Chiriaco, F.M. Surace, S. Sharma, X. Turkeshi, M. Dalmonte et al., *Dissipative Floquet Dynamics: from Steady State to Measurement Induced Criticality in Trapped-ion Chains*, [2107.05669](#).
- [14] L. D'Alessio, Y. Kafri, A. Polkovnikov and M. Rigol, *From quantum chaos and eigenstate thermalization to statistical mechanics and thermodynamics*, *Advances in Physics* **65** (2016) 239.
- [15] D.A. Huse, R. Nandkishore, V. Oganesyan, A. Pal and S.L. Sondhi, *Localization-protected quantum order*, *Phys. Rev. B* **88** (2013) 014206.
- [16] J.Z. Imbrie, V. Ros and A. Scardicchio, *Local integrals of motion in many-body localized systems*, *Ann. Phys. (Leipzig)* **529** (2017) 1600278.
- [17] D.A. Abanin, E. Altman, I. Bloch and M. Serbyn, *Colloquium: Many-body localization, thermalization, and entanglement*, *Rev. Mod. Phys.* **91** (2019) 021001.
- [18] M. Serbyn, D.A. Abanin and Z. Papić, *Quantum many-body scars and weak breaking of ergodicity*, *Nature Physics* **17** (2021) 675.
- [19] J.M. Deutsch, *Quantum statistical mechanics in a closed system*, *Phys. Rev. A* **43** (1991) 2046.
- [20] M. Srednicki, *Chaos and quantum thermalization*, *Phys. Rev. E* **50** (1994) 888.
- [21] M. Rigol, V. Dunjko and M. Olshanii, *Thermalization and its mechanism for generic isolated quantum systems*, *Nature* **452** (2008) 854.
- [22] M. Rigol, *Quantum quenches and thermalization in one-dimensional fermionic systems*, *Phys. Rev. A* **80** (2009) 053607.
- [23] M. Rigol, *Breakdown of thermalization in finite one-dimensional systems*, *Phys. Rev. Lett.* **103** (2009) 100403.

- [24] L.F. Santos and M. Rigol, *Localization and the effects of symmetries in the thermalization properties of one-dimensional quantum systems*, *Phys. Rev. E* **82** (2010) 031130.
- [25] G. Roux, *Finite-size effects in global quantum quenches: Examples from free bosons in an harmonic trap and the one-dimensional Bose-Hubbard model*, *Phys. Rev. A* **81** (2010) 053604.
- [26] G. Biroli, C. Kollath and A.M. Läuchli, *Effect of rare fluctuations on the thermalization of isolated quantum systems*, *Phys. Rev. Lett.* **105** (2010) 250401.
- [27] P.W. Anderson, *Absence of diffusion in certain random lattices*, *Phys. Rev.* **109** (1958) 1492.
- [28] D. Basko, I. Aleiner and B. Altshuler, *Metal-insulator transition in a weakly interacting many-electron system with localized single-particle states*, *Ann. Phys. (N.Y.)* **321** (2006) 1126 .
- [29] V. Oganesyan and D.A. Huse, *Localization of interacting fermions at high temperature*, *Physical Review B - Condensed Matter and Materials Physics* **75** (2007) 155111.
- [30] M. Žnidarič, T.c.v. Prosen and P. Prelovšek, *Many-body localization in the Heisenberg XXZ magnet in a random field*, *Phys. Rev. B* **77** (2008) 064426.
- [31] A. Pal and D.A. Huse, *Many-body localization phase transition*, *Physical Review B - Condensed Matter and Materials Physics* **82** (2010) 174411.
- [32] B. Bauer and C. Nayak, *Area laws in a many-body localized state and its implications for topological order*, *Journal of Statistical Mechanics: Theory and Experiment* **2013** (2013) P09005.
- [33] M. Serbyn, Z. Papić and D.A. Abanin, *Local conservation laws and the structure of the many-body localized states*, *Phys. Rev. Lett.* **111** (2013) 127201.
- [34] D.J. Luitz, N. Laflorencie and F. Alet, *Many-body localization edge in the random-field heisenberg chain*, *Phys. Rev. B* **91** (2015) 081103.
- [35] N.D. Mermin and H. Wagner, *Absence of Ferromagnetism or Antiferromagnetism in One- or Two-Dimensional Isotropic Heisenberg Models*, *Phys. Rev. Lett.* **17** (1966) 1133.
- [36] A. Chandran, V. Khemani, C.R. Laumann and S.L. Sondhi, *Many-body localization and symmetry-protected topological order*, *Phys. Rev. B* **89** (2014) 144201.

- [37] Y. Bahri, R. Vosk, E. Altman and A. Vishwanath, *Localization and topology protected quantum coherence at the edge of hot matter*, *Nature communications* **6** (2015) 1.
- [38] L. D'Alessio and M. Rigol, *Long-time behavior of isolated periodically driven interacting lattice systems*, *Phys. Rev. X* **4** (2014) 041048.
- [39] A. Lazarides, A. Das and R. Moessner, *Fate of many-body localization under periodic driving*, *Phys. Rev. Lett.* **115** (2015) 030402.
- [40] P. Ponte, Z. Papić, F.m.c. Huveneers and D.A. Abanin, *Many-body localization in periodically driven systems*, *Phys. Rev. Lett.* **114** (2015) 140401.
- [41] P. Ponte, A. Chandran, Z. Papić and D.A. Abanin, *Periodically driven ergodic and many-body localized quantum systems*, *Annals of Physics* **353** (2015) 196.
- [42] D.A. Abanin, W. De Roeck and F. Huveneers, *Theory of many-body localization in periodically driven systems*, *Annals of Physics* **372** (2016) 1.
- [43] V. Khemani, A. Lazarides, R. Moessner and S.L. Sondhi, *Phase structure of driven quantum systems*, *Phys. Rev. Lett.* **116** (2016) 250401.
- [44] D.V. Else, B. Bauer and C. Nayak, *Floquet time crystals*, *Phys. Rev. Lett.* **117** (2016) 090402.
- [45] H. Watanabe and M. Oshikawa, *Absence of quantum time crystals*, *Phys. Rev. Lett.* **114** (2015) 251603.
- [46] H. Bernien, S. Schwartz, A. Keesling, H. Levine, A. Omran, H. Pichler et al., *Probing many-body dynamics on a 51-atom quantum simulator*, *Nature* **551** (2017) 579.
- [47] C.J. Turner, A.A. Michailidis, D.A. Abanin, M. Serbyn and Z. Papić, *Weak ergodicity breaking from quantum many-body scars*, *Nat. Phys.* **14** (2018) 745.
- [48] C.J. Turner, A.A. Michailidis, D.A. Abanin, M. Serbyn and Z. Papić, *Quantum scarred eigenstates in a Rydberg atom chain: Entanglement, breakdown of thermalization, and stability to perturbations*, *Phys. Rev. B* **94** (2018) 155134.
- [49] E.J. Heller, *Bound-State Eigenfunctions of Classically Chaotic Hamiltonian Systems: Scars of Periodic Orbits*, *Phys. Rev. Lett.* **53** (1984) 1515.

- [50] P. Fendley, K. Sengupta and S. Sachdev, *Competing density-wave orders in a one-dimensional hard-boson model*, *Phys. Rev. B* **69** (2004) 075106.
- [51] I. Lesanovsky and H. Katsura, *Interacting Fibonacci anyons in a Rydberg gas*, *Phys. Rev. A* **86** (2012) 041601.
- [52] C.-J. Lin and O.I. Motrunich, *Exact Quantum Many-Body Scar States in the Rydberg-Blockaded Atom Chain*, *Phys. Rev. Lett.* **122** (2019) 173401.
- [53] C.N. Yang,  *$\eta$  pairing and off-diagonal long-range order in a Hubbard model*, *Phys. Rev. Lett.* **63** (1989) 2144.
- [54] D.P. Arovas, *Two exact excited states for the  $S = 1$  AKLT chain*, *Physics Letters A* **137** (1989) 431.
- [55] S. Moudgalya, N. Regnault and B.A. Bernevig, *Entanglement of exact excited states of Affleck-Kennedy-Lieb-Tasaki models: Exact results, many-body scars, and violation of the strong eigenstate thermalization hypothesis*, *Phys. Rev. B* **98** (2018) 235156.
- [56] M. Schechter and T. Iadecola, *Weak Ergodicity Breaking and Quantum Many-Body Scars in Spin-1 XY Magnets*, *Phys. Rev. Lett.* **123** (2019) 147201.
- [57] T. Iadecola, M. Schechter and S. Xu, *Quantum many-body scars from magnon condensation*, *Physical Review B* **100** (2019) 184312.
- [58] T. Iadecola and M. Schechter, *Quantum many-body scar states with emergent kinetic constraints and finite-entanglement revivals*, *Phys. Rev. B* **101** (2020) 024306.
- [59] S. Chattopadhyay, H. Pichler, M.D. Lukin and W.W. Ho, *Quantum many-body scars from virtual entangled pairs*, *Phys. Rev. B* **101** (2020) 174308.
- [60] N. Shibata, N. Yoshioka and H. Katsura, *Onsager's scars in disordered spin chains*, *Phys. Rev. Lett.* **124** (2020) 180604.
- [61] D.K. Mark, C.-J. Lin and O.I. Motrunich, *Exact eigenstates in the Lesanovsky model, proximity to integrability and the PXP model, and approximate scar states*, *Phys. Rev. B* **101** (2020) 094308.
- [62] D.K. Mark, C.-J. Lin and O.I. Motrunich, *Unified structure for exact towers of scar states in the Affleck-Kennedy-Lieb-Tasaki and other models*, *Phys. Rev. B* **101** (2020) 195131.

- [63] S. Moudgalya, N. Regnault and B.A. Bernevig,  $\eta$ -pairing in Hubbard models: From spectrum generating algebras to quantum many-body scars, *Phys. Rev. B* **102** (2020) 085140.
- [64] N. Shiraishi and T. Mori, Systematic construction of counterexamples to the eigenstate thermalization hypothesis, *Phys. Rev. Lett.* **119** (2017) 030601.
- [65] C.-J. Lin, A. Chandran and O.I. Motrunich, Slow thermalization of exact quantum many-body scar states under perturbations, *Phys. Rev. Research* **2** (2020) 033044.
- [66] P. Sierant, A. Maksymov, M. Kuś and J. Zakrzewski, Fidelity susceptibility in gaussian random ensembles, *Phys. Rev. E* **99** (2019) 050102.
- [67] A. Maksymov, P. Sierant and J. Zakrzewski, Energy level dynamics across the many-body localization transition, *Phys. Rev. B* **99** (2019) 224202.
- [68] D. Sels and A. Polkovnikov, Dynamical obstruction to localization in a disordered spin chain, [2009.04501](#).
- [69] S. Choi, C.J. Turner, H. Pichler, W.W. Ho, A.A. Michailidis, Z. Papić et al., Emergent  $SU(2)$  Dynamics and Perfect Quantum Many-Body Scars, *Phys. Rev. Lett.* **122** (2019) 220603.
- [70] M. Pandey, P.W. Claeys, D.K. Campbell, A. Polkovnikov and D. Sels, Adiabatic Eigenstate Deformations as a Sensitive Probe for Quantum Chaos, *Phys. Rev. X* **10** (2020) 041017.
- [71] M. Schecter and T. Iadecola, Many-body spectral reflection symmetry and protected infinite-temperature degeneracy, *Physical Review B* **98** (2018) 35139.
- [72] W.-L. You, Y.-W. Li and S.-J. Gu, Fidelity, dynamic structure factor, and susceptibility in critical phenomena, *Phys. Rev. E* **76** (2007) 022101.
- [73] S. Moudgalya, S. Rachel, B.A. Bernevig and N. Regnault, Exact excited states of nonintegrable models, *Phys. Rev. B* **98** (2018) 235155.
- [74] K. Bull, I. Martin and Z. Papić, Systematic Construction of Scarred Many-Body Dynamics in 1D Lattice Models, *Phys. Rev. Lett.* **123** (2019) 030601.

- [75] S. Ok, K. Choo, C. Mudry, C. Castelnovo, C. Chamon and T. Neupert, *Topological many-body scar states in dimensions one, two, and three*, *Phys. Rev. Research* **1** (2019) 033144.
- [76] A. Hudomal, I. Vasić, N. Regnault and Z. Papić, *Quantum scars of bosons with correlated hopping*, *Communications Physics* **3** (2020) 1.
- [77] S. Pai and M. Pretko, *Dynamical scar states in driven fracton systems*, *Phys. Rev. Lett.* **123** (2019) 136401.
- [78] S. Moudgalya, B.A. Bernevig and N. Regnault, *Quantum many-body scars in a Landau level on a thin torus*, *Phys. Rev. B* **102** (2020) 195150.
- [79] H. Zhao, J. Vovrosh, F. Mintert and J. Knolle, *Quantum many-body scars in optical lattices*, *Phys. Rev. Lett.* **124** (2020) 160604.
- [80] K. Lee, R. Melendrez, A. Pal and H.J. Changlani, *Exact three-colored quantum scars from geometric frustration*, *Phys. Rev. B* **101** (2020) 241111.
- [81] V. Khemani, C.R. Laumann and A. Chandran, *Signatures of integrability in the dynamics of Rydberg-blockaded chains*, *Phys. Rev. B* **99** (2019) 161101.
- [82] C.-J. Lin, V. Calvera and T.H. Hsieh, *Quantum many-body scar states in two-dimensional Rydberg atom arrays*, *Phys. Rev. B* **101** (2020) 220304.
- [83] D. Pérez-García, F. Verstraete, M.M. Wolf and J.I. Cirac, *PEPS as unique ground states of local Hamiltonians*, *Quantum Inf. Comput.* **8** (2008) 650.
- [84] J. Wurtz and A. Polkovnikov, *Emergent conservation laws and nonthermal states in the mixed-field ising model*, *Phys. Rev. B* **101** (2020) 195138.
- [85] S. Sugiura, P.W. Claeys, A. Dymarsky and A. Polkovnikov, *Adiabatic landscape and optimal paths in ergodic systems*, [2004.13735](#).
- [86] P. Sala, T. Rakovszky, R. Verresen, M. Knap and F. Pollmann, *Ergodicity Breaking Arising from Hilbert Space Fragmentation in Dipole-Conserving Hamiltonians*, *Phys. Rev. X* **10** (2020) 011047.
- [87] S. Moudgalya, A. Prem, R.M. Nandkishore, N. Regnault and B.A. Bernevig, *Thermalization and its absence within krylov subspaces of a constrained hamiltonian*, [1910.14048](#).

- [88] O.Golinelli, *Statistics of delta peaks in the spectral density of large random trees*, [0301437](#).
- [89] S.H. Cvetkovic D.M, Doob M., *Spectra of Graphs: Theory and Applications*, Academic Press, New York (1980).
- [90] D. Jaksch, J.I. Cirac, P. Zoller, S.L. Rolston, R. Côté and M.D. Lukin, *Fast Quantum Gates for Neutral Atoms*, *Phys. Rev. Lett.* **85** (2000) 2208.
- [91] A. Barrat, M. Barthélemy and A. Vespignani, *Dynamical Processes on Complex Networks*, Cambridge University Press (2008), [10.1017/CBO9780511791383](#).
- [92] M. Sade, T. Kalisky, S. Havlin and R. Berkovits, *Localization transition on complex networks via spectral statistics*, *Phys. Rev. E* **72** (2005) 066123.
- [93] M. Bauer and O. Golinelli, *Exactly solvable model with two conductor-insulator transitions driven by impurities*, *Phys. Rev. Lett.* **86** (2001) 2621.
- [94] L. Jahnke, J.W. Kantelhardt, R. Berkovits and S. Havlin, *Wave localization in complex networks with high clustering*, *Phys. Rev. Lett.* **101** (2008) 175702.
- [95] F. Pietracaprina and N. Laflorencie, *Hilbert-space fragmentation, multifractality, and many-body localization*, *Annals of Physics* (2021) 168502.
- [96] D. Nickelsen and M. Kastner, *Classical Lieb-Robinson Bound for Estimating Equilibration Timescales of Isolated Quantum Systems*, *Phys. Rev. Lett.* **122** (2019) 180602.
- [97] D. Nickelsen and M. Kastner, *Modelling equilibration of local many-body quantum systems by random graph ensembles*, *Quantum* **4** (2020) 273.
- [98] V. Khemani, M. Hermele and R. Nandkishore, *Localization from Hilbert space shattering: From theory to physical realizations*, *Phys. Rev. B* **101** (2020) 174204.
- [99] J.-Y. Desaulles, A. Hudomal, C.J. Turner and Z. Papić, *A proposal for realising quantum scars in the tilted 1D Fermi-Hubbard model*, *Phys. Rev. Lett.* **126** (2021) 210601.
- [100] S. Coleman, *Aspects of Symmetry: Selected Erice Lectures*, Cambridge University Press (1985), [10.1017/CBO9780511565045](#).

- [101] E. Fradkin, *Field Theories of Condensed Matter Systems*, Cambridge University Press (2013), [10.1017/CBO9781139015509](https://doi.org/10.1017/CBO9781139015509).
- [102] M. Creutz, *Quarks, gluons and lattices*, Cambridge University Press, Cambridge (1997).
- [103] A. Polkovnikov, K. Sengupta, A. Silva and M. Vengalattore, *Colloquium: Nonequilibrium dynamics of closed interacting quantum systems*, *Rev. Mod. Phys.* **83** (2011) 863.
- [104] L.M. Sieberer, M. Buchhold and S. Diehl, *Keldysh field theory for driven open quantum systems*, *Reports on Progress in Physics* **79** (2016) 096001.
- [105] W.W. Ho, S. Choi, H. Pichler and M.D. Lukin, *Periodic Orbits, Entanglement, and Quantum Many-Body Scars in Constrained Models: Matrix Product State Approach*, *Phys. Rev. Lett.* **122** (2019) 040603.
- [106] A.A. Michailidis, C.J. Turner, Z. Papić, D.A. Abanin and M. Serbyn, *Slow quantum thermalization and many-body revivals from mixed phase space*, *Phys. Rev. X* **10** (2020) 011055.
- [107] S. Coleman and J. Mandula, *All Possible Symmetries of the S Matrix*, *Phys. Rev.* **159** (1967) 1251.
- [108] P. Fendley, K. Schoutens and J. de Boer, *Lattice Models with  $\mathcal{N} = 2$  Supersymmetry*, *Phys. Rev. Lett.* **90** (2003) 120402.
- [109] P. Fendley, B. Nienhuis and K. Schoutens, *Lattice fermion models with supersymmetry*, *Journal of Physics A: Mathematical and General* **36** (2003) 12399.
- [110] P. Fendley and K. Schoutens, *Exact Results for Strongly Correlated Fermions in 2 + 1 Dimensions*, *Phys. Rev. Lett.* **95** (2005) 046403.
- [111] L. Huijse and K. Schoutens, *Superfrustration of charge degrees of freedom*, *European Physical Journal B* **64** (2008) 543.
- [112] L. Huijse, J. Halverson, P. Fendley and K. Schoutens, *Charge frustration and quantum criticality for strongly correlated fermions*, *Physical Review Letters* **101** (2008) 146406.
- [113] S.-A. Cheong and C.L. Henley, *Exact ground states and correlation functions of chain and ladder models of interacting hardcore bosons or spinless fermions*, *Phys. Rev. B* **80** (2009) 165124.
- [114] M. Beccaria and C. Hagendorf, *A staggered fermion chain with supersymmetry on open intervals*, *Journal of Physics A: Mathematical and Theoretical* **45** (2012) 365201.

- [115] B. Bauer, L. Huijse, E. Berg, M. Troyer and K. Schoutens, *Supersymmetric multicritical point in a model of lattice fermions*, *Phys. Rev. B* **87** (2013) 165145.
- [116] C. Hagendorf, *Spin Chains with Dynamical Lattice Supersymmetry*, *Journal of Statistical Physics* **150** (2013) 609.
- [117] G. Pupillo, A. Micheli, M. Boninsegni, I. Lesanovsky and P. Zoller, *Strongly Correlated Gases of Rydberg-Dressed Atoms: Quantum and Classical Dynamics*, *Phys. Rev. Lett.* **104** (2010) 223002.
- [118] N. Henkel, R. Nath and T. Pohl, *Three-Dimensional Roton Excitations and Supersolid Formation in Rydberg-Excited Bose-Einstein Condensates*, *Phys. Rev. Lett.* **104** (2010) 195302.
- [119] J. Honer, H. Weimer, T. Pfau and H.P. Büchler, *Collective Many-Body Interaction in Rydberg Dressed Atoms*, *Phys. Rev. Lett.* **105** (2010) 160404.
- [120] J. Zeiher, R. van Bijnen, P. Schauß, S. Hild, J.-y. Choi, T. Pohl et al., *Many-body interferometry of a Rydberg-dressed spin lattice*, *Nature Physics* **12** (2016) 1095–1099.
- [121] A.W. Glaetzle, M. Dalmonte, R. Nath, I. Rousochatzakis, R. Moessner and P. Zoller, *Quantum Spin-Ice and Dimer Models with Rydberg Atoms*, *Phys. Rev. X* **4** (2014) 041037.
- [122] A. Mitra, M.J. Martin, G.W. Biedermann, A.M. Marino, P.M. Poggi and I.H. Deutsch, *Robust Mølmer-Sørensen gate for neutral atoms using rapid adiabatic Rydberg dressing*, *Phys. Rev. A* **101** (2020) 030301.
- [123] M. Dalmonte, W. Lechner, Z. Cai, M. Mattioli, A.M. Läuchli and G. Pupillo, *Cluster luttinger liquids and emergent supersymmetric conformal critical points in the one-dimensional soft-shoulder hubbard model*, *Phys. Rev. B* **92** (2015) 045106.
- [124] M. Mattioli, M. Dalmonte, W. Lechner and G. Pupillo, *Cluster Luttinger Liquids of Rydberg-Dressed Atoms in Optical Lattices*, *Phys. Rev. Lett.* **111** (2013) 165302.
- [125] E. Guardado-Sanchez, B.M. Spar, P. Schauss, R. Belyansky, J.T. Young, P. Bienias et al., *Quench Dynamics of a Fermi Gas with Strong Nonlocal Interactions*, *Phys. Rev. X* **11** (2021) 021036.
- [126] A.C. Cubero, G. Mussardo and M. Panfil, *Quench dynamics in two-dimensional integrable SUSY models*, *Journal of Statistical Mechanics: Theory and Experiment* **2016** (2016) 033115.

- [127] M. Troyer and U.-J. Wiese, *Computational Complexity and Fundamental Limitations to Fermionic Quantum Monte Carlo Simulations*, *Phys. Rev. Lett.* **94** (2005) 170201.
- [128] M. Dalmonte and S. Montangero, *Lattice gauge theory simulations in the quantum information era*, *Contemporary Physics* **57** (2016) 388.
- [129] J. Preskill, *Simulating quantum field theory with a quantum computer*, *PoS LATTICE2018* (2019) 024.
- [130] M.C. Bañuls, R. Blatt, J. Catani, A. Celi, J.I. Cirac, M. Dalmonte et al., *Simulating lattice gauge theories within quantum technologies*, *The European Physical Journal D* **74** (2020) 1.
- [131] R.P. Feynman, *Simulating Physics with Computers.*, *Int. J. Theor. Phys.* **21** (1982) 467.
- [132] J. Zhang, G. Pagano, P.W. Hess, A. Kyprianidis, P. Becker, H. Kaplan et al., *Observation of a many-body dynamical phase transition with a 53-qubit quantum simulator*, *Nature* **551** (2017) 601.
- [133] C. Gross and I. Bloch, *Quantum simulations with ultracold atoms in optical lattices*, *Science* **357** (2017) 995.
- [134] C. Monroe, W.C. Campbell, L.-M. Duan, Z.-X. Gong, A.V. Gorshkov, P.W. Hess et al., *Programmable quantum simulations of spin systems with trapped ions*, *Rev. Mod. Phys.* **93** (2021) 025001.
- [135] A. Mazurenko, C.S. Chiu, G. Ji, M.F. Parsons, M. Kanász-Nagy, R. Schmidt et al., *A cold-atom Fermi–Hubbard antiferromagnet*, *Nature* **545** (2017) 462.
- [136] F. Arute, K. Arya, R. Babbush, D. Bacon, J.C. Bardin, R. Barends et al., *Quantum supremacy using a programmable superconducting processor*, *Nature* **574** (2019) 505.
- [137] N. Friis, O. Marty, C. Maier, C. Hempel, M. Holzäpfel, P. Jurcevic et al., *Observation of entangled states of a fully controlled 20-qubit system*, *Phys. Rev. X* **8** (2018) 021012.
- [138] R. Harris, Y. Sato, A.J. Berkley, M. Reis, F. Altomare, M.H. Amin et al., *Phase transitions in a programmable quantum spin glass simulator*, *Science* **361** (2018) 162.
- [139] K.G. Wilson, *Confinement of quarks*, *Phys. Rev. D* **10** (1974) 2445.
- [140] J.B. Kogut, *An introduction to lattice gauge theory and spin systems*, *Rev. Mod. Phys.* **51** (1979) 659.

- [141] J. Kogut and L. Susskind, *Hamiltonian formulation of Wilson's lattice gauge theories*, *Phys. Rev. D* **11** (1975) 395.
- [142] C. Hamer, *Lattice model calculations for  $SU(2)$  Yang-Mills theory in  $1 + 1$  dimensions*, *Nuclear Physics B* **121** (1977) 159 .
- [143] S. Chandrasekharan and U.-J. Wiese, *An introduction to chiral symmetry on the lattice*, *Progress in Particle and Nuclear Physics* **53** (2004) 373.
- [144] S. Coleman, *More about the massive Schwinger model*, *Annals of Physics* **101** (1976) 239.
- [145] D. Horn, *Finite matrix models with continuous local gauge invariance*, *Physics Letters B* **100** (1981) 149.
- [146] P. Orland and D. Rohrlich, *Lattice gauge magnets: Local isospin from spin*, *Nuclear Physics B* **338** (1990) 647.
- [147] S. Chandrasekharan and U.-J. Wiese, *Quantum link models: A discrete approach to gauge theories*, *Nuclear Physics B* **492** (1997) 455.
- [148] R. Brower, S. Chandrasekharan and U.-J. Wiese, *QCD as a quantum link model*, *Phys. Rev. D* **60** (1999) 094502.
- [149] H. Weimer, M. Müller, I. Lesanovsky, P. Zoller and H.P. Büchler, *A Rydberg quantum simulator*, *Nature Physics* **6** (2010) 382.
- [150] L. Tagliacozzo, A. Celi, A. Zamora and M. Lewenstein, *Optical abelian lattice gauge theories*, *Annals of Physics* **330** (2013) 160.
- [151] L. Tagliacozzo, A. Celi, P. Orland, M. Mitchell and M. Lewenstein, *Simulation of non-Abelian gauge theories with optical lattices*, *Nature Communications* **4** (2013) 1.
- [152] A. Mezzacapo, E. Rico, C. Sabín, I.L. Egusquiza, L. Lamata and E. Solano, *Non-Abelian  $SU(2)$  Lattice Gauge Theories in Superconducting Circuits*, *Phys. Rev. Lett.* **115** (2015) 240502.
- [153] D. Banerjee, M. Bögli, M. Dalmonte, E. Rico, P. Stebler, U.-J. Wiese et al., *Atomic quantum simulation of  $U(n)$  and  $SU(n)$  non-abelian lattice gauge theories*, *Phys. Rev. Lett.* **110** (2013) 125303.
- [154] E. Zohar, J.I. Cirac and B. Reznik, *Quantum simulations of gauge theories with ultracold atoms: Local gauge invariance from angular-momentum conservation*, *Phys. Rev. A* **88** (2013) 023617.

- [155] E. Zohar, J.I. Cirac and B. Reznik, *Cold-Atom Quantum Simulator for  $SU(2)$  Yang-Mills Lattice Gauge Theory*, *Phys. Rev. Lett.* **110** (2013) 125304.
- [156] C. Laflamme, W. Evans, M. Dalmonte, U. Gerber, H. Mejía-Díaz, W. Bietenholz et al.,  *$CP(N-1)$  Quantum Field Theories with Alkaline-Earth Atoms in Optical Lattices*, *Annals of Physics* **370** (2016) 117.
- [157] A.S. Dehkharghani, E. Rico, N.T. Zinner and A. Negretti, *Quantum simulation of abelian lattice gauge theories via state-dependent hopping*, *Phys. Rev. A* **96** (2017) 043611.
- [158] E. Zohar and B. Reznik, *Confinement and lattice quantum-electrodynamic electric flux tubes simulated with ultracold atoms*, *Phys. Rev. Lett.* **107** (2011) 275301.
- [159] E. Zohar, J.I. Cirac and B. Reznik, *Simulating Compact Quantum Electrodynamics with Ultracold Atoms: Probing Confinement and Nonperturbative Effects*, *Phys. Rev. Lett.* **109** (2012) 125302.
- [160] D. Banerjee, M. Dalmonte, M. Müller, E. Rico, P. Stebler, U.-J. Wiese et al., *Atomic Quantum Simulation of Dynamical Gauge Fields Coupled to Fermionic Matter: From String Breaking to Evolution after a Quench*, *Phys. Rev. Lett.* **109** (2012) 175302.
- [161] K. Kasamatsu, I. Ichinose and T. Matsui, *Atomic Quantum Simulation of the Lattice Gauge-Higgs Model: Higgs Couplings and Emergence of Exact Local Gauge Symmetry*, *Phys. Rev. Lett.* **111** (2013) 115303.
- [162] S. Notarnicola, E. Ercolessi, P. Facchi, G. Marmo, S. Pascazio and F.V. Pepe, *Discrete abelian gauge theories for quantum simulations of QED*, *Journal of Physics A: Mathematical and Theoretical* **48** (2015) 30FT01.
- [163] Y. Kuno, K. Kasamatsu, Y. Takahashi, I. Ichinose and T. Matsui, *Real-time dynamics and proposal for feasible experiments of lattice gauge-Higgs model simulated by cold atoms*, *New Journal of Physics* **17** (2015) 063005.
- [164] K. Stannigel, P. Hauke, D. Marcos, M. Hafezi, S. Diehl, M. Dalmonte et al., *Constrained dynamics via the zeno effect in quantum simulation: Implementing non-abelian lattice gauge theories with cold atoms*, *Phys. Rev. Lett.* **112** (2014) 120406.
- [165] T. Banks, L. Susskind and J. Kogut, *Strong-coupling calculations of lattice gauge theories:  $(1 + 1)$ -dimensional exercises*, *Phys. Rev. D* **13** (1976) 1043.

- [166] E.A. Martinez, C.A. Muschik, P. Schindler, D. Nigg, A. Erhard, M. Heyl et al., *Real-time dynamics of lattice gauge theories with a few-qubit quantum computer*, *Nature* **534** (2016) 516.
- [167] P. Sala, T. Shi, S. Kühn, M.C. Bañuls, E. Demler and J.I. Cirac, *Variational study of  $U(1)$  and  $SU(2)$  lattice gauge theories with Gaussian states in  $1+1$  dimensions*, *Phys. Rev. D* **98** (2018) 034505.
- [168] Y. Atas, J. Zhang, R. Lewis, A. Jahanpour, J.F. Haase and C.A. Muschik,  *$SU(2)$  hadrons on a quantum computer*, [2102.08920](#).
- [169] E. Zohar and J.I. Cirac, *Removing staggered fermionic matter in  $U(N)$  and  $SU(N)$  lattice gauge theories*, *Phys. Rev. D* **99** (2019) 114511.
- [170] I. Raychowdhury and J.R. Stryker, *Loop, string, and hadron dynamics in  $su(2)$  hamiltonian lattice gauge theories*, *Phys. Rev. D* **101** (2020) 114502.
- [171] I. Buluta and F. Nori, *Quantum simulators*, *Science* **326** (2009) 108.
- [172] H.P. Büchler, M. Hermele, S.D. Huber, M.P.A. Fisher and P. Zoller, *Atomic quantum simulator for lattice gauge theories and ring exchange models*, *Phys. Rev. Lett.* **95** (2005) 040402.
- [173] J.I. Cirac, P. Maraner and J.K. Pachos, *Cold atom simulation of interacting relativistic quantum field theories*, *Phys. Rev. Lett.* **105** (2010) 190403.
- [174] U.-J. Wiese, *Ultracold quantum gases and lattice systems: quantum simulation of lattice gauge theories*, *Annalen der Physik* **525** (2013) 777.
- [175] E. Zohar, J.I. Cirac and B. Reznik, *Quantum simulations of lattice gauge theories using ultracold atoms in optical lattices*, *Reports on Progress in Physics* **79** (2015) 014401.
- [176] D. Marcos, P. Rabl, E. Rico and P. Zoller, *Superconducting Circuits for Quantum Simulation of Dynamical Gauge Fields*, *Phys. Rev. Lett.* **111** (2013) 110504.
- [177] G.K. Brennen, G. Pupillo, E. Rico, T.M. Stace and D. Vodola, *Loops and strings in a superconducting lattice gauge simulator*, *Phys. Rev. Lett.* **117** (2016) 240504.
- [178] J. Preskill, *Quantum Computing in the NISQ era and beyond*, *Quantum* **2** (2018) 79.

- [179] B. Yang, H. Sun, R. Ott, H.-Y. Wang, T.V. Zache, J.C. Halimeh et al., *Observation of gauge invariance in a 71-site Bose-Hubbard quantum simulator*, *Nature* **587** (2020) 392.
- [180] A. Ciavarella, N. Klco and M.J. Savage, *Trailhead for quantum simulation of  $SU(3)$  Yang-Mills lattice gauge theory in the local multiplet basis*, *Phys. Rev. D* **103** (2021) 094501.
- [181] S. Ebadi, T.T. Wang, H. Levine, A. Keesling, G. Semeghini, A. Omran et al., *Quantum phases of matter on a 256-atom programmable quantum simulator*, *Nature* **595** (2021) 227.
- [182] P. Scholl, M. Schuler, H.J. Williams, A.A. Eberharter, D. Barredo, K.-N. Schymik et al., *Quantum simulation of 2D antiferromagnets with hundreds of Rydberg atoms*, *Nature* **595** (2021) 233.
- [183] J.-y. Choi, S. Hild, J. Zeiher, P. Schauß, A. Rubio-Abadal, T. Yefsah et al., *Exploring the many-body localization transition in two dimensions*, *Science* **352** (2016) 1547.
- [184] D. Barredo, V. Lienhard, S. de Léséleuc, T. Lahaye and A. Browaeys, *Synthetic three-dimensional atomic structures assembled atom by atom*, *Nature* **561** (2018) 79.
- [185] E.A. Calzetta and B.L. Hu, *Nonequilibrium Quantum Field Theory*, Cambridge Univ. Press, Cambridge (2008), [10.1017/CBO9780511535123](https://doi.org/10.1017/CBO9780511535123).
- [186] SESAM COLLABORATION collaboration, *Observation of string breaking in qcd*, *Phys. Rev. D* **71** (2005) 114513.
- [187] F. Hebenstreit, J. Berges and D. Gelfand, *Real-Time Dynamics of String Breaking*, *Phys. Rev. Lett.* **111** (2013) 201601.
- [188] Y. Kuno, S. Sakane, K. Kasamatsu, I. Ichinose and T. Matsui, *Quantum simulation of  $(1+1)$ -dimensional  $U(1)$  gauge-Higgs model on a lattice by cold Bose gases*, *Phys. Rev. D* **95** (2017) 094507.
- [189] J. Schwinger, *Gauge Invariance and Mass. II*, *Phys. Rev.* **128** (1962) 2425.
- [190] F. Hebenstreit, J. Berges and D. Gelfand, *Simulating fermion production in 1+1 dimensional QED*, *Phys. Rev. D* **87** (2013) 105006.
- [191] B. Buyens, J. Haegeman, H. Verschelde, F. Verstraete and K. Van Acoleyen, *Confinement and String Breaking for  $QED_2$  in the Hamiltonian Picture*, *Phys. Rev. X* **6** (2016) 041040.

- [192] T. Pichler, M. Dalmonte, E. Rico, P. Zoller and S. Montangero, *Real-Time Dynamics in  $U(1)$  Lattice Gauge Theories with Tensor Networks*, *Phys. Rev. X* **6** (2016) 011023.
- [193] K. Rajagopal and F. Wilczek, *Emergence of coherent long wavelength oscillations after a quench: application to QCD*, *Nuclear Physics B* **404** (1993) 577.
- [194] I. Bloch, J. Dalibard and S. Nascimbène, *Quantum simulations with ultracold quantum gases*, *Nat. Phys.* **8** (2012) 267.
- [195] J. Zeiher, J.-y. Choi, A. Rubio-Abadal, T. Pohl, R. van Bijnen, I. Bloch et al., *Coherent Many-Body Spin Dynamics in a Long-Range Interacting Ising Chain*, *Phys. Rev. X* **7** (2017) 041063.
- [196] B.M. McCoy and M.-L. Yan, *Gauge-invariant correlation functions for the ising-gauge ising-higgs system in 2 dimensions*, *Nuclear Physics B* **215** (1983) 278.
- [197] N. Chepiga and F. Mila, *DMRG investigation of constrained models: from quantum dimer and quantum loop ladders to hard-boson and Fibonacci anyon chains*, *SciPost Phys.* **6** (2019) 33.
- [198] T. Chanda, J. Zakrzewski, M. Lewenstein and L. Tagliacozzo, *Confinement and Lack of Thermalization after Quenches in the Bosonic Schwinger Model*, *Phys. Rev. Lett.* **124** (2020) 180602.
- [199] Y.-P. Huang, D. Banerjee and M. Heyl, *Dynamical Quantum Phase Transitions in  $U(1)$  Quantum Link Models*, *Phys. Rev. Lett.* **122** (2019) 250401.
- [200] V. Kasper, F. Hebenstreit, M. Oberthaler and J. Berges, *Schwinger pair production with ultracold atoms*, *Physics Letters B* **760** (2016) 742.
- [201] E. Rico, T. Pichler, M. Dalmonte, P. Zoller and S. Montangero, *Tensor networks for lattice gauge theories and atomic quantum simulation*, *Phys. Rev. Lett.* **112** (2014) 201601.
- [202] C. Hamer, J. Kogut, D. Crewther and M. Mazzolini, *The massive Schwinger model on a lattice: Background field, chiral symmetry and the string tension*, *Nuclear Physics B* **208** (1982) 413.
- [203] M. Bañuls, K. Cichy, I. Cirac and K. Jansen, *The mass spectrum of the Schwinger model with matrix product states*, *J. High Energy Phys.* **2013** (2013) 158.

- [204] F. Fucito, F. Marchesoni, E. Marinari, G. Parisi, L. Peliti, S. Ruffo et al., *Approach to equilibrium in a chain of nonlinear oscillators*, *Journal de Physique* **43** (1982) 707.
- [205] T. Langen, T. Gasenzer and J. Schmiedmayer, *Prethermalization and universal dynamics in near-integrable quantum systems*, *J. Stat. Mech.: Theory Exp* **2016** (2016) 064009.
- [206] A. Omran, H. Levine, A. Keesling, G. Semeghini, T.T. Wang, S. Ebadi et al., *Generation and manipulation of Schrödinger cat states in Rydberg atom arrays*, *Science* **365** (2019) 570.
- [207] P.P. Mazza, G. Peretto, A. Lerose, M. Collura and A. Gambassi, *Suppression of transport in nondisordered quantum spin chains due to confined excitations*, *Phys. Rev. B* **99** (2019) 180302.
- [208] M. Brenes, M. Dalmonte, M. Heyl and A. Scardicchio, *Many-Body Localization Dynamics from Gauge Invariance*, *Physical Review Letters* **120** (2018) 030601.
- [209] M. Kormos, M. Collura, G. Takács and P. Calabrese, *Real time confinement following a quantum quench to a non-integrable model*, *Nature Physics* **13** (2017) 246.
- [210] A.J.A. James, R.M. Konik and N.J. Robinson, *Nonthermal states arising from confinement in one and two dimensions*, *Phys. Rev. Lett.* **122** (2019) 130603.
- [211] J. Park, Y. Kuno and I. Ichinose, *Glassy dynamics from quark confinement: Atomic quantum simulation of the gauge-Higgs model on a lattice*, *Phys. Rev. A* **100** (2019) 013629.
- [212] C. Kokail, C. Maier, R. van Bijnen, T. Brydges, M.K. Joshi, P. Jurcevic et al., *Self-Verifying Variational Quantum Simulation of the Lattice Schwinger Model*, *Nature* **569** (2019) 355.
- [213] S. Notarnicola, M. Collura and S. Montangero, *Real-time-dynamics quantum simulation of (1 + 1)-dimensional lattice QED with Rydberg atoms*, *Phys. Rev. Research* **2** (2020) 013288.
- [214] A. Celi, B. Vermersch, O. Viyuela, H. Pichler, M.D. Lukin and P. Zoller, *Emerging Two-Dimensional Gauge Theories in Rydberg Configurable Arrays*, *Phys. Rev. X* **10** (2020) 021057.
- [215] V. Kasper, T.V. Zache, F. Jendrzejewski, M. Lewenstein and E. Zohar, *Non-Abelian gauge invariance from dynamical decoupling*, [2012.08620](https://arxiv.org/abs/2012.08620).

- [216] Z. Davoudi, N.M. Linke and G. Pagano, *Toward simulating quantum field theories with controlled phonon-ion dynamics: A hybrid analog-digital approach*, [2104.09346](#).
- [217] A.V. Gorshkov, M. Hermele, V. Gurarie, C. Xu, P.S. Julienne, J. Ye et al., *Two-orbital  $SU(N)$  magnetism with ultracold alkaline-earth atoms*, *Nature Physics* **6** (2010) 289 [[0905.2610](#)].
- [218] F. Scazza, C. Hofrichter, M. Höfer, P.C. De Groot, I. Bloch and S. Fölling, *Observation of two-orbital spin-exchange interactions with ultracold  $SU(N)$ -symmetric fermions*, *Nature Physics* **10** (2014) 779 [[1403.4761](#)].
- [219] S. Kivelson, *Wannier functions in one-dimensional disordered systems: Application to fractionally charged solitons*, *Phys. Rev. B* **26** (1982) 4269.
- [220] N. Marzari and D. Vanderbilt, *Maximally localized generalized Wannier functions for composite energy bands*, *Physical Review B - Condensed Matter and Materials Physics* **56** (1997) [[0108084](#)].
- [221] G. Cappellini, M. Mancini, G. Pagano, P. Lombardi, L. Livi, M. Siciliani de Cumis et al., *Direct Observation of Coherent Interorbital Spin-Exchange Dynamics*, *Phys. Rev. Lett.* **113** (2014) 120402.
- [222] M. Höfer, L. Riegger, F. Scazza, C. Hofrichter, D.R. Fernandes, M.M. Parish et al., *Observation of an orbital interaction-induced feshbach resonance in  $^{173}\text{Yb}$* , *Phys. Rev. Lett.* **115** (2015) 265302.
- [223] B.M. McCoy and T.T. Wu, *Two-dimensional Ising field theory in a magnetic field: Breakup of the cut in the two-point function*, *Phys. Rev. D* **18** (1978) 1259.
- [224] N. Ishimura and H. Shiba, *Dynamical Correlation Functions of One-Dimensional Anisotropic Heisenberg Model with Spin 1/2. I —Ising-Like Antiferromagnets—*, *Progress of Theoretical Physics* **63** (1980) 743.
- [225] B. Lake, A.M. Tsvelik, S. Notbohm, D. Alan Tennant, T.G. Perring, M. Reehuis et al., *Confinement of fractional quantum number particles in a condensed-matter system*, *Nature Physics* **6** (2009) 50.
- [226] C.M. Morris, R. Valdés Aguilar, A. Ghosh, S.M. Koohpayeh, J. Krizan, R.J. Cava et al., *Hierarchy of bound states in the one-dimensional ferromagnetic Ising chain  $\text{CoNb}_2\text{O}_6$  investigated by high-resolution time-domain terahertz spectroscopy.*, *Phys. Rev. Lett.* **112** (2014) 137403.

- [227] B. Grenier, S. Petit, V. Simonet, E. Canévet, L.-P. Regnault, S. Raymond et al., *Longitudinal and transverse Zeeman ladders in the Ising-like chain antiferromagnet BaCo(2)V(2)O(8)*, *Phys. Rev. Lett.* **114** (2015) 017201.
- [228] Z. Wang, M. Schmidt, A.K. Bera, A.T.M.N. Islam, B. Lake, A. Loidl et al., *Spinon confinement in the one-dimensional Ising-like antiferromagnet SrCo<sub>2</sub>V<sub>2</sub>O<sub>8</sub>*, *Phys. Rev. B* **91** (2015) 140404.
- [229] Z. Wang, J. Wu, S. Xu, W. Yang, C. Wu, A.K. Bera et al., *From confined spinons to emergent fermions: Observation of elementary magnetic excitations in a transverse-field Ising chain*, *Phys. Rev. B* **94** (2016) 125130.
- [230] Z. Wang, J. Wu, W. Yang, A.K. Bera, D. Kamenskyi, A.T. Islam et al., *Experimental observation of Bethe strings*, *Nature* **554** (2018) 219.
- [231] Z. Wang, M. Schmidt, A. Loidl, J. Wu, H. Zou, W. Yang et al., *Quantum Critical Dynamics of a Heisenberg-Ising Chain in a Longitudinal Field: Many-Body Strings versus Fractional Excitations*, *Phys. Rev. Lett.* **123** (2019) 067202.
- [232] S.B. Rutkevich, *Decay of the metastable phase in  $d = 1$  and  $d = 2$  ising models*, *Phys. Rev. B* **60** (1999) 14525.
- [233] M.J. Bhaseen and A.M. Tsvelik, *Aspects of Confinement in Low Dimensions*, *In: From Fields to Strings: Circumnavigating Theoretical Physics: Ian Kogan Memorial Collection (In 3 Volumes)* (2005) 661.
- [234] S.B. Rutkevich, *Large- $n$  Excitations in the Ferromagnetic Ising Field Theory in a Weak Magnetic Field: Mass Spectrum and Decay Widths*, *Phys. Rev. Lett.* **95** (2005) 250601.
- [235] K. Hida, *Haldane Gap in the Spin-1/2 Double Chain Heisenberg Antiferromagnet -Numerical Diagonalization and Projector Monte Carlo Study-*, *Journal of the Physical Society of Japan* **60** (1991) 1347.
- [236] D.G. Shelton, A.A. Nersesyan and A.M. Tsvelik, *Antiferromagnetic spin ladders: Crossover between spin  $s=1/2$  and  $s=1$  chains*, *Phys. Rev. B* **53** (1996) 8521.
- [237] A.A. Nersesyan and A.M. Tsvelik, *One-Dimensional Spin-Liquid without Magnon Excitations*, *Physical Review Letters* **78** (1997) 3939.

- [238] I. Affleck, *Soliton Confinement and the Excitation Spectrum of Spin-Peierls Antiferromagnets*, In: *Dynamical Properties of Unconventional Magnetic Systems. NATO ASI Series (Series E: Applied Sciences)* **349** (1998) .
- [239] D. Augier, E. Sørensen, J. Riera and D. Poilblanc, *Soliton bound states in the Raman spectrum of pure and doped spin-Peierls chains*, *Phys. Rev. B* **60** (1999) 1075.
- [240] M. Greiter, *Two-leg  $t - J$  ladder: A spin liquid generated by Gutzwiller projection of magnetic bands*, *Physical Review B* **65** (2002) 134443.
- [241] M. Greiter, *Fictitious flux confinement: Magnetic pairing in coupled spin chains or planes*, *Physical Review B* **66** (2002) 054505.
- [242] G. Delfino, G. Mussardo and P. Simonetti, *Non-integrable quantum field theories as perturbations of certain integrable models*, *Nuclear Physics B* **473** (1996) 469.
- [243] G. Delfino and G. Mussardo, *Non-integrable aspects of the multi-frequency sine-Gordon model*, *Nuclear Physics B* **516** (1998) 675.
- [244] P. Fonseca and A. Zamolodchikov, *Ising field theory in a magnetic field: analytic properties of the free energy*, *Journal of statistical physics* **110** (2003) 527.
- [245] P. Jung, R.W. Helmes and A. Rosch, *Transport in Almost Integrable Models: Perturbed Heisenberg Chains*, *Physical Review Letters* **96** (2006) 067202.
- [246] S.B. Rutkevich, *Energy spectrum of bound-spinons in the quantum ising spin-chain ferromagnet*, *Journal of Statistical Physics* **131** (2008) 917.
- [247] S.B. Rutkevich, *On the weak confinement of kinks in the one-dimensional quantum ferromagnet  $\text{CoNb}_2\text{O}_6$* , *Journal of Statistical Mechanics: Theory and Experiment* **2010** (2010) P07015.
- [248] R. Steinigeweg, J. Herbrych, X. Zotos and W. Brenig, *Heat conductivity of the Heisenberg spin-1/2 ladder: From weak to strong breaking of integrability*, *Physical Review Letters* **116** (2015) 017202.
- [249] A.K. Bera, B. Lake, F.H.L. Essler, L. Vanderstraeten, C. Hubig, U. Schollwöck et al., *Spinon confinement in a quasi-one-dimensional anisotropic Heisenberg magnet*, *Phys. Rev. B* **96** (2017) 054423.

- [250] T. Tonegawa, T. Hikihara, K. Okamoto, S.C. Furuya and T. Sakai, *Ground-State Phase Diagram of an Anisotropic  $S = 1/2$  Ladder with Different Leg Interactions*, *Journal of the Physical Society of Japan* **87** (2018) 104002.
- [251] S.B. Rutkevich, *Kink confinement in the antiferromagnetic XXZ spin-(1/2) chain in a weak staggered magnetic field*, *EPL* **121** (2018) 37001.
- [252] T. Suzuki and S.-i. Suga, *Quantized excitation spectra by magnon confinement in quasi-one-dimensional  $S = 1$  spin systems*, *Phys. Rev. B* **98** (2018) 180406.
- [253] Y. Fan, J. Yang, W. Yu, J. Wu and R. Yu, *Phase diagram and quantum criticality of Heisenberg spin chains with Ising anisotropic interchain couplings*, *Phys. Rev. Research* **2** (2020) 013345.
- [254] S. Pai and M. Pretko, *Fractons from confinement in one dimension*, *Phys. Rev. Research* **2** (2020) 013094.
- [255] N.J. Robinson, A.J.A. James and R.M. Konik, *Signatures of rare states and thermalization in a theory with confinement*, *Phys. Rev. B* **99** (2019) 195108.
- [256] F. Liu, R. Lundgren, P. Titum, G. Pagano, J. Zhang, C. Monroe et al., *Confined quasiparticle dynamics in long-range interacting quantum spin chains*, *Phys. Rev. Lett.* **122** (2019) 150601.
- [257] R. Verdel, F. Liu, S. Whitsitt, A.V. Gorshkov and M. Heyl, *Real-time dynamics of string breaking in quantum spin chains*, *Phys. Rev. B* **102** (2020) 014308.
- [258] O.A. Castro-Alvaredo, M. Lencsés, I.M. Szécsényi and J. Viti, *Entanglement oscillations near a quantum critical point*, *Phys. Rev. Lett.* **124** (2020) 230601.
- [259] J. Vovrosh and J. Knolle, *Confinement and Entanglement Dynamics on a Digital Quantum Computer*, *Scientific Reports* **11** (2020) 11577.
- [260] R.C. Myers, M. Rozali and B. Way, *Holographic quenches in a confined phase*, *Journal of Physics A: Mathematical and Theoretical* **50** (2017) 494002.
- [261] A.C. Cubero and N.J. Robinson, *Lack of thermalization in (1+1)-d QCD at large  $N_c$* , [1908.00270](#).
- [262] W. Tan, P. Becker, F. Liu, G. Pagano, K. Collins, A. De et al., *Domain-wall confinement and dynamics in a quantum simulator*, *Nature Physics* (2021) 1.

- [263] Z. Cai, C. Wu and U. Schollwöck, *Confinement: A real-time visualization*, *Phys. Rev. B* **85** (2012) 075102.
- [264] G. Magnifico, M. Dalmonte, P. Facchi, S. Pascazio, F.V. Pepe and E. Ercolessi, *Real Time Dynamics and Confinement in the  $\mathbb{Z}_n$  Schwinger-Weyl lattice model for 1+1 QED*, *Quantum* **4** (2020) 281.
- [265] J. Greensite, *An introduction to the confinement problem*, vol. 821, Springer (2011), [10.1007/978-3-642-14382-3](https://doi.org/10.1007/978-3-642-14382-3).
- [266] B. Hayes, *Computing science: Getting your quarks in a row*, *American Scientist* **96** (2008) 450.
- [267] H. Shiba, *Quantization of Magnetic Excitation Continuum Due to Interchain Coupling in Nearly One-Dimensional Ising-Like Antiferromagnets*, *Prog. Theor. Phys* **64** (1980) 466.
- [268] E. Sørensen, I. Affleck, D. Augier and D. Poilblanc, *Soliton approach to spin-peierls antiferromagnets: Large-scale numerical results*, *Phys. Rev. B* **58** (1998) R14701.
- [269] R. Shankar and G. Murthy, *Deconfinement in  $d = 1$ : Asymptotic and half-asymptotic particles*, *Phys. Rev. B* **72** (2005) 224414.
- [270] G. Delfino, P. Grinza and G. Mussardo, *Decay of particles above threshold in the Ising field theory with magnetic field*, *Nucl. Phys. B* **737** (2006) 291.
- [271] P. Fonseca and A. Zamolodchikov, *Ising Spectroscopy I: Mesons at  $T < T_c$* , [hep-th/0612304](https://arxiv.org/abs/hep-th/0612304).
- [272] B.M. McCoy, *The connection between statistical mechanics and quantum field theory*, [hep-th/9403084](https://arxiv.org/abs/hep-th/9403084).
- [273] R. Balian, J.M. Drouffe and C. Itzykson, *Gauge fields on a lattice. II. Gauge-invariant Ising model*, *Phys. Rev. D* **11** (1975) 2098.
- [274] L. Susskind, *Lattice fermions*, *Phys. Rev. D* **16** (1977) 3031.
- [275] U. Borla, R. Verresen, J. Shah and S. Moroz, *Gauging the Kitaev chain*, *SciPost Phys.* **10** (2021) 148.
- [276] P. Karpov, G.-Y. Zhu, M. Heller and M. Heyl, *Spatiotemporal dynamics of particle collisions in quantum spin chains*, [2011.11624](https://arxiv.org/abs/2011.11624).
- [277] A. Milsted, J. Liu, J. Preskill and G. Vidal, *Collisions of false-vacuum bubble walls in a quantum spin chain*, [2012.07243](https://arxiv.org/abs/2012.07243).

- [278] B. Buyens, J. Haegeman, F. Hebenstreit, F. Verstraete and K. Van Acoleyen, *Real-time simulation of the Schwinger effect with matrix product states*, *Phys. Rev. D* **96** (2017) 114501.
- [279] M.C. Bañuls, J.I. Cirac and M.B. Hastings, *Strong and weak thermalization of infinite nonintegrable quantum systems*, *Phys. Rev. Lett.* **106** (2011) 050405.
- [280] C.-J. Lin and O.I. Motrunich, *Quasiparticle explanation of the weak-thermalization regime under quench in a nonintegrable quantum spin chain*, *Phys. Rev. A* **95** (2017) 023621.
- [281] A. Leroš, B. Žunkovič, A. Silva and A. Gambassi, *Quasilocalized excitations induced by long-range interactions in translationally invariant quantum spin chains*, *Phys. Rev. B* **99** (2019) 121112.
- [282] R.V. Jensen and R. Shankar, *Statistical behavior in deterministic quantum systems with few degrees of freedom*, *Phys. Rev. Lett.* **54** (1985) 1879.
- [283] J. Eisert, M. Friesdorf and C. Gogolin, *Quantum many-body systems out of equilibrium*, *Nat. Phys.* **11** (2015) 124.
- [284] S. Goldstein, D.A. Huse, J.L. Lebowitz and R. Tumulka, *Thermal equilibrium of a macroscopic quantum system in a pure state*, *Phys. Rev. Lett.* **115** (2015) 100402.
- [285] T. Mori, T.N. Ikeda, E. Kaminishi and M. Ueda, *Thermalization and prethermalization in isolated quantum systems: a theoretical overview*, *J. Phys. B* **51** (2018) 112001.
- [286] G. Delfino, *Quantum quenches with integrable pre-quench dynamics*, *Journal of Physics A: Mathematical and Theoretical* **47** (2014) 402001.
- [287] D.A. Huse, R. Nandkishore and V. Oganesyan, *Phenomenology of fully many-body-localized systems*, *Phys. Rev. B* **90** (2014) 174202.
- [288] J.H. Bardarson, F. Pollmann and J.E. Moore, *Unbounded growth of entanglement in models of many-body localization*, *Phys. Rev. Lett.* **109** (2012) 017202.
- [289] R. Vasseur and J.E. Moore, *Nonequilibrium quantum dynamics and transport: from integrability to many-body localization*, *Journal of Statistical Mechanics: Theory and Experiment* **2016** (2016) 064010.
- [290] M. Serbyn, Z. Papić and D.A. Abanin, *Universal slow growth of entanglement in interacting strongly disordered systems*, *Phys. Rev. Lett.* **110** (2013) 260601.

- [291] M. Serbyn, Z. Papić and D.A. Abanin, *Criterion for many-body localization-delocalization phase transition*, *Phys. Rev. X* **5** (2015) 041047.
- [292] W. De Roeck and F.c. Huveneers, *Scenario for delocalization in translation-invariant systems*, *Phys. Rev. B* **90** (2014) 165137.
- [293] W. De Roeck and F. Huveneers, *Asymptotic quantum many-body localization from thermal disorder*, *Comm. Math. Phys.* **332** (2014) 1017.
- [294] M. Schiulaz, A. Silva and M. Müller, *Dynamics in many-body localized quantum systems without disorder*, *Phys. Rev. B* **91** (2015) 184202.
- [295] N.Y. Yao, C.R. Laumann, J.I. Cirac, M.D. Lukin and J.E. Moore, *Quasi-many-body localization in translation-invariant systems*, *Phys. Rev. Lett.* **117** (2016) 240601.
- [296] G. Carleo, F. Becca, M. Schirò and M. Fabrizio, *Localization and glassy dynamics of many-body quantum systems*, *Scientific Reports* **2** (2012) 243.
- [297] A. Bols and W. De Roeck, *Asymptotic localization in the Bose-Hubbard model*, *J. Math. Phys.* **59** (2018) 021901.
- [298] J.M. Hickey, S. Genway and J.P. Garrahan, *Signatures of many-body localisation in a system without disorder and the relation to a glass transition*, *J. Stat. Mech.: Theory Exp.* **2016** (2016) 054047.
- [299] M. van Horsen, E. Levi and J.P. Garrahan, *Dynamics of many-body localization in a translation-invariant quantum glass model*, *Phys. Rev. B* **92** (2015) 100305.
- [300] A.A. Michailidis, M. Žnidarič, M. Medvedyeva, D.A. Abanin, T. Prosen and Z. Papić, *Slow dynamics in translation-invariant quantum lattice models*, *Phys. Rev. B* **97** (2018) 104307.
- [301] S. Choudhury, E. Kim and Q. Zhou, *Frustration induced quasi-many-body localization without disorder*, [1807.05969](https://arxiv.org/abs/1807.05969).
- [302] E. van Nieuwenburg, Y. Baum and G. Refael, *From Bloch oscillations to many-body localization in clean interacting systems*, *PNAS* **116** (2019) 9269.
- [303] M. Schulz, C.A. Hooley, R. Moessner and F. Pollmann, *Stark many-body localization*, *Phys. Rev. Lett.* **122** (2019) 040606.

- [304] J. Schwinger, *On gauge invariance and vacuum polarization*, *Phys. Rev.* **82** (1951) 664.
- [305] G.H. Wannier, *Wave Functions and Effective Hamiltonian for Bloch Electrons in an Electric Field*, *Phys. Rev.* **117** (1960) 432.
- [306] G. Vidal, *Classical simulation of infinite-size quantum lattice systems in one spatial dimension*, *Phys. Rev. Lett.* **98** (2007) 070201.
- [307] N. Datta, J. Frohlich, L. Rey-Bellet and R. Fernández, *Low-temperature phase diagrams of quantum lattice systems. ii. convergent perturbation expansions and stability in systems with infinite degeneracy*, *Helvetica Physica Acta* **69** (1996) 752.
- [308] S. Bravyi, D.P. DiVincenzo and D. Loss, *Schrieffer–Wolff transformation for quantum many-body systems*, *Ann. Phys.* **326** (2011) 2793 .
- [309] A.H. MacDonald, S.M. Girvin and D. Yoshioka,  $\frac{t}{U}$  expansion for the Hubbard model, *Phys. Rev. B* **37** (1988) 9753.
- [310] D. Abanin, W. De Roeck, W.W. Ho and F. Huveneers, *A rigorous theory of many-body prethermalization for periodically driven and closed quantum systems*, *Commun. Math. Phys.* **354** (2017) 809.
- [311] W. De Roeck and V. Verreet, *Very slow heating for weakly driven quantum many-body systems*, [1911.01998](https://arxiv.org/abs/1911.01998).
- [312] C.-J. Lin and O.I. Motrunich, *Explicit construction of quasiconserved local operator of translationally invariant nonintegrable quantum spin chain in prethermalization*, *Phys. Rev. B* **96** (2017) 214301.
- [313] D.V. Else, W.W. Ho and P.T. Dumitrescu, *Long-Lived Interacting Phases of Matter Protected by Multiple Time-Translation Symmetries in Quasiperiodically Driven Systems*, *Phys. Rev. X* **10** (2020) 021032.
- [314] C. Itzykson and J.-B. Zuber, *Quantum Field Theory*, Dover (2006).
- [315] H. Fukuyama, R.A. Bari and H.C. Fogedby, *Tightly bound electrons in a uniform electric field*, *Phys. Rev. B* **8** (1973) 5579.
- [316] H.C. Fogedby, *The Ising chain in a skew magnetic field*, *J. Phys. C: Solid State Phys.* **11** (1978) 2801.
- [317] P. Calabrese and J. Cardy, *Entanglement entropy and quantum field theory*, *Journal of Statistical Mechanics: Theory and Experiment* **2004** (2004) P06002.

- [318] P. Calabrese and J. Cardy, *Evolution of entanglement entropy in one-dimensional systems*, *Journal of Statistical Mechanics: Theory and Experiment* **2005** (2005) P04010.
- [319] M. Fagotti and P. Calabrese, *Evolution of entanglement entropy following a quantum quench: Analytic results for the XY chain in a transverse magnetic field*, *Phys. Rev. A* **78** (2008) 010306.
- [320] V. Alba and P. Calabrese, *Entanglement dynamics after quantum quenches in generic integrable systems*, *SciPost Phys.* **4** (2018) 17.
- [321] H. Kim and D.A. Huse, *Ballistic spreading of entanglement in a diffusive nonintegrable system*, *Phys. Rev. Lett.* **111** (2013) 127205.
- [322] A. Nahum, J. Ruhman, S. Vijay and J. Haah, *Quantum entanglement growth under random unitary dynamics*, *Phys. Rev. X* **7** (2017) 031016.
- [323] A. Chan, A. De Luca and J.T. Chalker, *Solution of a minimal model for many-body quantum chaos*, *Phys. Rev. X* **8** (2018) 041019.
- [324] A. Smith, J. Knolle, R. Moessner and D.L. Kovrizhin, *Absence of ergodicity without quenched disorder: From quantum disentangled liquids to many-body localization*, *Phys. Rev. Lett.* **119** (2017) 176601.
- [325] A. Smith, J. Knolle, R. Moessner and D.L. Kovrizhin, *Dynamical localization in  $\mathbb{Z}_2$  lattice gauge theories*, *Phys. Rev. B* **97** (2018) 245137.
- [326] W.H. Zurek, U. Dorner and P. Zoller, *Dynamics of a quantum phase transition*, *Phys. Rev. Lett.* **95** (2005) 105701.
- [327] Z. Lan, M. van Horssen, S. Powell and J.P. Garrahan, *Quantum slow relaxation and metastability due to dynamical constraints*, *Phys. Rev. Lett.* **121** (2018) 040603.
- [328] N. Pancotti, G. Giudice, J.I. Cirac, J.P. Garrahan and M.C. Bañuls, *Quantum East Model: Localization, Nonthermal Eigenstates, and Slow Dynamics*, *Phys. Rev. X* **10** (2020) 021051.
- [329] A. Smith, J. Knolle, D.L. Kovrizhin and R. Moessner, *Disorder-free localization*, *Phys. Rev. Lett.* **118** (2017) 266601.
- [330] S. Kühn, E. Zohar, J.I. Cirac and M.C. Bañuls, *Non-abelian string breaking phenomena with matrix product states*, *J. High Energy Phys* **2015** (2015) 130.

- [331] K. Rajagopal and F. Wilczek, *The Condensed Matter Physics of QCD*, *In: At The Frontier of Particle Physics* (2001) 2061.
- [332] G. 't Hooft, *A two-dimensional model for mesons*, *Nuclear Physics B* **75** (1974) 461.
- [333] B. Buyens, J. Haegeman, K. Van Acoleyen, H. Verschelde and F. Verstraete, *Matrix Product States for Gauge Field Theories*, *Phys. Rev. Lett.* **113** (2014) 091601.
- [334] T. Norsen, J. Lande and S.B. McKagan, *How and why to think about scattering in terms of wave packets instead of plane waves*, [0808.3566](#).
- [335] J. Simon, W.S. Bakr, R. Ma, M.E. Tai, P.M. Preiss and M. Greiner, *Quantum simulation of antiferromagnetic spin chains in an optical lattice*, *Nature* **472** (2011) 307.
- [336] F. Meinert, M.J. Mark, E. Kirilov, K. Lauber, P. Weinmann, A.J. Daley et al., *Quantum Quench in an Atomic One-Dimensional Ising Chain*, *Phys. Rev. Lett.* **111** (2013) 053003.
- [337] S. de Léséleuc, S. Weber, V. Lienhard, D. Barredo, H.P. Büchler, T. Lahaye et al., *Accurate Mapping of Multilevel Rydberg Atoms on Interacting Spin-1/2 Particles for the Quantum Simulation of Ising Models*, *Phys. Rev. Lett.* **120** (2018) 113602.
- [338] Z. Tu, D.E. Kharzeev and T. Ullrich, *Einstein-Podolsky-Rosen Paradox and Quantum Entanglement at Subnucleonic Scales*, *Phys. Rev. Lett.* **124** (2020) 062001.
- [339] D.E. Kharzeev and E.M. Levin, *Deep inelastic scattering as a probe of entanglement*, *Phys. Rev. D* **95** (2017) 114008.
- [340] C. Gutfeld, H. Kastrup, K. Stergios and J. Westphalen, *Meson-meson scattering in the massive Schwinger model — a status report*, *Nuclear Physics B - Proceedings Supplements* **63** (1998) 266 .
- [341] S. Dürr, Z. Fodor, J. Frison, C. Hoelbling, R. Hoffmann, S.D. Katz et al., *Ab Initio Determination of Light Hadron Masses*, *Science* **322** (2008) 1224.
- [342] M. Rigobello, S. Notarnicola, G. Magnifico and S. Montangelo, *Entanglement generation in QED scattering processes*, [2105.03445](#).
- [343] S. Coleman, *Fate of the false vacuum: Semiclassical theory*, *Phys. Rev. D* **15** (1977) 2929.

- [344] C.G. Callan and S. Coleman, *Fate of the false vacuum. II. First quantum corrections*, *Phys. Rev. D* **16** (1977) 1762.
- [345] S. Coleman and F. De Luccia, *Gravitational effects on and of vacuum decay*, *Phys. Rev. D* **21** (1980) 3305.
- [346] M.S. Turner and F. Wilczek, *Is our vacuum metastable*, *Nature* **298** (1982) 633.
- [347] T. Byrnes, P. Sriganesh, R. Bursill and C. Hamer, *Density matrix renormalisation group approach to the massive Schwinger model*, *Nuclear Physics B - Proceedings Supplements* **109** (2002) 202.
- [348] M.C. Banuls, K. Cichy, J.I. Cirac, K. Jansen and H. Saito, *Matrix Product States for Lattice Field Theories*, *PoS LATTICE* **2013** (2014) 332.
- [349] P. Silvi, E. Rico, T. Calarco and S. Montangero, *Lattice gauge tensor networks*, *New Journal of Physics* **16** (2014) 103015.
- [350] L. Tagliacozzo, A. Celi and M. Lewenstein, *Tensor Networks for Lattice Gauge Theories with Continuous Groups*, *Phys. Rev. X* **4** (2014) 041024.
- [351] M.C. Bañuls and K. Cichy, *Review on novel methods for lattice gauge theories*, *Reports on Progress in Physics* **83** (2020) 024401.
- [352] T.P. Billam, R. Gregory, F. Michel and I.G. Moss, *Simulating seeded vacuum decay in a cold atom system*, *Physical Review D* **100** (2019) 065016.
- [353] T.P. Billam, K. Brown and I.G. Moss, *Simulating cosmological supercooling with a cold-atom system*, *Physical Review A* **102** (2020) 043324.
- [354] S. Abel and M. Spannowsky, *Quantum-field-theoretic simulation platform for observing the fate of the false vacuum*, *PRX Quantum* **2** (2021) 010349.
- [355] K.L. Ng, B. Opanchuk, M. Thenabadu, M. Reid and P.D. Drummond, *Fate of the false vacuum: Finite temperature, entropy, and topological phase in quantum simulations of the early universe*, *PRX Quantum* **2** (2021) 010350.
- [356] T.P. Billam, K. Brown, A.J. Groszek and I.G. Moss, *Simulating cosmological supercooling with a cold atom system II*, [2104.07428](#).
- [357] A. Sinha, T. Chanda and J. Dziarmaga, *Nonadiabatic dynamics across a first-order quantum phase transition: Quantized bubble nucleation*, *Physical Review B* **103** (2021) L220302.

- [358] R.J.V. Tortora, P. Calabrese and M. Collura, *Relaxation of the order-parameter statistics and dynamical confinement*, *EPL (Europhysics Letters)* **132** (2020) 50001.
- [359] S. Sachdev, *Quantum Phase Transitions*, Cambridge University Press (1999).
- [360] G. Mussardo, *Statistical field theory: an introduction to exactly solved models in statistical physics; 1st ed.*, Oxford graduate texts, Oxford Univ. Press, New York, NY (2010).
- [361] D. Spitz and J. Berges, *Schwinger pair production and string breaking in non-Abelian gauge theory from real-time lattice improved Hamiltonians*, *Physical Review D* **99** (2019) 036020.
- [362] O. Pomponio, M. Werner, G. Zarand and G. Takacs, *Bloch oscillations and the lack of the decay of the false vacuum in a one-dimensional quantum spin chain*, [2105.00014](#).
- [363] H.J. Schulz, *Dynamics of Coupled Quantum Spin Chains*, *Phys. Rev. Lett.* **77** (1996) 2790.
- [364] F.H.L. Essler, A.M. Tsvelik and G. Delfino, *Quasi-one-dimensional spin- $\frac{1}{2}$  Heisenberg magnets in their ordered phase: Correlation functions*, *Phys. Rev. B* **56** (1997) 11001.
- [365] A.W. Sandvik, *Multichain mean-field theory of quasi-one-dimensional quantum spin systems*, *Phys. Rev. Lett.* **83** (1999) 3069.
- [366] G. Pagano, M. Mancini, G. Cappellini, P. Lombardi, F. Schäfer, H. Hu et al., *A one-dimensional liquid of fermions with tunable spin*, *Nature Physics* **10** (2014) 198.
- [367] A. LeClair, A. Ludwig and G. Mussardo, *Integrability of coupled conformal field theories*, *Nuclear Physics B* **512** (1998) 523.
- [368] A. Zabrodin, *Integrable models of field theory and scattering on quantum hyperboloids*, *Modern Physics Letters A* **07** (1992) 441.
- [369] I.V. Gornyi, A.D. Mirlin and D.G. Polyakov, *Interacting Electrons in Disordered Wires: Anderson Localization and Low-T Transport*, *Phys. Rev. Lett.* **95** (2005) 206603.
- [370] E. Altman and R. Vosk, *Universal dynamics and renormalization in many-body-localized systems*, *Annual Review of Condensed Matter Physics* **6** (2015) 383.

- [371] R. Nandkishore and D.A. Huse, *Many-body localization and thermalization in quantum statistical mechanics*, *Annual Review of Condensed Matter Physics* **6** (2015) 15.
- [372] F. Haake, *Quantum signatures of chaos*, in *Quantum Coherence in Mesoscopic Systems*, pp. 583–595, Springer (1991).
- [373] L. Fleishman and P.W. Anderson, *Interactions and the anderson transition*, *Phys. Rev. B* **21** (1980) 2366.
- [374] B.L. Altshuler, Y. Gefen, A. Kamenev and L.S. Levitov, *Quasiparticle lifetime in a finite system: A nonperturbative approach*, *Phys. Rev. Lett.* **78** (1997) 2803.
- [375] J.Z. Imbrie, *On Many-Body Localization for Quantum Spin Chains*, *Journal of Statistical Physics* **163** (2016) 998.
- [376] V. Ros, M. Müller and A. Scardicchio, *Integrals of motion in the many-body localized phase*, *Nuclear Physics B* **891** (2015) 420.
- [377] W. De Roeck and F. Huveneers, *Asymptotic quantum many-body localization from thermal disorder*, *Communications in Mathematical Physics* **332** (2014) 1017.
- [378] W. De Roeck and F. Huveneers, *Scenario for delocalization in translation-invariant systems*, *Phys. Rev. B* **90** (2014) 165137.
- [379] W. De Roeck, F. Huveneers, M. Müller and M. Schiulaz, *Absence of many-body mobility edges*, *Physical Review B* **93** (2016) 014203.
- [380] A. Chandran, A. Pal, C.R. Laumann and A. Scardicchio, *Many-body localization beyond eigenstates in all dimensions*, *Phys. Rev. B* **94** (2016) 144203.
- [381] P. Prelovšek, O.S. Barišić and M. Žnidarič, *Absence of full many-body localization in the disordered hubbard chain*, *Physical Review B* **94** (2016) 241104.
- [382] A.C. Potter and R. Vasseur, *Symmetry constraints on many-body localization*, *Physical Review B* **94** (2016) 224206.
- [383] I.V. Protopopov, W.W. Ho and D.A. Abanin, *Effect of  $su(2)$  symmetry on many-body localization and thermalization*, *Physical Review B* **96** (2017) 041122.
- [384] I.V. Protopopov, R.K. Panda, T. Parolini, A. Scardicchio, E. Demler and D.A. Abanin, *Non-Abelian Symmetries and Disorder: A Broad Nonergodic Regime and Anomalous Thermalization*, *Phys. Rev. X* **10** (2020) 011025.

- [385] A. De Luca and A. Scardicchio, *Ergodicity breaking in a model showing many-body localization*, *Europhys. Lett.* **101** (2013) 37003.
- [386] J. Goold, C. Gogolin, S.R. Clark, J. Eisert, A. Scardicchio and A. Silva, *Total correlations of the diagonal ensemble herald the many-body localization transition*, *Phys. Rev. B* **92** (2015) 180202.
- [387] F. Pietracaprina, G. Parisi, A. Mariano, S. Pascazio and A. Scardicchio, *Entanglement critical length at the many-body localization transition*, *Journal of Statistical Mechanics: Theory and Experiment* **2017** (2017) 113102.
- [388] M. Žnidarič, A. Scardicchio and V.K. Varma, *Diffusive and Subdiffusive Spin Transport in the Ergodic Phase of a Many-Body Localizable System*, *Phys. Rev. Lett.* **117** (2016) 040601.
- [389] F. Alet and N. Laflorencie, *Many-body localization: an introduction and selected topics*, *Comptes Rendus Physique* **19** (2018) 498.
- [390] N. Macé, F. Alet and N. Laflorencie, *Multifractal scalings across the many-body localization transition*, *Physical review letters* **123** (2019) 180601.
- [391] R. Vosk, D.A. Huse and E. Altman, *Theory of the Many-Body Localization Transition in One-Dimensional Systems*, *Phys. Rev. X* **5** (2015) 031032.
- [392] P.T. Dumitrescu, A. Goremykina, S.A. Parameswaran, M. Serbyn and R. Vasseur, *Kosterlitz-thouless scaling at many-body localization phase transitions*, *Physical Review B* **99** (2019) 094205.
- [393] A. Chandran, C.R. Laumann and V. Oganesyan, *Finite size scaling bounds on many-body localized phase transitions*, **1509.04285**.
- [394] A.B. Harris, *Effect of random defects on the critical behaviour of ising models*, *Journal of Physics C: Solid State Physics* **7** (1974) 1671.
- [395] J. Šuntajs, J. Bonča, T.c.v. Prosen and L. Vidmar, *Quantum chaos challenges many-body localization*, *Phys. Rev. E* **102** (2020) 062144.
- [396] P. Sierant, D. Delande and J. Zakrzewski, *Thouless time analysis of anderson and many-body localization transitions*, *Phys. Rev. Lett.* **124** (2020) 186601.
- [397] D. Abanin, J. Bardarson, G. De Tomasi, S. Gopalakrishnan, V. Khemani, S. Parameswaran et al., *Distinguishing localization from chaos: Challenges in finite-size systems*, *Annals of Physics* **427** (2021) 168415.

- [398] R.K. Panda, A. Scardicchio, M. Schulz, S.R. Taylor and M. Žnidarič, *Can we study the many-body localisation transition?*, *EPL (Europhysics Letters)* **128** (2020) 67003.
- [399] M. Schreiber, S.S. Hodgman, P. Bordia, H.P. Lüschen, M.H. Fischer, R. Vosk et al., *Observation of many-body localization of interacting fermions in a quasi-random optical lattice*, *Science* **349** (2015) 842.
- [400] J. Smith, A. Lee, P. Richerme, B. Neyenhuis, P.W. Hess, P. Hauke et al., *Many-body localization in a quantum simulator with programmable random disorder*, *Nat. Phys.* **12** (2016) 907.
- [401] A.L. Burin, *Energy delocalization in strongly disordered systems induced by the long-range many-body interaction*, *arXiv preprint cond-mat/0611387* (2006) .
- [402] N.Y. Yao, C.R. Laumann, S. Gopalakrishnan, M. Knap, M. Müller, E.A. Demler et al., *Many-body localization in dipolar systems*, *Phys. Rev. Lett.* **113** (2014) 243002.
- [403] A.L. Burin, *Localization in a random xy model with long-range interactions: intermediate case between single-particle and many-body problems*, *Physical Review B* **92** (2015) 104428.
- [404] R.M. Nandkishore and S. Sondhi, *Many-body localization with long-range interactions*, *Physical Review X* **7** (2017) .
- [405] A.A. Akhtar, R.M. Nandkishore and S.L. Sondhi, *Symmetry breaking and localization in a random schwinger model with commensuration*, *Phys. Rev. B* **98** (2018) 115109.
- [406] P. Sierant and J. Zakrzewski, *Many-body localization of bosons in optical lattices*, *New Journal of Physics* **20** (2018) 043032.
- [407] V.E. Kravtsov, I.M. Khaymovich, E. Cuevas and M. Amini, *A random matrix model with localization and ergodic transitions*, *New Journal of Physics* **17** (2015) 122002.
- [408] M. Serbyn, Z. Papić and D.A. Abanin, *Thouless energy and multifractality across the many-body localization transition*, *Physical Review B* **96** (2017) .
- [409] K. Agarwal, S. Gopalakrishnan, M. Knap, M. Müller and E. Demler, *Anomalous diffusion and griffiths effects near the many-body localization transition*, *Phys. Rev. Lett.* **114** (2015) 160401.
- [410] D.J. Luitz and Y. Bar Lev, *Anomalous thermalization in ergodic systems*, *Phys. Rev. Lett.* **117** (2016) 170404.

- [411] D.J. Luitz and Y.B. Lev, *The ergodic side of the many-body localization transition*, *Annalen der Physik* **529** (2017) 1600350.
- [412] D.J. Luitz, I.M. Khaymovich and Y.B. Lev, *Multifractality and its role in anomalous transport in the disordered XXZ spin-chain*, *SciPost Phys. Core* **2** (2020) 6.
- [413] S. Coleman, *Quantum sine-Gordon equation as the massive Thirring model*, *Phys. Rev. D* **11** (1975) 2088.
- [414] G.H. Wannier, *The structure of electronic excitation levels in insulating crystals*, *Phys. Rev.* **52** (1937) 191.
- [415] T. Uehlinger, G. Jotzu, M. Messer, D. Greif, W. Hofstetter, U. Bissbort et al., *Artificial graphene with tunable interactions*, *Physical Review Letters* **111** (2013) [1308.4401].
- [416] M. Abramowitz and I.A. Stegun, *Handbook of Mathematical Functions with Formulas, Graphs, and Mathematical Tables*, Applied mathematics series, Dover, New York, ninth dover printing, tenth gpo printing ed. (1965).
- [417] “*NIST Digital Library of Mathematical Functions.*” <http://dlmf.nist.gov/>, Release 1.0.24 of 2019-09-15.
- [418] J.D. Johnson, S. Krinsky and B.M. McCoy, *Vertical-Arrow Correlation Length in the Eight-Vertex Model and the Low-Lying Excitations of the  $X - Y - Z$  Hamiltonian*, *Phys. Rev. A* **8** (1973) 2526.